



**DEVELOPMENT OF SMOOTHED FINITE
ELEMENT METHOD (SFEM)**

NGUYEN THOI TRUNG

(B.Eng, Polytechnic, Vietnam; B.Sci, Science, Vietnam;
M.Sci, Science, Vietnam; M.Eng, Liege, Belgium)

A THESIS SUBMITTED
FOR THE DEGREE OF DOCTOR OF PHILOSOPHY
DEPARTMENT OF MECHANICAL ENGINEERING
NATIONAL UNIVERSITY OF SINGAPORE

2009

Acknowledgements

I would like to express my deepest gratitude to my main supervisor, Prof. Liu Gui Rong, for his dedicated support, guidance and continuous encouragement during my Ph.D. study. To me, Prof. Liu is also kind mentor who inspires me not only in my research work but also in many aspects of my life.

I would also like to extend a great thank to my co-supervisor, Prof. Lam Khin Yong, for his valuable advices in many aspects of my research work.

To my family: Mother, two younger sisters, I greatly appreciate their eternal love and strong support. Special, thanks are conveyed to my Mother, who sacrificed all her life to bring up and support her children. I am really indebted to her a lot. Without her endless encouragement, understanding and full support, it is impossible to finish this thesis. I also express my deepest gratitude to my deceased Father who has always supported my spirit, especially in the most difficult moments. I also want to send the dearest love to my daughter: Nguyen Phan Minh Tu (Alpha) who always gives me the motivation to create, especially for two new methods: Alpha-FEM-Q4 and Alpha-FEM-T3/Alpha-FEM-T4.

Highly appreciation is extended to my closest friend: Dr. Nguyen Xuan Hung for the interactive discussion, professional opinions, full cooperation and future objectives.

I would also like to give many thanks to my fellow colleagues and friends in Center for ACES, Dr. Li Zirui, Dr Dai Keyang, Dr. Zhang Guiyong, Dr. Bernard Kee Buck Tong, Dr. Deng Bin, Dr. Zhang Jian, Dr. Khin Zaw, Dr. Song Chenxiang, Dr. Xu Xu, Dr. Zhang Zhiqian, Dr. Bao Phuong, Mr. Chenlei, Mrs Nasibeh, Mr Li Quang Binh, etc. The constructive suggestions, professional opinions, interactive discussion among our group definitely help to improve the quality of my research work. And most importantly, these guys have made my life in Center for ACES a joyful one.

I am also indebted to my close friends at NUS: Dr. Tran Chi Trung, Dr. Luong Van Hai, Mr. Tran Viet Anh for the help, the cooperation and the understanding during four last years.

I would also like to give many thanks to my friends at NUS: Mr. Vu Duc Huan, Mr. Vo Trong Nghia, Mr. Ngo Minh Hung, Mr. Tran Hien, Mr. Truong Manh Thang, Mr. Trinh Ngoc Thanh, Mr. Pham Quang Son, Mrs. Nguyen Thi Hien Luong, Mr. Vu Do Huy Cuong, Mr. Tran Duc Chuyen, Mr. Luong Van Tuyen, Mr. Nguyen Bao Thanh, Dr. Vu Khac Kien, Mr. Nguyen Hoang Dat, etc, who have made my life in Singapore a joyful one and a new family.

Lastly, I appreciate the National University of Singapore for granting me research scholarship which makes my Ph.D. study possible. Many thanks are conveyed to Mechanical department and Center for ACES for their material support to every aspect of this work.

Table of contents

Acknowledgements	i
Table of contents	iii
Summary.....	viii
Nomenclature	x
List of Figures.....	xiv
List of Tables	xxvi
Chapter 1 Introduction	1
1.1. Background	2
1.1.1 Background of the Finite Element Method (FEM)	3
1.1.2 General procedure of the FEM	4
1.1.3 Some main features of the FEM	9
1.1.4 Motivation of the thesis	11
1.2. Strain smoothing technique	12
1.3. Objectives of the thesis	13
1.4. Organization of the thesis	15
Chapter 2 Brief on the Finite Element Method (FEM)	18
2.1 Brief on governing equations for elastic solid mechanics problems	19
2.2 Hilbert spaces	20
2.3 Brief on the variational formulation and weak form	25
2.4 Domain discretization: creation of finite-dimensional space.....	27
2.5 Formulation of discretized linear system of equations	29
2.6 FEM solution: existence, uniqueness, error and convergence.....	31
2.7 Some other properties of the FEM solution.....	34
Chapter 3 Fundamental theories of smoothed finite element methods (S-FEM)	36
3.1 General formulation of the S-FEM models	36
3.1.1 Strain smoothing technique	36

3.1.2	Smoothing domain creation	38
3.1.3	Smoothed strain field	39
3.1.4	Smoothed strain-displacement matrix.....	41
3.1.5	Smoothed stiffness matrix.....	43
3.2	Construction of shape functions for the S-FEM models	45
3.3	Minimum number of smoothing domains	48
3.4	Numerical procedure for the S-FEM models.....	50
3.5	General properties of the S-FEM models	51
 Chapter 4 Cell-based Smoothed FEM (CS-FEM)		64
4.1	Creation of the cell-based smoothing domains	64
4.2	Formulation of the CS-FEM for quadrilateral elements	65
4.3	Formulation of the CS-FEM for n -sided polygonal elements	65
4.4	Evaluation of shape functions in the CS-FEM and n CS-FEM	66
4.5	Some properties of the CS-FEM	70
4.6	Domain discretization with polygonal elements.....	74
4.7	Standard patch test	75
4.8	Stability of the CS-FEM and n CS-FEM	76
4.9	Selective CS-FEM: volumetric locking free.....	78
4.10	Numerical examples.....	79
4.10.1	A rectangular cantilever loaded at the end	81
4.10.2	Infinite plate with a circular hole.....	84
4.11	Concluding remarks	87
 Chapter 5 Node-based Smoothed FEM (NS-FEM)		110
5.1	Introduction	110
5.2	Creation of the node-based smoothing domains	112
5.3	Formulation of the NS-FEM	113
5.3.1	General formulation	113
5.3.2	NS-FEM-T3 for 2D problems	113
5.3.3	NS-FEM-T4 for 3D problems	114
5.4	Evaluation of the shape function values in the NS-FEM	115
5.5	Properties of the NS-FEM	117
5.6	Numerical implementation	118

5.6.1	Rank test for the stiffness matrix: stability analysis	118
5.6.2	Standard 2D patch tests	119
5.6.3	Standard 3D patch tests and a mesh sensitivity analysis	119
5.7	Numerical examples	121
5.7.1	A rectangular cantilever loaded at the end	123
5.7.2	Infinite plate with a circular hole	125
5.7.3	3-D Lamé problem	127
5.7.4	3D cubic cantilever: an analysis about the upper bound property	128
5.7.5	A 3D L-shaped block: an analysis about the upper bound property	129
5.8	Remarks	129
Chapter 6 Edge-based Smoothed FEM (ES-FEM)		151
6.1	Introduction	151
6.2	Creation of edge-based smoothing domains	152
6.3	Formulation of the ES-FEM	153
6.3.1	Static analyses	153
6.3.2	Dynamic analyses	154
6.4	Evaluation of the shape function values in the ES-FEM	156
6.5	A smoothing-domain-based selective ES/NS-FEM	157
6.6	Numerical implementation	159
6.6.1	Rank analysis for the ES-FEM stiffness matrix	159
6.6.2	Temporal stability of the ES-FEM-T3	160
6.6.3	Standard patch test	161
6.6.4	Mass matrix for dynamic analysis	162
6.7	Numerical examples	162
6.7.1	A rectangular cantilever loaded at the end: a static analysis	163
6.7.2	Infinite plate with a circular hole: a static analysis	165
6.7.3	A cylindrical pipe subjected to an inner pressure: a static analysis	168
6.7.4	Free vibration analysis of a shear wall	170
6.7.5	Free vibration analysis of a connecting rod	171
6.7.6	Transient vibration analysis of a cantilever beam	172
6.7.7	Transient vibration analysis of a spherical shell	172
6.8	Remarks	173

Chapter 7 Face-based Smoothed FEM (FS-FEM)	212
7.1 Introduction	212
7.2 Creation of the face-based smoothing domains	214
7.3 Formulation of the FS-FEM-T4.....	214
7.3.1 Static analysis	214
7.3.2 Nonlinear analysis of large deformation	216
7.4 A smoothing-domain-based selective FS/NS-FEM-T4 model	218
7.5 Stability of the FS-FEM-T4	219
7.6 Irons first-order patch test and a mesh sensitivity analysis	220
7.7 Numerical examples	220
7.7.1 3D Lamé problem: a linear elasticity analysis	221
7.7.2 A 3D cubic cantilever: a linear elasticity analysis	223
7.7.3 A 3D cantilever beam: a geometrically nonlinear analysis	223
7.7.4 An axletree base: a geometrically nonlinear analysis	225
7.8 Remarks	226
Chapter 8: Alpha FEM using triangular (αFEM-T3) and tetrahedral elements	
(αFEM-T4)	237
8.1 Introduction	237
8.2 Idea of the α FEM-T3 and α FEM-T4	238
8.2.1 α FEM-T3 for 2D problems	238
8.2.2 α FEM-T4 for 3D problems	241
8.2.3 Properties of the α FEM-T3 and α FEM-T4	241
8.3 Nearly exact solution for linear elastic problems	247
8.4 Standard patch tests	249
8.4.1 Standard patch test for 2D problems	249
8.4.2 Irons first-order patch test for 3D problems	249
8.5 Numerical examples	250
8.5.1 A cantilever beam under a tip load: a convergence study	250
8.5.2 Cook's membrane: test for membrane elements	251
8.5.3 Semi-infinite plane: a convergence study	252
8.5.4 3D Lamé problem: a convergence study	254
8.5.5 3D cubic cantilever: accuracy study	255

8.5.6	A 3D L-shaped block: accuracy study	256
8.6	Remarks	257
Chapter 9 Conclusions and Recommendations		276
9.1	Conclusions Remarks	276
9.1.1	Original contributions	277
9.1.2	Some insight comments	282
9.1.3	Crucial contributions	283
9.2	Recommendations for future work	285
References		287
Publications arising from the thesis		299

Summary

Among the methods which require meshing, the standard FEM or the compatible displacement FEM derived from the minimum potential energy principle is considered to be the most important.

Compared to other numerical methods, the FEM has three following main advantages:

(1) The FEM can handle relatively easily the problems with different continuums of matter, complicated geometry, general boundary condition, multi-material domains or nonlinear material properties.

(2) The FEM has a clear structure and versatility which make it easy to comprehend and feasible to construct general purpose software packages for applications.

(3) The FEM has a solid theoretical foundation which gives high reliability and in many cases makes it possible to mathematically analyze and estimate the error of the approximate finite element solution.

However, using the lower-order elements, the FEM has also three following major shortcomings associated with a fully-compatible model:

(1) Overly-stiffness and inaccuracy in stress solutions of triangular and tetrahedral elements.

(2) Existence of constraint conditions on constructing the shape functions of approximation functions and on the shape of elements used.

(3) Difficulty of finding an FEM model which produces an upper bound of the exact solution to facilitate the procedure of evaluating the quality of numerical solutions (the global error, bounds of solutions, convergence rates, etc).

To overcome these three shortcomings of FEM, this thesis focuses on formulating and developing five new FEM models, including four smoothed FEM (S-FEM) models and one alpha-FEM model by combining the existing standard FEM and the strain smoothing technique used in Meshfree methods. The results of the research showed following four crucial contributions:

First, four S-FEM models and the α FEM, are promising to provide more feasible options for numerical methods in terms of high accuracy, low computational cost, easy implementation, versatility and general applicability (especially for the methods using triangular and tetrahedral elements). Four S-FEM models and the α FEM can be applied for both compressible and nearly incompressible materials.

Second, the S-FEM models give more the freedom and convenience in the construction of shape functions. The S-FEM models, which permits to use the severe distorted or n -sided polygonal elements (CS-FEM, NS-FEM and ES-FEM), remove the constrained conditions on the shape of elements of the standard FEM.

Third, the NS-FEM which possesses interesting properties of an equilibrium FEM model is promising to provide a much simpler tool to estimate the quality of the solution (the global error, bounds of solutions, convergence rates, etc) by combining itself with the standard compatible FEM.

Fourth, the α FEM, which provides the nearly exact solution in the strain energy by only using the coarse meshes of 3-node triangular and 4-node tetrahedral elements, has a very meaningful contribution in providing more the reference benchmark solutions with high accuracy to verify the accuracy, reliability and efficiency of numerical methods, especially in 3D problems or 2D problems with complicated geometry domains, or in many fields without having the analytical solutions such as fluid mechanics, solid mechanics, heat mechanics, etc.

Nomenclature

$a(\mathbf{u}, \mathbf{v})$	bilinear form
$A_k^s = \int_{\Omega_k^s} d\Omega$	area of smoothing domain Ω_k^s
$\mathbf{b} = [b_x \quad b_y]^T$	vector of external body forces
$\mathbf{B}_I(\mathbf{x})$	compatible strain gradient matrix
$\bar{\mathbf{B}}_I(\mathbf{x})$	smoothed gradient strain matrix
c	damping parameter
\mathbf{C}	damping matrix
\mathbf{d}	vector of nodal displacements using the standard FEM
\mathbf{D}	symmetric positive definite (SPD) matrix of material constants
$\mathbf{e} = \mathbf{u} - \mathbf{u}^h$	difference between the exact solution and FEM solution
e_d	displacement error norm used for n -sided polygonal elements
e_e	energy error norm used for n -sided polygonal elements
E	Young modulus
$E(\boldsymbol{\varepsilon})$	exact strain energy
$E(\boldsymbol{\varepsilon}^h)$	strain energy obtained by the standard FEM
$\hat{E}(\alpha)$	strain energy obtained by the α FEM
$\bar{E}(\bar{\boldsymbol{\varepsilon}})$	smoothed strain energy obtained by the S-FEM models
\mathbf{E}	Green-Lagrange strain tensor

$f(\mathbf{v})$	linear functional
\mathbf{F}	formation gradient tensor
$\mathbb{H}^m(\Omega)$	Hilbert space on Ω
$\mathbb{H}^1(\Omega)$	Sobolev space on Ω
$\mathbb{H}_0^1(\Omega)$	subspace of $\mathbb{H}^1(\Omega)$ with vanishing values on Γ_u
\mathbf{I}	unit matrix
\mathbf{J}	Jacobi matrix of standard FEM
$\mathbb{L}^2(\Omega)$	space of square integrable functions on Ω
\mathbf{M}	mass matrix
\mathbf{n}	unit outward normal matrix
$\mathbf{n}_k^s(\mathbf{x})$	outward normal vector matrix on the boundary Γ_k^s
n_s	number of triangular smoothing domains in polygonal element
n_f	node being fixed
n_t	unconstrained nodes
N_e	total number of elements
N_n	total number of nodes
N_{eg}	total number of edges
N_f	total number of faces
N_u	un-prescribed nodal unknowns
N_s	total number of smoothing domains
N_s^{\min}	minimum number of smoothing domains
$\mathbf{N}_I(\mathbf{x})$	nodal basis shape function
$\mathbf{K} \equiv \mathbf{K}^{\text{FEM}}$	stiffness matrix of the FEM

$\bar{\mathbf{K}}$	smoothed stiffness matrix of the S-FEM models
$\hat{\mathbf{K}}$	stiffness matrix of the alpha-FEM models
\mathbf{S}	2 nd Piola-Kirchhoff stress tensor
$\mathbf{t} = \begin{bmatrix} t_x & t_y \end{bmatrix}^T$	prescribed traction vector in the x -axis and y -axis
$\mathbf{u} = \begin{bmatrix} u & v \end{bmatrix}^T$	exact displacement vector in the x -axis and y -axis
$\mathbf{w}_0 = \begin{bmatrix} w_{0x} & w_{0y} \end{bmatrix}^T$	prescribed displacement vector the x -axis and y -axis
\mathbf{u}^h	approximation solution obtained by the FEM
$\bar{\mathbf{u}}$	approximation solution obtained by the S-FEM models
$\hat{\mathbf{u}}$	approximation solution obtained by the alpha-FEM models
ν	Poisson's ratio
\mathbb{V}^h	discrete finite-dimensional subspace of the space \mathbb{V}
\mathbb{U}^h	discrete finite-dimensional subspace of the space \mathbb{U}
$V_k^s = \int_{\Omega_k^s} d\Omega$	volume of the smoothing domain
$\mathbf{x}_i = \begin{bmatrix} x_i & y_i \end{bmatrix}^T$	coordinates of the field nodes associated with the element
α_{ir}	prescribed irregularity factor
$\mu = E / [2(1 + \nu)]$	shearing modulus
$\lambda = \frac{2\nu\mu}{1 - 2\nu}$	Lame's parameter
ρ	mass density
$\boldsymbol{\varepsilon}$	exact strain vector
$\boldsymbol{\varepsilon}^h$	compatible strain obtained by the FEM
$\bar{\boldsymbol{\varepsilon}}$	smoothing strain obtained by the S-FEM models
$\hat{\boldsymbol{\varepsilon}}$	smoothing strain obtained by the alpha-FEM models

$\boldsymbol{\sigma}$	exact stress
δ	Kronecker delta function
Ω	problem domain
Ω_i^e	element domain
Ω_k^s	smoothing domain
Γ	problem boundary
Γ_u	(Dirichlet) essential boundary
Γ_t	(Neumann) natural boundary
Γ_k^s	boundary of the smoothing domain Ω_k^s
∇_s	symmetric differential operator matrix
$\nabla \mathbf{v}$	gradient of \mathbf{v}
$\ \mathbf{v}\ _{L^2(\Omega)}$	norm in $L^2(\Omega)$ space
$\ \mathbf{v}\ _{\mathbb{H}^1(\Omega)}$	norm in $\mathbb{H}^1(\Omega)$ space
$ \mathbf{v} _{\mathbb{H}^1(\Omega)}$	seminorm in $\mathbb{H}^1(\Omega)$ space
$(\mathbf{v}, \mathbf{w})_{\mathbb{H}^1(\Omega)}$	scalar product in $\mathbb{H}^1(\Omega)$ space
$\pi^h \mathbf{u}$	suitable interpolant of \mathbf{u}
$\Phi_k(\mathbf{x})$	smoothing function

List of Figures

- Figure 3.1.** Division of quadrilateral element into the smoothing domains (SDs) in the CS-FEM by connecting the mid-segment-points of opposite segments of smoothing domains. (a) 1 SD; (b) 2 SDs; (c) 3 SDs; (d) 4 SDs; (e) 8 SDs; (f) 16 SDs.
- Figure 3.2.** n -sided polygonal elements and the smoothing domain (shaded area) associated with node k in the NS-FEM.
- Figure 3.3.** Triangular elements and the smoothing domains (shaded areas) associated with edges in the ES-FEM.
- Figure 3.4.** Two adjacent tetrahedral elements and the smoothing domain $\Omega^{(k)}$ (shaded domain) formed based on their interface k in the FS-FEM.
- Figure 3.5.** Division of the smoothing domain Ω_k^s associated with the edge k into two adjacent smoothing cells $\Omega_{k,1}^s$ and $\Omega_{k,2}^s$ that have the common inner boundary $\Gamma_{k,1-2}^{s(\text{inner})}$.
- Figure 3.6.** Division of a 6-sided convex polygonal element into six triangular sub-domains by connecting n field nodes with the central point O .
- Figure 4.1.** Division of a quadrilateral element into smoothing domains (SDs) in the CS-FEM by connecting the mid-segment-points of opposite segments of smoothing domains. (a) 1 SD; (b) 2 SDs; (c) 3 SDs; (d) 4 SDs; (e) 8 SDs; (f) 16 SDs.
- Figure 4.2.** Position of Gauss points at mid-segment-points on segments of smoothing domains; (a) Four quadrilateral smoothing domains in a quadrilateral element; (b) Six triangular smoothing domains in a 6-sided convex polygonal element.
- Figure 4.3.** Division of an isoparametric elements into quadrilateral smoothing domains. The lower-left quadrant is further divided into 4 smoothing domains by connecting the mid-segment-points of opposite segments. (a) Quadrilateral smoothing domains of a CS-FEM element (no mapping is needed); (b) element in the natural coordinate for the isoparametric FEM element (mapping is needed).
- Figure 4.4.** (a) Voronoi diagram without adding the nodes along the boundary

- outside the domain; (b) Voronoi diagram with the nodes added along the boundary outside the domain; (c) Final Voronoi diagram.
- Figure 4.5.** Meshes used for the patch test. (a) a mesh with a concave quadrilateral element; (b) a mesh with a quadrilateral element using three collinear points; (c) a mesh with general convex quadrilateral elements; (d) a mesh with rectangular elements; (e) a mesh with parallelogram elements.
- Figure 4.6.** Domain discretization of a square patch using 36 n -sided polygonal elements.
- Figure 4.7.** Cantilever loaded at the end.
- Figure 4.8.** Domain discretization of the cantilever; (a) using 4-node elements; (b) using n -sided polygonal elements.
- Figure 4.9.** Comparison of the relative error in displacement v between CS-FEM and analytical solution for the cantilever loaded at the end. The monotonic behavior of CS-FEM solution in displacement is clearly shown.
- Figure 4.10.** Convergence of strain energy solutions of CS-FEM and FEM for the cantilever loaded at the end. The monotonic behavior of CS-FEM solution in strain energy is clearly shown.
- Figure 4.11.** Comparison of the numerical results of CS-FEM and analytical solutions for the cantilever loaded at the end. (a) Shear stress τ_{xy} ; (b) Normal stress σ_{xx} .
- Figure 4.12.** Second order displacement gradients using the CS-FEM for the cantilever loaded at the end.
- Figure 4.13.** Relative error in displacement v along $y=0$ between the n CS-FEM and analytical solution for the cantilever loaded at the end.
- Figure 4.14.** Contour of relative deflection errors (m) of the cantilever using n CS-FEM.
- Figure 4.15.** Contour of the analytical and computed shear stress τ_{xy} (N/m^2) of the cantilever using the n CS-FEM.
- Figure 4.16.** Contour of the analytical and computed normal stress σ_{xx} (N/m^2) of the cantilever using the n CS-FEM.
- Figure 4.17.** Error in displacement norm of CS-FEM and FEM for the cantilever loaded at the end using the same meshes.
- Figure 4.18.** Error in energy norm of CS-FEM and FEM for the cantilever loaded at the end using the same meshes.

- Figure 4.19.** Infinite plate with a circular hole subjected to unidirectional tension and its quarter model with symmetric conditions imposed on the left and bottom edges.
- Figure 4.20.** Domain discretization of the infinite plate with a circular hole (a) using 4-node elements; (b) using n -sided polygonal elements.
- Figure 4.21.** Numerical and exact displacements of the infinite plate with a hole using the CS-FEM ($n_s = 4$). (a) Displacement u ; (b) Displacement v .
- Figure 4.22.** Numerical and exact stresses of the infinite plate with a hole using CS-FEM ($n_s = 4$). (a) σ_{xx} ; (b) σ_{yy} .
- Figure 4.23.** Convergence of strain energy solutions of CS-FEM and FEM for the infinite plate with a hole. The monotonic behavior of CS-FEM solution in strain energy is clearly shown.
- Figure 4.24.** Convergence of error in displacement norm of CS-FEM and FEM in the infinite plate with a hole using the same meshes.
- Figure 4.25.** Convergence of error in energy norm of solutions obtained using the CS-FEM and FEM in the infinite plate with a hole using the same meshes.
- Figure 4.26.** The exact displacement solution and the numerical solution computed using n CS-FEM for the infinite plate with a hole; (a) Displacement u ; (b) Displacement v .
- Figure 4.27.** The exact solution of stresses and the numerical obtained using n CS-FEM for the infinite plate with a hole; (a) σ_{xx} ; (b) σ_{yy} .
- Figure 4.28.** Contour plots of solutions for the infinite plate with a hole using n CS-FEM. (a) the error in displacement u ; (b) the normal stress errors σ_{xx} and σ_{yy} (N/m^2).
- Figure 4.29.** Error in displacement norm versus different Poisson's ratios of the infinite plate with a hole. (a) n -sided polygonal elements (451 nodes); (b) 4-node quadrilateral elements (289 nodes).
- Figure 5.1.** n -sided polygonal elements and the smoothing domains associated with nodes.
- Figure 5.2.** Position of Gauss points at mid-segment-points on the segments of smoothing domains associated with node k in a mesh of n -sided polygonal elements.
- Figure 5.3.** Domain discretization of a cubic patch with 4-node tetrahedral

- elements.
- Figure 5.4.** Domain discretization of the cantilever using triangular elements.
- Figure 5.5.** Comparison of the numerical results of NS-FEM models and analytical solutions for the cantilever loaded at the end. (a) Normal stress σ_{xx} ; (b) Shear stress τ_{xy} .
- Figure 5.6.** Contour of the analytical and the numerical normal stress σ_{xx} (N/m^2) for the cantilever obtained using the n NS-FEM.
- Figure 5.7.** Convergence of the strain energy solution for the cantilever problem. (a) n -sided polygonal elements; (b) triangular and 4-node elements.
- Figure 5.8.** Error in displacement norm for the NS-FEM solution in comparison with that of other methods for the cantilever problem using the same distribution of nodes.
- Figure 5.9.** Error in energy norm for the NS-FEM solution in comparison with those of other methods for the cantilever problem using the same distribution of nodes.
- Figure 5.10.** Domain discretization of the infinite plate with a circular hole using triangular elements.
- Figure 5.11.** Convergence of the strain energy solution for the infinite plate with a circular hole. (a) n -sided polygonal elements; (b) triangular and quadrilateral elements.
- Figure 5.12.** Computed and exact displacements of the n NS-FEM for the infinite plate with a circular hole. (a) displacement $u(m)$ of nodes along bottom side; (b) displacement $v(m)$ of nodes along left side.
- Figure 5.13.** Exact and the numerical stresses using the n NS-FEM for the infinite plate with a circular hole. (a) stress σ_{yy} of nodes along bottom side; (b) stress σ_{xx} of nodes along left side.
- Figure 5.14.** Error in displacement norm for NS-FEM in comparison with those of other methods for the infinite plate with a circular hole using the same distribution of nodes.
- Figure 5.15.** Error in energy norm for NS-FEM in comparison with those of other methods for the infinite plate with a circular hole using the same distribution of nodes.
- Figure 5.16.** Error in displacement norm versus Poisson's ratios close to 0.5 for the infinite plate with a circular hole. (a) n -sided polygonal elements (579 nodes); (b) 4-node quadrilateral elements (289 nodes).
- Figure 5.17.** Hollow sphere problem setting and its one-eighth model discretized

- using 4-node tetrahedral elements.
- Figure 5.18.** (a) Radial displacement v (m); (b) Radial and tangential stresses (N/m^2) for the hollow sphere subjected to inner pressure.
- Figure 5.19.** Convergence of the strain energy solution of the NS-FEM-T4 in comparison with other methods for the hollow sphere subjected to inner pressure.
- Figure 5.20.** Error in displacement norm for the NS-FEM-T4 solution in comparison with those of other methods for the hollow sphere subjected to inner pressure.
- Figure 5.21.** Error in energy norm for the NS-FEM-T4 solution in comparison with those of other methods for the hollow sphere subjected to inner pressure.
- Figure 5.22.** Displacement norm versus different Poisson's ratios for the hollow sphere subjected to inner pressure (507 nodes).
- Figure 5.23.** A 3D cubic cantilever subjected to a uniform pressure on the top surface, and a mesh with 4-node tetrahedral elements.
- Figure 5.24.** Convergence of the strain energy solution of the NS-FEM-T4 in comparison with other methods of the 3D cubic cantilever problem subjected to a uniform pressure.
- Figure 5.25.** Convergence of the deflection solution at point $A(1.0,1.0,-0.5)$ of the NS-FEM-T4 in comparison with other methods of the cubic cantilever subjected to a uniform pressure.
- Figure 5.26.** 3D block and an L -shaped quarter model.
- Figure 5.27.** Convergence of the strain energy solution of the 3D L -shaped block problem.
- Figure 6.1.** ES-FEM settings: domain discretization into arbitrary n -sided polygonal elements, and the smoothing domains created based on the edges of these elements.
- Figure 6.2.** ES-FEM-T3 settings: triangular elements (solid lines) and the edge-based smoothing domains (shaded areas).
- Figure 6.3.** Gauss points of the smoothing domains associated with edges for n -sided polygonal elements in the ES-FEM.
- Figure 6.4.** Mesh discretization using triangular elements for standard patch test.
- Figure 6.5.** Distribution of displacement v along the horizontal middle axis of the cantilever subjected to a parabolic traction at the free end. The ES-

- FEM-T3 performs much better than FEM-T3 and even better than the FEM-Q4.
- Figure 6.6.** Relative error in displacement v along horizontal middle axis of the cantilever subjected to a parabolic traction at the free end. The ES-FEM-T3 solution is very close to the exact one.
- Figure 6.7.** Normal stress σ_{xx} and shear stress σ_{xy} along the section of $x = L/2$ using the ES-FEM-T3 of the cantilever subjected to a parabolic traction at the free end.
- Figure 6.8.** Convergence of the strain energy solution obtained using the ES-FEM-T3 in comparison with other methods for the cantilever subjected to a parabolic traction at the free end using the same distribution of nodes.
- Figure 6.9.** Error in displacement norm obtained using the ES-FEM-T3 in comparison with other methods for the cantilever subjected to a parabolic traction at the free end using the same distribution of nodes.
- Figure 6.10.** Error in energy norm obtained using the ES-FEM-T3 in comparison with other methods for the cantilever subjected to a parabolic traction at the free end using the same distribution of nodes.
- Figure 6.11.** Comparison of the computation time of different methods for solving the cantilever subjected to a parabolic traction at the free end. For the same distribution of nodes, the FEM-T3 is the fastest to deliver the results.
- Figure 6.12.** Comparison of the efficiency (computation time for the solutions of same accuracy measured in displacement norm) for solving the cantilever subjected to a parabolic traction at the free end. The ES-FEM-T3 stands out clearly as a winner, even though it uses triangular elements. It wins by its superiority in convergence rate.
- Figure 6.13.** Comparison of the efficiency of computation time in terms of energy norm of the cantilever subjected to a parabolic traction at the free end. The CS-FEM-Q4 performed best, followed by the ES-FEM-T3 that uses triangular elements.
- Figure 6.14.** Normal stress σ_{xx} and shear stress σ_{xy} along the section of $x = 0$ using n ES-FEM of the cantilever subjected to a parabolic traction at the free end.
- Figure 6.15.** Convergence of the strain energy solution of n ES-FEM using n -sided polygonal elements in comparison with other methods for the cantilever subjected to a parabolic traction at the free end using the same meshes.
- Figure 6.16.** Error in displacement norm of n ES-FEM-T3 using n -sided polygonal elements in comparison with other methods for the cantilever subjected

- to a parabolic traction at the free end using the same meshes.
- Figure 6.17.** Error in energy norm of n ES-FEM-T3 using n -sided polygonal elements in comparison with other methods for the cantilever subjected to a parabolic traction at the free end using the same meshes.
- Figure 6.18.** Distribution of displacement u along the bottom boundary of the infinite plate with a hole subjected to unidirectional tension.
- Figure 6.19.** Distribution of displacement v along the left boundary of the infinite plate with a hole subjected to unidirectional tension.
- Figure 6.20.** Stress σ_{xx} along the left boundary ($x=0$) and stress σ_{yy} along the bottom boundary ($y=0$) using the ES-FEM-T3 for the infinite plate with a hole subjected to unidirectional tension.
- Figure 6.21.** Convergence of the strain energy solution of ES-FEM-T3 in comparison with other methods for the infinite plate with a hole subjected to unidirectional tension using the same distribution of nodes.
- Figure 6.22.** Error in displacement norm of the ES-FEM-T3 solution in comparison with other methods for the infinite plate with a hole subjected to unidirectional tension using the same distribution of nodes.
- Figure 6.23.** Error in energy norm of the ES-FEM-T3 solution in comparison with other methods for the infinite plate with a hole subjected to unidirectional tension using the same distribution of nodes.
- Figure 6.24.** Displacement u along the bottom boundary and displacement v along the left boundary using n ES-FEM of the infinite plate with a hole subjected to unidirectional tension.
- Figure 6.25.** Stress σ_{xx} along the left boundary ($x=0$) and stress σ_{yy} along the bottom boundary ($y=0$) using n ES-FEM of the infinite plate with a hole subjected to unidirectional tension.
- Figure 6.26.** Convergence of the strain energy solution of n ES-FEM using n -sided polygonal elements in comparison with other methods for the infinite plate with a hole subjected to unidirectional tension using the same meshes.
- Figure 6.27.** Error in displacement norm of n ES-FEM-T3 using n -sided polygonal elements in comparison with other methods for the infinite plate with a hole subjected to unidirectional tension using the same meshes.
- Figure 6.28.** Error in energy norm of n ES-FEM-T3 using n -sided polygonal elements in comparison with other methods for the infinite plate with a hole subjected to unidirectional tension using the same meshes.

- Figure 6.29.** Displacement norm with different Poisson's ratios. (a) n -sided polygonal elements (579 nodes); (b) triangular elements (289 nodes).
- Figure 6.30.** A thick cylindrical pipe subjected to an inner pressure and its quarter model.
- Figure 6.31.** Discretization of the domain of the thick cylindrical pipe subjected to an inner pressure; (a) 4-node quadrilateral elements; (b) 3-node triangular elements.
- Figure 6.32.** Discretization of the domain using n -sided polygonal elements of the thick cylindrical pipe subjected to an inner pressure.
- Figure 6.33.** Distribution of the radial displacement of the cylindrical pipe subjected to an inner pressure using the ES-FEM-T3.
- Figure 6.34.** Distribution of the radial and tangential stresses of the cylindrical pipe subjected to an inner pressure using the ES-FEM-T3.
- Figure 6.35.** Convergence of strain energy of ES-FEM-T3 in comparison with other methods for the cylindrical pipe subjected to an inner pressure using the same distribution of nodes.
- Figure 6.36.** Error in displacement norm of ES-FEM-T3 in comparison with other methods for the cylindrical pipe subjected to an inner pressure using the same distribution of nodes.
- Figure 6.37.** Error in energy norm of ES-FEM-T3 in comparison with other methods for the cylindrical pipe subjected to an inner pressure using the same distribution of nodes.
- Figure 6.38.** Computed and exact results of nodes along the radius of the thick cylindrical pipe subjected to an inner pressure using the n ES-FEM; (a) radial displacement u_r ; (b) radial stress σ_r and tangential stress σ_θ .
- Figure 6.39.** Convergence of the strain energy solution of n ES-FEM in comparison with other methods for the thick cylindrical pipe subjected to an inner pressure.
- Figure 6.40.** Error in displacement norm of n ES-FEM in comparison with other methods for the thick cylindrical pipe subjected to an inner pressure.
- Figure 6.41.** Error in energy norm of n ES-FEM in comparison with other methods for the thick cylindrical pipe subjected to an inner pressure.
- Figure 6.42.** Displacement norm with different Poisson's ratios the thick cylindrical pipe subjected to an inner pressure; (a) n -sided polygonal elements (464 nodes); (b) triangular elements (91 nodes).
- Figure 6.43.** A shear wall with four square openings.

- Figure 6.44.** Domain discretization using triangular and 4-node quadrilateral elements of the shear wall with four openings.
- Figure 6.45.** 1st to 6th modes of the shear wall by the NS-FEM-T3 and ES-FEM-T3.
- Figure 6.46.** 7th to 12th modes of the shear wall by the NS-FEM-T3 and ES-FEM-T3.
- Figure 6.47.** Geometric model, loading and boundary conditions of an automobile connecting bar.
- Figure 6.48.** Domain discretization using triangular and 4-node quadrilateral elements of the automobile connecting bar.
- Figure 6.49.** 1st to 6th modes of the connecting bar by NS-FEM-T3 and ES-FEM-T3.
- Figure 6.50.** 7th to 12th modes of the connecting bar by NS-FEM-T3 and ES-FEM-T3.
- Figure 6.51.** Transient responses for the cantilever beam subjected to a harmonic loading.
- Figure 6.52.** A spherical shell subjected to a concentrated loading at its apex.
- Figure 6.53.** Domain discretization of half of the spherical shell using triangular and 4-node quadrilateral elements.
- Figure 6.54.** Transient responses for the spherical shell subjected to a harmonic loading.
- Figure 6.55.** Transient responses obtained using the ES-FEM-T3 for the spherical shell subjected to a Heaviside step loading.
- Figure 7.1.** Two adjacent tetrahedral elements and the smoothing domain Ω_k^s (shaded domain) formed based on their interface k in the FS-FEM-T4.
- Figure 7.2.** Distribution of the radial displacement in the hollow sphere subjected to an inner pressure using the FS-FEM-T4.
- Figure 7.3.** Distribution of the radial and tangential stresses in the hollow sphere subjected to an inner pressure using the FS-FEM-T4.
- Figure 7.4.** Convergence of strain energy solution of FS-FEM-T4 in comparison with other methods for the hollow sphere subjected to an inner pressure.
- Figure 7.5.** Error in displacement norm of FS-FEM-T4 in comparison with other methods for the hollow sphere subjected to an inner pressure.

- Figure 7.6.** Error in energy norm of FS-FEM-T4 in comparison with other methods for the hollow sphere subjected to an inner pressure.
- Figure 7.7.** Error in displacement norm versus different Poisson's ratios of the hollow sphere subjected to an inner pressure.
- Figure 7.8.** Convergence of the strain energy solution of FS-FEM-T4 in comparison with other methods for the cubic cantilever subjected to a uniform pressure on the top surface.
- Figure 7.9.** Convergence of the deflection at point A(1.0,1.0,-0.5) of FS-FEM-T4 in comparison with other methods for the cubic cantilever subjected to a uniform pressure.
- Figure 7.10.** Initial and final configurations of the 3D cantilever beam subjected to a uniformly distributed load using the FS-FEM-T4 in the geometrically nonlinear analysis.
- Figure 7.11.** Domain discretization of the 3D cantilever beam subjected to a uniformly distributed load using severely distorted tetrahedral elements.
- Figure 7.12.** Tip deflection (*cm*) versus the load step of the 3D cantilever beam subjected to a uniformly distributed load in the geometrically nonlinear analysis.
- Figure 7.13.** Axletree base model.
- Figure 7.14.** Initial and final configurations viewed from the top of an 3D axletree base using 4-node tetrahedral elements in the geometrically nonlinear analysis.
- Figure 7.15.** Tip displacement (point A) in *z*-direction versus the load step of an 3D axletree base using 4-node tetrahedral elements in the geometrically nonlinear analysis.
-
- Figure 8.1.** An α FEM-T3 element: combination of the triangular elements of FEM-T3 and NS-FEM-T3. The NS-FEM-T3 is used for three quadrilaterals sub-domain, and the FEM-T3 is used for the Y-shaped sub-domain in the center.
- Figure 8.2.** Smoothing domain associated with nodes for triangular elements in the α FEM-T3.
- Figure 8.3.** Domain discretization of a cubic patch using four-node tetrahedral elements.
- Figure 8.4.** The strain energy curves of three meshes with the same aspect ratios intersect at $\alpha_{\text{exact}} = 0.6$ for the cantilever loaded at the end.

- Figure 8.5.** Error in displacement norm of α FEM-T3 ($\alpha_{\text{exact}} = 0.6$) in comparison with other methods for the cantilever loaded at the end using the same distribution of nodes.
- Figure 8.6.** Error in energy norm of α FEM-T3 ($\alpha_{\text{exact}} = 0.6$) in comparison with other methods for the cantilever loaded at the end using the same distribution of nodes.
- Figure 8.7.** Cook's membrane problem and its discretizations using 4-node quadrilateral and 3-node triangular elements.
- Figure 8.8.** The strain energy curves of four meshes with the same aspect ratios intersect at $\alpha_{\text{exact}} = 0.5085$ for Cook's membrane problem.
- Figure 8.9.** Convergence of tip displacement of α FEM-T3 ($\alpha_{\text{exact}} = 0.5085$) in comparison with other methods for Cook's membrane using the same distribution of nodes.
- Figure 8.10.** Semi-infinite plane subjected to a uniform pressure.
- Figure 8.11.** Domain discretization of the semi-infinite plane using 3-node triangular and 4-node quadrilateral elements.
- Figure 8.12.** The strain energy curves of three meshes with the same aspect ratios intersect at $\alpha_{\text{exact}} = 0.48$ for the semi-infinite plane subjected to a uniform pressure.
- Figure 8.13.** Convergence of strain energy of α FEM-T3 ($\alpha_{\text{exact}} = 0.48$) in comparison with other methods for the semi-infinite plane subjected to a uniform pressure.
- Figure 8.14.** Computed and exact displacements of the semi-infinite plane subjected to a uniform pressure using the α FEM-T3 ($\alpha_{\text{exact}} = 0.48$).
- Figure 8.15.** Computed and exact stresses of the semi-infinite plane subjected to a uniform pressure using the α FEM-T3 ($\alpha_{\text{exact}} = 0.48$).
- Figure 8.16.** Error in displacement norm of α FEM-T3 ($\alpha_{\text{exact}} = 0.48$) in comparison with other methods for the semi-infinite plane subjected to a uniform pressure using the same distribution of nodes.
- Figure 8.17.** Error in energy norm of α FEM-T3 ($\alpha_{\text{exact}} = 0.48$) in comparison with other methods for the semi-infinite plane subjected to a uniform pressure using the same distribution of nodes.
- Figure 8.18.** Displacement norm versus different Poisson's ratios of the material for the semi-infinite plane subjected to a uniform pressure (the mesh with 353 nodes and $h = 0.0559$ is used).

- Figure 8.19.** Using the strain energy curves of meshes with the same aspect ratios to find $\alpha_{\text{exact}} = 0.7$ for the hollow sphere subjected to inner pressure.
- Figure 8.20.** Distribution of the radial displacement of the hollow sphere subjected to inner pressure using α FEM-T4 ($\alpha_{\text{exact}} = 0.7$).
- Figure 8.21.** Distribution of the radial and tangential stresses of the hollow sphere subjected to inner pressure using α FEM-T4 ($\alpha_{\text{exact}} = 0.7$).
- Figure 8.22.** Convergence of strain energy solution of α FEM-T4 ($\alpha_{\text{exact}} = 0.7$) in comparison with others methods for the hollow sphere subjected to inner pressure.
- Figure 8.23.** Error in displacement norm of α FEM-T4 ($\alpha_{\text{exact}} = 0.7$) in comparison with other methods for the hollow sphere subjected to inner pressure.
- Figure 8.24.** Error in energy norm of the solution obtained using α FEM-T4 ($\alpha_{\text{exact}} = 0.7$) in comparison with other methods for the hollow sphere subjected to inner.
- Figure 8.25.** The strain energy curves of three meshes with the same aspect ratios to find $\alpha_{\text{exact}} = 0.62$ for the cubic cantilever.
- Figure 8.26.** Convergence of the strain energy solutions of α FEM-T4 ($\alpha_{\text{exact}} = 0.62$) in comparison with other methods for the cubic cantilever subjected to a uniform pressure on the top surface.
- Figure 8.27.** Convergence of the deflection at point A(1.0,1.0,-0.5) of α FEM-T4 ($\alpha_{\text{exact}} = 0.62$) in comparison with other methods for the cubic cantilever subjected to a uniform pressure on the top surface.
- Figure 8.28.** The strain energy curves of three meshes with the same aspect ratios to find $\alpha_{\text{exact}} = 0.7$ for the L -shaped 3D problem.
- Figure 8.29.** Convergence of the strain energy solutions of α FEM-T4 ($\alpha_{\text{exact}} = 0.7$) in comparison with other methods for L -shaped 3D problem.

List of Tables

- Table 3.1.** Typical types of smoothing domains.
- Table 3.2.** Minimum number of smoothing domains N_s^{\min} for problems with n_t (unconstrained) total nodal unknowns.
- Table 4.1.** Values of shape functions at different points within a quadrilateral element (Figure 4.2a).
- Table 4.2.** Values of shape functions at different points within an n-sided convex polygonal element (Figure 4.2b).
- Table 4.3.** Displacement norm of the standard patch test e_d (%) for the case of $n_s = 4$.
- Table 4.4.** Eigenvalues of a free square solid meshed using one element ($E = 3.0 \times 10^7$, $\nu = 0.3$).
- Table 4.5.** Eigenvalues of a square solid meshed with one element with fixed with 3 DOFs ($E = 3.0 \times 10^7$, $\nu = 0.3$).
- Table 4.6.** Eigenvalues of a free solid meshed with 4×4 elements ($E = 3.0 \times 10^7$, $\nu = 0.3$).
- Table 4.7.** Tip displacements ($\times 10^{-3}$ m) of the cantilever beam obtained using different regular elements (Analytical solution = 8.900×10^{-3} m).
- Table 4.8.** Displacement norm of the cantilever beam obtained using different element sizes ($\times 10^{-3}$).
- Table 4.9.** Strain energy for the cantilever beam obtained using different element sizes ($\times 10^{-1}$ Nm).
- Table 5.1.** Shape function values at different sites on the smoothing domain boundary for node k (cf. Figure 5.2).
- Table 5.2.** Existence of spurious zero-energy modes in an individual element.

Table 5.3.	Error in displacement norm and energy for the patch test.
Table 5.4.	Strain energy (Nm) obtained using different methods the cantilever problem using the same distribution of nodes.
Table 5.5.	Strain energy (Nm) obtained using different methods for the cantilever problem using the same polygonal meshes.
Table 5.6.	Error in displacement norm obtained using different methods for the cantilever problem using the same distribution of nodes.
Table 5.7.	Error in energy norm obtained using different methods for the cantilever problem using the same distribution of nodes.
Table 5.8.	Strain energy ($\times 10^{-2} Nm$) using different methods for the infinite plate with a circular hole using the same distribution of nodes.
Table 5.9.	Strain energy ($\times 10^{-2} Nm$) using different methods for the infinite plate with a circular hole using the same polygonal meshes.
Table 5.10.	Error in displacement norm obtained using different methods for the infinite plate with a circular hole using the same distribution of nodes.
Table 5.11.	Error in energy norm obtained using different methods for the infinite plate with a circular hole using the same distribution of nodes.
Table 5.12.	Strain energy ($\times 10^{-2} Nm$) obtained using different methods for the hollow sphere subjected to inner pressure.
Table 5.13.	Error in displacement norm obtained using different methods for the hollow sphere subjected to inner pressure.
Table 5.14.	Error in energy norm obtained using different methods for the hollow sphere subjected to inner pressure.
Table 5.15.	Strain energy obtained using different methods for the 3D cubic cantilever problem subjected to a uniform pressure.
Table 5.16.	Deflection at point A (1.0,1.0,-0.5) obtained using different methods for the 3D cubic cantilever problem subjected to a uniform pressure.
Table 5.17.	Strain energy obtained using different methods for the 3D L -shaped block problem.
Table 6.1.	Shape function values at different sites on the smoothing domain boundary associated with the edge 1-6 in Figure 6.3.
Table 6.2.	Existence of spurious zero energy modes in an element.

- Table 6.3.** Error in displacement norm (%) for solutions obtained using different methods for the cantilever problem using the same polygonal meshes.
- Table 6.4.** Error in energy norm for solutions obtained using different methods for the cantilever problem using the same polygonal meshes.
- Table 6.5.** Error in displacement norm (%) in solutions obtained using different methods for the infinite plate with a hole using the same polygonal meshes.
- Table 6.6.** Error in energy norm ($\times 10^{-3}$) in solutions obtained using different methods for the infinite plate with a hole using the same polygonal meshes.
- Table 6.7.** Strain energy (KNm) obtained using different methods for the cylindrical pipe subjected to an inner pressure using the same distribution of nodes.
- Table 6.8.** Error in displacement norm obtained using different methods for the cylindrical pipe subjected to an inner pressure using the same distribution of nodes.
- Table 6.9.** Error in energy norm obtained using different methods for the cylindrical pipe subjected to an inner pressure using the same distribution of nodes.
- Table 6.10.** Strain energy (KNm) using different methods for the thick cylindrical pipe using the same polygonal meshes.
- Table 6.11.** Error in displacement norm (%) in solutions obtained using different methods for the thick cylindrical pipe using the same polygonal meshes.
- Table 6.12.** Error in energy norm in solutions obtained using different methods for the thick cylindrical pipe using the same polygonal meshes.
- Table 6.13.** First 12 natural frequencies ω (rad/s) of a shear wall.
- Table 6.14.** First 12 natural frequencies (Hz) of a Connecting bar.
- Table 7.1.** Solution error in displacement and energy norms for the patch test.
- Table 7.2.** Tip deflection (cm) versus the irregularity factor α_{ir} for the 3D cantilever beam subjected to a uniformly distributed load.
- Table 7.3.** Tip deflection (cm) at the load steps for the 3D cantilever beam subjected to a uniformly distributed load.
- Table 7.4.** Tip displacement (point A) (cm) in z -direction at load steps for the 3D

axletree base using 4-node tetrahedral elements for the geometrically nonlinear analysis.

- Table 8.1.** Displacement norm e_d (%) of standard patch test for 2D problems.
- Table 8.2.** Displacement norm e_d (%) of Irons first-order patch test for 3D problems.
- Table 8.3.** Strain energy error e_e of Irons first-order patch test for 3D problems.
- Table 8.4.** Results of tip displacement obtained of different methods for Cook's problem.
- Table 8.5.** Results of tip displacement and strain energy obtained of different methods for Cook's problem.
- Table 8.6.** Strain energy (Nm) obtained using different methods for the semi-infinite plane subjected to a uniform pressure using the same distribution of nodes.
- Table 8.7.** Error in displacement norm obtained using different methods for the semi-infinite plane subjected to a uniform pressure using the same distribution of nodes.
- Table 8.8.** Error in energy norm obtained using different methods for the semi-infinite plane subjected to a uniform pressure using the same distribution of nodes.
- Table 8.9.** Displacement norm versus different Poisson's ratios of the semi-infinite plane subjected to a uniform pressure ($\times 10^{-4}$).

Chapter 1

Introduction

In reality, it is impossible to solve analytically the partial differential equations (PDEs) which govern almost all physical phenomena in nature such as solid and structure mechanics, fluid mechanics, heat conduction, seepage flow, electric and magnetic fields, and wave propagation, etc. The reason is that these phenomena depend on the input data of systems, such as physical geometry, material properties, boundary conditions and loading conditions, which are usually very complicated. As a result, many numerical methods for finding suitable approximate solutions of PDEs have been proposed and developed. In particular, with the powerful development of the digital computer, many complicated and sophisticated computations using numerical methods now can be performed fast and accurately impressively. The basic idea in almost numerical methods is to discretize given continuous problem domain with infinite unknowns to obtain discrete problem domain or a system of equations with only finite unknowns that will be solved using a digital computer. Using numerical methods associated with computer-aided design (CAD) tools, one can model, simulate and analyze many complicated problems. This alleviates the need for expensive and time-consuming experimental testing and makes it possible to determine the optimization among many optional designs. Therefore, developing indispensable numerical methods in terms of high accuracy, low

computational cost, easy implementation, versatility and general applicability is the key issue in the numerical simulation.

Up to now, the most popular numerical methods can be listed as finite element methods (FEM), finite difference methods (FDM), finite volume methods (FVM), boundary element methods (BEM) and meshfree methods. Basically, these numerical methods can be divided into two main groups. The first group includes methods which require meshing such as the FEM, FDM, FVM, and BEM and the second group includes methods which do not require meshing such as meshfree methods. Among the methods which require meshing, the FEM is considered to be the most important, indispensable technique and one of the greatest inventions in 20th century. The method is now widely used in all branches of engineering and science such as mechanics, mathematics, physics, chemistry, biology, etc and in many famous computational and design software packages such as COMSOL, ANSYS, ABAQUS, SAMCEP, NASTRAN, SAP, and so on. The next Section, therefore, will review the FEM in more detail. The background including principles, early contributions, key points in the development process, the general procedure and some main features of FEM including advantages and shortcomings will be briefly presented. In particular, the shortcomings will help us to define some existing problems of FEM and main research directions performed in the thesis.

1.1 Background

The FEM has a long history of development and hence has various advanced versions. The FEM introduced in this thesis is the standard version that is displacement-based and fully compatible. It is derived from the minimum potential energy principle which is the most popular and widely used. The method is based on parametric displacement fields ensuring compatibility of deformations both internal to elements and across boundary.

Once the displacement field is properly assumed, the strain field is already available using simply the strain-displacement relation, known as the *compatible* strain field. Under these conditions, whole displacement field of connected structure is continuous and piecewise differentiable. In this thesis, we focus only on lower-order elements in two-dimensional (2D) (3-node triangular, 4-node quadrilateral elements) and three-dimensional (3D) (4-node tetrahedral, 8-node hexahedral elements) because these elements are the bases for the development of new finite elements in this thesis, and also they are most widely used in solving practical engineering problems.

1.1.1 Background of the Finite Element Method (FEM)

The FEM was introduced by three independent research groups: Courant [33], Syngge [146] and, Argyris and Kelsey [6, 8] from the fields of applied mathematics, physics and engineering respectively. The early contributions were presented by Argyris and Kelsey [6, 8] and Turner *et al.* [150]. These papers presented the application of simple finite elements (pin-jointed bar and triangular plate with in-plane loads) for the analysis of aircraft structure and were considered as one of the key contributions in the development of the FEM. The name “Finite Element” was coined in the paper by Clough [29]. The important early contributions and broad interpretation in the theoretical foundation, numerical implementation and its applicability to the general field problems were presented by Argyris [7] and Zienkiewicz and Cheung [159]. With this broad interpretation of FEM, it had been found that the finite element equations can also be derived by using a weighted residual method such as Galerkin method or the least squares approach. This led to a widespread interest among applied mathematicians in applying the FEM for the solution of linear and non-linear differential equations. More details for milestones of FEM history can be found by Felippa [44, 45].

Since the early 1960s, a large number of researches have been devoted to the FEM and a large number of publications on the FEM are available. Some key approaches in the development process of the FEM can be listed as follows:

(1) Reduced-integration techniques and stabilization: Mauder et al. [94], Belytschko and Tsay [17], Belytschko and Ong [16], Belytschko and Bachrach [15], Hughes et al. [53, 56, 58];

(2) Removal of the volumetric locking in the problems using the nearly incompressible material: Hermann [52], Hughes [53, 54]; Treat of the shear locking in the plate and shell problems: Hughes et al. [56, 58], Zienkiewicz et al. [161], Bathe and Dvorkin [13], Lyly et al. [92];

(3) Hybrid or mixed variational principles for stresses and displacements: Veubeke [151], Pian et al. [120, 121, 122], Arnold [9], Brezzi and Fortin [22], Simo and Hughes [137], Atluri [10]; Assumed or enhanced strain formulation based on Hu-Washizu principle: Simo et al. [138, 139, 140].

(4) Mixed variational principles for rotational fields: Hughes and Brezzi [55], Atluri and Cazzani [11], Ibrahimgegovic et al. [59], Iura and Atluri [60], Gruttmann et al. [51].

(5) Development of the extended finite element methods (XFEM) for modeling cracks, holes and inclusions (Melenk and Babuska [95], Moes et al. [97], Dolbow et al. [41], Sukumar et al. [143]) and so on. Development of the NURBS-Enhanced finite element Method (NSFEM): Hughes et al. [57], Sevilla et al. [134, 135].

1.1.2 General procedure of the FEM

In the FEM, the actual continuum or body of matter like solid, liquid or gas is represented as an assemblage of subdivisions called finite *elements*. These elements are considered to be interconnected at specified joints which are called *nodes*. The nodes

usually lie on the element boundaries where adjacent elements are considered to be connected. Since the actual variation of the field variable (like displacement, temperature, pressure, etc) inside the continuum is not known, we assume that the variation of the field variable inside a finite element can be approximated by a simple function. These approximating functions are defined in terms of the values of the field variables at the nodes. When the approximating functions are replaced into the field equations (like equilibrium equations and boundary conditions) for the whole continuum in the weakform, we obtain a discretized system of equations, in which the unknowns will be the nodal values of the field variable. By solving the discretized system of equations, which are generally in the form of the matrix equations, the nodal values of the field variable will be known. Then the approximation of the field variable for the whole problem domain is finally determined.

The solution of a general continuum problem by the FEM always follows an orderly step-by-step process. With reference to static solid mechanics problems, the step-by-step procedure in the FEM can be presented as follows.

Step (1): Establishment of the weak form

The governing partial differential equations (PDEs) for solid mechanics problems are called the *strong* form which requires strong continuity on the field variables (displacements). When solving such PDEs directly, *trial* functions of the field variables have to be differentiable up to the highest order of the PDEs. Generally, it is impossible to find the exact analytical solution that satisfies these strong form PDEs precisely, except for a few simple cases. Therefore, numerical methods are often used as practical means for approximated solutions. The FEM uses a *variational* formulation leading to a *weak* form which reduces the order of differentiation on the trial functions. In mechanics, such a weak form is equivalent to the well-known *principle of minimum potential energy*.

Step (2): Discretization of the problem domain

Once the weak form is established, the problem domain is divided into a set of non-overlapping and non-gap sub-domains called *elements*. These elements are interconnected at the *nodes* located on the element vertices (and boundaries for higher order elements). The elements properly connected by these nodes constitute a *mesh*, and the domain discretization is often called meshing. The number, type, size and the arrangement of the elements have to be decided properly by the analyst. The elements should be small enough to capture the local variation of the displacements and hence to produce results of acceptable accuracy, but not too small for limited computational resources. For efficiency reasons, small elements are used where the results (such as displacement gradient) change rapidly, whereas larger elements can be used where the displacement gradient is relatively smooth.

Step (3): Shape function creation

Based on the elements, *shape functions* for constructing the displacement field using nodal displacements is now created using polynomial basis functions (monomials). The shape function defines the “shape” of the variation of the displacements, so that the variation displacement within the element can be determined, when the nodal displacements are given. Therefore, the nodal values of displacements become the unknowns in the discretized system of equations, and are known as *nodal* degrees of freedom (DOF). Hence, it is often more convenient in the formulation to express these shape functions based on nodes, and they are called *nodal shape functions*. The nodal shape functions satisfy the following requirements.

- i) **Local support:** The nodal shape function for a node has influence only on the vicinity nodes that are the nodes of the elements connected to the node. This property is ensured naturally in the FEM, because it is created based on elements. This local

support property of shape functions ensures the sparse stiffness and mass matrices for an FEM model.

- ii) **Linear independence:** all the nodal shape functions must be linearly independent. This is also naturally achieved by the non-overlapping and non-gap division of elements, and the element-based shape function construction.
- iii) **Compatibility requirement:** the approximated displacements should be differentiable at least up to the r th order inside the elements, and up to the $(r-1)$ th order on the interfaces of the elements, where r is the order of the highest derivative appearing in the weakform.
- iv) **Partitions of unity:** sum of all the nodal shape functions at any point in the problem domain must be the unity. This is needed to ensure the proper representation of constant field or rigid motion of the solid, which is essential to any numerical model.
- v) **Linear reproducibility:** The constant term and linear terms are used in the formulation of shape functions. This is a sufficient condition for the shape functions to be used to formulate a convergent FEM model.
- vi) **Completeness requirement:** reproducibility of polynomials up to r th order. This can be viewed as a general expression of condition (iv) and (v).

Step (4): Evaluation of the strain field

Using the constructed displacement field, the strain field can be evaluated via differentiation using simply the compatible strain-displacement relation.

Step (5): Formation of the element stiffness matrices and vectors

The stiffness matrix and the load vector of an element can now be computed using the weak form established in step (1), the displacement functions assumed using the shape functions created in step (3), and the strain field obtained in step (4). The integration of

the weak form can be performed effectively using the numerical integration techniques, such as the Gauss quadrature with a sufficient number of Gauss points.

Step (6): Assembly of the global matrices/vectors

Since the whole problem domain is composed of finite elements, the individual elemental stiffness matrices and vectors computed in step (5) can now be added together by superposition based on nodes (called the direct assembly) to obtain the global equilibrium system of equations. Such a direct assembly is possible because of the continuity or compatibility of the displacement field is ensured and no gaps occurring anywhere in the domain.

Step (7): Solution for the unknown nodal displacements

The global stiffness matrix obtained from step (6) is symmetric but usually singular because of the possible rigid body movements. To remove the singularity, we must impose proper boundary conditions to constraint the rigid body movements, which leads to a modification to the stiffness matrix and the load vector. The modified stiffness matrix becomes symmetric positive definite (SPD), as long as the original problem is well-posed, and therefore the nodal displacements can be solved with ease using standard routines of linear algebraic equation systems. Once the solution of the displacements at nodes is computed, the function of the displacement field for the whole problem domain can finally be determined.

Step (8): Retrieval of element strains and stresses

From the computed nodal displacements, the element strains can be computed using the strain-displacement relation, and then the stresses using the constitutive relation. Some post-processing technique or recovery procedures can also be performed at this step to improve the accuracy of the strain and stress fields.

1.1.3 Some main features of the FEM

Compared to other numerical methods, the FEM has three following main advantages:

(1) The FEM can handle relatively easily the problems with different continuums of matter (gas, fluid, solid, electric, wave, magnet, etc), complicated geometry, general boundary condition, multi-material domains or nonlinear material properties.

(2) The FEM has a clear structure and versatility which make it easy to comprehend and feasible to construct general purpose software packages for applications.

(3) The FEM has a solid theoretical foundation which gives high reliability and in many cases makes it possible to mathematically analyze and estimate the error of the approximate finite element solution.

However, using the lower-order elements, the FEM has also three following major shortcomings associated with the fully-compatible formulation:

(1) Overly-stiffness and inaccuracy in stress solutions of linear elements

Because the standard FEM is based on the fully-compatible formulation which is stiffer than the real model, the numerical results obtained are under-estimated compared to the exact results. In particular, the numerical results in displacement and stress solutions are mostly unsatisfied for linear triangular or tetrahedral elements because these elements are too stiff. This is a big shortcoming of the FEM, because these elements are favored by all researchers. The reason is that these elements can be easily formulated and implemented very effectively in the finite element programs using piecewise linear approximation. Furthermore, most FEM codes for adaptive analyses are based on triangular and tetrahedral elements, due to the simple fact that triangular and tetrahedral meshes can be automatically generated. Although many researchers such as Allman [1, 2], Bergan and Felippa [19], Cook [31], Piltner and Taylor [123], Dohrmann et al. [39, 40] have concentrated on improving the performance of these elements, the practical

applications of these elements are still limited due to the usage of more degrees of freedom at the nodes or expensive computation.

(2) Meshing issue

Because the FEM is meshing based technology, it leads to constrained conditions on the shape of elements, especially for quadrilateral and hexahedral isoparametric elements. The shape of these elements needs to satisfy the certain requirement of the inner angles. In other words, the positivity of Jacobian determinant of mapping process should be ensured in numerical implementation. This requirement will limit the applications of such elements in computing the problems such as large deformation, crack, destruction, etc. It is because the shape of these elements can not become extremely distorted during the deformed process. In addition, the n -sided polygonal elements in applications of finite deformation or structured materials cannot be used in the standard FEM, due to the lack of feasible shape functions. Therefore, more research needs to be done to remove the constraint conditions on the shape of elements in the FEM which should lead to the effective usage of two following elements

- i. The extremely distorted elements
- ii. The n -sided polygonal elements.

However, the development of the extremely distorted elements has not received much attention among researchers. Instead, the researchers have concentrated on formulating and developing the meshfree methods using only nodes [67], without using the meshes or elements. In the second direction of research, although some authors such as Ghosh and Mallett [49], Sukumar et al. [142, 144, 145], Natarajan et al. [100] have proposed some n -sided polygonal elements in the FEM settings, the practical applications of these elements are still limited due to the expensive computation or the difficulties of constructing the shape functions.

(3) Solution certificate

The solution from a numerical method such as the FEM contains modeling and computational errors. Finding an approximate solution using the above-mentioned FEM procedure is important but not sufficient for advanced applications, and it becomes more and more important to obtain information about the quality of the solution (the global error, bounds of solutions, convergence rates, etc). This not only make the numerical result more applicable to practical engineering problems with certain confidence, but also guide us on how to further improve the solutions.

In reality, however, it is very difficult to estimate the quality of solution of complicated problems without knowing the exact solution. So far, many researchers focus on the so-called dual analyses in the FEM [4, 38, 151] by combing the mentioned compatible FEM model which produces a lower bound of the real solution with an equilibrium FEM model which produces an upper bound. Many new modified FEM models which produce an upper bound have been proposed such as the equilibrium FEM model based on complementary energy principle by Veubeke [151], the recovered equilibrium FEM model based on the recovery of a statically admissible stress field from the displacement FEM model by Ladeveze et al. [65, 66] and the hybrid equilibrium FEM model by Almeida *et al.* [3] and Pereira *et al.* [118]. However, mathematical complexity, difficult implementation and expensive computation have limited these models in the practical application.

1.1.4 Motivation of the thesis

In order to overcome three above-mentioned major shortcomings of the FEM, it is crucial to research new FEM models which can

(1) Reduce significantly the over-stiffness of elements to obtain more accurate solutions, especially for linear triangular and tetrahedral elements.

(2) Obtain the upper bound of the exact solution in certain quantities to be able to easily evaluate the quality of the solution (the global error, bounds of solutions, convergence rates, etc).

(3) Be simple to implement, easy to comprehend and applicable for various kinds of elements, especially for triangular, tetrahedral, extremely distorted and n -sided polygonal elements.

In this thesis, to formulate such new FEM models, we combine the standard FEM with a strain smoothing technique. The next section, therefore, will present generally the strain smoothing technique.

1.2 Strain smoothing technique

The strain smoothing technique was proposed by Chen *et al.* [24] to stabilize the solutions in the context of the meshfree method and then applied in the natural element method using *n-sided polygonal natural elements* by Yoo *et al.* [156]. Using the strain smoothing technique in numerical methods, the compatible strains are replaced by smoothing strains by multiplying the compatible strains with a smoothing function which normally is a constant function. As a result, the numerical integration on the domain can be transferred to the line integration on the boundary of the domain by using the Divergence's theorem, and the constrained conditions on the shape of integrated domain can be removed. Liu *et al.* [83, 86] have applied this technique for the meshfree methods to formulate the linear conforming point interpolation method (LC-PIM) using PIM shape functions. In the integration of the weak form of LC-PIM, *triangular and tetrahedral elements* have been used. In particular, Liu *et al.* [83] have provided an intuitive

explanation and showed numerically that when a reasonably fine mesh is used, the LC-PIM has *an upper-bound property in the strain energy*.

Due to the complex field approximation in the meshfree methods which increase the computational cost, the following question is naturally arisen:

Can we apply the strain smoothing technique in the standard FEM model which has low computational cost?

If this can be done, we expect that the advantages of the strain smoothing technique relating to the upper bound [83], triangular, tetrahedral [83, 86] and n -sided polygonal elements [156] mentioned above can help to formulate the new FEM models which meet the requirements presented in Section 1.1.4.

1.3 Objective of the thesis

Based on the background of the FEM and the strain smoothing technique mentioned above, the objective of the thesis is to formulate and develop five new FEM models, including four smoothed FEM (S-FEM) models and one alpha-FEM model, in which four S-FEM models can

- ❖ Provide more accurate solutions compared to those of the standard FEM (especially for triangular and tetrahedral elements) in term of displacement, strain energy, and stress solutions for both compressible and nearly incompressible materials;
- ❖ Possess interesting properties of an equilibrium FEM model such as: (i) the upper bound property of the strain energy for force driven problems; (ii) natural immunization from the volumetric locking; (iii) ultra-accuracy and super-convergence of stress solutions;

- ❖ Use directly only shape functions themselves and no derivative of shape functions to calculate the stiffness matrix, and use more flexible domain discretizations such as extremely distorted elements and n -sided polygonal elements.

and the alpha-FEM model can

- ❖ Provide the nearly exact solution in the strain energy even with coarse meshes by using triangular and tetrahedral elements;

The formulation of four new S-FEM models is performed by combining the existing standard FEM and the strain smoothing technique. Based on four different smoothed entities such as cells (elements), nodes, edges and faces, four different smoothed finite element method (S-FEM) models such as cell-based S-FEM (CS-FEM), node-based S-FEM (NS-FEM), edge-based S-FEM (ES-FEM) and face-based S-FEM (FS-FEM) will be formulated, respectively. Each of four new S-FEM models will have different characters and advantages.

The formulation of the alpha-FEM is performed by a rational combination of the NS-FEM and existing standard FEM models with an alpha scaled variable to give a so-called alpha-FEM for triangular and tetrahedral elements (α FEM-T3, α FEM-T4) which gives nearly exact solution in strain energy for practical problems. .

Four proposed S-FEM models and the α FEM should provide more new FEM elements which are accurate, flexible, effective and simple. The S-FEM model which possesses interesting properties of an equilibrium FEM model should also provide a much simpler tool to estimate the quality of the solution (the global error, bounds of solutions, convergence rates, etc) by combining itself with the standard compatible FEM. This should have considerable impact on developing new quasi-equilibrium FEM elements and error estimation theories in the FEM. In addition, the α FEM should provide more the reference solutions with high accuracy of new benchmark problems used to verify the

accuracy, reliability and efficiency of numerical methods, especially in 3D problems or 2D problems with complicated geometry domains.

Due to the limit of the length of the thesis, we only present mainly the crucial properties for new methods. More applications and developments of the new methods, such as in the plates, visco-elastoplasticity, piezo-electric material, adaptive analyses, crack, etc, can be referred in the papers arising from the thesis.

The numerical examples illustrated in the thesis are mainly for solid mechanics. The main reason for choosing the solid mechanics is its simple theoretical foundation which helps us comprehend the new numerical methods faster and easier. In addition, the solid mechanics also possesses many analytical and numerical solutions of different problems which make it easy to verify the accuracy, reliability and efficiency of the new FEM methods.

1.4 Organization of the thesis

The thesis consists of nine Chapters and is organized as follows:

In Chapter 1, background of FEM and strain smoothing technique are briefly presented. The motivation and the objective of the thesis are clearly described.

In Chapter 2, some of the essential mathematical and numerical aspects of the standard finite element method (FEM) are briefly presented including the governing equations (or strong form), weak formulation, domain discretization, formulation of linear system of equations. Theoretical issues on solution existence, uniqueness, error, convergence rate and major properties of the FEM are also presented in a concise form, without details on proofs

In Chapter 3, the fundamental theories to construct the S-FEM models are presented in detail including the general formulation, construction of the shape functions, minimum

number of the smoothing domains, numerical procedure and general properties of the S-FEM models.

In Chapter 4, the cell-based S-FEM (CS-FEM) model is presented. The method is first based on 4-node quadrilateral elements, and then extended to n -sided polygonal elements (n CS-FEM). Evaluation of shape functions is described in detail. Some properties of CS-FEM solution and domain discretization with polygonal elements are presented. The stability analysis of CS-FEM and n CS-FEM is conducted and a selective scheme for nearly incompressible material is proposed. Last, numerical examples will illustrate the properties of CS-FEM and n CS-FEM.

In Chapter 5, we present a node-based S-FEM (NS-FEM) model for upper bound solutions to solid mechanics problems. The formulation of NS-FEM is first presented generally, and then specifically for the triangular and tetrahedral elements. Evaluation of shape functions is described in detail and some properties of NS-FEM solution are presented. Last, numerical examples will illustrate the properties of NS-FEM.

In Chapter 6, we present an edge-based S-FEM (ES-FEM) model, which is both spatially and temporally stable and more accurate compared with many existing FEM models. The formulation of ES-FEM is presented and evaluation of shape functions is described in detail. Next a smoothing-domain-based selective scheme for nearly incompressible material is proposed. Both spatial and temporal stabilities of ES-FEM are analyzed. Last, numerical examples will illustrate the excellent properties of ES-FEM

In Chapter 7, we present a face-based S-FEM (FS-FEM) model which is extended from the idea of ES-FEM. The formulations of both linear and nonlinear analyses of large deformation are presented. A smoothing-domain-based selective scheme for nearly incompressible material is proposed. The stability analysis of FS-FEM is also discussed. Last, numerical examples will illustrate the properties of FS-FEM.

In Chapter 8, we present a novel alpha FEM using 3-node triangular (α FEM-T3) elements for 2D problems and 4-node tetrahedral elements (α FEM-T4) for 3D problems. The essential idea of the method is to introduce a scale factor $\alpha \in [0,1]$ to establish a continuous function of strain energy that contains contributions from both the standard FEM and NS-FEM. This novel combined formulation of FEM and NS-FEM makes the best use of the upper bound property of NS-FEM and the lower bound property of the standard FEM. Using meshes with the same aspect ratio, a unified approach has been proposed to obtain the nearly exact solution in strain energy for a given linear problem. Last, numerical examples will illustrate the interesting properties of α FEM.

Last, Chapter 9 presents the conclusive remarks including original contributions, some insight comments, crucial contributions, and some recommendations for the future works.

Chapter 2

Brief on the Finite Element Method (FEM)

In this chapter, some of the essential mathematical and numerical aspects of the standard finite element method (FEM) are briefly presented, because they are frequently used in this thesis and are the base to formulate the S-FEM models. The mathematics language is used and kept as simple as possible with the necessary terminologies, mathematics tools and numerical treatments used in the FEM. The governing equations (or strong form), weak formulation, domain discretization, formulation of linear system of equations are briefly presented. Theoretical issues on solution existence, uniqueness, error, convergence rate and major properties of the FEM are also presented in a concise form, without details on proofs.

The formulation given in this chapter is generally applicable to linear solid mechanics problems of multi-dimensions. For the sake of convenience and simplicity in discussion, we choose two-dimensional (2D) problems as a default. When we need to extend the formulation for three-dimensional (3D) problems, it will be stated.

2.1 Brief on governing equations for elastic solid mechanics problems

Consider a 2D elastic solid mechanics problem in a physical domain of $\Omega \in \mathbb{R}^2$ bounded by a Lipschitz-continuous boundary Γ with $\Gamma = \Gamma_u \cup \Gamma_t$, $\Gamma_u \cap \Gamma_t = \emptyset$, equilibrium equations are governed by

$$\nabla_s^T \boldsymbol{\sigma} + \mathbf{b} = \mathbf{0} \quad \text{in } \Omega \quad (2.1)$$

where $\mathbf{0} = [0 \ 0]^T$ is a null vector; $\boldsymbol{\sigma} = [\sigma_{xx} \ \sigma_{yy} \ \sigma_{xy}]^T$ is the stress vector;

$\mathbf{b} = [b_x \ b_y]^T$ is the vector of external body forces in the x -axis and y -axis, respectively,

and ∇_s is a symmetric differential operator matrix given by

$$\nabla_s = \begin{bmatrix} \frac{\partial}{\partial x} & \mathbf{0} \\ \mathbf{0} & \frac{\partial}{\partial y} \\ \frac{\partial}{\partial y} & \frac{\partial}{\partial x} \end{bmatrix} \quad (2.2)$$

The essential boundary or Dirichlet condition is given as follows.

$$\mathbf{u} = \mathbf{w}_0 \quad \text{on } \Gamma_u \quad (2.3)$$

where \mathbf{u} is the displacement vector of the form

$$\mathbf{u} = \begin{bmatrix} u \\ v \end{bmatrix} \quad (2.4)$$

where u , v are the displacement components in the x -axis and y -axis, respectively;

$\mathbf{w}_0 = [w_{0x} \ w_{0y}]^T$ is the prescribed displacement vector on the essential boundary Γ_u . In

this thesis, for simplicity in discussion, we only consider the force-driving problems with the homogeneous essential boundary condition which means that

$$\mathbf{u} = \mathbf{0} \quad \text{on } \Gamma_u \quad (2.5)$$

The natural boundary or Newman condition is given as follows

$$\mathbf{n}^T \boldsymbol{\sigma} = \mathbf{t} \quad \text{on } \Gamma_t \quad (2.6)$$

where $\mathbf{t} = [t_x \quad t_y]^T$ is the prescribed traction vector on the natural boundary Γ , and \mathbf{n} is the unit outward normal matrix given by

$$\mathbf{n} = \begin{bmatrix} n_x & 0 \\ 0 & n_y \\ n_y & n_x \end{bmatrix} \quad (2.7)$$

in which n_x and n_y are the unit outward normal components in x -axis and y -axis, respectively.

The strain-displacement relation or the compatibility equation is given by

$$\boldsymbol{\varepsilon} = \nabla_s \mathbf{u} \quad (2.8)$$

where $\boldsymbol{\varepsilon}$ is the strain vector of the form

$$\boldsymbol{\varepsilon} = [\varepsilon_{xx} \quad \varepsilon_{yy} \quad \gamma_{xy}]^T \quad (2.9)$$

The stress-strain relation or the Hooke's law is

$$\boldsymbol{\sigma} = \mathbf{D}\boldsymbol{\varepsilon} \quad (2.10)$$

where \mathbf{D} is a matrix of material constants. Note that in this thesis, we just consider solids or structure made of materials that are physically *stable*: meaning that any amount of strains will result in stresses and hence some positive strain energy. Matrix \mathbf{D} is hence a symmetric positive definite (SPD) matrix.

2.2 Hilbert spaces

Finding an approximate solution using the FEM procedure is important but not sufficient for advanced applications, and it is more and more important to obtain information about the quality of the approximation. This not only makes the FEM result more applicable to practical engineering problems with certain confidence, but also guides us on how to further improve the solutions. The knowledge of functional analysis is therefore necessary to achieve this goal.

For general problems, we are not able to obtain the quantitative information about the *error* between the exact and approximate solutions, since the exact solution is unknown. Instead, we can satisfy with an *estimate* of such error with not only about the amount of the error but also the *rate of convergence* of a family of approximate solutions that converge to the exact solution. To perform such a convergence analysis in the FEM, spaces of functions to which the solution belongs have to be defined precisely. The spaces of functions used in the FEM are generally normed spaces equipped with inner product induced norms to measure the “magnitude” of the functions or the derivatives of the functions in a certain manner. With the aid of such norms, the procedure of obtaining an error estimate and the rate of convergence can be presented in precise forms.

The Hilbert spaces and inequalities are essential for the variational formulation of the second-order elastic solid mechanics problems (2.1). Let Ω be a bounded domain in \mathbb{R}^2 , and define the space $\mathbb{L}^2(\Omega; \mathbb{R}^1)$ of scalar functions $v \in \mathbb{R}^1$ on Ω as

$$\mathbb{L}^2(\Omega; \mathbb{R}^1) = \left\{ v \mid v \in \mathbb{R}^1 \text{ is defined on } \Omega \text{ and } \int_{\Omega} v^2 d\Omega < \infty \right\} \quad (2.11)$$

which shows that any function $v \in \mathbb{R}^1$ in $\mathbb{L}^2(\Omega; \mathbb{R}^1)$ are square integrable (in meaning of Lebesgue integration [127]) over Ω . Such a function can be continuous or discontinuous, but it has to be bounded in the integral sense defined in Eq. (2.11). In other words, the function is at least piecewise continuous over the problem domain Ω . The space $\mathbb{L}^2(\Omega; \mathbb{R}^1)$ is associated with the scalar inner product $(\cdot, \cdot)_{\mathbb{L}^2(\Omega; \mathbb{R}^1)}$

$$(v, w)_{\mathbb{L}^2(\Omega; \mathbb{R}^1)} = \int_{\Omega} v w d\Omega \quad (2.12)$$

and equipped with the corresponding norm $\|\cdot\|_{\mathbb{L}^2(\Omega; \mathbb{R}^1)}$:

$$\|v\|_{\mathbb{L}^2(\Omega; \mathbb{R}^1)} = \left(\int_{\Omega} v^2 d\Omega \right)^{1/2} \equiv (v, v)^{1/2} \quad (2.13)$$

Next we define the notation of general differentiations

$$D^\alpha v = \frac{\partial^{|\alpha|} v}{\partial x^{\alpha_1} \partial y^{\alpha_2}} \quad (2.14)$$

where here $\alpha = (\alpha_1, \alpha_2)$ is a nonnegative integer and $|\alpha| = \alpha_1 + \alpha_2$. For example, for a problem with a partial derivative of order 2, $D^\alpha v$ is one among three differentiations with $\alpha = (2, 0)$ or $\alpha = (1, 1)$ or $\alpha = (0, 2)$ with $|\alpha| = 2$.

We now define the Hilbert spaces $\mathbb{H}^m(\Omega; \mathbb{R}^1)$, where m is a non-negative integer, as

$$\mathbb{H}^m(\Omega; \mathbb{R}^1) = \left\{ v \mid D^\alpha v \in \mathbb{L}^2(\Omega; \mathbb{R}^1), \forall |\alpha| \leq m \right\} \quad (2.15)$$

which includes all functions whose derivatives up to m^{th} order are all square integrable.

The spaces $\mathbb{H}^m(\Omega; \mathbb{R}^1)$ is associated with the inner product $(\cdot, \cdot)_{\mathbb{H}^m(\Omega; \mathbb{R}^1)}$

$$(v, w)_{\mathbb{H}^m(\Omega; \mathbb{R}^1)} = \sum_{|\alpha| \leq m} \int_{\Omega} (D^\alpha v)(D^\alpha w) d\Omega \quad (2.16)$$

and equipped with the induced (full) norm

$$\|v\|_{\mathbb{H}^m(\Omega; \mathbb{R}^1)} = \left(\sum_{|\alpha| \leq m} \int_{\Omega} |D^\alpha v|^2 d\Omega \right)^{1/2} \quad (2.17)$$

as well as the semi-norm $|\cdot|_{\mathbb{H}^m(\Omega; \mathbb{R}^1)}$ (that includes only the m^{th} derivative):

$$|v|_{\mathbb{H}^m(\Omega; \mathbb{R}^1)} = \left(\int_{\Omega} |D^\alpha v|^2 d\Omega \right)^{1/2} \quad (2.18)$$

Note that $\mathbb{H}^0(\Omega; \mathbb{R}^1) = \mathbb{L}^2(\Omega; \mathbb{R}^1)$ [127]. The $\mathbb{H}^1(\Omega; \mathbb{R}^1)$ is the most relevant to the 2D elastic solid mechanics problem governed by Eq. (2.1)

$$\mathbb{H}^1(\Omega; \mathbb{R}^1) = \left\{ v \mid v \in \mathbb{L}^2(\Omega; \mathbb{R}^1), \partial v / \partial x_i \in \mathbb{L}^2(\Omega; \mathbb{R}^1), x_i = x, y \right\} \quad (2.19)$$

with the scalar product $(\cdot, \cdot)_{\mathbb{H}^1(\Omega; \mathbb{R}^1)}$

$$(v, w)_{\mathbb{H}^1(\Omega; \mathbb{R}^1)} = \int_{\Omega} (v w + \nabla v \cdot \nabla w) d\Omega \quad (2.20)$$

where ∇v is the gradient of v defined by

$$\nabla v = \begin{bmatrix} \frac{\partial v}{\partial x} & \frac{\partial v}{\partial y} \end{bmatrix}^T \quad (2.21)$$

and the corresponding norm $\|\cdot\|_{\mathbb{H}^1(\Omega; \mathbb{R}^1)}$

$$\|v\|_{\mathbb{H}^1(\Omega; \mathbb{R}^1)} = \left[\int_{\Omega} (v^2 + |\nabla v|^2) d\Omega \right]^{\frac{1}{2}} \quad (2.22)$$

and the seminorm $|\cdot|_{\mathbb{H}^1(\Omega; \mathbb{R}^1)}$

$$|v|_{\mathbb{H}^1(\Omega; \mathbb{R}^1)} = \left[\int_{\Omega} |\nabla v|^2 d\Omega \right]^{\frac{1}{2}} \quad (2.23)$$

We further define the space $\mathbb{H}_0^1(\Omega; \mathbb{R}^1) = \{v \in \mathbb{H}^1(\Omega; \mathbb{R}^1) | v = 0 \text{ on } \Gamma_u\}$ to be the subset of $\mathbb{H}^1(\Omega; \mathbb{R}^1)$ with vanishing values on Γ_u , and $\mathbb{H}_0^1(\Omega; \mathbb{R}^1)$ is equipped with the same scalar product and norms as $\mathbb{H}^1(\Omega; \mathbb{R}^1)$.

Note that the functional analysis has some following important results:

Lemma 2.1: Cauchy-Schwarz inequality

If u and v are members of an inner product space with inner product (\cdot, \cdot) , then we have the following Cauchy-Schwarz inequality [127]:

$$|(u, v)| \leq (u, u)^{\frac{1}{2}} (v, v)^{\frac{1}{2}}$$

or

$$\left| (v, w)_{\mathbb{L}^2(\Omega; \mathbb{R}^1)} \right| \leq \|u\|_{\mathbb{L}^2(\Omega; \mathbb{R}^1)} \|v\|_{\mathbb{L}^2(\Omega; \mathbb{R}^1)} \quad (2.24)$$

which gives a relationship between the inner product (\cdot, \cdot) and norm $\|\cdot\|$.

Lemma 2.2: Poincare-Friedrichs in $\mathbb{H}_0^1(\Omega; \mathbb{R}^1)$

When the domain Ω is bounded, there exists a constant C such that

$$\forall v \in \mathbb{H}_0^1(\Omega; \mathbb{R}^1), \quad \|v\|_{\mathbb{L}^2(\Omega; \mathbb{R}^1)} \leq C |v|_{\mathbb{H}^1(\Omega; \mathbb{R}^1)} \quad (2.25)$$

which is known as Poincare-Friedrichs inequality [127]. This inequality is one of the most important inequality to ensure the stability of the weakform.

Lemma 2.3: Equivalency between semi-norm and norm in $\mathbb{H}_0^1(\Omega; \mathbb{R}^1)$

Using Poincare-Friedrichs inequality in Lemma 2.2, and the definition of semi-norm (2.23) and norm (2.22), we are easy to obtain the following results

$$C_1 \|v\|_{\mathbb{H}^1(\Omega; \mathbb{R}^1)} \leq |v|_{\mathbb{H}^1(\Omega; \mathbb{R}^1)} \leq C_2 \|v\|_{\mathbb{H}^1(\Omega; \mathbb{R}^1)} \quad (2.26)$$

where C_1 and C_2 are positive real numbers. Equation (2.26) implies that the semi-norm $| \cdot |_{\mathbb{H}^1(\Omega; \mathbb{R}^1)}$ in the space $\mathbb{H}_0^1(\Omega; \mathbb{R}^1)$ is equivalent to the norm $\| \cdot \|_{\mathbb{H}^1(\Omega; \mathbb{R}^1)}$. This will permit us to use flexibly between the semi-norm $| \cdot |_{\mathbb{H}^1(\Omega; \mathbb{R}^1)}$ and norm $\| \cdot \|_{\mathbb{H}^1(\Omega; \mathbb{R}^1)}$ in the following proofs later.

As the field variables \mathbf{v} of 2D solid mechanics problems are in the vector form, $\mathbf{v}^T = \{v_1 \quad v_2\}$, the space $\mathbb{L}^2(\Omega)$ need to be defined generally for this case as follows

$$\mathbb{L}^2(\Omega; \mathbb{R}^2) = \left\{ \mathbf{v} = (v_x, v_y); v_i \in \mathbb{L}^2(\Omega; \mathbb{R}^1); \quad i = x, y \right\} \quad (2.27)$$

which is equipped with the corresponding norm

$$\|\mathbf{v}\|_{\mathbb{L}^2(\Omega; \mathbb{R}^2)} = \left(\sum_{i=1}^2 \|v_i\|_{\mathbb{L}^2(\Omega; \mathbb{R}^1)}^2 \right)^{1/2} \quad (2.28)$$

Similarly, the space $\mathbb{H}^1(\Omega; \mathbb{R}^2)$ for this case is defined as,

$$\mathbb{H}^1(\Omega; \mathbb{R}^2) = \left\{ \mathbf{v} = (v_x, v_y); v_i \in \mathbb{H}^1(\Omega; \mathbb{R}^1), \quad i = x, y \right\} \quad (2.29)$$

which is equipped with the corresponding norm

$$\|\mathbf{v}\|_{\mathbb{H}^1(\Omega; \mathbb{R}^2)} = \left(\sum_{i=1}^2 \|v_i\|_{\mathbb{H}^1(\Omega; \mathbb{R}^1)}^2 \right)^{1/2} \quad (2.30)$$

and seminorm

$$|\mathbf{v}|_{\mathbb{H}^1(\Omega; \mathbb{R}^2)} = \left(\sum_{i=1}^2 |v_i|_{\mathbb{H}^1(\Omega; \mathbb{R}^1)}^2 \right)^{1/2} \quad (2.31)$$

Also, the space $\mathbb{H}_0^1(\Omega; \mathbb{R}^2) = \{ \mathbf{v} \in \mathbb{H}^1(\Omega; \mathbb{R}^2) \mid \mathbf{v} = \mathbf{0} \text{ on } \Gamma_u \}$ to be the subset of $\mathbb{H}^1(\Omega; \mathbb{R}^2)$ with vanishing values on Γ_u , and $\mathbb{H}_0^1(\Omega; \mathbb{R}^2)$ is equipped with the same scalar product and norms as $\mathbb{H}^1(\Omega; \mathbb{R}^2)$. The definitions of the space $\mathbb{H}^1(\Omega; \mathbb{R}^2)$ by (2.29) and norms by (2.30) and (2.31) are quite straightforward to extend for $\mathbb{H}^1(\Omega; \mathbb{R}^3)$ for the field variables of 3D solid mechanics problems.

2.3 Brief on the variational formulation and weak form

We now ready to derive the weak form. By multiplying Eq. (2.1) with a test function $\mathbf{v} \in \mathbb{H}_0^1(\Omega; \mathbb{R}^2)$ and performing integration over the entire problem domain Ω , we have

$$\int_{\Omega} \mathbf{v}^T \nabla_s^T \boldsymbol{\sigma} d\Omega + \int_{\Omega} \mathbf{v}^T \mathbf{b} d\Omega = 0, \quad \forall \mathbf{v} \in \mathbb{H}_0^1(\Omega; \mathbb{R}^2) \quad (2.32)$$

Applying Green's divergence theorem [127], and using the boundary conditions (2.5) and (2.6), we obtain

$$\underbrace{\int_{\Omega} (\nabla_s \mathbf{v})^T \mathbf{D}(\nabla_s \mathbf{u}) d\Omega}_{a(\mathbf{u}, \mathbf{v})} = \underbrace{\int_{\Omega} \mathbf{v}^T \mathbf{b} d\Omega + \int_{\Gamma_t} \mathbf{v}^T \mathbf{t} d\Gamma}_{f(\mathbf{v})}, \quad \forall \mathbf{v} \in \mathbb{H}_0^1(\Omega; \mathbb{R}^2) \quad (2.33)$$

The 2D solid mechanics problem governed by Eq. (2.1) and boundary conditions (2.5) and (2.6) can be stated in the following well-known *weak statement*:

$$\text{Find } \mathbf{u} \in \mathbb{H}_0^1(\Omega; \mathbb{R}^2) \text{ such that } a(\mathbf{u}, \mathbf{v}) = f(\mathbf{v}) \quad \forall \mathbf{v} \in \mathbb{H}_0^1(\Omega; \mathbb{R}^2) \quad (2.34)$$

where $a(\mathbf{u}, \mathbf{v})$ is the bilinear form

$$a(\mathbf{u}, \mathbf{v}) = \int_{\Omega} (\nabla_s \mathbf{u})^T \mathbf{D}(\nabla_s \mathbf{v}) d\Omega \quad (2.35)$$

and $f(\mathbf{v})$ is the linear functional

$$f(\mathbf{v}) = \int_{\Omega} \mathbf{v}^T \mathbf{b} d\Omega + \int_{\Gamma_t} \mathbf{v}^T \mathbf{t} d\Gamma \quad (2.36)$$

The above weak formulation transforms the equilibrium system of equations (2.1) and boundary conditions (2.5) and (2.6) into a single equation (2.34), in which all of the features of solution are presented. In Eq. (2.34), we need only to perform the first derivatives for trial function \mathbf{u} . This is because the part of the 2nd order derivatives on the trial function \mathbf{u} has been “transferred” to the test function \mathbf{v} . As a result, the continuity requirement on function \mathbf{u} is one order *weakened* compared with the requirement of 2nd order differentiable in the strong formulation in Eq. (2.1). Therefore, the formulation (2.34) is a *weak form* of the classical original *strong form* with equilibrium equations (2.1) and boundary conditions (2.5) and (2.6). Both functions \mathbf{u} and \mathbf{v} now can belong to the space $\mathbb{H}_0^1(\Omega; \mathbb{R}^2)$, and hence it is a Galerkin weak form. We know that it is generally difficult to prove the existence of a solution of the strong form. However, using the weak form it is easy to prove the existence of a solution to Eq. (2.34).

Clearly, the bi-linear form, Eq. (2.35), is a symmetric bilinear form on $\mathbb{H}_0^1(\Omega; \mathbb{R}^2)$ and $f(\mathbf{v})$ is a continuous linear form under the following hypothesis $\mathbf{b} \in \mathbb{L}^2(\Omega; \mathbb{R}^2)$ and $\mathbf{t} \in \mathbb{L}^2(\Gamma_t; \mathbb{R}^2)$. For stable materials, using the Cauchy-Schwarz inequality in Lemma 2.1, and the equivalence of the full and semi norms of functions in $\mathbb{H}_0^1(\Omega; \mathbb{R}^2)$ by Lemma 2.3, it is easy to prove that

$$|a(\mathbf{u}, \mathbf{v})| \leq C_1 \|\mathbf{u}\|_{\mathbb{H}^1(\Omega; \mathbb{R}^2)} \|\mathbf{v}\|_{\mathbb{H}^1(\Omega; \mathbb{R}^2)} \quad (2.37)$$

where C_1 is a constant independent of $\mathbf{v}, \mathbf{u} \in \mathbb{H}_0^1(\Omega; \mathbb{R}^2)$. The forgoing equation implies that $a(\mathbf{u}, \mathbf{v})$ is continuous.

In addition, letting $\mathbf{u} = \mathbf{v}$, and using Poincare-Friedrichs inequality in Lemma 2.2, we have the following inequality

$$a(\mathbf{v}, \mathbf{v}) \geq \alpha \|\mathbf{v}\|_{\mathbb{H}^1(\Omega; \mathbb{R}^2)}^2 \quad (2.38)$$

where α is a constant independent of $\mathbf{v} \in \mathbb{H}_0^1(\Omega; \mathbb{R}^2)$, implying that $a(\mathbf{v}, \mathbf{v})$ is \mathbb{H} -elliptic [61, 127].

Based on the Lax-Milgram theorem [127] and the symmetric bilinear, continuous and \mathbb{H} -elliptic properties of the bilinear form $a(\mathbf{u}, \mathbf{v})$ and the continuous linear functional $f(\mathbf{v})$ assumed above, there exists a unique function $\mathbf{u} \in \mathbb{H}_0^1(\Omega; \mathbb{R}^2)$ such that Eq. (2.34) holds and the following basic stability inequality is satisfied

$$\|\mathbf{u}\|_{\mathbb{H}^1(\Omega; \mathbb{R}^2)} \leq \frac{1}{\alpha} \|f\|_{\mathbb{H}^{-1}(\Omega; \mathbb{R}^2)} \quad (2.39)$$

where

$$\|f\|_{\mathbb{H}^{-1}(\Omega; \mathbb{R}^2)} = \sup_{\substack{\mathbf{v} \in \mathbb{H}_0^1(\Omega; \mathbb{R}^2) \\ \mathbf{v} \neq \mathbf{0}}} \frac{|(f, \mathbf{v})|}{\|\mathbf{v}\|_{\mathbb{H}^1(\Omega; \mathbb{R}^2)}} \quad (2.40)$$

Inequality (2.39) assures that a small change in the linear functional $f(\mathbf{v})$ leads to a correspondingly small change in the solution $\mathbf{u} \in \mathbb{H}_0^1(\Omega; \mathbb{R}^2)$. In other words, the solution $\mathbf{u} \in \mathbb{H}_0^1(\Omega; \mathbb{R}^2)$ depends continuously on the data $f(\mathbf{v})$.

2.4 Domain discretization: creation of finite-dimensional space

Since this section backward, to simplify the symbols of finite-dimensional space, we let $\mathbb{V}_0 \equiv \mathbb{H}_0^1(\Omega; \mathbb{R}^2)$.

In the variational problem stated in Eq. (2.34), \mathbb{V}_0 is an infinite-dimensional space. It is generally impossible to solve the governing equations either in strong form (2.1) or weak form (2.34) in analytical means for the *exact* solution. Fortunately, the weak formulation (2.34) can be naturally used to obtain *approximate* solutions. In the FEM formulation, this is conveniently done by creating a discrete solutions space of finite-dimensional that is a subspace of the infinite-dimensional space: $\mathbb{V}_0^h \subset \mathbb{V}_0$, and an

approximated solution $\mathbf{u}^h \in \mathbb{V}_0^h$ is sought using variational form (2.34). Here h stands for finite dimension. At the limit of $h \rightarrow 0$, we expect $\mathbb{V}_0^h \rightarrow \mathbb{V}_0$, and $\mathbf{u}^h \rightarrow \mathbf{u}$. We can also find indication on how fast \mathbf{u}^h approaches to \mathbf{u} .

Note that in the analysis process, we assume that there is no “geometric” error caused by the domain discretization, so that we can focus only on the error of the approximation of variational form (2.34) induced by the use of the finite-dimensional space \mathbb{V}_0^h that deviates from \mathbb{V}_0 . We assume that the domain Ω in \mathbb{R}^2 is polygonal. That is, boundary Γ of Ω is made up of straight segments. Under these assumptions, it is easy to see that the whole domain can be covered exactly by polygonal elements, and it is now discretized into N_e of non-overlapping and non-gap elements and N_n nodes, such that $\Omega = \bigcup_{i=1}^{N_e} \Omega_i^e$ and $\Omega_i^e \cap \Omega_j^e = \emptyset$, $i \neq j$. We require that in the element mesh, there is no duplicated and hanging nodes.

We need now to create functions in \mathbb{V}_0^h for the assumption of displacement fields. Because the nodal shape functions are linearly independent, it is qualified as basis to form a space for an FEM model. An assumed displacement function for each displacement component can be expressed as a linear combination of the nodal shape functions with the nodal displacements as the coefficients. The finite element space \mathbb{V}_0^h can be spanned by the N_n independent nodal basis shape functions $\mathbf{N}_1, \mathbf{N}_2, \dots, \mathbf{N}_{N_n}$:

$$\mathbb{V}_0^h = \text{span} \{ \mathbf{N}_I \}_{I=1}^{N_n} \quad (2.41)$$

where $\mathbf{N}_I(\mathbf{x}) = \begin{bmatrix} N_I(\mathbf{x}) & 0 \\ 0 & N_I(\mathbf{x}) \end{bmatrix}$ is the matrix of shape functions, each for one displacement component. For node I , the nodal shape function $N_I(\mathbf{x})$ satisfies the following conditions:

- (i) $N_I(\mathbf{x}) \in \mathbb{H}^1(\Omega; \mathbb{R}^1)$ (Bounded and continuous in Ω)
- (ii) $N_I(\mathbf{x})$ is nonzero only within the elements that are connected to node I . (compact support)
- (iii) $N_I(\mathbf{x}_J) = \delta_{IJ}$ (Delta function property) (2.42)
- (iv) $\sum_{I=1}^{n_n^e} N_I(\mathbf{x}) = 1$ (partition of unity)
- (v) $\sum_{I=1}^{n_n^e} N_I(\mathbf{x}) \mathbf{x}_I = \mathbf{x}$ (linear compatibility)

where δ_{IJ} is the Kronecker delta; n_n^e is the number of the nodes of the element that hosts \mathbf{x} , and \mathbf{x}_I is the coordinate of I^{th} node of the element hosting \mathbf{x} .

The finite solution \mathbf{u}^h should come from space \mathbb{V}_0^h , and hence should have the form

$$\mathbf{u}^h = \sum_{I=1}^{N_n} \mathbf{N}_I(\mathbf{x}) \mathbf{d}_I \quad (2.43)$$

where $\mathbf{x} = [x \ y]^T$ and $\mathbf{d}_I = \mathbf{u}^h(\mathbf{x}_I)$ which is the nodal displacement vector at node I of the FEM solution.

2.5 Formulation of discretized linear system of equations

Using Eq. (2.34), the FEM weak statement becomes

$$\text{Find } \mathbf{u}^h \in \mathbb{V}_0^h \text{ such that } a(\mathbf{u}^h, \mathbf{v}^h) = f(\mathbf{v}^h) \quad \forall \mathbf{v}^h \in \mathbb{V}_0^h \quad (2.44)$$

Substituting Eq. (2.43) as the trial function and set $\mathbf{N}_I(\mathbf{x})$, $I=1, \dots, N_n$, as the test function \mathbf{v}^h into Eq. (2.44), we have the following system of N_n equations.

$$\sum_{J=1}^{N_n} a(\mathbf{N}_J, \mathbf{N}_I) \mathbf{d}_J = f(\mathbf{N}_I), \quad I=1, \dots, N_n \quad (2.45)$$

which can be written as the standard matrix form of discretized algebraic equations:

$$\mathbf{Kd} = \mathbf{f} \quad (2.46)$$

where \mathbf{d} is the vector of nodal displacements for all the nodes in the entire problem domain, and \mathbf{K} is the stiffness matrix of the FEM model with entries of

$$\mathbf{K}_{IJ} = \int_{\Omega} \mathbf{B}_I^T \mathbf{D} \mathbf{B}_J d\Omega = \sum_{i=1}^{N_e} \underbrace{\int_{\Omega_i^e} \mathbf{B}_I^T \mathbf{D} \mathbf{B}_J d\Omega}_{\mathbf{K}_{IJ,i}^e} \quad (2.47)$$

with the *strain-displacement matrix* defined as

$$\mathbf{B}_I(\mathbf{x}) = \nabla_s \mathbf{N}_I(\mathbf{x}) = \begin{bmatrix} \frac{\partial N_I(\mathbf{x})}{\partial x} & 0 \\ 0 & \frac{\partial N_I(\mathbf{x})}{\partial y} \\ \frac{\partial N_I(\mathbf{x})}{\partial y} & \frac{\partial N_I(\mathbf{x})}{\partial x} \end{bmatrix} \quad (2.48)$$

Vector \mathbf{f} is the external force vector acting at all the nodes in the entire problem domain, with entries of

$$\begin{aligned} \mathbf{f}_I &= \int_{\Omega} \mathbf{N}_I^T(\mathbf{x}) \mathbf{b} d\Omega + \int_{\Gamma_I} \mathbf{N}_I^T(\mathbf{x}) \mathbf{t} d\Gamma \\ &= \sum_{i=1}^{N_e} \int_{\Omega_i^e} \mathbf{N}_I^T(\mathbf{x}) \mathbf{b} d\Omega + \sum_{i=1}^{N_e} \int_{\Gamma_{I,i}^e} \mathbf{N}_I^T(\mathbf{x}) \mathbf{t} d\Gamma \end{aligned} \quad (2.49)$$

From Eqs. (2.47) and (2.49), it is seen that the actual evaluation of matrices \mathbf{K}_{IJ} and \mathbf{f}_I reduces to the evaluation of matrices for each element, and then to take the summation of these contributions from all elements. The condition (ii) in Eq. (2.42) leads to $\mathbf{K}_{IJ,i}^e = 0$ for node I and J that do not belong to the same Ω_i^e , which means that the stiffness matrix will be sparse. Generally, the evaluation of Eqs. (2.47) and (2.49) can be performed effectively using the Gauss integration technique [80].

Once Eq. (2.46) is obtained, we need to impose the boundary condition (2.5) to constraint the rigid body movements, which leads to a modification to the stiffness matrix

\mathbf{K} and the load vector \mathbf{f} , then the vector of nodal displacements \mathbf{d} can be solved easily, as long as the original problem is well-posed. The strains and stresses in each element can be retrieved. Recovery procedures can also be performed to improve the accuracy of the strain and stress fields.

We shall now address the following questions:

- Can the FEM procedure ensure the *existence* and *uniqueness* of the solution (\mathbf{K} is indeed not singular)?
- How is the solution depending on the input data?
- How to *estimate* of the error in the FEM solution?
- What is the *rate of convergence* of the FEM solutions, when mesh is refined?

The following Section will hence provide answers for all these questions.

2.6 FEM solution: existence, uniqueness, error and convergence

The theory of the functional analysis [61, 127] proved the following important theorems:

Theorem 2.1 (existence and uniqueness): Let \mathbb{V}_0^h be a finite-dimensional subspace of the Hilbert space \mathbb{V}_0 , $a: \mathbb{V}_0^h \times \mathbb{V}_0^h \rightarrow \mathbb{R}$ a continuous, \mathbb{H} -elliptic bilinear form, and $f: \mathbb{V}_0^h \rightarrow \mathbb{R}$ a bounded linear functional. Then there exists a unique function $\mathbf{u}^h \in \mathbb{V}_0^h$ that satisfies the discrete variational form (2.44). Furthermore, if $f(\mathbf{u}^h)$ is of the form

$$f(\mathbf{u}^h) = \int_{\Omega} (\mathbf{u}^h)^T \mathbf{b} d\Omega + \int_{\Gamma_t} (\mathbf{u}^h)^T \mathbf{t} d\Gamma \quad (2.50)$$

with $\mathbf{b} \in \mathbb{L}^2(\Omega; \mathbb{R}^2)$ and $\mathbf{t} \in \mathbb{L}^2(\Gamma_t; \mathbb{R}^2)$, then

$$\|\mathbf{u}^h\|_{\mathbb{H}^1(\Omega; \mathbb{R}^2)} \leq C_3 \left(\|\mathbf{b}\|_{\mathbb{L}^2(\Omega; \mathbb{R}^2)} + \|\mathbf{t}\|_{\mathbb{L}^2(\Gamma_t; \mathbb{R}^2)} \right) \quad (2.51)$$

where C_3 is a constant. \square

Theorem 2.1 provides the answer to the question of existence and uniqueness of the FEM solution. In addition, the stability estimate (2.51) for the finite element solution, which is similar to the stability estimate (2.39) for the continuous problems, reflects a very important property of the FEM. It assures us that a small change in the linear functional $f(\mathbf{u}^h)$ results correspondingly in only a “small” change in the solution $\mathbf{u}^h \in \mathbb{V}_0^h$. In other words, the solution $\mathbf{u}^h \in \mathbb{V}_0^h$ depends continuously on the data $f(\mathbf{u}^h)$. This implies that our numerical problem is well-posed, under the conditions for both the model creation and the inputs (external forces) specified in Theorem 2.1.

Note that the continuity of the bilinear form a requires the original problem being well-posed physically: for solid mechanics problems the material must be stable. The \mathbb{H} -ellipticity of the bilinear form a requires also a stable material [67] and sufficient essential boundary condition to constrain all the rigid movements.

We next proceed to examine the error $\mathbf{e} = \mathbf{u} - \mathbf{u}^h$, which is the difference between the exact solution and FEM solution. We state the following theorem.

Theorem 2.2 (“best” approximation): Let $\mathbf{u} \in \mathbb{V}_0$ is the exact solution of the original problem governed by equilibrium equations (2.1) and boundary conditions (2.5) and (2.6), and $\mathbf{u}^h \in \mathbb{V}_0^h$ is the finite element solution of the variational formulation (2.34), where $\mathbb{V}_0^h \subset \mathbb{V}_0$. Then

$$\|\mathbf{u} - \mathbf{u}^h\|_{\mathbb{H}^1(\Omega; \mathbb{R}^2)} \leq C_4 \|\mathbf{u} - \mathbf{v}^h\|_{\mathbb{H}^1(\Omega; \mathbb{R}^2)}, \quad \forall \mathbf{v}^h \in \mathbb{V}_0^h \quad (2.52)$$

where C_4 is a constant independent of $\mathbf{v}^h \in \mathbb{V}_0^h$. \square

Theorem 2.2 implies that the approximation $\mathbf{u}^h \in \mathbb{V}_0^h$ is the best possible approximation of the exact solution among all functions $\mathbf{v}^h \in \mathbb{V}_0^h$, in the sense that

$\|\mathbf{u} - \mathbf{v}^h\|_{\mathbb{H}^1(\Omega; \mathbb{R}^2)}$, $\forall \mathbf{v}^h \in \mathbb{V}_0^h$ is always larger than or equal to $\|\mathbf{u} - \mathbf{u}^h\|_{\mathbb{H}^1(\Omega; \mathbb{R}^2)}$. In addition, the optimal feature of the FEM solution, allow us to find a quantitative estimate of the bound of the solutions error, by choosing a suitable function $\mathbf{v}^h \in \mathbb{V}_0^h$ and estimating $\|\mathbf{u} - \mathbf{v}^h\|_{\mathbb{H}^1(\Omega; \mathbb{R}^2)}$. Usually, one chooses $\mathbf{v}^h = \mathcal{I}_h \mathbf{u}$ where $\mathcal{I}_h \mathbf{u} \in \mathbb{V}_0^h$ is a suitable *interpolant* of $\mathbf{u} \in \mathbb{V}_0$. This will further lead to the following Theorem 2.3.

Theorem 2.3 (*h*-dependence): If Ω is a convex polygonal domain and $\mathbf{u}^h \in \mathbb{V}_0^h$, with piecewise linear functions, is the finite element solution of the classical original problem governed by equilibrium equations (2.1) and boundary conditions (2.5) and (2.6), then there are constants C_5 , C_6 independent of \mathbf{u} and h such that

$$\|\mathbf{u} - \mathbf{u}^h\|_{\mathbb{L}^2(\Omega; \mathbb{R}^2)} \leq C_5 h^2 |\mathbf{u}|_{\mathbb{H}^2(\Omega; \mathbb{R}^2)} \quad (2.53)$$

and

$$\|\mathbf{u} - \mathbf{u}^h\|_{\mathbb{H}^1(\Omega; \mathbb{R}^2)} \leq C_6 h |\mathbf{u}|_{\mathbb{H}^2(\Omega; \mathbb{R}^2)} \quad (2.54)$$

where semi-norm $|\mathbf{u}|_{\mathbb{H}^2(\Omega; \mathbb{R}^2)}$ is written explicitly from Eq. (2.18) as

$$|\mathbf{u}|_{\mathbb{H}^2(\Omega; \mathbb{R}^2)} = \left[\int_{\Omega} \left(\left| \frac{\partial^2 \mathbf{u}}{\partial x^2} \right|^2 + \left| \frac{\partial \mathbf{u}}{\partial x} \frac{\partial \mathbf{u}}{\partial y} \right|^2 + \left| \frac{\partial^2 \mathbf{u}}{\partial y^2} \right|^2 \right) d\Omega \right]^{\frac{1}{2}} \quad (2.55)$$

□

By Theorem 2.3, we have the qualitative information that $\|\mathbf{u} - \mathbf{u}^h\|_{\mathbb{L}^2(\Omega; \mathbb{R}^2)}$ and $\|\mathbf{u} - \mathbf{u}^h\|_{\mathbb{H}^1(\Omega; \mathbb{R}^2)}$ approaches zero when the size of element h approaches zero if the second order derivative of the exact solution \mathbf{u} is bounded on the domain Ω . In addition, the power of h in Eqs. (2.53) and (2.54) also show the theoretical convergence rate of the finite element solutions in the corresponding norms. For problems of second-order PDE as shown in Eq. (2.1) with boundary conditions (2.5) and (2.6), the theoretical

convergence rate of itself \mathbf{u}^h is 2 in norm $\|\cdot\|_{\mathbb{L}^2(\Omega; \mathbb{R}^2)}$, and the theoretical convergence rate of the first derivative of \mathbf{u}^h is 1 in norm $\|\cdot\|_{\mathbb{H}^1(\Omega; \mathbb{R}^2)}$. In practice, these convergence rates also depend on the regularity of the exact solution \mathbf{u} as shown in right hand side parts of Eqs. (2.53) and (2.54). For example, for problems with singularities (at reentrant and crack tips), the practical convergence rates may become smaller than the theoretical convergence rates [61, 127].

In practical computation of solid mechanics, the norm $\|\mathbf{u} - \mathbf{u}^h\|_{\mathbb{H}^1(\Omega; \mathbb{R}^2)}$ is usually replaced by the seminorm $|\mathbf{u} - \mathbf{u}^h|_{\mathbb{H}^1(\Omega; \mathbb{R}^2)}$ which represents the total error between approximate energy and exact energy over the whole domain. Whereas the norm $\|\mathbf{u} - \mathbf{u}^h\|_{\mathbb{L}^2(\Omega; \mathbb{R}^2)}$ represents the total error between the approximated and exact solutions in displacement. Generalization of the above theory of the FEM for the interpolation with polynomials of higher order can be found in refs [61, 127].

2.7 Some other properties of the FEM solution

Property 2.1: Fully compatible property.

An FEM model created following strictly the weak statement Eq. (2.44) is said fully compatible. Essentially a fully compatible FEM model is established using: (1) compatibility displacements: the approximated displacements should be continuous on the element interfaces and differentiable inside the elements; (2) compatible strain fields that obtained using the strain-displacement relation; (3) essential boundary conditions are satisfied.

Property 2.2: Lower bound property.

The strain energy of a force-driven fully compatible FEM model is a lower bound of the exact strain energy

$$E(\boldsymbol{\varepsilon}^h) = \frac{1}{2} a(\mathbf{u}^h, \mathbf{u}^h) \leq \frac{1}{2} a(\mathbf{u}, \mathbf{u}) = E(\boldsymbol{\varepsilon}) \quad (2.56)$$

where $\boldsymbol{\varepsilon}^h = \nabla_s \mathbf{u}^h$ is the strains obtained using the FEM displacements $\mathbf{u}^h \in \mathbb{V}_0^h \subset \mathbb{V}_0$, $\boldsymbol{\varepsilon} = \nabla_s \mathbf{u}$ is the exact strain obtained using the exact displacements $\mathbf{u} \in \mathbb{V}_0$, and $E(\boldsymbol{\varepsilon})$ is the exact strain energy of the system defined as

$$E(\boldsymbol{\varepsilon}) = \frac{1}{2} \int_{\Omega} \boldsymbol{\varepsilon}^T \mathbf{D} \boldsymbol{\varepsilon} \, d\Omega \quad (2.57)$$

For the FEM model, the strain energy can be evaluated using any of the following expressions

$$E(\boldsymbol{\varepsilon}^h) = \frac{1}{2} \int_{\Omega} (\boldsymbol{\varepsilon}^h)^T \mathbf{D} \boldsymbol{\varepsilon}^h \, d\Omega = \frac{1}{2} a(\mathbf{u}^h, \mathbf{u}^h) = \frac{1}{2} \mathbf{d}^T \mathbf{K} \mathbf{d} \quad (2.58)$$

and for the exact model we should have

$$E(\boldsymbol{\varepsilon}) = \frac{1}{2} \int_{\Omega} \boldsymbol{\varepsilon}^T \mathbf{D} \boldsymbol{\varepsilon} \, d\Omega = \frac{1}{2} a(\mathbf{u}, \mathbf{u}) \quad (2.59)$$

The proof of the lower bound property can be found in [54, 151] in variational formulation. The lower bound property implies the well-known fact that the FEM solution underestimates the strain energy. This property of FEM provides a good global measure of the lower bound of the FEM solution with respect to the exact solution.

Property 2.3: Monotonic convergence property.

For a given sequence of n_m nested element meshes M_1, M_2, \dots, M_{n_m} , such that the corresponding solution spaces satisfies $\mathbb{V}_0^{M_1} \subset \mathbb{V}_0^{M_2} \dots \subset \mathbb{V}_0^{M_{n_m}} \subset \mathbb{V}_0$, then the following inequalities stand

$$E(\boldsymbol{\varepsilon}^{M_1}) \leq E(\boldsymbol{\varepsilon}^{M_2}) \leq \dots \leq E(\boldsymbol{\varepsilon}^{M_{n_m}}) \leq E(\boldsymbol{\varepsilon}) \quad (2.60)$$

where $\boldsymbol{\varepsilon}^{M_i}$ is the FEM compatible solution of strains obtained using mesh M_i . This property can be shown easily using the arguments given by Oliveira [116].

Property 2.4: Reproducibility of the exact solution of the FEM.

If the exact solution $\mathbf{u} \in \mathbb{V}_0^h \subset \mathbb{V}_0$, then the FEM will reproduce the exact solution \mathbf{u} . This property can be easily proven [80, 116].

Chapter 3

Fundamental theories of smoothed finite element methods (S-FEM)

In a standard FEM model, we use directly the compatible strain field to evaluate the energy potential functional. In an S-FEM model, however, we will modify compatible strain field. The modified strain field is then used to evaluate the strain energy potential functional, and a proper energy weak form is used to construct the discretized model. Such a strain modification must be done in a proper way to ensure stability, convergence and to obtain special property for the S-FEM models constructed. In this thesis, we will use the strain smoothing technique [25].

This chapter presents the fundamental theories to construct the S-FEM models. The following discussions and formulations are mainly performed for problems in two-dimensional domains (2D). The extension to three-dimensional (3D) domains can be more complicated in implementation, but it should be trivial technically.

3.1 General formulation of the S-FEM models

3.1.1 Strain smoothing technique

The strain smoothing technique is the most frequently used technique to modify the compatible strain field. As in the FEM presented in [Chapter 2](#), we first assume a

displacement field $\mathbf{u}^h(\mathbf{x})$ in a space $\mathbb{V}_0^h \subset \mathbb{V}_0$ using shape functions in the form of Eq. (2.41). The compatible strain field $\boldsymbol{\varepsilon}^h(\mathbf{x})$ is obtained using the strain-displacement relation $\boldsymbol{\varepsilon}^h(\mathbf{x}) = \nabla_S \mathbf{u}^h(\mathbf{x})$. Such a compatible strain field is then used to construct the S-FEM models.

In the S-FEM models, the compatible strains $\boldsymbol{\varepsilon}^h(\mathbf{x})$ in each smoothing domain Ω_k^s now are replaced by smoothing strains $\bar{\boldsymbol{\varepsilon}}_k$ by multiplying the compatible strains with a smoothing function $\Phi_k(\mathbf{x})$ as follows:

$$\bar{\boldsymbol{\varepsilon}}_k = \int_{\Omega_k^s} \boldsymbol{\varepsilon}^h(\mathbf{x}) \Phi_k(\mathbf{x}) d\Omega \quad (3.1)$$

where Ω_k^s is a smoothing domain and $\Phi_k(\mathbf{x})$ is a smoothing function that satisfies at least unity property

$$\int_{\Omega_k^s} \Phi_k(\mathbf{x}) d\Omega = 1 \quad (3.2)$$

In this thesis, we use the following Heaviside-type constant step smoothing function:

$$\Phi_k(\mathbf{x}) = \begin{cases} 1/A_k^s & \mathbf{x} \in \Omega_k^s \\ 0 & \mathbf{x} \notin \Omega_k^s \end{cases} \quad (3.3)$$

where $A_k^s = \int_{\Omega_k^s} d\Omega$ is the area of smoothing domain Ω_k^s . In this case we have

$$\bar{\boldsymbol{\varepsilon}}_k(\mathbf{x}) = \frac{1}{A_k^s} \int_{\Omega_k^s} \boldsymbol{\varepsilon}^h(\mathbf{x}) d\Omega = \frac{1}{A_k^s} \int_{\Omega_k^s} \nabla_S \mathbf{u}^h(\mathbf{x}) d\Omega \quad (3.4)$$

Recall that various smoothing techniques have been used for different purposes, including in the nonlocal continuum mechanics [43] to introduce the size effects, and in the smoothed particle hydrodynamics [91, 72] to approximate field functions. The strain smoothing technique was used to resolve the material instabilities [24] and the spatial instability in the nodal integrated meshfree methods [152, 25]. It is also used to

approximate the derivative in the strong form models of solids [87], compressible fluids [81, 82], and incompressible fluids [155].

In this thesis, the strain smoothing operation defined in Eq. (3.4) will be applied to create modified strain field in finite element settings. To develop the S-FEM models of different properties, four different smoothing domains created based on elements (cells), nodes, edges and faces will be used. Then, four respectively different S-FEM models: cell-based S-FEM (CS-FEM) [70, 73, 77], node-based S-FEM (NS-FEM) [78], edge-based S-FEM (ES-FEM) [76] and face-based S-FEM (FS-FEM) [103] will be formulated. Each of four S-FEM models will have different properties, advantages and disadvantages. In addition, by a rational combination of the NS-FEM and the standard FEM models with a scaling factor alpha, a new numerical method, named alpha-FEM that uses triangular and tetrahedral elements (α FEM-T3, α FEM-T4) [74], is formulated. The alpha-FEM can give nearly exact solutions in strain energy.

The general formulation for the S-FEM models will be presented in this section. Each of the S-FEM models will be presented in detail in following chapters.

3.1.2 Smoothing domain creation

In the S-FEM models, a mesh of elements is required, and it can be created exactly in the same manner as in the standard FEM. Upon the element mesh, the problem domain Ω can then be divided into a set of N_s “non-overlap” and “no-gap” smoothing domains

such that $\Omega = \bigcup_{k=1}^{N_s} \Omega_k^s$ and $\Omega_i^s \cap \Omega_j^s = \emptyset$, $i \neq j$. In theory, such a division can be arbitrary

when continuous shape functions are used. In practice, however, it is usually performed based on the element’s entities, such as elements (cells), or nodes, or edges, or faces. To

ensure the stability of the S-FEM models, the number of the smoothing domain created has to satisfy certain conditions, as will be discussed in detail in Section 3.3.

Table 3.1 lists a number of types of smoothing domains of the S-FEM models. In the CS-FEM, for example, the number of the smoothing domains N_s can be the same as the element number N_e , meaning one element is used as one smoothing domain. For stability reasons, it is often to subdivide each element Ω_i^e into $n_i^s \in [1, \infty)$ smoothing domains as shown in Figure 3.1. For the NS-FEM using n -sided polygonal elements, the smoothing domain Ω_k^s associated with the node k is created by connecting sequentially the mid-edge-point to the central points of the surrounding n -sided polygonal elements of the node k as shown in Figure 3.2. For the ES-FEM using triangular elements, the smoothing domain Ω_k^s associated with the edge k is created by connecting two endpoints of the edge to central points of adjacent elements as shown in Figure 3.3. For the FS-FEM using tetrahedral elements, the smoothing domain Ω_k^s associated with the face k is created by connecting three field nodes of the face to the centers of the adjacent elements as shown in Figure 3.4. More details of the discretization of the domain Ω into N_s smoothing domains Ω_k^s for different S-FEM models will be presented in the following chapters.

3.1.3 Smoothed strain field

In an S-FEM model, the assumed displacement field is always continuous over the problem domain, and the integration of the weak form is based on N_s smoothed domains created by one of the ways described in Section 3.1.2. Each of the N_s smoothing domains Ω_k^s can, in general, be viewed consisting of $n_s \geq 1$ sub-smoothing cells $\Omega_{k,p}^s$ such that the compatible strain field $\boldsymbol{\varepsilon}^h(\mathbf{x}) = \nabla_s \mathbf{u}^h(\mathbf{x})$ is continuous inside each of the sub-smoothing

cells $\Omega_{k,p}^s$ but can be discontinuous on the common inner boundaries of domains Ω_k^s .

For example, for an ES-FEM model using 3-node triangular elements of linear shape functions, as shown in Figure 3.5, a smoothing domain Ω_k^s associated with the inner edge k will include $n_s = 2$ triangular sub-smoothing cells $\Omega_{k,1}^s$ and $\Omega_{k,2}^s$ on both sides of the edge. The compatible strain field $\boldsymbol{\varepsilon}^h(\mathbf{x})$ is piecewise constants and discontinuous along the edge k (or called the common inner boundary $\Gamma_{k,1-2}^s(\text{inner})$ of $\Omega_{k,1}^s$ and $\Omega_{k,2}^s$).

By using the piece-wise constant smoothing function in Eq. (3.3), and applying the Divergence theorem on each sub-smoothing cell $\Omega_{k,p}^s$, the smoothed strain $\bar{\boldsymbol{\varepsilon}}_k(\mathbf{x})$ of the smoothing domain Ω_k^s in Eq. (3.4) can be evaluated as follows.

$$\bar{\boldsymbol{\varepsilon}}_k = \int_{\Omega_k^s} \nabla_S \mathbf{u}^h(\mathbf{x}) \frac{1}{A_k^s} d\Omega = \frac{1}{A_k^s} \sum_{p=1}^{n_s} \int_{\Omega_{k,p}^s} \nabla_S \mathbf{u}^h(\mathbf{x}) d\Omega = \frac{1}{A_k^s} \sum_{p=1}^{n_s} \int_{\Gamma_{k,p}^s} \mathbf{n}_{k,p}^s(\mathbf{x}) \mathbf{u}^h(\mathbf{x}) d\Gamma \quad (3.5)$$

where $\Gamma_{k,p}^s$ is the boundary of the smoothing cell $\Omega_{k,p}^s$, and $\mathbf{n}_{k,p}^s(\mathbf{x})$ is the matrix of the components of the outward normal vector on the boundary $\Gamma_{k,p}^s$ and has the form similar to Eq. (2.7).

The smoothing cell boundary segments $\Gamma_{k,p}^s$ are now categorized into two types: the inner boundaries $\Gamma_{k,p}^s(\text{inner})$ which locates inside the smoothing domain Ω_k^s , and the outer boundaries $\Gamma_{k,p}^s(\text{outer})$ which is on the boundary of the smoothing domain Ω_k^s as shown in Figure 3.5. Because (again) the displacement field is continuous, we has the following results for two adjacent smoothing cells $\Omega_{k,1}^s$ and $\Omega_{k,2}^s$ that have the common inner boundary $\Gamma_{k,1-2}^s(\text{inner})$ as shown in Figure 3.5:

$$\mathbf{n}_{k,1}^s(\mathbf{x}) \mathbf{u}^h(\mathbf{x}) + \mathbf{n}_{k,2}^s(\mathbf{x}) \mathbf{u}^h(\mathbf{x}) = \mathbf{0} \quad \text{on } \Gamma_{k,1-2}^s(\text{inner}) \quad (3.6)$$

where $\mathbf{n}_{k,1}^s(\mathbf{x})$ is the matrix of the components of the outward normal vector on the boundary $\Gamma_{k,1-2}^s$ of the smoothing cell $\Omega_{k,1}^s$, and $\mathbf{n}_{k,2}^s(\mathbf{x})$ is that on the boundary $\Gamma_{k,1-2}^s$ of the smoothing cell $\Omega_{k,2}^s$ as shown in Figure 3.5.

Eq. (3.6) implies that when a continuous displacement field is used, the summation of two integrations $\sum_{p=1}^2 \int_{\Gamma_{k,1-2}^s} \mathbf{n}_{k,p}^s(\mathbf{x}) \mathbf{u}^h(\mathbf{x}) d\Gamma$ of two adjacent smoothing cells $\Omega_{k,1}^s$ and $\Omega_{k,2}^s$ on the inner boundaries $\Gamma_{k,1-2}^s$ will vanish, due to the opposite sign of $\mathbf{n}_{k,1}^s(\mathbf{x})$ and $\mathbf{n}_{k,2}^s(\mathbf{x})$. Hence, the summation in Eq. (3.5) for all inner boundaries $\Gamma_{k,p}^s$ will vanish and Eq. (3.5) is reduced into a much simpler form that keeps the summation over only outer boundaries, as follows

$$\bar{\boldsymbol{\varepsilon}}_k = \frac{1}{A_k^s} \sum_{p=1}^{n_s} \int_{\Gamma_{k,p}^s} \mathbf{n}_{k,p}^s(\mathbf{x}) \mathbf{u}^h(\mathbf{x}) d\Gamma = \frac{1}{A_k^s} \int_{\Gamma_k^s} \mathbf{n}_k^s(\mathbf{x}) \mathbf{u}^h(\mathbf{x}) d\Gamma \quad (3.7)$$

where $\Gamma_k^s = \sum_{p=1}^{n_s} \Gamma_{k,p}^s$ which is the boundary of the smoothing domain Ω_k^s , and $\mathbf{n}_k^s(\mathbf{x})$

is the matrix of the components of the outward normal vector on the boundary Γ_k^s and also has the form

$$\mathbf{n}_k^s(\mathbf{x}) = \begin{bmatrix} n_{kx}^s & 0 \\ 0 & n_{ky}^s \\ n_{ky}^s & n_{kx}^s \end{bmatrix} \quad (3.8)$$

in which n_{kx}^s and n_{ky}^s are the unit outward normal components in x -axis and y -axis, respectively.

3.1.4 Smoothed strain-displacement matrix

Now, substituting Eq. (2.43) as the trial function $\mathbf{u}^h \in \mathbb{V}^h(\Omega)$ into Eq. (3.5), one obtains the smoothed strain as

$$\bar{\boldsymbol{\varepsilon}}_k = \sum_{I \in S_k^s} \bar{\mathbf{B}}_I \bar{\mathbf{d}}_I \quad (3.9)$$

where $\bar{\mathbf{d}}_I$ is the nodal displacement vector at node I of the S-FEM solution; S_k^s is the set of the “supporting” nodes for the smoothing domain Ω_k^s , which consists all the nodes of the elements associated with the smoothing domain Ω_k^s . For example, for the ES-FEM using 3-node triangular elements as shown in Figure 3.3, S_k^s is the set of nodes $\{A, B, C\}$ for the boundary edge m , and $\{D, E, F, G\}$ for the inner edge k . The “smoothed” strain-displacement matrix $\bar{\mathbf{B}}_I$ is evaluated using

$$\bar{\mathbf{B}}_I = \frac{1}{A_k^s} \int_{\Gamma_k^s} \mathbf{n}_k^s(\mathbf{x}) \mathbf{N}_I(\mathbf{x}) d\Gamma = \begin{bmatrix} \bar{b}_{Ix} & 0 \\ 0 & \bar{b}_{Iy} \\ \bar{b}_{Iy} & \bar{b}_{Ix} \end{bmatrix} \quad (3.10)$$

with

$$\bar{b}_{Ih} = \frac{1}{A_k^s} \int_{\Gamma_k^s} n_{kh}^s(\mathbf{x}) N_I(\mathbf{x}) d\Gamma, \quad (h = x, y) \quad (3.11)$$

When a linearly compatible displacement field along the boundary Γ_k^s is used, one Gaussian point is sufficient for the line-integration along each segment $\Gamma_{k,p}^s$ of boundary Γ_k^s , Eq. (3.11) can be further simplified to a summation form

$$\bar{b}_{Ih} = \frac{1}{A_k^s} \sum_{p=1}^{n_{\Gamma}^s} n_{kh,p}^s N_I(\mathbf{x}_p^{GP}) l_{k,p}^s, \quad (h = x, y) \quad (3.12)$$

where n_{Γ}^s is the total number of the boundary segments $\Gamma_{k,p}^s \subset \Gamma_k^s$. For example, in the ES-FEM using 3-node triangular elements as shown in Figure 3.3, $n_{\Gamma}^s = 3$ for the boundary edge m , which is the total number of three boundary segments (AB, BI, IA), and $n_{\Gamma}^s = 4$ for the inner edge k , which is the total number of four boundary segments (DH, HF, FO, OD); \mathbf{x}_p^{GP} is the midpoint (Gaussian point) of the boundary segments $\Gamma_{k,p}^s$, whose length and outward unit normal are denoted as $l_{k,p}^s$ and $n_{kh,p}^s$, respectively.

When the assumed displacement field is continuous, from the definition of the smoothed strain field $\bar{\boldsymbol{\varepsilon}}_k$ in Eq. (3.1) and Eqs. (3.5) and (3.7), it is easy to reveal the relation between the smoothed strain-displacement matrix $\bar{\mathbf{B}}_I$ with the standard compatible strain-displacement matrix $\mathbf{B}_I(\mathbf{x})$ of the FEM:

$$\bar{\mathbf{B}}_I = \frac{1}{A_k^s} \int_{\Gamma_k^s} \mathbf{n}_k^s(\mathbf{x}) \mathbf{N}_I(\mathbf{x}) d\Gamma = \frac{1}{A_k^s} \int_{\Omega_k^s} \nabla_S \mathbf{N}_I(\mathbf{x}) d\Omega = \frac{1}{A_k^s} \int_{\Omega_k^s} \mathbf{B}_I(\mathbf{x}) d\Omega \quad (3.13)$$

which means that the smoothed strain-displacement matrix $\bar{\mathbf{B}}_I$ is the average of the standard compatible strain-displacement matrix $\mathbf{B}_I(\mathbf{x})$ over the smoothing domain Ω_k^s .

Note that as recommended by Yoo *et al.* [156], higher-order gradients can be readily obtained by recursive application of Eq. (3.5), as long as lower-order gradients can be interpolated from nodal values. For example, the second order of the displacement gradients $D^2(\bar{\mathbf{u}}(\mathbf{x}))$ can be obtained from the first order of the displacement gradients $D^1(\bar{\mathbf{u}}(\mathbf{x}))$ in the same way

$$D^2(\bar{\mathbf{u}}(\mathbf{x})) = \int_{\Omega_k^s} \nabla_S D^1(\bar{\mathbf{u}}(\mathbf{x})) \frac{1}{A_k^s} d\Omega = \frac{1}{A_k^s} \int_{\Gamma_k^s} \mathbf{n}_k^s(\mathbf{x}) D^1(\bar{\mathbf{u}}(\mathbf{x})) d\Gamma \quad (3.14)$$

where $\bar{\mathbf{u}}(\mathbf{x})$ is the displacement solution of an S-FEM model.

3.1.5 Smoothed stiffness matrix

Following the formulation procedure similar to the standard FEM, with substitutions of the compatible strain $\boldsymbol{\varepsilon}^h$ by the smoothing strain $\bar{\boldsymbol{\varepsilon}}$, the element domain Ω_i^e by the smoothing domain Ω_k^s , the total number of elements N_e by the total number of smoothing domains N_s , and the compatible strain-displacement matrix \mathbf{B} by the smoothed strain-displacement matrix $\bar{\mathbf{B}}$, the final discretized algebraic system of equations of the S-FEM models has the form of

$$\bar{\mathbf{K}}\bar{\mathbf{d}} = \mathbf{f} \quad (3.15)$$

where $\bar{\mathbf{K}}$ is the *smoothed* stiffness matrix whose entries are calculated by

$$\bar{\mathbf{K}}_{IJ} = \int_{\Omega} \bar{\mathbf{B}}_I^T \mathbf{D} \bar{\mathbf{B}}_J d\Omega = \sum_{k=1}^{N_s} \int_{\Omega_k^s} \bar{\mathbf{B}}_I^T \mathbf{D} \bar{\mathbf{B}}_J d\Omega = \sum_{k=1}^{N_s} \bar{\mathbf{B}}_I^T \mathbf{D} \bar{\mathbf{B}}_J A_k^s \quad (3.16)$$

Note that in Eq. (3.15), the load vector \mathbf{f} is without bar-hat, because no smoothing function is applied to the linear functional in the S-FEM models. The load vector is therefore computed exactly in the same way as that in the FEM. Further more in Eq. (3.16), $\bar{\mathbf{K}}$ is symmetric positive definite (SPD) and $\bar{\mathbf{K}}_{IJ}$ needs to be computed only when nodes I and J share a same smoothing domain. Otherwise, it is zero. Hence, $\bar{\mathbf{K}}$ will be also sparse for the S-FEM models. Hence, Eq. (3.15) can be solved by using standard routines with ease because $\bar{\mathbf{K}}$ is SPD and sparse.

Also note that $\bar{\mathbf{K}}$ will be banded if the nodes are properly numbered, as that in the FEM. For the S-FEM models, the bandwidth of $\bar{\mathbf{K}}$ will be determined by the largest difference of node numbers of the nodes of the elements contributing to the smoothing domains. Specifically, when the smoothing domains are located inside the elements such as in the CS-FEM, the bandwidth of $\bar{\mathbf{K}}$ will be same as that of \mathbf{K} in the FEM. It is because the number of nodes related to the smoothing domains is identical to that related to the elements. However, when the smoothing domains cover parts of adjacent elements such as in the NS-FEM, ES-FEM or FS-FEM, the bandwidth of $\bar{\mathbf{K}}$ will be larger than that of \mathbf{K} in the FEM. It is because the number of nodes supporting the smoothing domains is larger than that of the elements.

From Eqs. (3.7), (3.10) and (3.12), it is seen that the numerical integration on the domain Ω_k^s now can be transferred to the integration on the boundary of the smoothing domain Γ_k^s . Further more, no derivative of shape functions is involved in computing the field gradients and only shape function values at some Gauss points along boundaries of

smoothing domains are needed. This makes the computing procedure of the stiffness matrix in the S-FEM models easier than that in the FEM. We now can use directly the shape functions, not the derivative of shape functions, to calculate the stiffness matrix on the basis of boundaries of physical smoothing domains. No mapping is needed.

3.2 Construction of shape functions for the S-FEM models

In general, the S-FEM models work well for general n -sided polygonal elements. This is because the smoothed strain field can be computed using Eq. (3.7), where only the assumed displacement values are needed at location on the smoothing domain boundaries. No derivatives of the assumed displacement field are required. Making use of this important feature, Dai *et al.* [37] devised a simple but important scheme to compute the shape function values for general n -sided polygonal elements. Here we present this scheme in a great detail.

Consider an n -sided convex polygonal element Ω_i^e . We first divide the element into n non-overlapping and non-gap triangular sub-domains $\Omega_{i,p}^e$ ($p=1,2,\dots,n$) by simply connecting n field nodes with the central point O of the polygon, as shown in Figure 3.6. The coordinates of the central point O are calculated by

$$x_O = \frac{1}{n} \sum_{p=1}^n x_p, \quad y_O = \frac{1}{n} \sum_{p=1}^n y_p \quad (3.17)$$

where $\mathbf{x}_p = [x_p \ y_p]^T$ ($p=1,2,\dots,n$) are coordinates of n field nodes, respectively.

We then assume that the displacement vector \mathbf{d}_O at the central point O is the simple average of n displacement vectors \mathbf{d}_p ($p=1,2,\dots,n$) of n field nodes as follows

$$\mathbf{d}_O = \frac{1}{n} \sum_{p=1}^n \mathbf{d}_p \quad (3.18)$$

On the first triangular sub-domain $\Omega_{i,1}^e$ (triangle 1-2- O), we now construct a linear displacement field using

$$\bar{\mathbf{u}}_{i,1}^e = \mathbf{N}_1 \mathbf{d}_1 + \mathbf{N}_2 \mathbf{d}_2 + \mathbf{N}_3 \mathbf{d}_O \quad \text{on } \Omega_{i,1}^e \quad (3.19)$$

where \mathbf{N}_j ($j=1,2,3$) are the linear shape functions of the standard FEM created by three points: 1-2- O [80]. Substituting Eq. (3.18) into Eq. (3.19), one obtains

$$\bar{\mathbf{u}}_{i,1}^e = \left(\mathbf{N}_1 + \frac{1}{n} \mathbf{N}_3 \right) \mathbf{d}_1 + \left(\mathbf{N}_2 + \frac{1}{n} \mathbf{N}_3 \right) \mathbf{d}_2 + \frac{1}{n} \mathbf{N}_3 \mathbf{d}_3 + \dots + \frac{1}{n} \mathbf{N}_3 \mathbf{d}_{n-1} + \frac{1}{n} \mathbf{N}_3 \mathbf{d}_n \quad (3.20)$$

which implies that the shape function vector $\mathbf{N}_{i,1}^e$ for the triangular sub-domain $\Omega_{i,1}^e \subset \Omega_i^e$ has the form

$$\mathbf{N}_{i,1}^e = \left[\mathbf{N}_1 + \frac{1}{n} \mathbf{N}_3 \quad \mathbf{N}_2 + \frac{1}{n} \mathbf{N}_3 \quad \frac{1}{n} \mathbf{N}_3 \quad \dots \quad \frac{1}{n} \mathbf{N}_3 \quad \frac{1}{n} \mathbf{N}_3 \right]_{1 \times n} \quad (3.21)$$

Next, a linear displacement field on the second triangular sub-domain $\Omega_{i,2}^e$ (triangle 2-3- O) is constructed as

$$\bar{\mathbf{u}}_{i,2}^e = \mathbf{N}_1 \mathbf{d}_2 + \mathbf{N}_2 \mathbf{d}_3 + \mathbf{N}_3 \mathbf{d}_O \quad \text{on } \Omega_{i,2}^e \quad (3.22)$$

or

$$\bar{\mathbf{u}}_{i,2}^e = \frac{1}{n} \mathbf{N}_3 \mathbf{d}_1 + \left(\mathbf{N}_1 + \frac{1}{n} \mathbf{N}_3 \right) \mathbf{d}_2 + \left(\mathbf{N}_2 + \frac{1}{n} \mathbf{N}_3 \right) \mathbf{d}_3 + \frac{1}{n} \mathbf{N}_3 \mathbf{d}_4 + \dots + \frac{1}{n} \mathbf{N}_3 \mathbf{d}_n \quad (3.23)$$

which implies that the shape function vector $\mathbf{N}_{i,2}^e$ for the triangular sub-domain $\Omega_{i,2}^e \subset \Omega_i^e$ has the form

$$\mathbf{N}_{i,2}^e = \left[\frac{1}{n} \mathbf{N}_3 \quad \mathbf{N}_1 + \frac{1}{n} \mathbf{N}_3 \quad \mathbf{N}_2 + \frac{1}{n} \mathbf{N}_3 \quad \frac{1}{n} \mathbf{N}_3 \quad \dots \quad \frac{1}{n} \mathbf{N}_3 \right]_{1 \times n} \quad (3.24)$$

Following the similar procedure, we can construct linear displacement fields on all remaining triangular sub-domains from $\mathbf{N}_{i,3}^e$ to $\mathbf{N}_{i,n}^e$. Due to the linear compatible property of the displacement fields $\bar{\mathbf{u}}_{i,p}^e$ ($p=1,2,\dots,n$) along the boundary segments of the triangular sub-domains, it is easy to verify that the union of n linear displacement fields $\bar{\mathbf{u}}_{i,p}^e$ ($p=1,2,\dots,n$) creates a displacement field $\bar{\mathbf{u}}_i^e$ which is continuous on the

whole n -sided polygonal element and linear compatible along the boundary segments of the triangular sub-domains

$$\bar{\mathbf{u}}_i^e(\mathbf{x}) = \bigcup_{p=1}^n \bar{\mathbf{u}}_{i,p}^e(\mathbf{x}) = \bar{\mathbf{u}}_{i,m}^e(\mathbf{x}) \quad , \quad \mathbf{x} \in \Omega_{i,m}^e \quad (3.25)$$

Extending this approximation to the whole problem domain, the global displacement field created from the union of elemental displacement fields (3.25) is continuous and linear compatible along the boundary segments of the triangular sub-domains of elements.

The union of shape function vectors $\mathbf{N}_{i,p}^e$ ($p=1,2,\dots,n$) also creates a shape function vector \mathbf{N}_i^e (on the n -sided polygonal element Ω_i^e) which is continuous and linear compatible along boundary segments of the triangular sub-domains of element

$$\mathbf{N}_i^e(\mathbf{x}) = \bigcup_{p=1}^n \mathbf{N}_{i,p}^e(\mathbf{x}) = \mathbf{N}_{i,m}^e(\mathbf{x}) \quad , \quad \mathbf{x} \in \Omega_{i,m}^e \quad (3.26)$$

Remark 3.1 Properties of the shape functions for n -sided polygonal elements

It is easy to verify the following properties of the shape function vector

$$\mathbf{N}_{i,p}^e = \underbrace{\left[\mathbf{N}_{i,p1}^e \quad \mathbf{N}_{i,p2}^e \quad \cdots \quad \mathbf{N}_{i,pj}^e \quad \cdots \quad \mathbf{N}_{i,pn}^e \right]}_{1 \times n} \quad \text{for any discrete point } \mathbf{x} \in \Omega_{i,p}^e \subset \Omega_i^e ,$$

($p=1,2,\dots,n$): (i) Kronecker delta at nodes \mathbf{x}_p and \mathbf{x}_{p+1} ; (ii) partition of unity:

$$\sum_{j=1}^n \mathbf{N}_{i,pj}^e(\mathbf{x}) = 1; \quad \text{(iii) linear consistency: } \sum_{j=1}^n \mathbf{N}_{i,pj}^e(\mathbf{x}) \mathbf{x}_j = \mathbf{x}; \quad \text{(iv) linear compatibility: linear}$$

shape functions on triangular sub-domain $\Omega_{i,p}^e \subset \Omega_i^e$ and ; and (v) $\mathbf{N}_{i,pj}^e(\mathbf{x}) \geq 0$.

Remark 3.2 Implicit shape function for n -sided polygonal element

Note that the displacement field constructed using Eq. (3.25) is implicit for n -sided polygonal elements: we cannot, in general, write out the exact forms of the displacement field explicitly. However, this is perfectly fine for the S-FEM models, because we do not need to compute the derivatives of the displacement field and hence no explicit form is

required. All we need in an S-FEM model is to evaluate the shape function values on the boundaries of the smoothing domains to compute the smoothed strain field. This evaluation is performed very easily by using the simple point linear interpolation and/or averaging in a proper manner from the available values of shape functions of field nodes. The detail evaluation of shape functions for S-FEM models will be presented in the following chapters.

Remark 3.3 Shape function for 3-node triangular element

Note that for the 3-node triangular elements, above approach of creating shape functions will give exactly the linear shape function used in triangular elements of the standard FEM.

Remark 3.4 Shape function for 4-node tetrahedral element in 3D problems

For the 4-node tetrahedral elements, the S-FEM models use the linear shape functions used in tetrahedral elements of the standard FEM.

3.3 Minimum number of smoothing domains

For an S-FEM model, the key to ensure the stability is the use of sufficient number of smoothing domains that are linearly independent. The independence of smoothing domain is measured by the linearly independence of the columns of the global smoothed stiffness matrix [68]. When the smoothing domains are created associated with the element mesh entities (elements/cells, nodes, edges or faces), they do not overlap and do not have any gap, these smoothing domains are hence linearly independent. To ensure the stability and hence the full rank of the (global) smoothed stiffness matrix, a minimum number of linearly independent smoothing domains N_s must be used. Based on the study in [68], such a minimum number of smoothing domains should relate properly to the number of

the un-prescribed nodal unknowns N_u , depending on the type of physical problems. The key consideration is to ensure the independent energy equations sampled by all these smoothing domains at least equal to the total number of the un-prescribed nodal unknowns N_u .

For 1D solid mechanics problem models with n_f node fixed, we have immediately $N_s^{\min} = N_u = N_n - n_f$. This is because one node carries only one unknown (displacement component in the x direction); and one energy equation can be sampled from one (independent) smoothing domain.

For 2D solid mechanics problem models with n_t (unconstrained) nodes used for displacement field construction, the total number of unknowns in the model should be $N_u = 2n_t$, because one node carries two unknowns (displacement components in x and y directions). On the other hand, the total number of energy equations that can be sampled from all the smoothing domains should be $3N_s$, because one smoothing domain gives three independent equations to measure the strain energy norm (each of three strain components produces strain energy independently). Therefore, we must have $N_s^{\min} = 2n_t / 3$.

Exactly the same analysis can be done for 3D solid mechanics problem models. We now summarize the discussions to Table 3.2.

In general, it is found that among the four element mesh entities: elements, nodes, edges (for 2D problems) or faces (for 3D problems), the number of element is usually least followed by nodes. The number of edges and faces is always larger than that of nodes for any discretization. Therefore, the S-FEM models using smoothing domains associated with edges (ES-FEM) or faces (FS-FEM) are always stable (spatially and temporally) because the number of smoothing domains N_s is always much larger than the

minimum number of smoothing domains N_s^{\min} . For the S-FEM model using smoothing domains associated with nodes (NS-FEM), it satisfies exactly the minimum number of smoothing domains N_s^{\min} . The NS-FEM is only spatially stable but temporally unstable. It hence works well only for static problems, but does not work well for dynamics problems without stabilization. For the S-FEM model using smoothing domains associated with elements (cells) (CS-FEM), the stability of the method is not ensured when the whole element is used as one smoothing domain because the minimum number of smoothing domains N_s^{\min} may or may not be satisfied, depends on the problem and discretization. The element stiffness matrix hence can contain spurious zeros energy modes, and the global stiffness matrix after imposing essential boundary conditions can be singular. Therefore, the stability of CS-FEM will only be ensured when more than one smoothing domain is used for each element. The details of the stability analyses of the methods will be presented in the following chapters.

3.4 Numerical procedure for the S-FEM models

The numerical procedure for the S-FEM models is outlined as follows.

- (1) Divide the problem domain into a set of elements and obtain information on node coordinates and element connectivity;
- (2) Create the smoothing domains by determining the area/volume of the smoothing domains Ω_k^s and the information of the nodes of the elements contributing to the smoothing domains;
- (3) Loop over smoothing domains Ω_k^s
 - a. Determine the outward unit normal of each boundary segment/area for the smoothing domain;

- b. Compute the smoothed strain-displacement matrix $\bar{\mathbf{B}}_I$;
 - c. Evaluate the smoothed stiffness matrix $\bar{\mathbf{K}}_{II}$ and load vector of the current smoothing domain;
 - d. Assemble the contribution of the current smoothing domain to form element matrices and vectors.
- (4) Implement essential boundary conditions;
 - (5) Solve the linear system of equations to obtain the nodal displacements;
 - (6) Evaluate strains and stresses at locations of interest.

3.5 General properties of the S-FEM models

Remark 3.5 Stress equilibrium state within smoothing domains

The assumed smoothing strains defined in Eq. (3.7) ensure a stress equilibrium state within the smoothing domain where there is not the body force.

Based on the assumption made in Eq. (3.4), the assumed smoothing strains become constants at any point in the smoothing domain. Therefore, the stresses obtained will also be constant in a smoothing domain. These constant stresses satisfy the equilibrium Eq. (2.1) when the external body load vector $\mathbf{b} = \mathbf{0}$.

Remark 3.5 is a simple but a quite powerful statement: applying the strain smoothing technique to a smoothing domain in the problem domain results in a stress equilibrium status in the smoothing domain. We, therefore, call the smoothing operation a local *stress equilibrator*. The S-FEM models will not satisfy the equilibrium equation for every point in the problem domain, but will in all the smoothed domains.

Remark 3.6 Compatibility of smoothed strain field

(i) When the smoothing domain is located within the element such as in the CS-FEM, the smoothed strains defined in Eq. (3.7), will not be compatible, unless the assumed displacement field is linear.

(ii) When the smoothing domain covers parts of adjacent elements such as in the NS-FEM, ES-FEM or FS-FEM, the assumed smoothed strains defined in Eq. (3.7), will not be compatible for any assumed continuous displacement field.

We first examine item (i). When the smoothing domain locates within the element such as in the CS-FEM, if the order of the assumed displacement field is higher than first order, the compatible strain $\boldsymbol{\varepsilon}^h(\mathbf{x}) = \nabla_s \mathbf{u}^h(\mathbf{x})$ will not be constant. The assumed smoothing strains defined in Eq. (3.7) are however constants. Hence the compatibility condition is violated.

We then examine item (ii). When the smoothing domain covers parts of adjacent elements such as in the NS-FEM, ES-FEM or FS-FEM, the smoothed strain given in Eq. (3.7) is the area-weighted average of the compatible strains over the portions of the elements forming the smoothing domain. Because the strains in these elements will be in general different, the average strain will be different from these element strains for any assumed continuous displacement field. Hence the compatibility condition is violated.

Remark 3.6 (i) implies that the stress equilibrators in the CS-FEM will destroy the compatibility in the smoothing domains with assumed displacement fields of bilinear or higher order. It also implies that when the linear displacement field is used (3-node triangular element), the CS-FEM will be identical to the standard FEM, because the stress equilibrators are useless to a constant stress field derived from the linear displacement field. The CS-FEM can therefore only be applied with significance to elements of higher order.

Remark 3.6 (ii) implies that the stress equilibrator in the NS-FEM, ES-FEM and FS-FEM will destroy the compatibility in the smoothing domains for any assumed continuous displacement field. The NS-FEM, ES-FEM and FS-FEM therefore can be applied with significance for any elements.

Remark 3.7 The S-FEM models are energy consistent [73], when linear compatible shape functions along the boundaries of smoothing domains are used, and there is not the body force in smoothing domains.

Proof

In general, we observe a unique “complementary” situation for the S-FEM models: the equilibrium is ensured in each smoothing domain without having the body force, as shown in Remark 3.5, but the compatibility is destroyed within the smoothing domain, as shown in Remark 3.6 . On the boundaries of the smoothing domains, however, the equilibrium (stress continuity) is not guaranteed, but the displacement continuity is ensured due to the use of the same linear compatible shape functions on the common boundaries of the smoothing domains. It is this unique complementary satisfaction of *equilibrium* or *compatibility* conditions within the smoothing domains and on the boundaries of the smoothing domains that ensures no energy loss in any of the violation of equilibrium or compatibility conditions. We therefore state that the S-FEM models are *energy consistent* [73] when the linear compatible shape functions along the boundaries of smoothing domains are used, and there is not the body force in smoothing domains. \square

Remark 3.8: The S-FEM models are stable, if at least the minimum number of independent smoothed domains defined in Table 3.2 is used in creating the model.

Consequently, all the columns of the smoothed strain matrix will be linearly independent [69], and the stiffness matrix created will be SPD. The solution of such an S-

FEM model is hence stable and converges to the exact solution of a physically well-posed linear elasticity problem with stable material.

Theorem 3.1 The S-FEM models are variationally consistent

Proof

In the S-FEM models, the smoothed strain $\bar{\boldsymbol{\varepsilon}}$ is used to replace the compatible strain $\boldsymbol{\varepsilon}^h = \nabla_s \mathbf{u}^h$, the variational consistency thus needs to be examined. To this end, we start with the modified Hellinger-Reissner variational principle with the smoothed strain $\bar{\boldsymbol{\varepsilon}}$ and compatible displacements \mathbf{u}^h as independent field variables [122]:

$$U(\mathbf{u}^h, \bar{\boldsymbol{\varepsilon}}) = -\int_{\Omega} \frac{1}{2} \bar{\boldsymbol{\varepsilon}}^T \mathbf{D} \bar{\boldsymbol{\varepsilon}} d\Omega + \int_{\Omega} (\mathbf{D} \bar{\boldsymbol{\varepsilon}})^T \nabla_s \mathbf{u}^h d\Omega - \int_{\Omega} (\mathbf{u}^h)^T \mathbf{b} d\Omega - \int_{\Gamma_f} (\mathbf{u}^h)^T \mathbf{t} d\Gamma \quad (3.27)$$

Performing the variation using the chain rule, one obtains

$$\begin{aligned} \delta U(\mathbf{u}^h, \bar{\boldsymbol{\varepsilon}}) = & -\int_{\Omega} (\delta \bar{\boldsymbol{\varepsilon}})^T \mathbf{D} \bar{\boldsymbol{\varepsilon}} d\Omega + \int_{\Omega} \delta \bar{\boldsymbol{\varepsilon}}^T \mathbf{D} (\nabla_s \mathbf{u}^h) d\Omega + \int_{\Omega} \bar{\boldsymbol{\varepsilon}}^T \mathbf{D} (\nabla_s \delta \mathbf{u}^h) d\Omega - \\ & - \int_{\Omega} (\delta \mathbf{u}^h)^T \mathbf{b} d\Omega - \int_{\Gamma_f} (\delta \mathbf{u}^h)^T \mathbf{t} d\Gamma = 0 \end{aligned} \quad (3.28)$$

Substituting the approximations (2.43) for \mathbf{u}^h and (3.9) for $\bar{\boldsymbol{\varepsilon}}$ into Eq. (3.28) and using the arbitrary property of variation, we obtain

$$\bar{\mathbf{K}} \bar{\mathbf{d}} = \mathbf{f} \quad (3.29)$$

where \mathbf{f} is the system load vector similar to that of the FEM with entries given by Eq. (2.49) and $\bar{\mathbf{K}}$ is the *smoothed* stiffness matrix whose entries are given by

$$\begin{aligned} \bar{\mathbf{K}}_{IJ} = & -\int_{\Omega} \bar{\mathbf{B}}_I^T \mathbf{D} \bar{\mathbf{B}}_J d\Omega + 2 \int_{\Omega} \bar{\mathbf{B}}_I^T \mathbf{D} \mathbf{B}_J(\mathbf{x}) d\Omega \\ = & -\sum_{k=1}^{N_s} \int_{\Omega_k^s} \bar{\mathbf{B}}_I^T \mathbf{D} \bar{\mathbf{B}}_J d\Omega + 2 \sum_{k=1}^{N_s} \int_{\Omega_k^s} \bar{\mathbf{B}}_I^T \mathbf{D} \mathbf{B}_J(\mathbf{x}) d\Omega \end{aligned} \quad (3.30)$$

Using smoothed strain-displacement matrices $\bar{\mathbf{B}}_I$ in Eq. (3.10), the following orthogonal condition [137] is satisfied for the integration (3.30) on each of smoothing domains $\Omega_k^s \in \Omega$ as follows

$$\begin{aligned}
\int_{\Omega_k^s} \bar{\mathbf{B}}_I^T \mathbf{D} \mathbf{B}_J(\mathbf{x}) d\Omega &= \bar{\mathbf{B}}_I^T \mathbf{D} \int_{\Omega_k^s} \mathbf{B}_J(\mathbf{x}) d\Omega = \bar{\mathbf{B}}_I^T \mathbf{D} A_k^s \int_{\Omega_k^s} \frac{\mathbf{B}_J(\mathbf{x})}{A_k^s} d\Omega = \bar{\mathbf{B}}_I^T \mathbf{D} \bar{\mathbf{B}}_J A_k^s \\
&= \int_{\Omega_k^s} \bar{\mathbf{B}}_I^T \mathbf{D} \bar{\mathbf{B}}_J d\Omega
\end{aligned} \tag{3.31}$$

By combining the orthogonal condition (3.31) and Eq. (3.30), one has

$$\bar{\mathbf{K}}_{IJ} = \int_{\Omega} \bar{\mathbf{B}}_I^T \mathbf{D} \bar{\mathbf{B}}_J d\Omega = \sum_{k=1}^{N_s} \int_{\Omega_k^s} \bar{\mathbf{B}}_I^T \mathbf{D} \bar{\mathbf{B}}_J d\Omega \tag{3.32}$$

The S-FEM models use directly Eq. (3.32) (or Eq. (3.16)) to calculate the stiffness matrix, therefore, the S-FEM models are “variationally consistent”. \square

Note that although the two-field Hellinger-Reissner principle is used, the S-FEM models have only the displacements as unknowns. Therefore, it is very much different from the so-called mixed FEM formulation, where stresses (or strains) are usually also unknowns.

The orthogonal condition (3.31) can be expressed in the similar form for any compatible strain $\boldsymbol{\varepsilon}^h = \nabla_s \mathbf{u}^h$ and the smoothed strain $\bar{\boldsymbol{\varepsilon}}$ by Eq. (3.7) as

$$\int_{\Omega_k^s} \bar{\boldsymbol{\varepsilon}}^T \mathbf{D} \boldsymbol{\varepsilon}^h d\Omega = \int_{\Omega_k^s} \bar{\boldsymbol{\varepsilon}}^T \mathbf{D} \bar{\boldsymbol{\varepsilon}} d\Omega \tag{3.33}$$

Theorem 3.2 Softening effect [83]

For any given admissible displacement field $\mathbf{v}^h \in \mathbb{V}^h \subset \mathbb{V}$, the strain energy $\bar{E}(\mathbf{v}^h)$ for an S-FEM model obtained from the smoothed strains is no larger than the strain energy $E(\mathbf{v}^h)$ for a FEM model obtained from the compatible strains:

$$\bar{E}(\mathbf{v}^h) \leq E(\mathbf{v}^h) \tag{3.34}$$

in which

$$\bar{E}(\mathbf{v}^h) = \frac{1}{2} \int_{\Omega} \bar{\boldsymbol{\varepsilon}}^T(\mathbf{v}^h) \mathbf{D} \bar{\boldsymbol{\varepsilon}}(\mathbf{v}^h) d\Omega = \frac{1}{2} \sum_{k=1}^{N_s} \int_{\Omega_k^s} \bar{\boldsymbol{\varepsilon}}_k^T \mathbf{D} \bar{\boldsymbol{\varepsilon}}_k d\Omega = \frac{1}{2} \sum_{k=1}^{N_s} \bar{\boldsymbol{\varepsilon}}_k^T \mathbf{D} \bar{\boldsymbol{\varepsilon}}_k A_k^s \tag{3.35}$$

$$E(\mathbf{v}^h) = \frac{1}{2} \int_{\Omega} (\boldsymbol{\varepsilon}^h(\mathbf{v}^h))^T \mathbf{D} \boldsymbol{\varepsilon}^h(\mathbf{v}^h) d\Omega = \frac{1}{2} \sum_{k=1}^{N_s} \int_{\Omega_k^s} (\boldsymbol{\varepsilon}^h)^T \mathbf{D} \boldsymbol{\varepsilon}^h d\Omega \quad (3.36)$$

where $\bar{\boldsymbol{\varepsilon}} = \bar{\boldsymbol{\varepsilon}}(\mathbf{v}^h)$ by Eq. (3.7) is the smoothed strain in an S-FEM model and $\boldsymbol{\varepsilon}^h = \nabla_s \mathbf{v}^h$ is the compatible strains obtained in the FEM.

Proof

Examine the following equation on the smoothing domain Ω_k^s ,

$$\int_{\Omega_k^s} (\bar{\boldsymbol{\varepsilon}}_k - \boldsymbol{\varepsilon}^h)^T \mathbf{D} (\bar{\boldsymbol{\varepsilon}}_k - \boldsymbol{\varepsilon}^h) d\Omega = \int_{\Omega_k^s} \bar{\boldsymbol{\varepsilon}}_k^T \mathbf{D} \bar{\boldsymbol{\varepsilon}}_k d\Omega - 2 \int_{\Omega_k^s} \bar{\boldsymbol{\varepsilon}}_k^T \mathbf{D} \boldsymbol{\varepsilon}^h d\Omega + \int_{\Omega_k^s} (\boldsymbol{\varepsilon}^h)^T \mathbf{D} \boldsymbol{\varepsilon}^h d\Omega \quad (3.37)$$

Using the orthogonal condition (3.33) and \mathbf{D} which is SPD, we have

$$\underbrace{\int_{\Omega_k^s} (\bar{\boldsymbol{\varepsilon}}_k - \boldsymbol{\varepsilon}^h)^T \mathbf{D} (\bar{\boldsymbol{\varepsilon}}_k - \boldsymbol{\varepsilon}^h) d\Omega}_{\geq 0} = \int_{\Omega_k^s} (\boldsymbol{\varepsilon}^h)^T \mathbf{D} \boldsymbol{\varepsilon}^h d\Omega - \int_{\Omega_k^s} \bar{\boldsymbol{\varepsilon}}_k^T \mathbf{D} \bar{\boldsymbol{\varepsilon}}_k d\Omega \geq 0 \quad (3.38)$$

which combines with Eqs. (3.35) and (3.36) to give Eq. (3.34). \square

Eq. (3.34) can be expressed in discrete form of arbitrary (but admissible) nodal displacement \mathbf{v}^h as

$$\underbrace{\frac{1}{2} (\mathbf{v}^h)^T \bar{\mathbf{K}} \mathbf{v}^h}_{\bar{E}(\mathbf{v}^h)} \leq \underbrace{\frac{1}{2} (\mathbf{v}^h)^T \mathbf{K} \mathbf{v}^h}_{E(\mathbf{v}^h)} \quad (3.39)$$

Theorem 3.3 Upper bound to FEM solution in the strain energy [83]

For an elastic solid mechanics problem, when the same mesh is used, the strain energy obtained from the solution $\bar{\mathbf{u}}$ of the S-FEM models is no less than that from the solution \mathbf{u}^h of the FEM:

$$\bar{E}(\bar{\mathbf{u}}) \geq E(\mathbf{u}^h) \quad (3.40)$$

where

$$\bar{E}(\bar{\mathbf{u}}) = \frac{1}{2} \bar{\mathbf{u}}^T \bar{\mathbf{K}} \bar{\mathbf{u}} \quad (3.41)$$

$$E(\mathbf{u}^h) = \frac{1}{2}(\mathbf{u}^h)^T \mathbf{K} \mathbf{u}^h \quad (3.42)$$

Proof

From the Theorem 3.2 (or Eq. (3.39)), we obtain for any admissible \mathbf{v}^h :

$$\underbrace{\frac{1}{2}(\mathbf{v}^h)^T \mathbf{K} \mathbf{v}^h - \frac{1}{2}(\mathbf{v}^h)^T \bar{\mathbf{K}} \mathbf{v}^h}_{\geq 0} = \frac{1}{2}(\mathbf{v}^h)^T (\mathbf{K} - \bar{\mathbf{K}}) \mathbf{v}^h \geq 0 \quad (3.43)$$

Eq. (3.43) implies that matrix $(\mathbf{K} - \bar{\mathbf{K}})$ is SPD. In mechanics, it implies that \mathbf{K} is “stiffer” than $\bar{\mathbf{K}}$. In addition, the solution of the FEM can be expressed as

$$\mathbf{u}^h = \mathbf{K}^{-1} \mathbf{f} \quad (3.44)$$

and the solution of the S-FEM models can be expressed as

$$\bar{\mathbf{u}} = \bar{\mathbf{K}}^{-1} \mathbf{f} \quad (3.45)$$

The difference between the strain energy of the FEM and that of the S-FEM models hence becomes

$$\begin{aligned} \bar{E}(\bar{\mathbf{u}}) - E(\mathbf{u}^h) &= \frac{1}{2}(\bar{\mathbf{K}}^{-1} \mathbf{f})^T \bar{\mathbf{K}} (\bar{\mathbf{K}}^{-1} \mathbf{f}) - \frac{1}{2}(\mathbf{K}^{-1} \mathbf{f})^T \mathbf{K} (\mathbf{K}^{-1} \mathbf{f}) \\ &= \frac{1}{2} \mathbf{f}^T \bar{\mathbf{K}}^{-1} \mathbf{f} - \frac{1}{2} \mathbf{f}^T \mathbf{K}^{-1} \mathbf{f} \\ &= \frac{1}{2} \mathbf{f}^T \underbrace{(\bar{\mathbf{K}}^{-1} - \mathbf{K}^{-1})}_{\text{SPD}} \mathbf{f} \geq 0 \end{aligned} \quad (3.46)$$

which gives Eq. (3.40). \square

Note that, in the working of Eq. (3.46), we used the fact that $(\bar{\mathbf{K}}^{-1} - \mathbf{K}^{-1})$ is SPD. This can be proven based on the facts that $\bar{\mathbf{K}}$, \mathbf{K} , and $(\mathbf{K} - \bar{\mathbf{K}})$ are all SPD (see Eq. (3.43)).

Theorem 3.3 shows one very important property of the S-FEM models. In mechanics, this means that the S-FEM models are “softer” than the FEM model. In other words, the common effect of the strain smoothing technique is the reduction of the over-stiffness of the standard compatible FEM model. This effect is called “softening effect” which contrasts with “stiffening effect” caused by the assumed displacement field using the

FEM shape functions in a conforming/fully-compatible model. Due to the softening effect, the strain energy of the S-FEM models becomes larger than that of the FEM.

Now, the following question is naturally arisen: How can we adjust the softening effect in the S-FEM models to ensure that the obtained solution gives an upper bound in the strain energy compared with the exact strain energy or gives a close-to-exact solution? All these questions will be addressed in the following chapters.

Theorem 3.4 Monotonic convergence property [68]

Upon a division of domain Ω into a set of N_s^{D1} smoothing domains $\Omega = \sum_{k=1}^{N_s^{D1}} \Omega_k^s$, if a new division N_s^{D2} is created by sub-dividing the k^{th} smoothing domain into n_s sub-smoothing-domains such that $\Omega_k^s = \sum_{p=1}^{n_s} \Omega_{k,p}^s$, $\Omega_{k,m}^s \cap \Omega_{k,n}^s = \emptyset$, $m \neq n$, then the following inequality stands

$$\bar{E}_{D1}(\bar{\mathbf{u}}) \geq \bar{E}_{D2}(\bar{\mathbf{u}}) \quad (3.47)$$

where $\bar{E}_D(\bar{\mathbf{u}})$ is the strain energy solution obtained from a S-FEM model using N_s^D smoothing domains.

This implies that the ‘‘softening’’ effect provided by the smoothing operation will be monotonically reduced with the increase of the number of smoothing domains constructed in a nested manner. A simple proof can be given using the triangle inequality of norms: sum of energy norm of functions is no-less than the norm of the summed functions [68]. In addition, a specific proof for CS-FEM will be conducted in [Chapter 4: Remark 4.5](#).

Theorem 3.5 Convergence property

When $N_s \rightarrow \infty$, the solution $\bar{\mathbf{u}}$ of the S-FEM models will approach the solution $\mathbf{u}^h \in \mathbb{V}^h \subset \mathbb{V}$ of the standard compatible FEM model.

Proof

Assume that the problem has the solution $\mathbf{u}^h \in \mathbb{V}^h \subset \mathbb{V}$ of the standard compatible displacement FEM model. Now we consider finding the solution $\bar{\mathbf{u}}$ of the S-FEM models for the same problem. In a given division N_s of domain Ω into a set of smoothing domains such that $\Omega = \sum_{k=1}^{N_s} \Omega_k^s$, when $N_s \rightarrow \infty$ and each smoothing domain Ω_k^s approaches zero, the smoothing function $\Phi_k(\mathbf{x})$ in Eq. (3.3) approaches to the Delta function. At such a limit $\bar{\boldsymbol{\varepsilon}} \rightarrow \boldsymbol{\varepsilon}^h$, $\bar{\mathbf{B}} \rightarrow \mathbf{B}$, $\bar{\mathbf{K}} \rightarrow \mathbf{K}$ and the solution $\bar{\mathbf{u}}$ of the S-FEM models hence will approach the solution \mathbf{u}^h of the standard compatible FEM model. \square

Theorem 3.5 also implies that in the case the smoothing domain Ω_k^s is associated with the number of nodes N_n (NS-FEM), or edges N_{eg} (ES-FEM) or faces N_f (FS-FEM) of the FEM, the solution $\bar{\mathbf{u}}$ of the S-FEM models will approach to the exact solution, because the solution \mathbf{u}^h of the standard compatible FEM model also approaches the exact solution when N_n , N_{eg} or N_f approaches infinity.

Property 3.1 In the S-FEM models, the unknowns of only the displacement are as same as in the standard FEM.

Property 3.2 By constructing linear compatible shape functions based on physical coordinates, complicated elements such as n -sided convex polygonal elements can be used in the S-FEM models.

Property 3.3 In the S-FEM models, the domain discretization is more flexible than that in the standard FEM when n -sided convex polygonal elements can be used.

Name	Method for creation (number of smoothing domains)	S-FEM Models	Problem domain
Cell-based smoothing domain (CSD)	Based on element ($N_s = N_e$) or cells created by dividing further the elements ($N_s = \sum_{i=1}^{N_e} n_i^s$)	CS-FEM (SFEM) [70, 73, 77]	1D, 2D, 3D
Node-based smoothing domain (NSD)	Based on each of the nodes of the mesh by connecting portions of the surrounding elements sharing the node ($N_s = N_n$)	NS-FEM [78]	1D, 2D, 3D
Edge-based smoothing domain (ESD)	Based on each edges of the mesh by connecting portions of the surrounding elements sharing the edge ($N_s = N_{eg}$)	ES-FEM [76]	2D, 3D
Face-based smoothing domain (FSD)	Based on each face of the element mesh by connecting portions of the surrounding elements sharing the face ($N_s = N_f$)	FS-FEM [103]	3D

Dimension of the problem	Minimum number of smoothing domains
1D	$N_s^{\min} = n_t$
2D	$N_s^{\min} = 2n_t/3$
3D	$N_s^{\min} = 3n_t/6 = n_t/2$

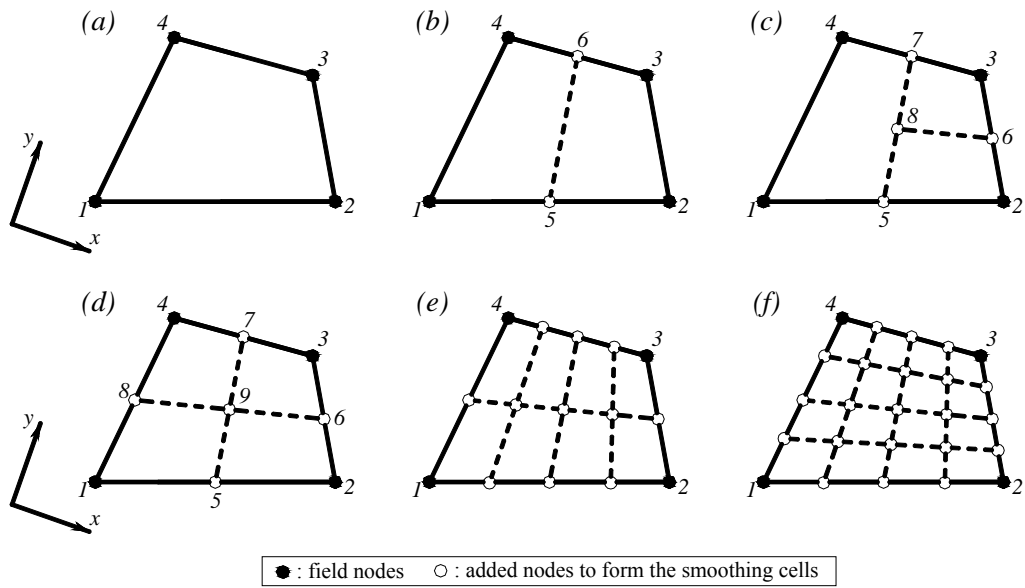


Figure 3.1. Division of quadrilateral element into the smoothing domains (SDs) in the CS-FEM by connecting the mid-segment-points of opposite segments of smoothing domains.
 (a) 1 SD; (b) 2 SDs; (c) 3 SDs; (d) 4 SDs; (e) 8 SDs; (f) 16 SDs.

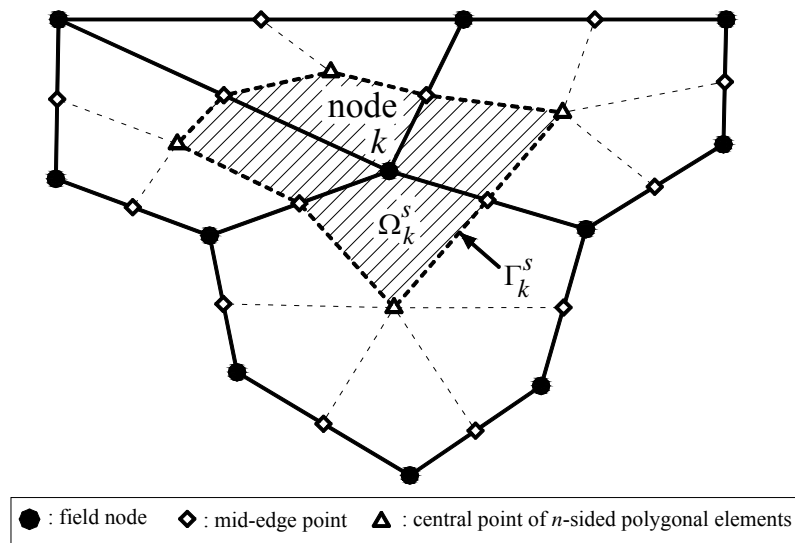


Figure 3.2. n -sided polygonal elements and the smoothing domain (shaded area) associated with node k in the NS-FEM.

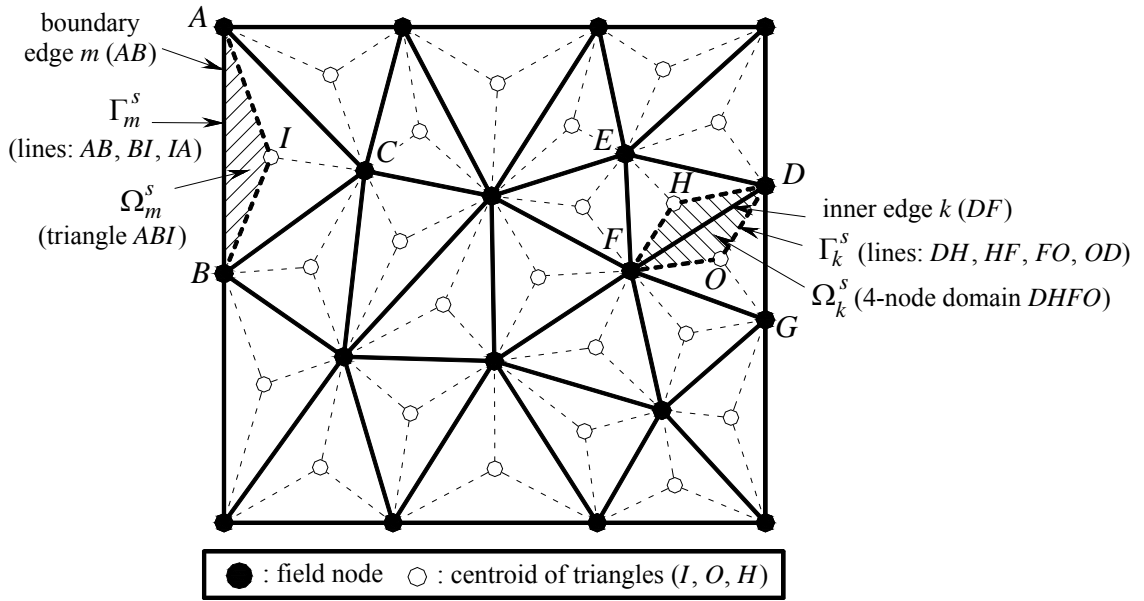


Figure 3.3. Triangular elements and the smoothing domains (shaded areas) associated with edges in the ES-FEM.

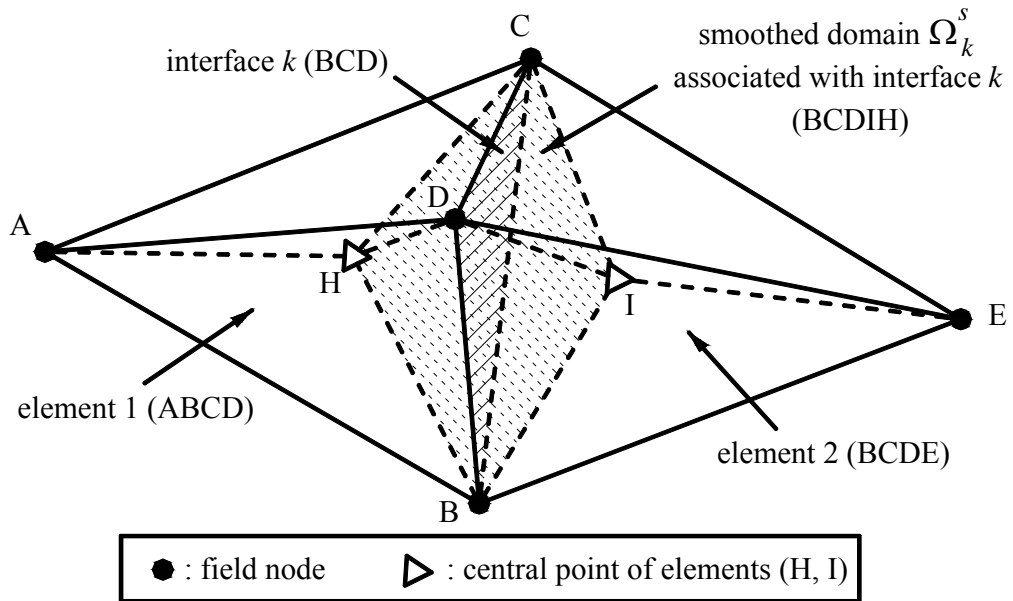


Figure 3.4. Two adjacent tetrahedral elements and the smoothing domain Ω_k^s (shaded domain) formed based on their interface k in the FS-FEM.

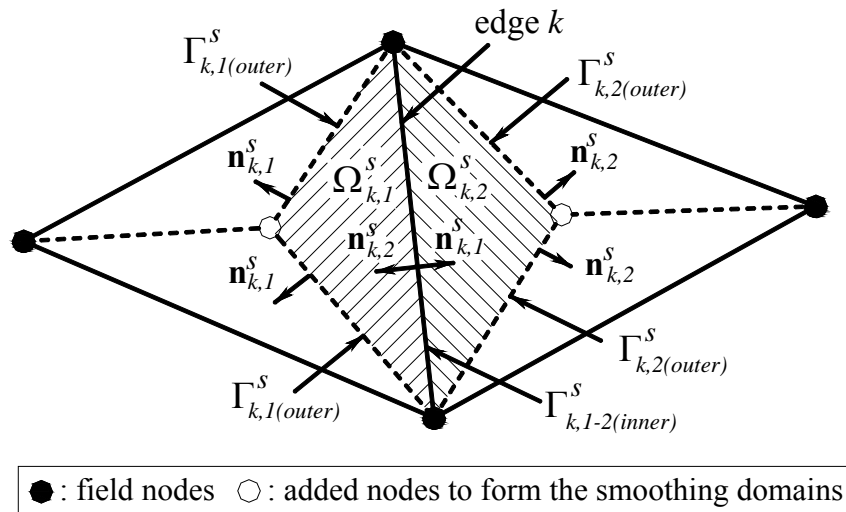


Figure 3.5. Division of the smoothing domain Ω_k^s associated with the edge k into two adjacent smoothing cells $\Omega_{k,1}^s$ and $\Omega_{k,2}^s$ that have the common inner boundary $\Gamma_{k,1-2}^s(\text{inner})$.

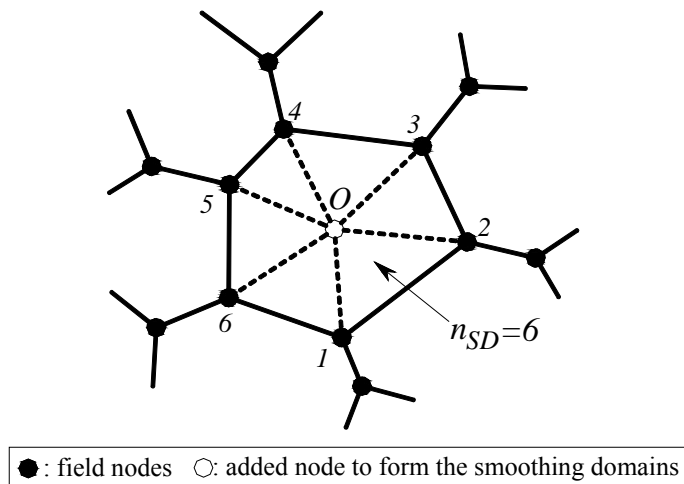


Figure 3.6. Division of a 6-sided convex polygonal element into six triangular sub-domains by connecting n field nodes with the central point O .

Chapter 4

Cell-based Smoothed FEM (CS-FEM)

This chapter introduces the cell-based S-FEM (CS-FEM) using the strain smoothing technique [24] for finite element settings. In the CS-FEM, the strain in an element is modified by smoothing the compatible strains over the smoothing domains created by subdividing the quadrilateral elements. The CS-FEM can improve the accuracy and convergence rate of the existing standard 4-node quadrilateral elements used in the FEM. In addition, the method works well for general n -sided polygonal elements (n CS-FEM). In theory, the n -sided polygonal elements can be concave [37]. In practice, however, we usually use convex polygonal elements, and hence our discussion in this chapter will assume the elements to be convex. Some properties of the CS-FEM will be presented and proved theoretically, and the stability analysis of CS-FEM and n CS-FEM is also conducted. Moreover, a selective CS-FEM is also formulated to overcome the volume-locking problems using nearly incompressible materials. Numerical examples will be presented to confirm the properties of the CS-FEM.

4.1 Creation of the cell-based smoothing domains

In the CS-FEM, the domain Ω is discretized into N_e quadrilateral elements as in the standard FEM, such that $\Omega = \bigcup_{i=1}^{N_e} \Omega_i^e$ and $\Omega_i^e \cap \Omega_j^e = \emptyset$, $i \neq j$. Each element Ω_i^e will be

further subdivided into $n_s \in [1, \infty)$ quadrilateral smoothing domains $\Omega_{i,m}^e$ in a non-overlapping and no gap manner such that $\Omega_i^e = \bigcup_{m=1}^{n_s} \Omega_{i,m}^e$, as shown in Figure 4.1.

Therefore, the entire problem domain Ω is divided into a total of $N_s = N_e \times n_s$ smoothing domains Ω_k^s such that $\Omega = \bigcup_{k=1}^{N_s} \Omega_k^s$. Note that the subdivision of each big smoothing domain into smaller smoothing domains is performed by connecting the mid-segment-points of opposite segments as shown in Figure 4.1. The strain smoothing operation (3.4) is performed over the quadrilateral smoothing domains.

4.2 Formulation of the CS-FEM for quadrilateral elements

Using the general formulation of the S-FEM models presented in Chapter 3 (Section 3.1), the discretized linear system of equations for the CS-FEM has the form of

$$\bar{\mathbf{K}}^{\text{CS-FEM}} \bar{\mathbf{d}} = \mathbf{f} \quad (4.1)$$

where $\bar{\mathbf{K}}^{\text{CS-FEM}}$ is the global *smoothed* stiffness matrix whose entries are given by

$$\bar{\mathbf{K}}_{IJ}^{\text{CS-FEM}} = \sum_{i=1}^{N_e} \sum_{m=1}^{n_s} \int_{\Omega_{i,m}^e} \bar{\mathbf{B}}_I^T \mathbf{D} \bar{\mathbf{B}}_J d\Omega = \sum_{i=1}^{N_e} \sum_{m=1}^{n_s} \bar{\mathbf{B}}_I^T \mathbf{D} \bar{\mathbf{B}}_J A_{i,m}^e = \sum_{k=1}^{N_s} \bar{\mathbf{B}}_I^T \mathbf{D} \bar{\mathbf{B}}_J A_k^s \quad (4.2)$$

where $A_{i,m}^e = \int_{\Omega_{i,m}^e} d\Omega$ is the area of quadrilateral smoothing domain $\Omega_{i,m}^e$, and the

smoothed strain-displacement matrix $\bar{\mathbf{B}}_I$, which is constant, is computed using Eq. (3.10). All we need now is the assumed displacement function values on the boundaries of these smoothing domains, which can be evaluated using shape functions created for the CS-FEM element using procedures given in Section 4.4.

4.3 Formulation of the CS-FEM for n -sided polygonal elements

The CS-FEM can be further extended to a more general case, using n -sided polygonal elements (n CS-FEM). The domain discretization Ω is based on N_e polygonal elements

with an arbitrary number of sides, such that $\Omega = \bigcup_{i=1}^{N_e} \Omega_i^e$ and $\Omega_i^e \cap \Omega_j^e = \emptyset$, $i \neq j$. Each n_i^e -side polygonal element Ω_i^e will be further subdivided into $n_s = n_i^e$ triangular smoothing domains in a non-overlapping and no gap manner such that $\Omega_i^e = \bigcup_{m=1}^{n_i^e} \Omega_{i,m}^s$. This subdivision is performed by connecting n_i^e field nodes to the central point of the polygonal element as shown in [Figure 3.6](#). Therefore, the entire problem domain Ω is consequently divided into $N_s = \sum_{i=1}^{N_e} n_i^e$ smoothing domains Ω_k^s such that $\Omega = \bigcup_{k=1}^{N_s} \Omega_k^s$. The strain smoothing operation (3.4) is performed over the triangular smoothing domains within each polygonal element.

Using the general formulation of the S-FEM models presented in Chapter 3 ([Section 3.1](#)), the linear system of equations of the n CS-FEM has the form of

$$\bar{\mathbf{K}}^{n\text{CS-FEM}} \bar{\mathbf{d}} = \mathbf{f} \quad (4.3)$$

where $\bar{\mathbf{K}}^{n\text{CS-FEM}}$ is the global smoothed stiffness matrix whose entries are given by

$$\bar{\mathbf{K}}_{IJ}^{n\text{CS-FEM}} = \sum_{i=1}^{N_e} \sum_{m=1}^{n_i^e} \int_{\Omega_{i,m}^s} \bar{\mathbf{B}}_I^T \mathbf{D} \bar{\mathbf{B}}_J d\Omega = \sum_{i=1}^{N_e} \sum_{m=1}^{n_i^e} \bar{\mathbf{B}}_I^T \mathbf{D} \bar{\mathbf{B}}_J A_{i,m}^s = \sum_{k=1}^{N_s} \bar{\mathbf{B}}_I^T \mathbf{D} \bar{\mathbf{B}}_J A_k^s \quad (4.4)$$

where $A_{i,m}^s = \int_{\Omega_{i,m}^s} d\Omega$ is the area of triangular smoothing domain $\Omega_{i,m}^s$, and the smoothed strain-displacement matrix $\bar{\mathbf{B}}_I$ is computed by [Eq. \(3.10\)](#). Note again that the smoothed strain is constant within the smoothing domain. In evaluating $\bar{\mathbf{B}}_I$, we need to use the shape function created for the n -sided polygonal element in [Chapter 3 \(Section 3.2\)](#).

4.4 Evaluation of shape functions in the CS-FEM and n CS-FEM

As presented in [Chapter 3](#), when a linear compatible displacement field along the boundary of the smoothing domains is used, the smoothed strain-displacement matrix $\bar{\mathbf{B}}_I$

can be computed using only the shape function values at mid-segment-points (Gauss points) on each of the segments $\Gamma_{k,p}^s \in \Gamma_k^s$ of the smoothing domain Ω_k^s . No derivatives of the shape functions are needed. Therefore, the most essential issue is to ensure the compatibility of the shape functions on all the interfaces of these smoothing domains. In our past practice, the shape function values at each Gauss point are evaluated by simple linear point interpolation (or averaging) using two endpoints of the segment containing the Gauss point. For example, for the quadrilateral element subdivided into four quadrilateral smoothing domains as shown in Figure 4.2a, the shape function values at Gauss point $g1$ are evaluated by averaging those of nodes #1 and #5, and those at Gauss point $g2$ is the average of those of points #5 and #9. For the 6-sided polygonal element subdivided into six triangular smoothing domains as shown in Figure 4.2b, the shape function values at Gauss point $g1'$ are the average of those of nodes #1' and O , and that at Gauss point $g2'$ is the average of those of points #1' and #2'. Therefore, in order to facilitate the evaluation of shape function values at Gauss points on the smoothing domain boundaries in the CS-FEM and n CS-FEM, we need first to evaluate the shape function values at the endpoints of segments such as points #1, #2, ..., #9 in Figure 4.2a and points #1', #2', ..., #6' and point O in Figure 4.2b.

For the quadrilateral elements, the subdivision of a big smoothing domain into smaller smoothing domains is performed by connecting the mid-segment-points of opposite segments as shown in Figure 4.1. Such a subdivision will ensure shape function values on the boundaries of physical smoothing domains to be linearly compatible on all the segments of the smoothing domains, which is essential to CS-FEM models. Note that in the standard FEM using quadrilateral elements, the compatibility on the element boundary is achieved by “mapping”, and the so-called isoparametric elements are the most popular. In the CS-FEM, this compatibility is achieved in much simpler manner:

linear interpolation or averaging, and no mapping is needed. The relation of the locations for the CS-FEM and the bi-linear isoparametric elements is illustrated in Figure 4.3. Shape function values on the lines 5-7, 6-8, 10-12 and 11-13 of smoothing domains of a CS-FEM element are identically linear corresponding to the mapped segments 5'-7', 6'-8', 10'-12' and 11'-13' on the isoparametric FEM elements.

In the CS-FEM, a four-node quadrilateral element can be, *in theory*, subdivided into some quadrilateral smoothing domains as shown in Figure 4.1. However, the numerical examples given in Section 4.10 will show that such a further division is often unnecessary and not preferable. A simple division of the element into four smoothing domains as shown in Figure 4.1d is one of the best choices for solid mechanics problems. Therefore, unless stated otherwise, the division of the element into four smoothing domains will be used mainly in this section for convenience of discussion. Figure 4.2a and Table 4.1 presents explicitly the shape function values at different points of a quadrilateral element divided into four quadrilateral smoothing domains. The number of support field nodes for the quadrilateral element is 4 (from #1 to #4). For the whole quadrilateral element, we have 12 line-segments (1-5, 5-2, 2-6, 6-3, 3-7, 7-4, 4-8, 8-1, 5-9, 6-9, 7-9, 8-9). Each line-segment needs only one Gauss point (due to linear interpolation), and therefore, there are a total of 12 Gauss points (from g_1 , to g_{12}) used for all these smoothing domains in Ω_i^e , and the shape function values at all these 12 Gauss points are tabulated in Table 4.1 by simple inspection.

For the n CS-FEM using n -sided polygonal elements, the shape function constructed in Chapter 3 (Section 3.2) is obviously linear compatible along the boundaries of the triangular smoothing domains. Hence, the evaluation of the shape function values at field nodes and the central points such as points #1', #2', ..., #6' and point O in Figure 4.2b is very straightforward. Figure 4.2b and Table 4.2 presents explicitly the shape function

values at different points of a 6-sided polygonal element divided into six triangular smoothing domains. The number of support field nodes for this 6-sided element is 6 (from #1' to #6'). We have a total of 12 segments ($1'-2'$, $2'-3'$, $3'-4'$, $4'-5'$, $5'-6'$, $6'-1'$, $1'-O$, $2'-O$, $3'-O$, $4'-O$, $5'-O$, $6'-O$). Each segment needs only one Gauss point (due again to the linear interpolation). Therefore, there are a total of 12 Gauss points (from g_1 to g_{12}) to be used for all the smoothing domains, and the shape function values at all these 12 Gauss points can be tabulated in Table 4.2 by, again, simple inspection.

It should be mentioned that the purpose of introducing of interior points such as point #9 in Figure 4.2a or point O in Figure 4.2b and points on the edges such as #5, #6, #7, #8 in Figure 4.2a is to facilitate the evaluation of the values of shape functions at some discrete points inside and on the segments of the interested element. There is no extra degrees of freedom are associated with these added points. In other words, these points carry no additional independent field variable. Therefore, the total degrees of freedom (DOFs) of a CS-FEM model will be exactly the same as the standard FEM using the same set of nodes.

We note now the following remark.

Remark 4.1 On shape of CS-FEM elements

It may be noted that the CS-FEM can have general n -sided polygonal elements easily. This is because the S-FEM models do not use the derivatives of the shape functions. The standard FEM, however, can only have T3 and Q4 elements. Any generalization to other type of FEM elements has to be very careful to ensure (1) compatibility and (2) attainability of the derivatives of the shape functions, which can be quite difficult, when the shape of the elements become too complicated. Even when we use Q4 elements, we have to resort to a sophisticated “mapping” procedure.

4.5 Some properties of the CS-FEM

Remark 4.2 Single smoothing domain vs. single Gauss point

If only one single smoothing domain ($n_s = 1$) is used individually for each element in the problem domain, the solution of the CS-FEM has the similar properties with that of the standard FEM using reduced integration (using one Gauss point), when the same mesh are used.

Remark 4.2 can be examined as follows. As shown in Eq. (3.13), the smoothed strain-displacement matrix $\bar{\mathbf{B}}_I$ of the CS-FEM is the average of the standard strain-displacement matrix $\mathbf{B}_I(\mathbf{x})$ over the smoothing domain Ω_I^e , the physical element domain. While for FEM using reduced integration, $\mathbf{B}_I(\mathbf{x})$ is computed at the center of the isoparametric element, at $\xi = \eta = 0$. We thus have $\mathbf{B}_I(\xi = 0, \eta = 0)$ in the FEM is also considered to be the average of $\mathbf{B}_I(\mathbf{x})$ over the isoparametric element. Therefore, it is

clear that $\int_{\Omega_I^e} \bar{\mathbf{B}}_I^T \mathbf{D} \bar{\mathbf{B}}_I d\Omega$ in the CS-FEM is equivalent to $\int_{-1}^1 \int_{-1}^1 \mathbf{B}_I^T \mathbf{D} \mathbf{B}_I \mathbf{J} d\xi d\eta$ in the FEM using reduced integration. The only difference is that $\mathbf{B}_I(\xi = 0, \eta = 0)$ in the FEM is the average of $\mathbf{B}_I(\mathbf{x})$ over the isoparametric element and $\bar{\mathbf{B}}_I$ in the CS-FEM is the average of $\mathbf{B}_I(\mathbf{x})$ over the element in the physical coordinates. In the case the elements are parallelograms, the results of the CS-FEM and FEM will be identical.

Therefore, the solution of the CS-FEM has the similar properties with that of the FEM using the reduced integration. The element stiffness matrix can contain spurious zeros energy modes (known as hourglass modes) and thus may not be *spatially* stable. This is because the global stiffness matrix, even after imposing essential boundary conditions to

remove the rigid body motion, may still be singular depending on the setting of the problem [62]. \square

Remark 4.3 Convergence to the compatible FEM model

If each quadrilateral element is subdivided *sequentially*^{*} into n_s quadrilateral smoothing domains $\Omega_{i,m}^e$, and when $n_s \rightarrow \infty$ and the smoothing domain $\Omega_{i,m}^e \rightarrow 0$ for all the elements in the problem domain, the stiffness matrix $\bar{\mathbf{K}}_{IJ}^{\text{CS-FEM}}$ in Eq. (4.2) will approach the stiffness matrix $\mathbf{K}_{IJ}^{\text{FEM}} = \int_{\Omega} \mathbf{B}_I^T(\mathbf{x}) \mathbf{D} \mathbf{B}_J(\mathbf{x}) d\Omega$ of the standard FEM using the isoparametric elements with “full” (2×2) Gauss integration. At such a limit, the solution of the CS-FEM will approach the solution of the standard compatible displacement FEM model.

The Remark 4.3 is derived from [Theorem 3.5](#).

Remark 4.4 Monotonic property

Consider a CS-FEM element Ω_i^e that is divided *sequentially* into $n_s \geq 1$ smoothing domains. Let the strain energy of an element with $n_s = p$ smoothing domains be

$$\bar{E}_{n_s=p}^{\text{CS-FEM}} = \sum_{m=1}^p \int_{\Omega_{i,m}^e} \bar{\boldsymbol{\varepsilon}}_{i,m}^T \mathbf{D} \bar{\boldsymbol{\varepsilon}}_{i,m} d\Omega = \sum_{m=1}^p \bar{\boldsymbol{\varepsilon}}_{i,m}^T \mathbf{D} \bar{\boldsymbol{\varepsilon}}_{i,m} A_{i,m}^e \quad (4.5)$$

We then have the following monotonic inequality

$$\bar{E}_{n_s=1}^{\text{CS-FEM}} < \bar{E}_{n_s=2}^{\text{CS-FEM}} < \dots < \bar{E}_{n_s=p-1}^{\text{CS-FEM}} < \bar{E}_{n_s=p}^{\text{CS-FEM}} < \bar{E}_{n_s=p+1}^{\text{CS-FEM}} < \dots < \bar{E}_{n_s \rightarrow \infty}^{\text{CS-FEM}} = E^{\text{FEM}} \quad (4.6)$$

Proof

Suppose that the domain Ω_i^e of the quadrilateral element has already been divided into $n_s = p \geq 1$ smoothing domains $\Omega_{i,m}^e$ such that $\Omega_i^e = \bigcup_{m=1}^p \Omega_{i,m}^e$. Let $\bar{E}_{n_s=p}^{\text{CS-FEM}}$ be the strain

* The division of $n_s = p + 1$ is performed by dividing any of the domains in the previous division of $n_s = p$

energy of the element when $n_s = p$. We now further divide the j^{th} smoothing domain $\Omega_{i,j}^e$ into two smoothing domains $\Omega_{i,j1}^e$ and $\Omega_{i,j2}^e$ such that $\Omega_{i,j}^e = \Omega_{i,j1}^e \cup \Omega_{i,j2}^e$ and $\Omega_{i,j1}^e \cap \Omega_{i,j2}^e = \emptyset$, which results in a total of $n_s = p+1$ smoothing domains. Then, the strain energy of the element becomes $\bar{E}_{n_s=p+1}^{\text{CS-FEM}}$. Let $\boldsymbol{\varepsilon}^h$ be the compatible strain of the corresponding FEM element. We have the following relationship for smoothed strains:

$$\begin{aligned} \bar{\boldsymbol{\varepsilon}}_{\Omega_{i,j}^e} &= \frac{1}{A_{i,j}^e} \int_{\Omega_{i,j}^e} \boldsymbol{\varepsilon}^h d\Omega = \frac{1}{A_{i,j}^e} \left[A_{i,j1}^e \int_{\Omega_{i,j1}^e} \frac{\boldsymbol{\varepsilon}^h}{A_{i,j1}^e} d\Omega + A_{i,j2}^e \int_{\Omega_{i,j2}^e} \frac{\boldsymbol{\varepsilon}^h}{A_{i,j2}^e} d\Omega \right] \\ &= \underbrace{\frac{A_{i,j1}^e}{A_{i,j}^e}}_{\alpha_1} \bar{\boldsymbol{\varepsilon}}_{\Omega_{i,j1}^e} + \underbrace{\frac{A_{i,j2}^e}{A_{i,j}^e}}_{\alpha_2} \bar{\boldsymbol{\varepsilon}}_{\Omega_{i,j2}^e} \\ &= \alpha_1 \bar{\boldsymbol{\varepsilon}}_{\Omega_{i,j1}^e} + \alpha_2 \bar{\boldsymbol{\varepsilon}}_{\Omega_{i,j2}^e} \end{aligned} \quad (4.7)$$

where $\bar{\boldsymbol{\varepsilon}}_{\Omega_{i,j}^e}$ is the smoothed strain of domain $\Omega_{i,j}^e$ corresponding to $n_s = p$; $\bar{\boldsymbol{\varepsilon}}_{\Omega_{i,j1}^e}$ and $\bar{\boldsymbol{\varepsilon}}_{\Omega_{i,j2}^e}$ are the smoothed strains of domains $\Omega_{i,j1}^e$ and $\Omega_{i,j2}^e$ corresponding to $n_s = p+1$; $A_{i,j}^e$ is the area of domain $\Omega_{i,j}^e$ corresponding to $n_s = p$, $A_{i,j1}^e$ and $A_{i,j2}^e$ are the areas of domains $\Omega_{i,j1}^e$ and $\Omega_{i,j2}^e$ corresponding to $n_s = p+1$; $\alpha_1 = A_{i,j1}^e / A_{i,j}^e > 0$ and $\alpha_2 = A_{i,j2}^e / A_{i,j}^e > 0$. Note that, we have the relationship

$$\alpha_1 + \alpha_2 = 1 \quad (4.8)$$

Considering the difference between $\bar{E}_{n_s=p+1}^{\text{CS-FEM}}$ and $\bar{E}_{n_s=p}^{\text{CS-FEM}}$, and using Eqs. (4.7) and (4.8), we obtain

$$\begin{aligned} \bar{E}_{n_s=p+1}^{\text{CS-FEM}} - \bar{E}_{n_s=p}^{\text{CS-FEM}} &= \left(\bar{\boldsymbol{\varepsilon}}_{\Omega_{i,j1}^e} \right)^T \mathbf{D} \bar{\boldsymbol{\varepsilon}}_{\Omega_{i,j1}^e} A_{i,j1}^e + \left(\bar{\boldsymbol{\varepsilon}}_{\Omega_{i,j2}^e} \right)^T \mathbf{D} \bar{\boldsymbol{\varepsilon}}_{\Omega_{i,j2}^e} A_{i,j2}^e - \left(\bar{\boldsymbol{\varepsilon}}_{\Omega_{i,j}^e} \right)^T \mathbf{D} \bar{\boldsymbol{\varepsilon}}_{\Omega_{i,j}^e} A_{i,j}^e \\ &= \left[\left(\bar{\boldsymbol{\varepsilon}}_{\Omega_{i,j1}^e} \right)^T \mathbf{D} \left(\bar{\boldsymbol{\varepsilon}}_{\Omega_{i,j1}^e} \right) \frac{A_{i,j1}^e}{A_{i,j}^e} + \left(\bar{\boldsymbol{\varepsilon}}_{\Omega_{i,j2}^e} \right)^T \mathbf{D} \left(\bar{\boldsymbol{\varepsilon}}_{\Omega_{i,j2}^e} \right) \frac{A_{i,j2}^e}{A_{i,j}^e} - \left(\bar{\boldsymbol{\varepsilon}}_{\Omega_{i,j}^e} \right)^T \mathbf{D} \left(\bar{\boldsymbol{\varepsilon}}_{\Omega_{i,j}^e} \right) \right] A_{i,j}^e \\ &= \left[\alpha_1 \left(\bar{\boldsymbol{\varepsilon}}_{\Omega_{i,j1}^e} \right)^T \mathbf{D} \bar{\boldsymbol{\varepsilon}}_{\Omega_{i,j1}^e} + \alpha_2 \left(\bar{\boldsymbol{\varepsilon}}_{\Omega_{i,j2}^e} \right)^T \mathbf{D} \bar{\boldsymbol{\varepsilon}}_{\Omega_{i,j2}^e} - \right. \\ &\quad \left. - \left(\alpha_1 \bar{\boldsymbol{\varepsilon}}_{\Omega_{i,j1}^e} + \alpha_2 \bar{\boldsymbol{\varepsilon}}_{\Omega_{i,j2}^e} \right)^T \mathbf{D} \left(\alpha_1 \bar{\boldsymbol{\varepsilon}}_{\Omega_{i,j1}^e} + \alpha_2 \bar{\boldsymbol{\varepsilon}}_{\Omega_{i,j2}^e} \right) \right] A_{i,j}^e \end{aligned} \quad (4.9)$$

$$\begin{aligned}
&= \left[(\alpha_1 - \alpha_1^2) \left(\bar{\boldsymbol{\varepsilon}}_{\Omega_{i,j1}^e} \right)^T \mathbf{D} \bar{\boldsymbol{\varepsilon}}_{\Omega_{i,j1}^e} + (\alpha_2 - \alpha_2^2) \left(\bar{\boldsymbol{\varepsilon}}_{\Omega_{i,j2}^e} \right)^T \mathbf{D} \bar{\boldsymbol{\varepsilon}}_{\Omega_{i,j2}^e} - \right. \\
&\quad \left. - \alpha_1 \alpha_2 \left(\left(\bar{\boldsymbol{\varepsilon}}_{\Omega_{i,j1}^e} \right)^T \mathbf{D} \bar{\boldsymbol{\varepsilon}}_{\Omega_{i,j2}^e} + \left(\bar{\boldsymbol{\varepsilon}}_{\Omega_{i,j2}^e} \right)^T \mathbf{D} \bar{\boldsymbol{\varepsilon}}_{\Omega_{i,j1}^e} \right) \right] A_{i,j}^e \\
&= \left[\alpha_1 (1 - \alpha_1) \left(\bar{\boldsymbol{\varepsilon}}_{\Omega_{i,j1}^e} \right)^T \mathbf{D} \bar{\boldsymbol{\varepsilon}}_{\Omega_{i,j1}^e} + \alpha_2 (1 - \alpha_2) \left(\bar{\boldsymbol{\varepsilon}}_{\Omega_{i,j2}^e} \right)^T \mathbf{D} \bar{\boldsymbol{\varepsilon}}_{\Omega_{i,j2}^e} - \right. \\
&\quad \left. - \alpha_1 \alpha_2 \left(\left(\bar{\boldsymbol{\varepsilon}}_{\Omega_{i,j1}^e} \right)^T \mathbf{D} \bar{\boldsymbol{\varepsilon}}_{\Omega_{i,j2}^e} + \left(\bar{\boldsymbol{\varepsilon}}_{\Omega_{i,j2}^e} \right)^T \mathbf{D} \bar{\boldsymbol{\varepsilon}}_{\Omega_{i,j1}^e} \right) \right] A_{i,j}^e \\
&= \left[\left(\bar{\boldsymbol{\varepsilon}}_{\Omega_{i,j1}^e} \right)^T \mathbf{D} \bar{\boldsymbol{\varepsilon}}_{\Omega_{i,j1}^e} + \left(\bar{\boldsymbol{\varepsilon}}_{\Omega_{i,j2}^e} \right)^T \mathbf{D} \bar{\boldsymbol{\varepsilon}}_{\Omega_{i,j2}^e} - \left(\left(\bar{\boldsymbol{\varepsilon}}_{\Omega_{i,j1}^e} \right)^T \mathbf{D} \bar{\boldsymbol{\varepsilon}}_{\Omega_{i,j2}^e} + \left(\bar{\boldsymbol{\varepsilon}}_{\Omega_{i,j2}^e} \right)^T \mathbf{D} \bar{\boldsymbol{\varepsilon}}_{\Omega_{i,j1}^e} \right) \right] \alpha_1 \alpha_2 A_{i,j}^e \\
&= \left(\bar{\boldsymbol{\varepsilon}}_{\Omega_{i,j1}^e} - \bar{\boldsymbol{\varepsilon}}_{\Omega_{i,j2}^e} \right)^T \mathbf{D} \left(\bar{\boldsymbol{\varepsilon}}_{\Omega_{i,j1}^e} - \bar{\boldsymbol{\varepsilon}}_{\Omega_{i,j2}^e} \right) \alpha_1 \alpha_2 A_{i,j}^e > 0
\end{aligned}$$

where we used the SPD property of \mathbf{D} matrix (assuming stable material).

By combining Eq. (4.9) with Remark 4.3, we obtain inequality (4.6). \square

The monotonic inequality (4.6) is a powerful and useful statement resulted from the application of smoothing operations to functions in a positive definite quadratic functional. Inequality (4.6) also shows that with the same displacement \mathbf{u}^h , the strain energy of the element with $n_s = p+1$ domains is larger than that of the element with $n_s = p$ domains. In other words, the stiffness matrix of the element with $n_s = p+1$ smoothing domains is stiffer than that of the element with $n_s = p$ smoothing domains which leads to the following remark.

Remark 4.5 Softening effects

Let $\bar{\mathbf{K}}_{n_s=p}^{\text{CS-FEM}}$ be the stiffness matrix of the element with $n_s = p$ smoothing domains, we then have

$$\bar{\mathbf{K}}_{n_s=1}^{\text{CS-FEM}} \prec \bar{\mathbf{K}}_{n_s=2}^{\text{CS-FEM}} \prec \dots \prec \bar{\mathbf{K}}_{n_s=p-1}^{\text{CS-FEM}} \prec \bar{\mathbf{K}}_{n_s=p}^{\text{CS-FEM}} \prec \bar{\mathbf{K}}_{n_s=p+1}^{\text{CS-FEM}} \prec \dots \prec \bar{\mathbf{K}}_{n_s \rightarrow \infty}^{\text{CS-FEM}} = \mathbf{K}^{\text{FEM}} \quad (4.10)$$

where symbol “ \prec ” stands for an engineering term of *softer*. This implies that use of larger smoothing domains provides more softening effects: the CS-FEM model is always softer than the FEM counterpart.

Remark 4.5 can be explained intuitively as follows, when the number of n_s in each element increases, the stiffness matrix $\bar{\mathbf{K}}_{IJ}^{\text{CS-FEM}}$ in Eq. (4.2) will become stiffer. The solution obtained will change monotonously from the solution of the CS-FEM ($n_s = 1$) to that of the compatible displacement FEM model ($n_s \rightarrow \infty$).

4.6 Domain discretization with polygonal elements

In this thesis, the n -sided polygonal elements will be used in the CS-FEM, NS-FEM and ES-FEM. Hence, one technique to discretize a problem domain into n -sided convex polygonal elements should be briefly described. This technique can be performed using the well-known Voronoi diagram, and the procedure can be described as follows [117].

The problem domain and its boundaries are first discretized by a set of properly scattered points $\mathbf{P} := \{p_1, p_2, \dots, p_n\}$. Based on the given points, the domain is further decomposed into the same number of Voronoi cells $\mathbf{C} := \{C_1, C_2, \dots, C_n\}$ according to the nearest-neighbor rule defined by

$$C_i = \{\mathbf{x} \in \mathfrak{R}^2 : d(\mathbf{x}, \mathbf{x}_i) < d(\mathbf{x}, \mathbf{x}_j), \forall j \neq i\}, \quad \forall i \quad (4.11)$$

In the numerical implementation, as illustrated in Figure 4.4a, the generated Voronoi diagram has not cell vertices along the boundaries, and hence additional nodes along the boundary outside the domain need to be added to enclose the cells on the boundaries. With this, the boundary cells are then bounded, but these additional nodes of these cells do not fall *within* the problem domain as shown in Figure 4.4b. Next, these nodes are ‘shifted’ inwards onto the boundaries as shown in Figure 4.4c. The final shape of these

Voronoi cells is generally irregular but they are all convex polygons. The initial point p_i is regarded as the representative point of the i th element. Once we get the information of these Voronoi diagrams, a set of polygonal elements is then formed for the numerical analysis.

The following points need to be noted: (i) The original discrete points \mathbf{P} only serve as numerical devices for domain discretization and are not used in following numerical analysis; (ii) If we prefer more regular elements, such as rectangular elements, hexagon elements, we need to arrange a special point pattern \mathbf{P} before the generation of Voronoi diagrams; (iii) For demonstration purpose, we arrange the initial points in an arbitrary form in the following numerical examples without concerning the computational cost. As a result, the number of element sides is generally changing from element to element, which is perfectly acceptable to the n CS-FEM method.

4.7 Standard patch test

The patch tests for CS-FEM are first conducted in great detail using as much as five patches as shown in Figure 4.5 [77]. In these tests, a total of 25 test cases are created by rotating each of these five patches with $\theta = 0, \pi/6, \pi/4, \pi/3$ and $\pi/2$. Each four-node quadrilateral element is subdivided into smoothing domains in the fashion described in Section 4.1. In this particular case, we use $n_s = 1, 2, 3, 4, 8$ and 16 quadrilateral smoothing domains as shown in Figure 4.1.

The CS-FEM is used to solve the patch test problem for numerical solutions of displacements. To evaluate the error in the solutions in a quantitative manner, the following error norm in displacement defined as follows.

$$e_d = \frac{\sum_{i=1}^{2 \times N_n} |u_i - \bar{u}_i|}{\sum_{i=1}^{2 \times N_n} |u_i|} \times 100\% \quad (4.12)$$

where N_n is the total number of nodes of the problem domain; u_i is the exact displacement and \bar{u}_i is the numerical displacement for a CS-FEM model. The dimensionless parameters* are taken as $E = 100$, $\nu = 0.3$ and the linear displacement field is specified on the boundary of the patches using

$$u = x \quad ; \quad v = y \quad (4.13)$$

It is found that the CS-FEM can pass all these standard patch tests within the machine precision for all above patch cases. Table 4.3 shows the results for the case of $n_s = 4$.

The patch test for the n CS-FEM is conducted for a square patch using 36 n -sided polygonal elements as shown in Figure 4.6. It is found again that the n CS-FEM can pass the standard patch test within machine precision with the displacement error of $e_d = 1.83e-13$ (%).

4.8 Stability of the CS-FEM and n CS-FEM

As analyzed in [Chapter 3](#), for any smoothed model, the stability of the model should be checked carefully, and in theory we know that the minimum number of smoothing domains has to be used to ensure the stability. In this section, an intensive eigenvalue analysis using quadrilateral elements is conducted to investigate numerically the stability properties of the CS-FEM and n CS-FEM. The results of the CS-FEM and n CS-FEM are compared with the standard FEM using the four-node isoparametric elements. Line integration is used for the CS-FEM and n CS-FEM, while domain (element) integration

* In this thesis, we often choose to use non-dimensional parameters because the purpose of the examples is just to examine our numerical results, and no much physical implications. Any set of physical units is applicable to our results, as long as these units are consistent for all the inputs and outputs.

using Gauss quadrature (1 GP and 2×2 GPs) is used for the FEM. First, a free vibration analysis using the singular value decomposition technique of a single free quadrilateral element is conducted. In the CS-FEM, we divide each element into $n_s = 1, 2, 4, 8$ and 16 quadrilateral smoothing domains (SDs) in the way shown in Figure 4.1. In the n CS-FEM, we divide each quadrilateral element into $n_s = 4$ triangular SDs.

The results for the eigenvalue analysis are listed in Table 4.4. It is shown that three first non-zero eigenvalues are similar for all cases. For the CS-FEM using $n_s = 1$, we found five zero eigenvalues which is similar in the FEM using only one Gauss point (GP=1). These zero eigenvalues represent five spurious zero-energy eigenmodes which do not carry proper deformation information. These results verify Remark 4.2 that the solution of CS-FEM (or n CS-FEM) using $n_s = 1$ for elements has the similar properties with that of FEM using reduced integration. The element stiffness matrix will contain spurious zeros energy modes, and the global stiffness matrix after imposing essential boundary conditions to remove the rigid motion can still be singular depending on the setting of the problem. The solution can therefore be unstable. When comparing the results of CS-FEM using $n_s > 1$ four-node SDs and n CS-FEM using $n_s = 4$ triangular SDs with that of FEM using full Gauss integration (2×2 GPs), it is seen that, except three zero-energy rigid-body-movement modes, all the other modes are non zero-energy modes, and hence there are no spurious modes, and the models are all spatially stable. We can now conclude that the solutions of the CS-FEM using of $n_s > 1$ quadrilateral SDs and of the n CS-FEM using $n_s = 4$ triangular SDs will be stable at least for static problems.

Table 4.4 also shows that when n_s increases from 2 to 16, two zero-energy eigenvalues 4th and 5th of the CS-FEM will increase monotonously and approach to those of FEM using 2×2 GPs. These results are consistent with Remark 4.3 and Remark 4.4

which show that when n_s approaches monotonously to infinity, the CS-FEM solution will approach monotonously to the solution of the standard displacement compatible FEM model. In addition, from the nonzero eigenvalues of Table 4.4, it is seen that the CS-FEM is softer than (fully) compatible FEM model which is consistent with Remark 4.5.

Further comparison studies are conducted using a single element with three degrees-of-freedom (DOFs) fixed and a free solid with 4×4 elements, and results are listed in Table 4.5 and Table 4.6. It is seen that the same findings mentioned above can be observed.

4.9 Selective CS-FEM: volumetric locking free [102]

Volumetric locking appears when the Poisson's ratio of the material approaches to 0.5. The application of selective formulations in the standard FEM [54] has been found effectively to overcome such a locking and hence the similar idea is employed in this chapter to formulate a CS-FEM that is free from volumetric locking. In the FEM, different quadrature orders are used for different material parts [54], while in the CS-FEM we can simply vary the number of smoothing domains for these two different material "parts" (μ -part and λ -part). As presented in Remark 4.2, the solution of CS-FEM using only one smoothing domain ($n_s = 1$) for each element has the same properties with that of FEM using reduced integration (one Gauss point). We also know that the λ -part is the culprit of the volumetric locking. Therefore, in the CS-FEM, we use $n_s = 1$ for each element for the λ -part and $n_s = n$ (number of sides of the elements) for the μ -part. The details are given below.

The material property matrix \mathbf{D} for isotropic materials is first decomposed into

$$\mathbf{D} = \mathbf{D}_1 + \mathbf{D}_2 \quad (4.14)$$

where \mathbf{D}_1 relates to the shearing modulus $\mu = E/[2(1+\nu)]$ and hence is termed as μ -part of \mathbf{D} , and \mathbf{D}_2 relates to the Lamé's parameter $\lambda = \frac{2\nu\mu}{1-2\nu}$ and hence is termed as λ -part of \mathbf{D} . For plane strain cases, we have

$$\mathbf{D} = \begin{bmatrix} \lambda + 2\mu & \lambda & 0 \\ \lambda & \lambda + 2\mu & 0 \\ 0 & 0 & \mu \end{bmatrix} = \mu \begin{bmatrix} 2 & 0 & 0 \\ 0 & 2 & 0 \\ 0 & 0 & 1 \end{bmatrix} + \lambda \begin{bmatrix} 1 & 1 & 0 \\ 1 & 1 & 0 \\ 0 & 0 & 0 \end{bmatrix} = \mathbf{D}_1 + \mathbf{D}_2 \quad (4.15)$$

and for axis-symmetric problems:

$$\mathbf{D} = \mu \begin{bmatrix} 2 & 0 & 0 & 0 \\ 0 & 2 & 0 & 0 \\ 0 & 0 & 1 & 0 \\ 0 & 0 & 0 & 2 \end{bmatrix} + \lambda \begin{bmatrix} 1 & 1 & 0 & 1 \\ 1 & 1 & 0 & 1 \\ 0 & 0 & 0 & 0 \\ 1 & 1 & 0 & 1 \end{bmatrix} = \mathbf{D}_1 + \mathbf{D}_2 \quad (4.16)$$

In the CS-FEM and n CS-FEM, we use $n_s = 1$ to calculate the stiffness matrix related to λ -part and $n_s = n$ (number of sides of the elements) to calculate the one related to the μ -part. The stiffness matrix of element Ω_i^e of the selective scheme becomes two parts:

$$\bar{\mathbf{K}}_i^e = \underbrace{\sum_{m=1}^{n_s=n} (\bar{\mathbf{B}}_{i,m}^e)^T \mathbf{D}_1 \bar{\mathbf{B}}_{i,m}^e A_{i,m}^e}_{\bar{\mathbf{K}}_1^{n_s=n}} + \underbrace{(\bar{\mathbf{B}}_i^e)^T \mathbf{D}_2 \bar{\mathbf{B}}_i^e A_i^e}_{\bar{\mathbf{K}}_2^{n_s=1}} \quad (4.17)$$

where $\bar{\mathbf{B}}_i^e$ and A_i^e are the smoothed strain-displacement matrix and area of the whole element Ω_i^e , respectively; $\bar{\mathbf{B}}_{i,m}^e$ and $A_{i,m}^e$ are the smoothed strain-displacement matrix and area of the smoothing domain $\Omega_{i,m}^e$, respectively.

It is clear that the selective CS-FEM is a little more expensive, but it is volumetric locking free and hence it is very useful for solids with Poisson's rate close to 0.5. Note also that the selective n CS-FEM can be implemented exactly in the same manner.

4.10 Numerical examples

To examine the accuracy and efficiency, the results of the CS-FEM methods will be compared with those of the standard FEM using quadrilateral elements (FEM-Q4) as well

as the analytical solution. For quantitative study of the error and convergence rate of these methods, two error norms are used here, *i.e.*, displacement norm and energy norm. The displacement norm is defined as

$$e_d = \|\mathbf{u} - \tilde{\mathbf{u}}\|_{\mathbb{L}^2(\Omega)} = \left(\int_{\Omega} (\mathbf{u} - \tilde{\mathbf{u}})^T (\mathbf{u} - \tilde{\mathbf{u}}) d\Omega \right)^{1/2} = \left(\sum_{i=1}^{N_e} \int_{\Omega_i^e} (\mathbf{u} - \tilde{\mathbf{u}})^T (\mathbf{u} - \tilde{\mathbf{u}}) d\Omega \right)^{1/2} \quad (4.18)$$

The energy norm is defined by

$$\begin{aligned} e_e = \|\mathbf{u} - \tilde{\mathbf{u}}\|_{\mathbb{H}^1(\Omega)} = \|\boldsymbol{\varepsilon} - \tilde{\boldsymbol{\varepsilon}}\|_{\mathbb{L}^2(\Omega)} &= \left[\int_{\Omega} \frac{1}{2} (\boldsymbol{\varepsilon} - \tilde{\boldsymbol{\varepsilon}})^T \mathbf{D} (\boldsymbol{\varepsilon} - \tilde{\boldsymbol{\varepsilon}}) \right]^{1/2} \\ &= \left[\sum_{i=1}^{N_e} \int_{\Omega_i^e} \frac{1}{2} (\boldsymbol{\varepsilon} - \tilde{\boldsymbol{\varepsilon}})^T \mathbf{D} (\boldsymbol{\varepsilon} - \tilde{\boldsymbol{\varepsilon}}) \right]^{1/2} \end{aligned} \quad (4.19)$$

where \mathbf{u} and $\boldsymbol{\varepsilon}$ are the exact or analytical solution for the displacement and strain, respectively; $\tilde{\mathbf{u}}$ and $\tilde{\boldsymbol{\varepsilon}}$ are the numerical solution for the displacement and strain, respectively, obtained using any numerical model.

For the CS-FEM, the strain obtained in an element is in general not constant due to the use of smoothing domains in the elements. It is only constant in each smoothing domain. Therefore, when computing the strains (or stresses) for an element, some treatments are required. One simple way is to average those strains of smoothing domains of the element, and the averaged strains are regarded as the strains of the element. Such an averaged strain can also be weighted using the respective area of the smoothing domains. Similarly, to calculate numerical strain (or stress) at a node, we can also simply average the strains of smoothing domains associated with the node. In addition, using the numerical strain $\bar{\boldsymbol{\varepsilon}}(\mathbf{x}_j)$ at the node \mathbf{x}_j , we can further construct a “recovery” bilinear strain field $\bar{\boldsymbol{\varepsilon}}^R$ for each element in the CS-FEM using the following approximation

$$\bar{\boldsymbol{\varepsilon}}^R = \sum_{j=1}^4 \mathbf{N}_j(\mathbf{x}) \bar{\boldsymbol{\varepsilon}}(\mathbf{x}_j) \quad (4.20)$$

where $\mathbf{N}_j(\mathbf{x})$ are the bilinear shape functions of FEM-Q4, and $\bar{\boldsymbol{\varepsilon}}(\mathbf{x}_j)$ are strain values at 4 nodes of the element. The recovery strain field $\bar{\boldsymbol{\varepsilon}}^R$ will be used as the final numerical results of strain field of CS-FEM models in evaluating the error using Eq. (4.19).

In order to evaluate the integrals in Eqs. (4.18) and (4.19) for quadrilateral elements, the mapping procedure using Gauss integration is performed on each element with a summation on all elements. In each element, a proper number of Gauss points depending on the order of the integrand will be used. For example, if the order of analytical strain $\boldsymbol{\varepsilon}$ in Eq. (4.19) is 2 which leads to a 4th order integrand in Eq. (4.19), then 3×3 Gauss points are used for each quadrilateral element. This is to ensure there is no addition error introduced in the error assessment procedure.

Note that the convergence rates of the displacement and energy norms are computed based on a *characteristic length* h of the elements in the mesh. In study here, the average length of sides of elements is used as h . For the quadrilateral elements, the average length of sides of elements is computed using

$$h = \sqrt{\frac{S_{\Omega}}{N_e}} \quad (4.21)$$

where S_{Ω} is the area of the whole problem domain, and N_e is the total number of elements in the problem domain.

4.10.1 A rectangular cantilever loaded at the end

A rectangular cantilever with a length L and height D is studied as a benchmark problem here. The cantilever is subjected to a parabolic traction at the free end as shown in Figure 4.7. The beam is assumed to have a unit thickness so that plane stress condition is valid. The analytical solution is available and can be found in a textbook by Timoshenko and Goodier [148].

$$\begin{aligned}
u_x &= \frac{Py}{6EI} \left[(6L - 3x)x + (2 + \nu)(y^2 - \frac{D^2}{4}) \right] \\
u_y &= -\frac{P}{6EI} \left[3\nu y^2(L - x) + (4 + 5\nu)\frac{D^2 x}{4} + (3L - x)x^2 \right]
\end{aligned} \tag{4.22}$$

where the moment of inertia I for a beam with rectangular cross section and unit thickness is given by $I = D^3/12$.

The stresses corresponding to the displacements Eq. (4.22) are

$$\sigma_{xx}(x, y) = \frac{P(L - x)y}{I} \quad ; \quad \sigma_{yy}(x, y) = 0 \quad ; \quad \tau_{xy}(x, y) = -\frac{P}{2I} \left(\frac{D^2}{4} - y^2 \right) \tag{4.23}$$

The related parameters are taken as $E = 3.0 \times 10^7$ N/m², $\nu = 0.3$, $D = 12$ m, $L = 48$ m and $P = 1000$ N. The domain discretizations for two different elements: 4-node quadrilateral and n -sided polygonal elements are shown in Figure 4.8. In order to consider the direction from which the numerical displacements converge to the exact solution. The following definition is also used

$$e_{\text{sign}} = \text{sign} \left(\sum_{i=1}^{2 \times N_n} (|\tilde{u}_i| - |u_i|) \right) \tag{4.24}$$

where \tilde{u}_i is the displacement at nodes of any numerical models.

If $e_{\text{sign}} = 1$, the displacement of the numerical solutions will converge to exact solution from above, and on the other hand, if $e_{\text{sign}} = -1$ indicates a convergence to exact solution from below.

In the computation, the nodes on the left boundary are constrained using the exact displacements obtained from analytical Eq. (4.22) and the loading on the right boundary uses a parabolic distributed shear stress given in Eq. (4.23). This is to remove the modeling error for the boundary conditions. The cantilever is analyzed using different number of elements and smoothing domains, $n_s = 1, 2, 3, 4, 8$ and 16, as shown in Figure 4.1. The exact strain energy of the problem is known as 4.4746 Nm.

Table 4.7 show tip deflections of the cantilever beam obtained using different regular elements. Figure 4.9 shows the relative error in the displacement components v of the CS-FEM solution with respect to the analytical solution at $y = 0$, where a regular mesh of 32×8 is used. Figure 4.10 shows the convergence of the strain energy solution when the degrees of freedom are increased in a set of CS-FEM models. It is seen that the results of CS-FEM ($n_s = 1$) and FEM using reduced integration are identical. This is because the elements used are (regular) rectangles. Both Figure 4.9 and Figure 4.10 show clearly the monotonic behavior of CS-FEM solution in displacement and strain energy, as predicted in inequality (4.6). The solutions change monotonously from the overestimated to the underestimated ones with the increase of n_s , and then approach the result of FEM using full integration (4 Gauss points). It is observed that an optimal value $n_s = 4$ gives the best results as compared to the analytical ones for this problem.

Figure 4.11 shows that both stresses computed at the center of the elements and at the node by the CS-FEM agree very well with the analytical solutions. Figure 4.12 illustrates the second-order displacement gradients of CS-FEM obtained by Eq. (3.14). It is seen again that the CS-FEM results agree well with the analytical solutions. The gradients near the boundaries are generally less accurate when compared with the internal region because of the asymmetric smoothing domains used on the boundaries. This phenomenon has the same root as those observed in the smoothed particle hydrodynamics (SPH) when a biased smoothing domain is used on the domain boundary [72]. This phenomenon is also reported in nodal-natural element method by Yoo *et al.* [156].

Figure 4.13 shows the relative error in displacement v between the n CS-FEM and analytical solutions along $y = 6$. It is seen that the computed displacement using the n CS-FEM is underestimated and approaches the exact solution with the increase of elements. This behavior is quite similar to the standard FEM results. Figure 4.14 shows the contour

of the distribution of the relative error in displacement v between n CS-FEM and analytical solution. It is observed that the n CS-FEM solution is accurate. Figure 4.15 and Figure 4.16 plot the contours of stress distribution obtained using the n CS-FEM compared with the analytical one. Very good agreement has been observed.

The displacement and energy norms of the CS-FEM are compared with those of FEM-Q4 in Table 4.8 and Table 4.9. The convergence rates are also plotted in Figure 4.17 and Figure 4.18. It is seen again that both error and convergence rate in displacement and energy norms of CS-FEM will approach those of FEM-Q4 when n_s increases. In addition, convergence rates in displacement norm of both methods are roughly the same and approximately 2. Although not very significant, the convergence rate of the CS-FEM solution is larger than that of FEM in terms of displacements. In terms of the error in energy norm, the CS-FEM solution error is much smaller than that of FEM-Q4, as shown in Figure 4.18. The convergence rate in energy norm of FEM-Q4 is approximate 1, while those of the CS-FEM are from 1.35 to 1.55, much higher than that of FEM-Q4. In particular, it is observed that the errors in both displacement and energy norms of CS-FEM at $n_s = 4$ are the best as compared with the analytical ones.

We note that this numerical example confirms the bound properties of the CS-FEM.

4.10.2 Infinite plate with a circular hole

Figure 4.19 represents a plate with a central circular hole of radius $a = 1$ m, subjected to a unidirectional tensile load of 1.0 N/m at infinity in the x -direction. Due to its symmetry, only the upper right quadrant of the plate is modeled. Figure 4.20 gives the discretization of the domain using quadrilateral and n -sided polygonal elements, respectively. Plane strain condition is considered and $E = 1.0 \times 10^3$ N/m², $\nu = 0.3$.

Symmetric conditions are imposed on the left and bottom edges, and the inner boundary of the hole is traction free. The exact solution for the stress is [148]

$$\begin{aligned}\sigma_{11} &= 1 - \frac{a^2}{r^2} \left[\frac{3}{2} \cos 2\theta + \cos 4\theta \right] + \frac{3a^4}{2r^4} \cos 4\theta \\ \sigma_{22} &= -\frac{a^2}{r^2} \left[\frac{1}{2} \cos 2\theta - \cos 4\theta \right] - \frac{3a^4}{2r^4} \cos 4\theta \\ \tau_{12} &= -\frac{a^2}{r^2} \left[\frac{1}{2} \sin 2\theta + \sin 4\theta \right] + \frac{3a^4}{2r^4} \sin 4\theta\end{aligned}\quad (4.25)$$

where (r, θ) are the polar coordinates and θ is measured counterclockwise from the positive x -axis. Traction boundary conditions are imposed on the right ($x = 5$) and top ($y = 5$) edges based on the exact solution Eq. (4.25). The displacement components corresponding to the stresses are

$$\begin{aligned}u_1 &= \frac{a}{8\mu} \left[\frac{r}{a} (\kappa + 1) \cos \theta + 2 \frac{a}{r} ((1 + \kappa) \cos \theta + \cos 3\theta) - 2 \frac{a^3}{r^3} \cos 3\theta \right] \\ u_2 &= \frac{a}{8\mu} \left[\frac{r}{a} (\kappa - 3) \sin \theta + 2 \frac{a}{r} ((1 - \kappa) \sin \theta + \sin 3\theta) - 2 \frac{a^3}{r^3} \sin 3\theta \right]\end{aligned}\quad (4.26)$$

where $\mu = E / (2(1 + \nu))$, κ is defined in terms of Poisson's ratio by $\kappa = 3 - 4\nu$ for plane strain cases. The exact strain energy of the problem is known as 1.1817×10^{-2} Nm.

Using the CS-FEM, the domain is discretized using quadrilateral elements divided into different smoothing domains, $n_s = 1, 2, 3, 4, 8$ and 16 , as shown in Figure 4.1. From the Figure 4.21 and Figure 4.22, it is observed that all the computed displacements and stresses using the CS-FEM ($n_s = 4$) are in a good agreement with the analytical solutions.

Figure 4.23 shows the strain energy results of CS-FEM versus degrees of freedom used in the model, and Figure 4.24 plots the convergence of error in displacement norm when mesh is refined. It is shown clearly that the results of CS-FEM change monotonously from $n_s = 1$ to $n_s = 16$ and approach the result of FEM using full integration (4 Gauss

points). Note that for this problem, the error in displacement norm of CS-FEM is smallest at $n_s = 1$, and all the computed strain energies are underestimated compared to the analytical solution. The bound property of the CS-FEM solution is again observed from this example.

Figure 4.25 shows the convergence of error in energy norm of solutions obtained using the CS-FEM for the infinite plate with a hole, together with those using the FEM with the same meshes. The results again show that the errors in energy norm of CS-FEM solution are much smaller than that of FEM-Q4. Convergence rate in energy norm of FEM-Q4 is about 1.1, while those of CS-FEM are from 1.79 to 1.81 which are much higher than that of FEM-Q4. Also note that the error in energy norm of CS-FEM solution obtained using $n_s = 4$ is the best.

Using the n CS-FEM, it is observed that all the computed displacements and stresses are in a very good agreement with the analytical solutions as shown in Figure 4.26 and Figure 4.27. With the refinement of the mesh, the accuracy is getting better and approaches the exact solution. The contour plots of the error in displacement and stresses are shown in Figure 4.28. Very accurate results are obtained.

Figure 4.29 plots the displacement norm versus Poisson's ratio changing from 0.4 to 0.4999999 for n -sided polygonal elements (451 nodes) and for 4-node quadrilateral elements (289 nodes). For the 4-node quadrilateral elements, we use Eq. (4.18) to calculate the error in the displacement norm, and for n -sided polygonal elements, we use the following relative error

$$e_d = \frac{\sum_{i=1}^{2 \times N_n} |u_i - \tilde{u}_i|}{\sum_{i=1}^{2 \times N_n} |u_i|} \times 100\% \quad (4.27)$$

The results show that the selective scheme presented in Section 4.9 is effective in overcoming the volumetric locking problems using nearly incompressible materials, while the CS-FEM ($n_s = 4$) and n CS-FEM are subjected to the volumetric locking. We have also observed that the locking starts as early as Poisson's ratio at 0.4.

4.11 Concluding remarks

In this work, we presented the cell-based S-FEM models including the CS-FEM using the quadrilateral elements and the n CS-FEM for general n -sided polygonal elements. Through the theoretical study, formulations and numerical examples, some remarks for the CS-FEM and n CS-FEM can be made as follows:

Remark 4.6 Shape function values

For the CS-FEM and n CS-FEM, the evaluation of the shape function values at points on the smoothing domain boundaries can be done with ease, using the simple point interpolation and/or averaging in a proper manner. The compatibility of the displacement field on the smoothing domain boundaries can always be ensured using such a point interpolation method, as long as the interpolation is based on the points on the smoothing domain boundaries.

Remark 4.7 Spatial stability of CS-FEM models

For the CS-FEM using quadrilateral elements, when the number of smoothing domains $n_s = 1$, the solution of CS-FEM has the similar properties with those of FEM using reduced integration. The element stiffness matrix may contain spurious zeros energy modes, and the global stiffness matrix after imposing sufficient essential boundary conditions can still be singular depending on the setting of the problem. When n_s approaches infinity, the solution of CS-FEM will approach to the solution of standard

compatible FEM model. When n_s is a finite number larger than 1, the solutions of CS-FEM in both displacement and strain energy will change monotonously from the solution of CS-FEM ($n_s = 1$) to that of FEM using full integration.

Remark 4.8 CS-FEM with $n_s = 4$: an always stable model

In practical computation, using $n_s = 4$ smoothing domains for each quadrilateral element in the CS-FEM is advised for all problems. The numerical solution of CS-FEM ($n_s = 4$) is always stable, accurate, much better than FEM-Q4, and often very close to the exact solutions.

Remark 4.9 CS-FEM vs. FEM

The errors in energy norm of CS-FEM are much smaller than that of FEM-Q4. The convergence rates in energy norm of CS-FEM are much higher than that of FEM-Q4. The errors and convergence rates in displacement norm of CS-FEM will approach those of FEM when the number of smoothing domains n_s increases.

Remark 4.10 On the n CS-FEM: an always stable and efficient model

In the n CS-FEM, n -sided polygonal elements using $n_s = n$ triangular smoothing domains are always stable and give good accuracy in computations.

Remark 4.11 Selective CS-FEM: Volumetric locking free

The selective scheme used in the CS-FEM is simple and very effective in overcoming the volumetric locking problems using nearly incompressible materials.

The CS-FEM has been studied further in theory [110] and extended for dynamic analyses [36], incompressible materials using selective integration [111], plate and shell analyses [114, 35, 101, 108, 115]. It is also extended for the extended finite element method (XFEM) to solve fracture mechanics problems in 2D continuum and plates [20].

Table 4.1. Values of shape functions at different points within a quadrilateral element (Figure 4.2a).					
Point	Node 1	Node 2	Node 3	Node 4	Description
1	1.0	0	0	0	Field node
2	0	1.0	0	0	Field node
3	0	0	1.0	0	Field node
4	0	0	0	1.0	Field node
5	1/2	1/2	0	0	Side midpoint
6	0	1/2	1/2	0	Side midpoint
7	0	0	1/2	1/2	Side midpoint
8	1/2	0	0	1/2	Side midpoint
9	1/4	1/4	1/4	1/4	Intersection of two bimedians
<i>g1</i>	3/4	1/4	0	0	Gauss point (Mid-segment of $\Gamma_{k,p}^s$)
<i>g2</i>	3/8	3/8	1/8	1/8	Gauss point (Mid-segment of $\Gamma_{k,p}^s$)
<i>g3</i>	3/8	1/8	1/8	3/8	Gauss point (Mid-segment of $\Gamma_{k,p}^s$)
<i>g4</i>	3/4	0	0	1/4	Gauss point (Mid-segment of $\Gamma_{k,p}^s$)
<i>g5</i>	1/4	3/4	0	0	Gauss point (Mid-segment of $\Gamma_{k,p}^s$)
<i>g6</i>	0	3/4	1/4	0	Gauss point (Mid-segment of $\Gamma_{k,p}^s$)
<i>g7</i>	1/8	3/8	3/8	1/8	Gauss point (Mid-segment of $\Gamma_{k,p}^s$)
<i>g8</i>	0	1/4	3/4	0	Gauss point (Mid-segment of $\Gamma_{k,p}^s$)
<i>g9</i>	0	0	3/4	1/4	Gauss point (Mid-segment of $\Gamma_{k,p}^s$)
<i>g10</i>	1/8	1/8	3/8	3/8	Gauss point (Mid-segment of $\Gamma_{k,p}^s$)
<i>g11</i>	0	0	1/4	3/4	Gauss point (Mid-segment of $\Gamma_{k,p}^s$)
<i>g12</i>	1/4	0	0	3/4	Gauss point (Mid-segment of $\Gamma_{k,p}^s$)

Point	Node 1'	Node 2'	Node 3'	Node 4'	Node 5'	Node 6'	Description
1'	1.0	0	0	0	0	0	Field node
2'	0	1.0	0	0	0	0	Field node
3'	0	0	1.0	0	0	0	Field node
4'	0	0	0	1.0	0	0	Field node
5'	0	0	0	0	1.0	0	Field node
6'	0	0	0	0	0	1.0	Field node
<i>O</i>	1/6	1/6	1/6	1/6	1/6	1/6	Centroid point
<i>g1'</i>	7/12	1/12	1/12	1/12	1/12	1/12	Gauss point (Mid-segment of $\Gamma_{k,p}^s$)
<i>g2'</i>	1/2	1/2	0	0	0	0	Gauss point (Mid-segment of $\Gamma_{k,p}^s$)
<i>g3'</i>	1/12	7/12	1/12	1/12	1/12	1/12	Gauss point (Mid-segment of $\Gamma_{k,p}^s$)
<i>g4'</i>	0	1/2	1/2	0	0	0	Gauss point (Mid-segment of $\Gamma_{k,p}^s$)
<i>g5'</i>	1/12	1/12	7/12	1/12	1/12	1/12	Gauss point (Mid-segment of $\Gamma_{k,p}^s$)
<i>g6'</i>	0	0	1/2	1/2	0	0	Gauss point (Mid-segment of $\Gamma_{k,p}^s$)
<i>g7'</i>	1/12	1/12	1/12	7/12	1/12	1/12	Gauss point (Mid-segment of $\Gamma_{k,p}^s$)
<i>g8'</i>	0	0	0	1/2	1/2	0	Gauss point (Mid-segment of $\Gamma_{k,p}^s$)
<i>g9'</i>	1/12	1/12	1/12	1/12	7/12	1/12	Gauss point (Mid-segment of $\Gamma_{k,p}^s$)
<i>g10'</i>	0	0	0	0	1/2	1/2	Gauss point (Mid-segment of $\Gamma_{k,p}^s$)
<i>g11'</i>	1/12	1/12	1/12	1/12	1/12	7/12	Gauss point (Mid-segment of $\Gamma_{k,p}^s$)
<i>g12'</i>	1/2	0	0	0	0	1/2	Gauss point (Mid-segment of $\Gamma_{k,p}^s$)

	Patch (a)	Patch (b)	Patch (c)	Patch (d)	Patch (e)
$\theta = 0$	1.11 e-13	7.78 e-14	5.69 e-14	2.58 e-13	9.51 e-13
$\theta = \pi/6$	7.22 e-14	1.38 e-13	9.48 e-14	3.05 e-13	4.26 e-13
$\theta = \pi/4$	5.78 e-14	1.11 e-13	1.85 e-13	3.80 e-13	7.72 e-13
$\theta = \pi/3$	1.16 e-13	8.28 e-14	9.43 e-14	2.09 e-13	4.82 e-13
$\theta = \pi/2$	1.31 e-13	7.82 e-14	1.03 e-13	2.05 e-13	6.93 e-13

Eigenvalues	FEM		CS-FEM					n CS-FEM
	1×1 GP	2×2 GPs	$n_s = 1$	$n_s = 2$	$n_s = 4$	$n_s = 8$	$n_s = 16$	$n_s = 4$
8	4.286e+7	4.286e+7	4.286e+7	4.286e+7	4.286e+7	4.286e+7	4.286e+7	4.286e+7
7	2.308e+7	2.308e+7	2.308e+7	2.308e+7	2.308e+7	2.308e+7	2.308e+7	2.308e+7
6	2.308e+7	2.308e+7	2.308e+7	2.308e+7	2.308e+7	2.308e+7	2.308e+7	2.308e+7
5	0	1.484e+7	0	0.824e+7	1.528e+7	1.319e+7	1.391e+7	2.225e+7
4	0	1.484e+7	0	0.288e+7	0.925e+7	1.185e+7	1.391e+7	2.225e+7
3	0	0	0	0	0	0	0	0
2	0	0	0	0	0	0	0	0
1	0	0	0	0	0	0	0	0

Eigenvalues	FEM		CS-FEM					n CS-FEM
	1×1 GP	2×2 GPs	$n_s = 1$	$n_s = 2$	$n_s = 4$	$n_s = 8$	$n_s = 16$	$n_s = 4$
8	2.935e+7	3.039e+7	2.935e+7	2.977e+7	2.997e+7	3.021e+7	3.029e+7	3.140e+7
7	1.474e+7	1.905e+7	1.474e+7	1.543e+7	1.925e+7	1.799e+7	1.863e+7	2.266e+7
6	1.154e+7	1.402e+7	1.154e+7	1.308e+7	1.378e+7	1.384e+7	1.392e+7	1.517e+7
5	1	0.843e+7	1	0.431e+7	0.568e+7	0.741e+7	0.798e+7	1.132e+7
4	1	0.229e+7	1	0.065e+7	0.220e+7	0.220e+7	0.220e+7	0.289e+7
3	1	1	1	1	1	1	1	1
2	0	1	0	1	1	1	1	1
1	0	1	0	1	1	1	1	1

Eigenvalues	FEM		CS-FEM					n CS-FEM
	1×1 GP	2×2 GPs	$n_s = 1$	$n_s = 2$	$n_s = 4$	$n_s = 8$	$n_s = 16$	$n_s = 4$
8	2.770e+6	8.439e+6	2.770e+6	6.220e+6	8.303e+6	8.343e+6	8.400e+6	8.823e+6
7	2.770e+6	6.182e+6	2.770e+6	5.748e+6	6.159e+6	6.163e+6	6.175e+6	6.226e+6
6	0	4.408e+6	0	3.576e+6	4.136e+6	4.177e+6	4.317e+6	5.053e+6
5	0	4.160e+6	0	3.508e+6	4.112e+6	4.063e+6	4.115e+6	4.478e+6
4	0	4.160e+6	0	3.320e+6	3.936e+6	4.024e+6	4.115e+6	4.478e+6
3	0	0	0	0	0	0	0	0
2	0	0	0	0	0	0	0	0
1	0	0	0	0	0	0	0	0

n_s	Mesh 16×4	Mesh 24×6	Mesh 32×8	Mesh 40×10	Mesh 48×12
FEM (GP = 1)	9.4542	9.1471	9.0319	8.9874	8.9581
1	9.4542	9.1471	9.0319	8.9874	8.9581
2	9.2915	9.0699	8.9948	8.9604	8.9419
3	9.0574	8.9693	8.9389	8.9249	8.9172
4	8.8355	8.8711	8.8837	8.8896	8.8927
8	8.7978	8.8542	8.8741	8.8834	8.8885
16	8.6920	8.8061	8.8469	8.8659	8.8763
FEM (GP = 4)	8.6453	8.7847	8.8347	8.8581	8.8708

Mesh	h	CS-FEM $n_s = 1$	CS-FEM $n_s = 2$	CS-FEM $n_s = 3$	CS-FEM $n_s = 4$	CS-FEM $n_s = 8$	CS-FEM $n_s = 16$	FEM (GP=4)
16×4	3.0	6.72	4.66	1.90	(-) 0.74	(-) 1.18	(-) 2.42	(-) 2.97
24×6	2	2.88	2.02	0.84	(-) 0.33	(-) 5.29	(-) 1.09	(-) 1.35
32×8	1.5	1.60	1.13	0.47	(-) 0.19	(-) 0.30	(-) 0.62	(-) 0.76
40×10	1.2	1.02	0.72	0.30	(-) 0.12	(-) 0.19	(-) 0.40	(-) 0.49
48×12	1	0.70	0.50	0.21	(-) 0.083	(-) 0.13	(-) 0.28	(-) 0.34

Note: sign (-) shows that the solution is smaller than the exact solution; $GP = 4$ for FEM quadrilateral element is the minimum number for full integration.

Mesh	h	CS-FEM $n_s = 1$	CS-FEM $n_s = 2$	CS-FEM $n_s = 3$	CS-FEM $n_s = 4$	CS-FEM $n_s = 8$	CS-FEM $n_s = 16$	FEM (GP=4)
16×4	3.0	2.96	3.29	2.84	2.38	2.45	2.63	3.71
24×6	2	1.75	1.88	1.59	1.30	1.33	1.41	2.49
32×8	1.5	1.19	1.26	1.04	0.85	0.86	0.90	1.88
40×10	1.2	0.87	0.92	0.75	0.60	0.61	0.64	1.50
48×12	1	0.68	0.71	0.58	0.46	0.47	0.48	1.25

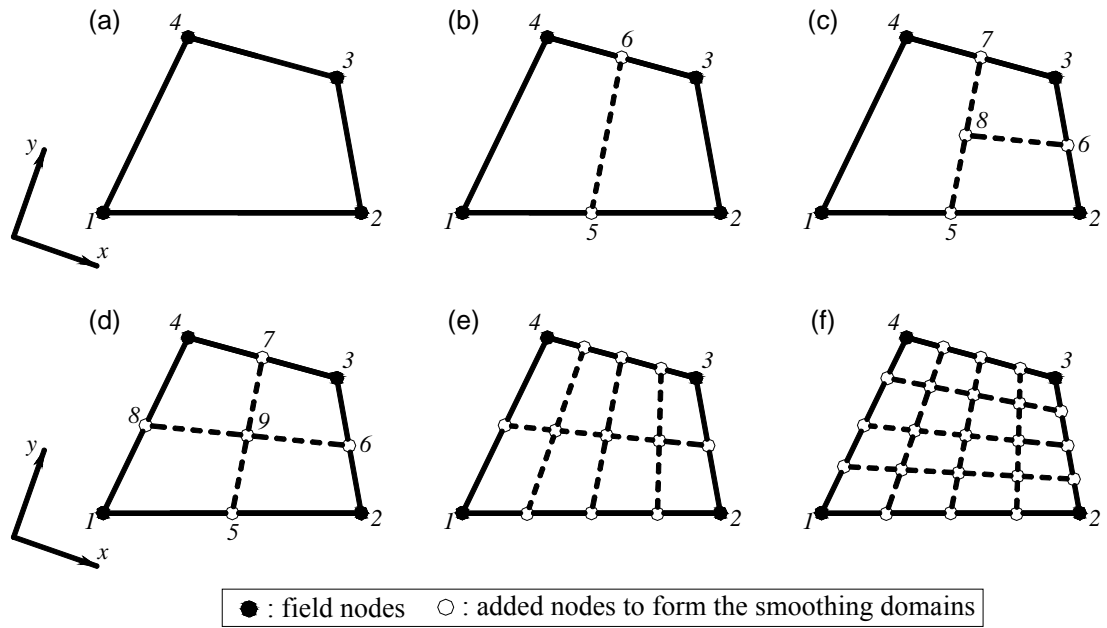


Figure 4.1. Division of a quadrilateral element into smoothing domains (SDs) in the CS-FEM by connecting the mid-segment-points of opposite segments of smoothing domains.
 (a) 1 SD; (b) 2 SDs; (c) 3 SDs; (d) 4 SDs; (e) 8 SDs; (f) 16 SDs.

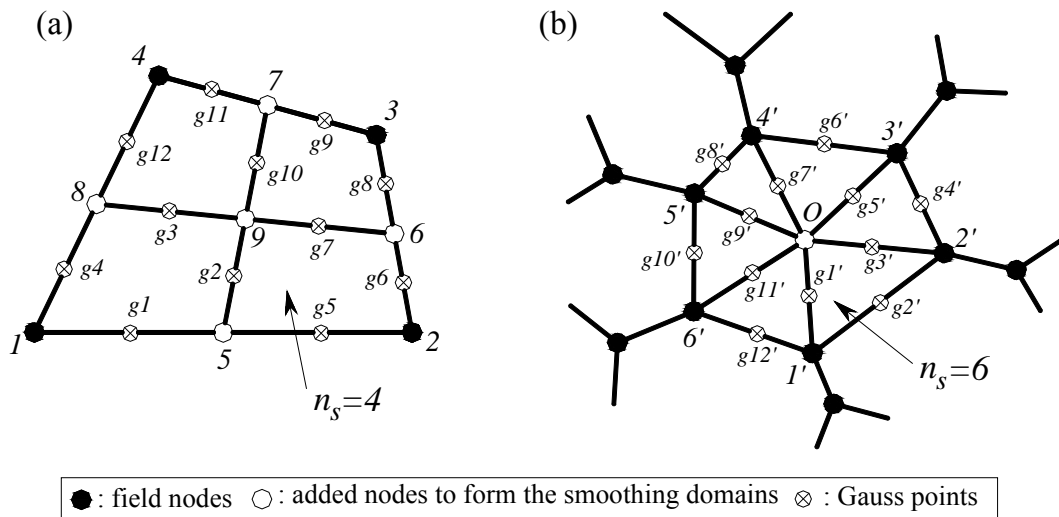


Figure 4.2. Position of Gauss points at mid-segment-points on segments of smoothing domains; (a) Four quadrilateral smoothing domains in a quadrilateral element; (b) Six triangular smoothing domains in a 6-sided convex polygonal element.

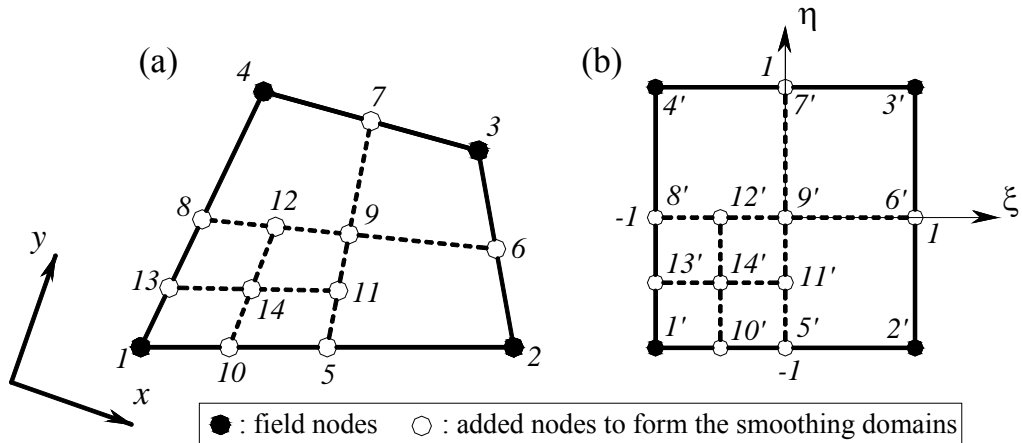


Figure 4.3. Division of an isoparametric elements into quadrilateral smoothing domains. The lower-left quadrant is further divided into 4 smoothing domains by connecting the mid-segment-points of opposite segments. (a) Quadrilateral smoothing domains of a CS-FEM element (no mapping is needed); (b) element in the natural coordinate for the isoparametric FEM element (mapping is needed).

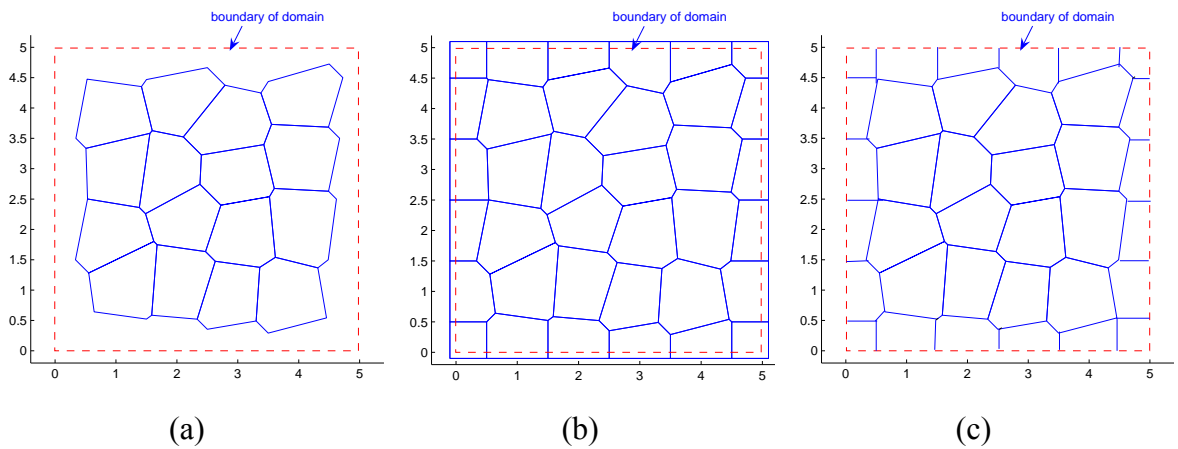


Figure 4.4. (a) Voronoi diagram without adding the nodes along the boundary outside the domain; (b) Voronoi diagram with the nodes added along the boundary outside the domain; (c) Final Voronoi diagram.

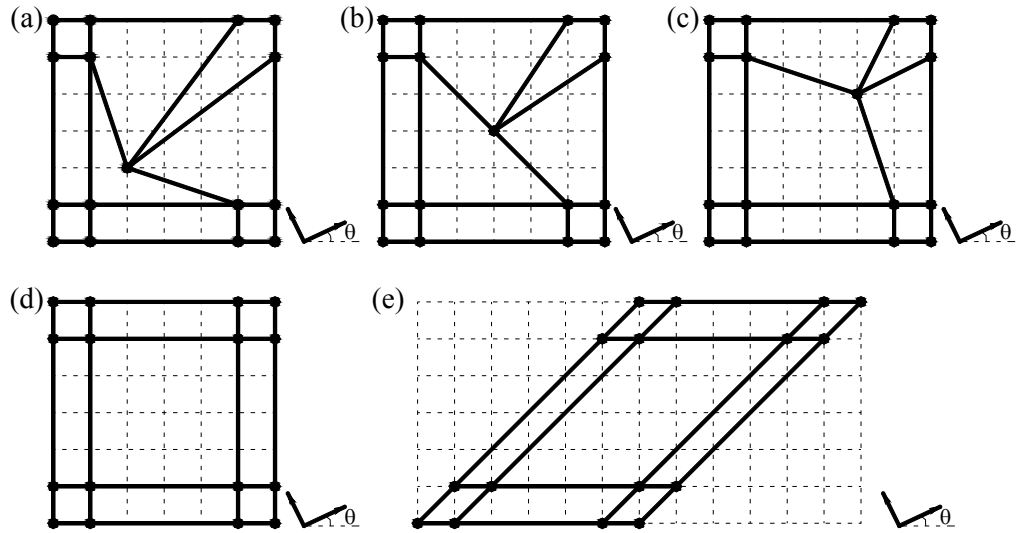


Figure 4.5. Meshes used for the patch test. (a) a mesh with a concave quadrilateral element; (b) a mesh with a quadrilateral element using three collinear points; (c) a mesh with general convex quadrilateral elements; (d) a mesh with rectangular elements; (e) a mesh with parallelogram elements.

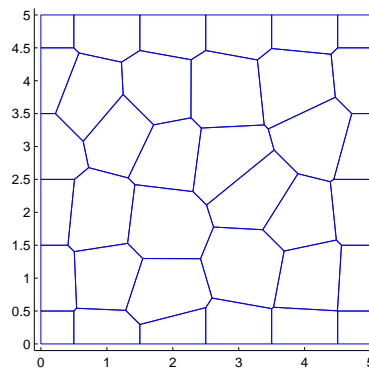


Figure 4.6. Domain discretization of a square patch using 36 n -sided polygonal elements.

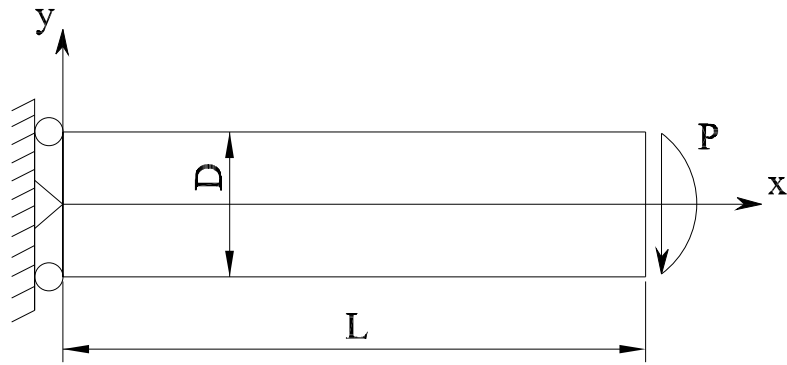
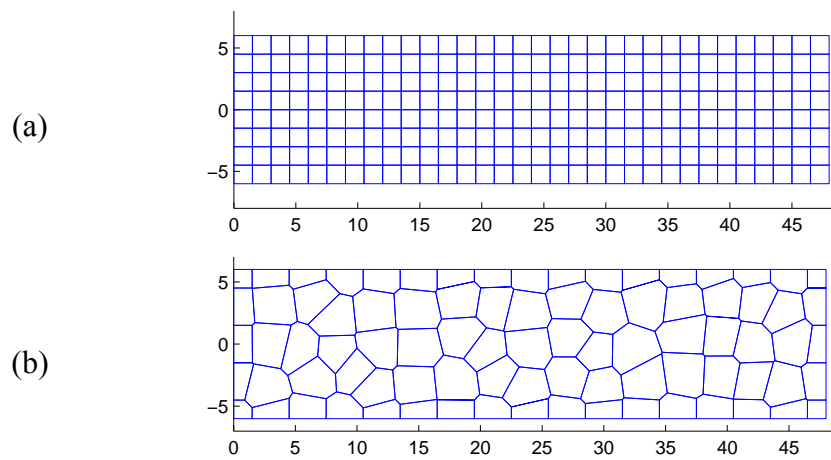


Figure 4.7. Cantilever loaded at the end.

Figure 4.8. Domain discretization of the cantilever; (a) using 4-node elements; (b) using n -sided polygonal elements.

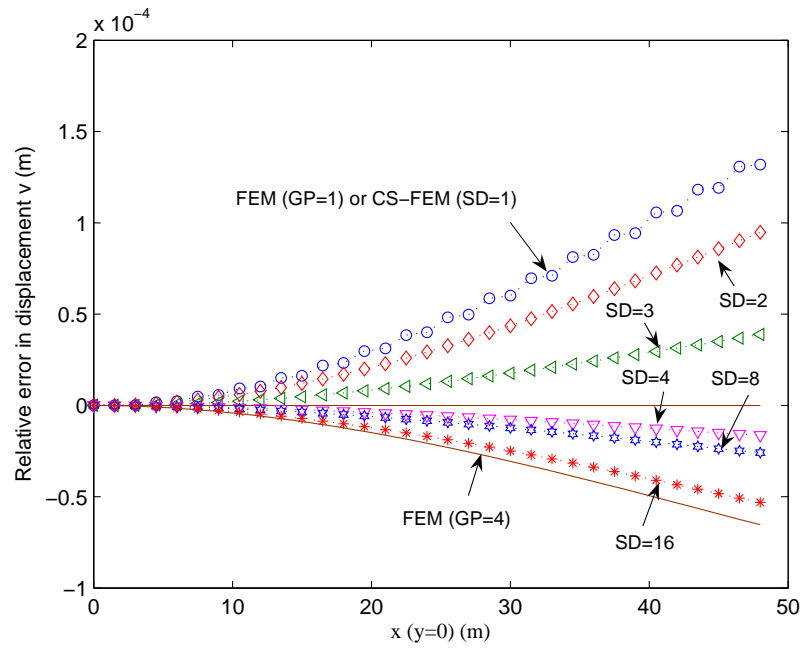


Figure 4.9. Comparison of the relative error in displacement v between CS-FEM and analytical solution for the cantilever loaded at the end. The monotonic behavior of CS-FEM solution in displacement is clearly shown.

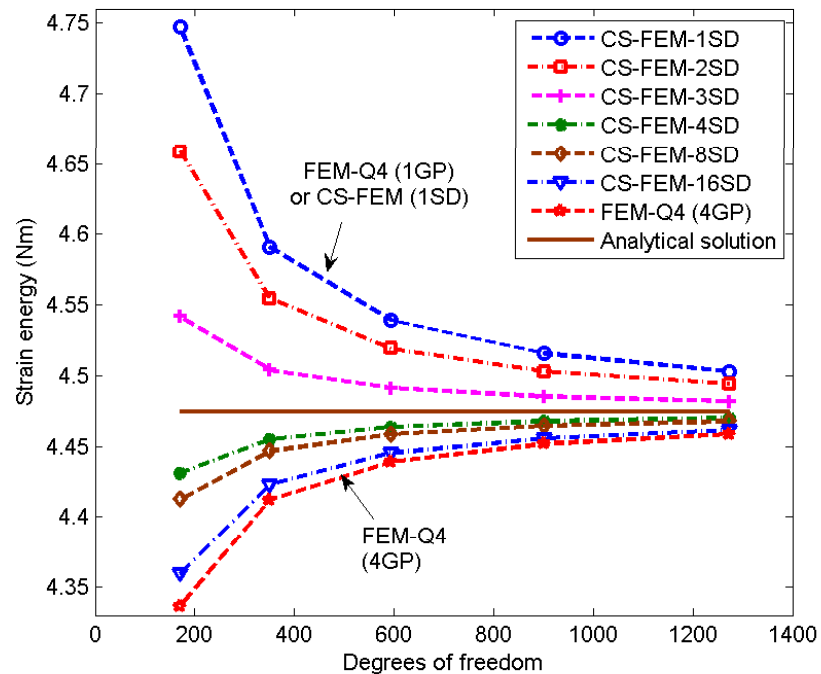


Figure 4.10. Convergence of strain energy solutions of CS-FEM and FEM for the cantilever loaded at the end. The monotonic behavior of CS-FEM solution in strain energy is clearly shown.

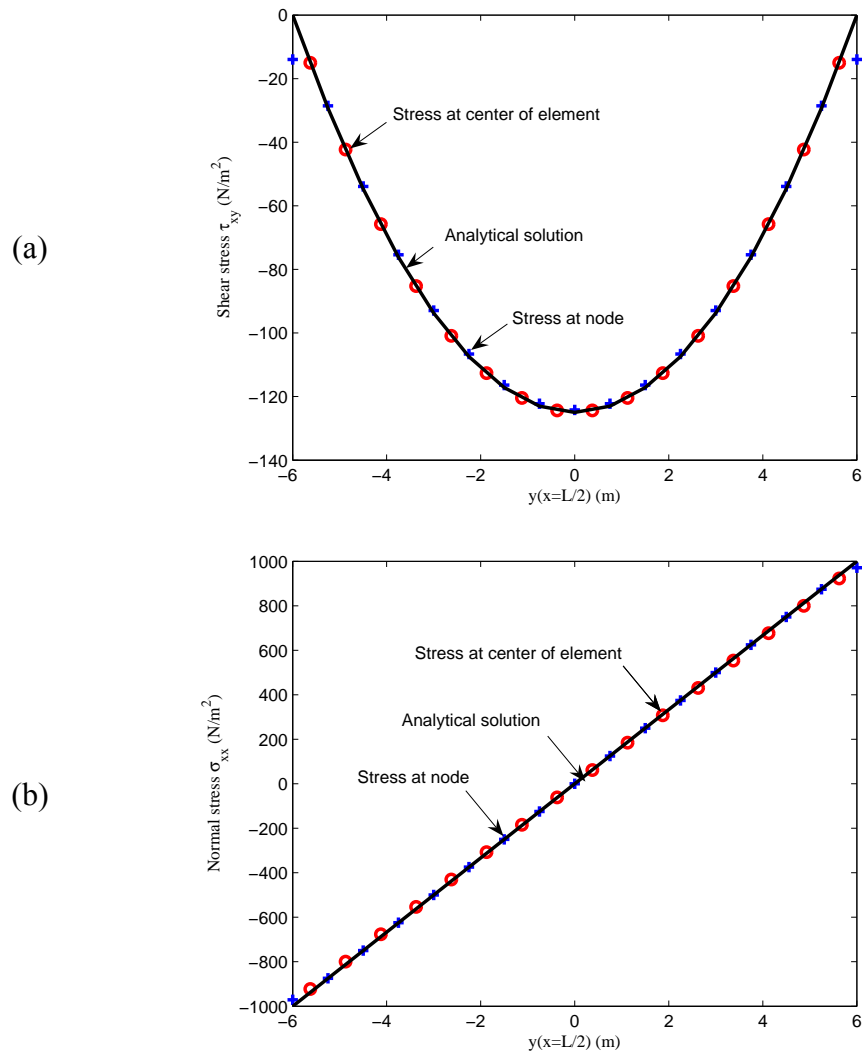


Figure 4.11. Comparison of the numerical results of CS-FEM and analytical solutions for the cantilever loaded at the end. (a) Shear stress τ_{xy} ; (b) Normal stress σ_{xx} .

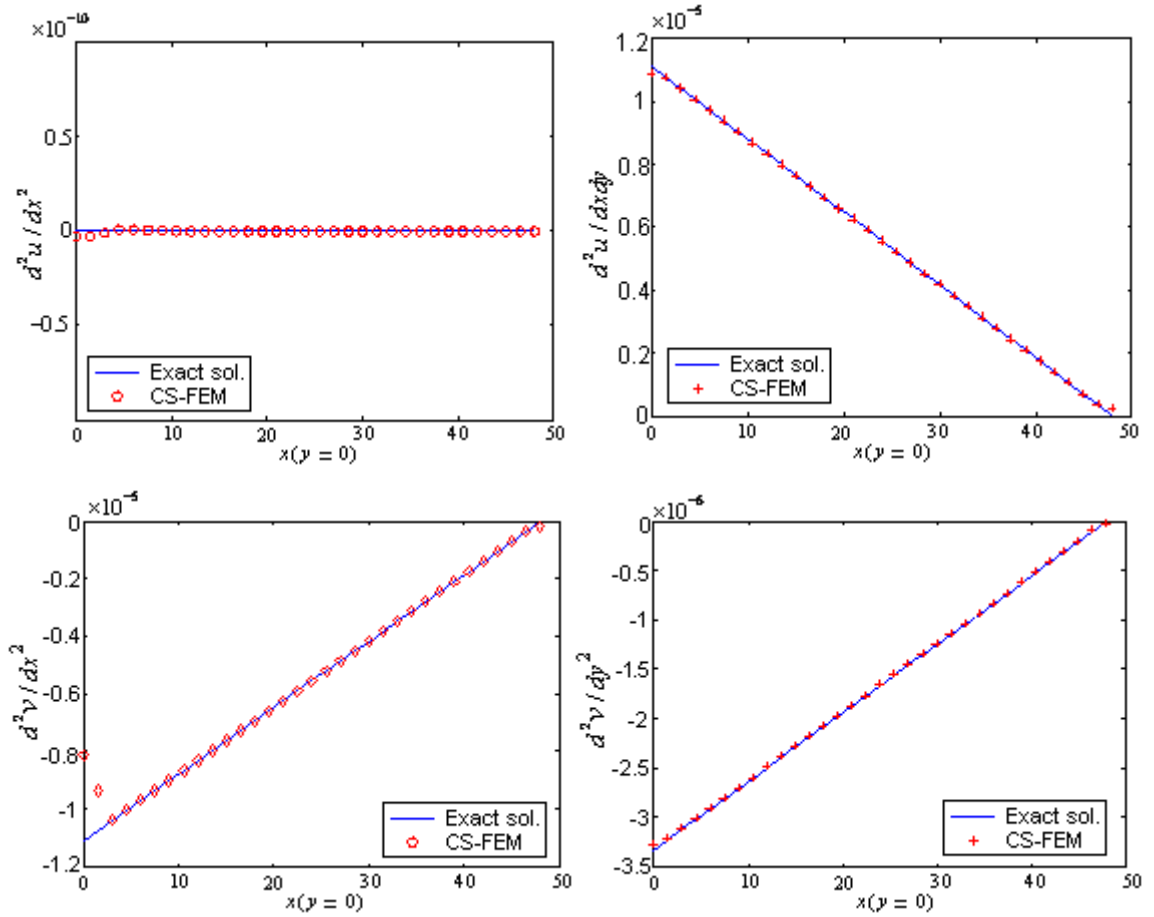


Figure 4.12. Second order displacement gradients using the CS-FEM for the cantilever loaded at the end.

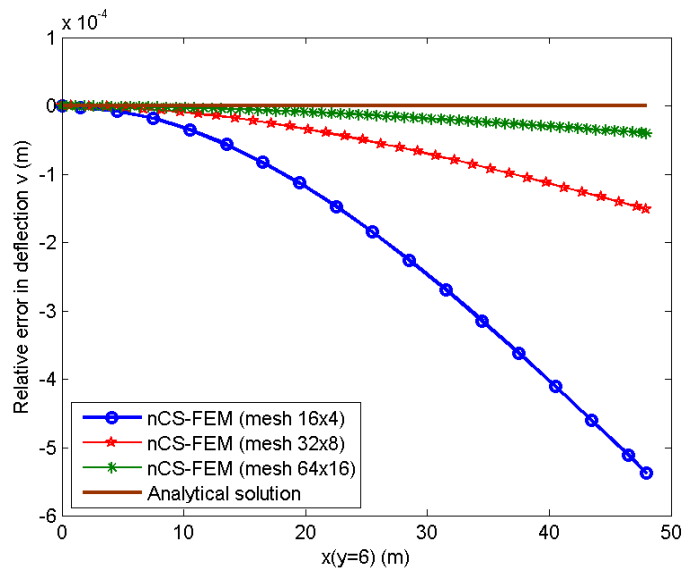


Figure 4.13. Relative error in displacement v along $y = 0$ between the n CS-FEM and analytical solution for the cantilever loaded at the end.

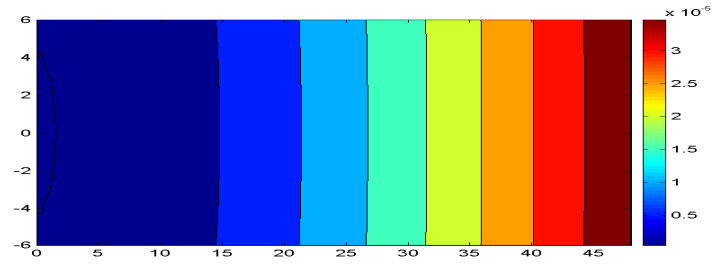


Figure 4.14. Contour of relative deflection errors (m) of the cantilever using n CS-FEM.

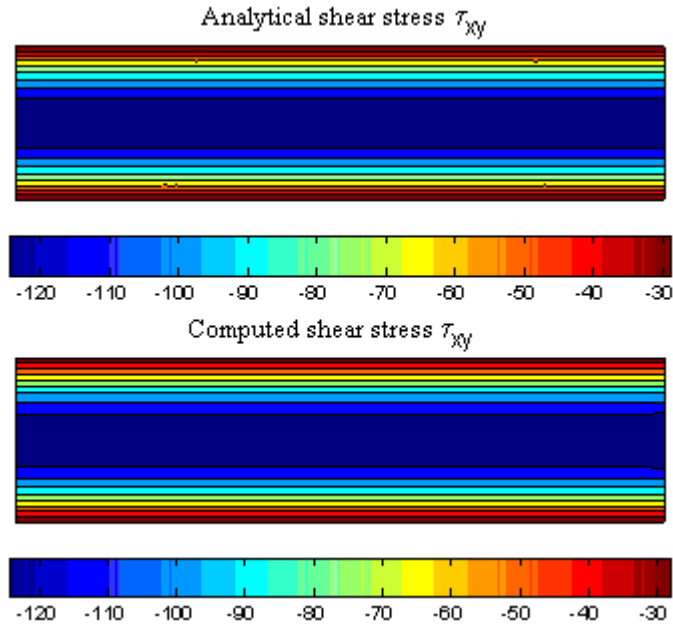


Figure 4.15. Contour of the analytical and computed shear stress τ_{xy} (N/m^2) of the cantilever using the n CS-FEM.

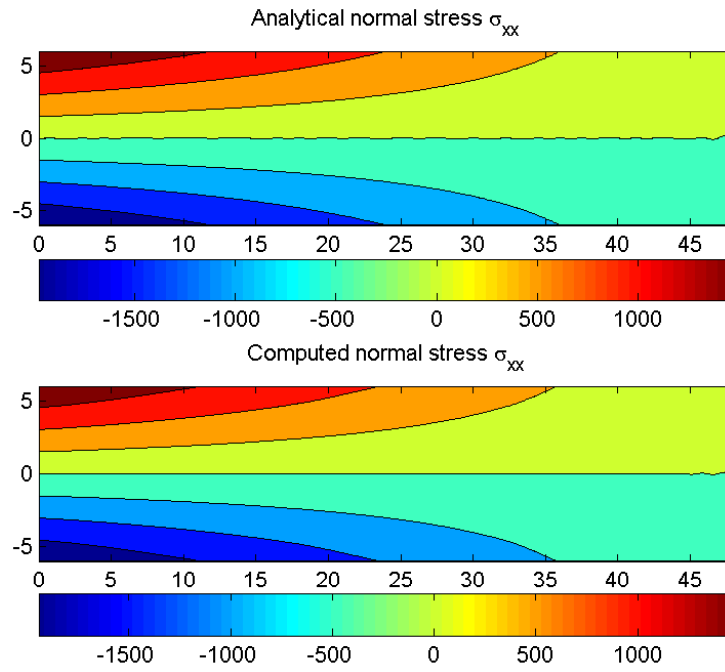


Figure 4.16. Contour of the analytical and computed normal stress σ_{xx} (N/m^2) of the cantilever using the n CS-FEM.

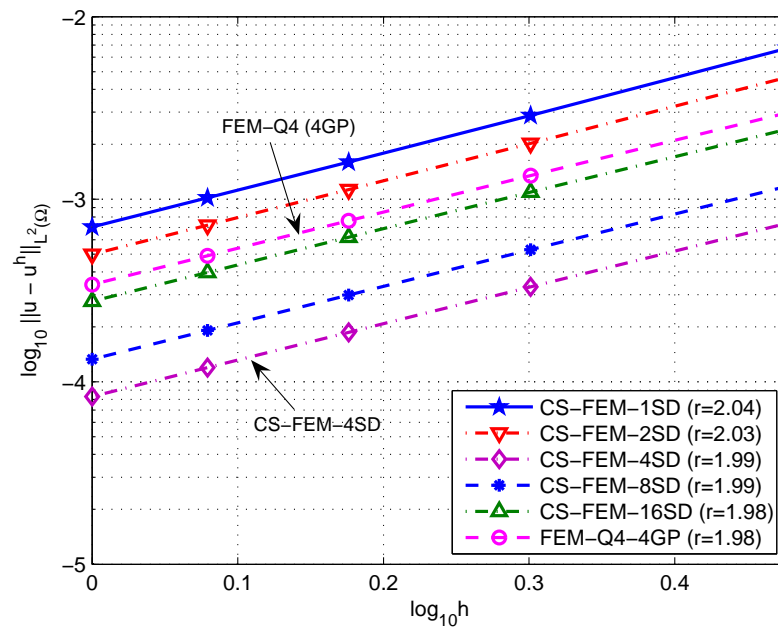


Figure 4.17. Error in displacement norm of CS-FEM and FEM for the cantilever loaded at the end using the same meshes.

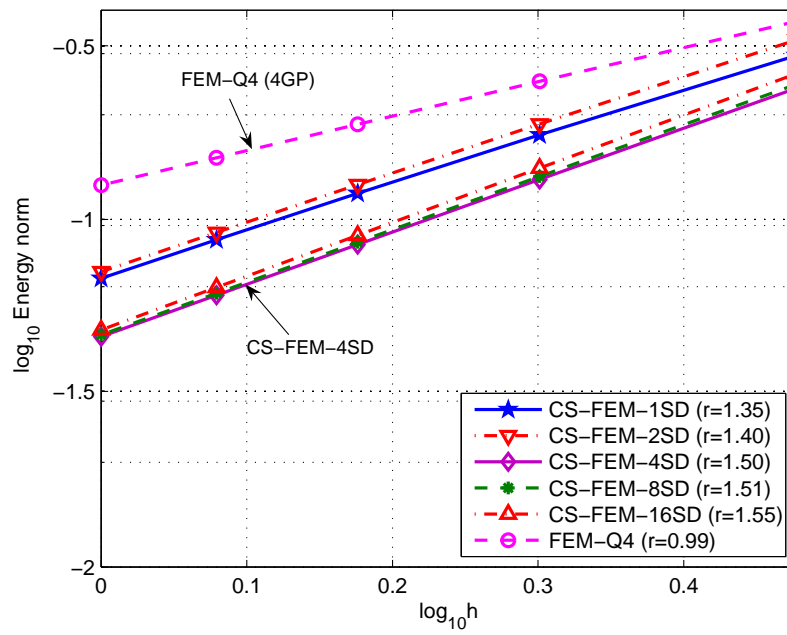


Figure 4.18. Error in energy norm of CS-FEM and FEM for the cantilever loaded at the end using the same meshes.

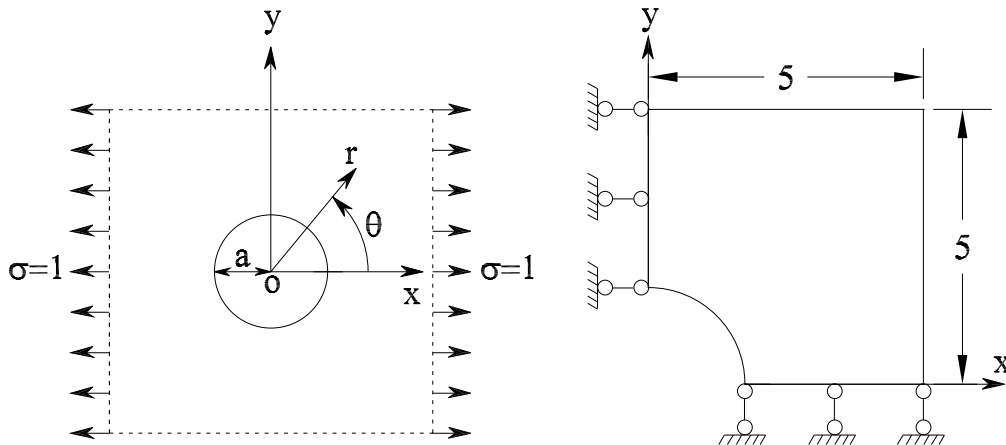


Figure 4.19. Infinite plate with a circular hole subjected to unidirectional tension and its quarter model with symmetric conditions imposed on the left and bottom edges.

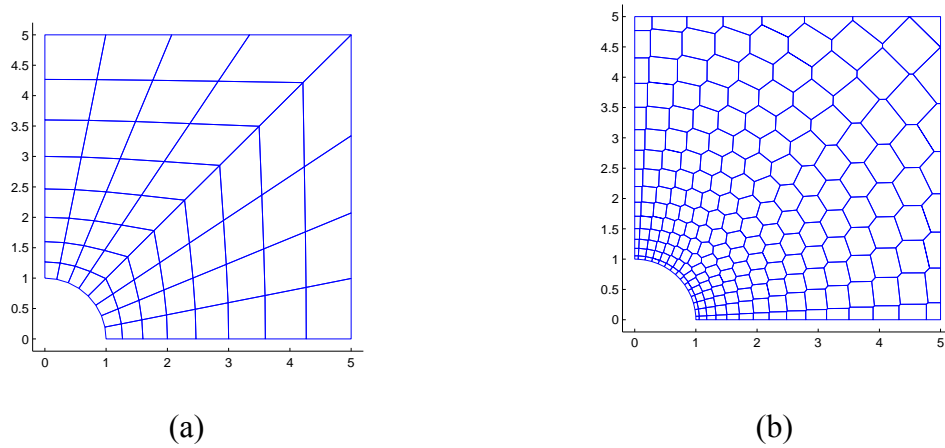


Figure 4.20. Domain discretization of the infinite plate with a circular hole (a) using 4-node elements; (b) using n -sided polygonal elements.

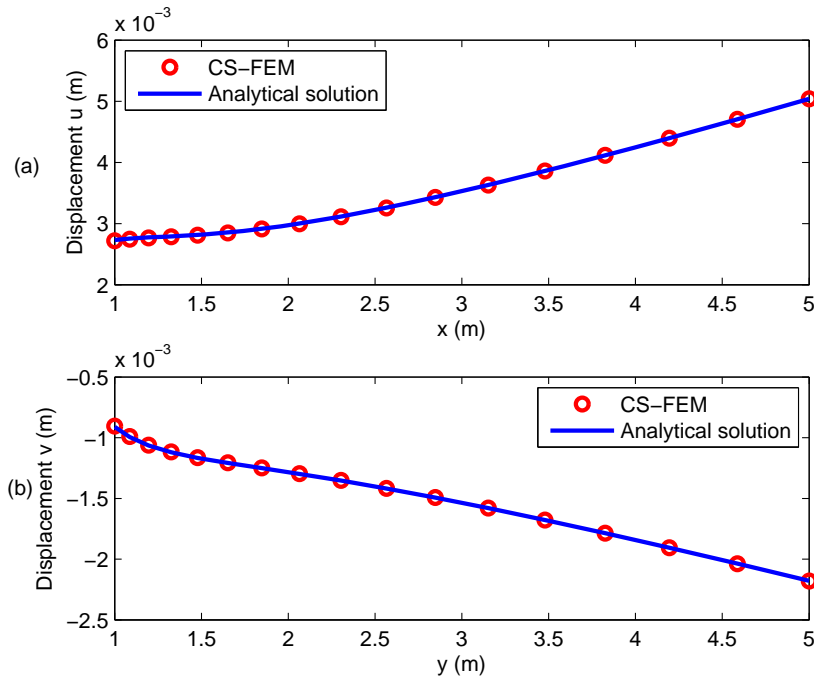


Figure 4.21. Numerical and exact displacements of the infinite plate with a hole using the CS-FEM ($n_s = 4$). (a) Displacement u ; (b) Displacement v .

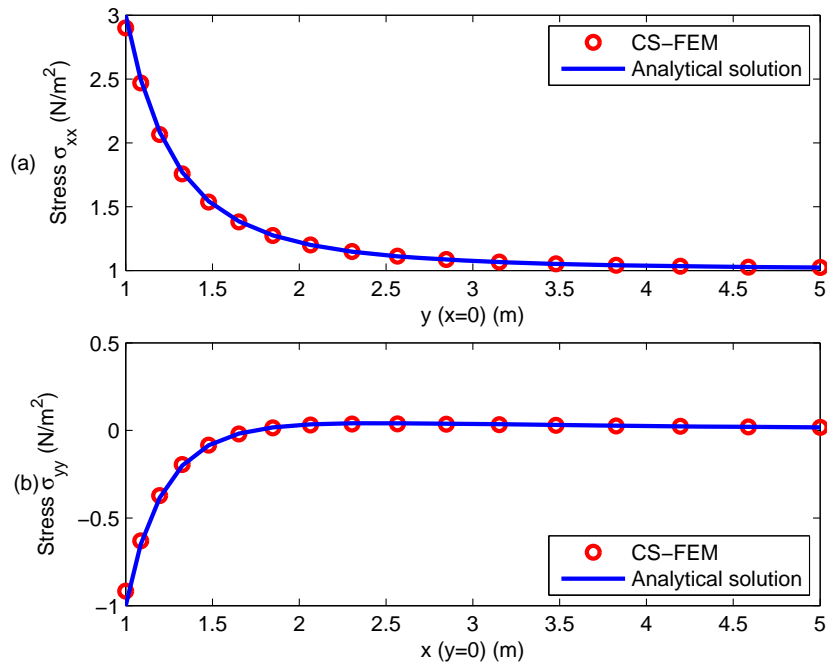


Figure 4.22. Numerical and exact stresses of the infinite plate with a hole using CS-FEM ($n_s = 4$). (a) σ_{xx} ; (b) σ_{yy} .

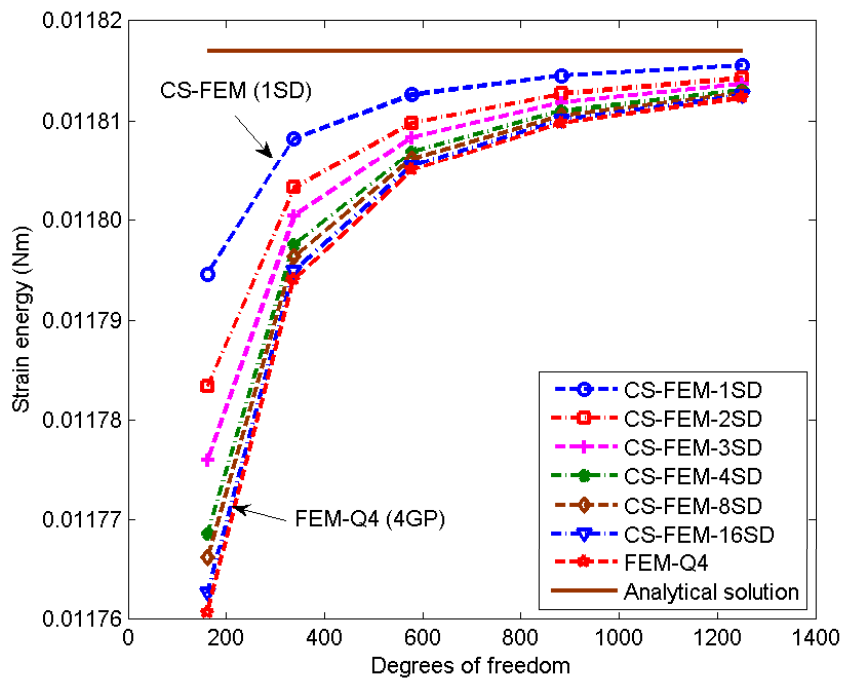


Figure 4.23. Convergence of strain energy solutions of CS-FEM and FEM for the infinite plate with a hole. The monotonic behavior of CS-FEM solution in strain energy is clearly shown.

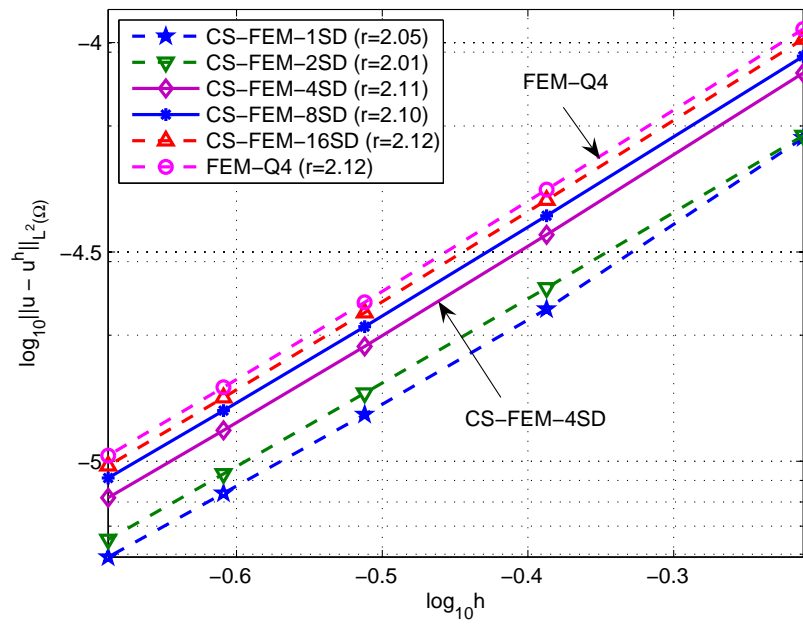


Figure 4.24. Convergence of error in displacement norm of CS-FEM and FEM in the infinite plate with a hole using the same meshes.

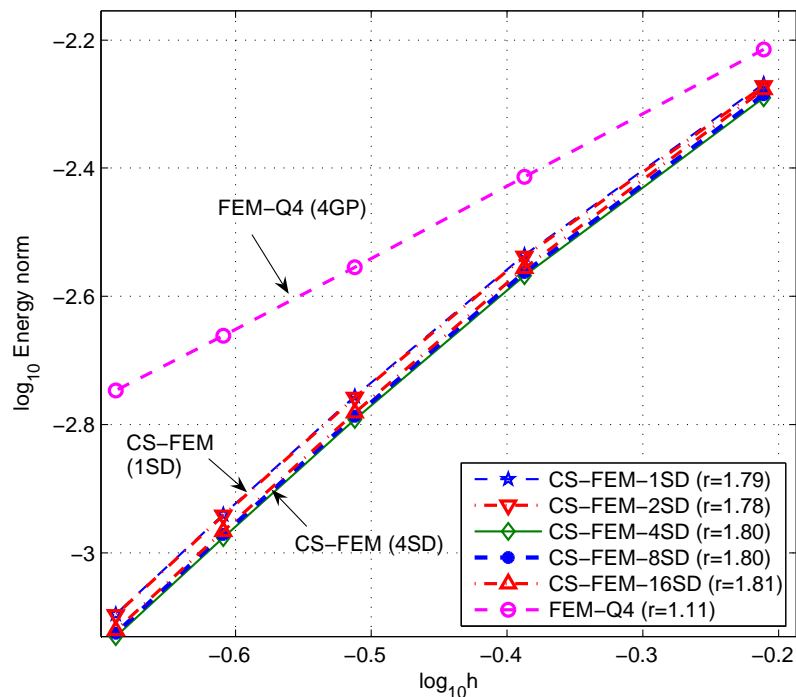


Figure 4.25. Convergence of error in energy norm of solutions obtained using the CS-FEM and FEM in the infinite plate with a hole using the same meshes.

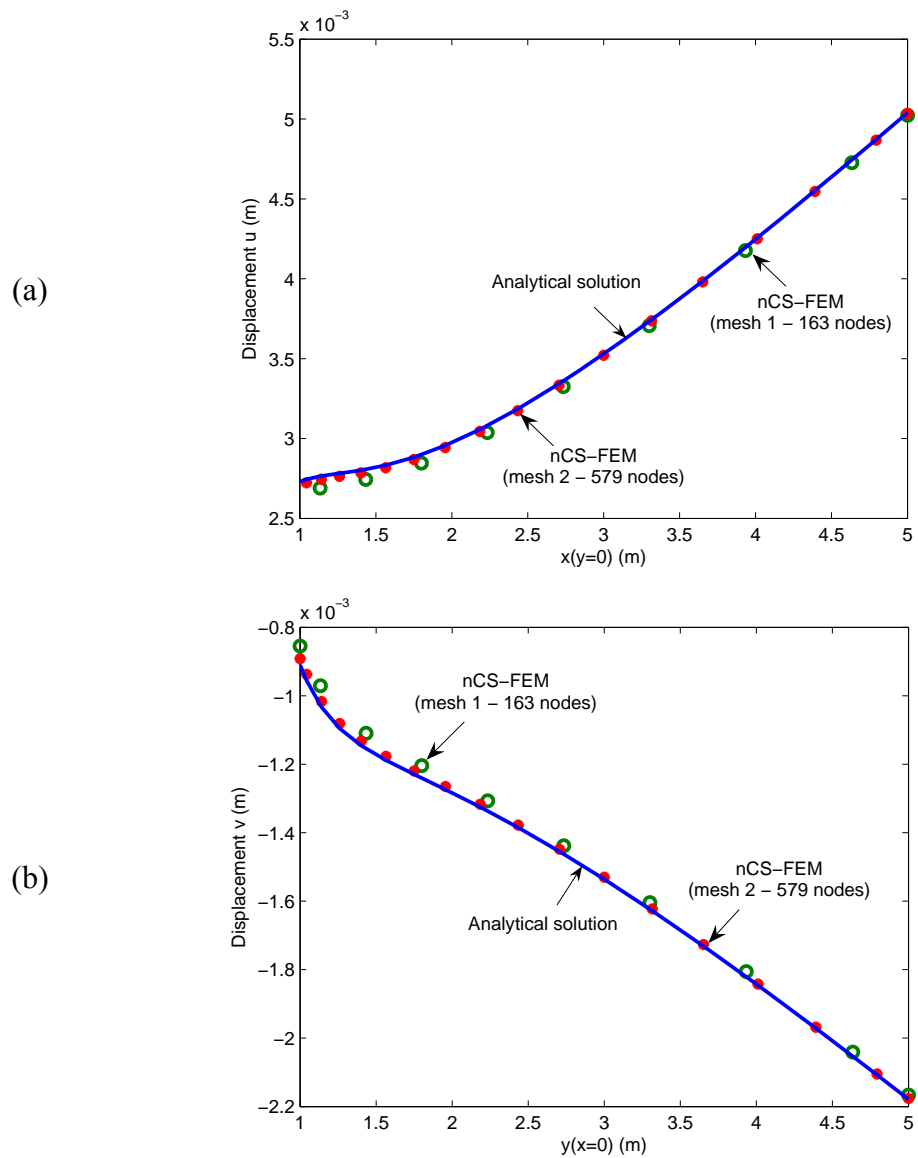


Figure 4.26. The exact displacement solution and the numerical solution computed using n CS-FEM for the infinite plate with a hole; (a) Displacement u ; (b) Displacement v .

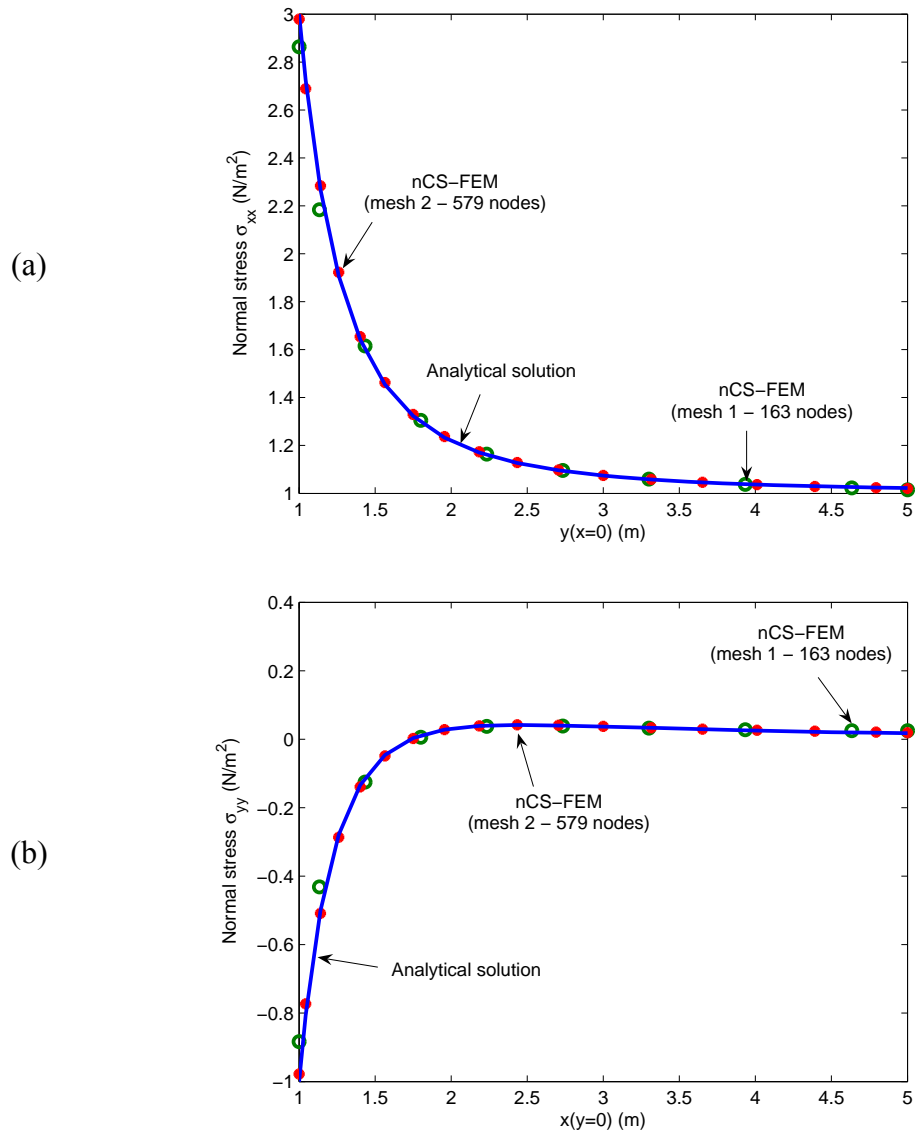


Figure 4.27. The exact solution of stresses and the numerical obtained using n CS-FEM for the infinite plate with a hole; (a) σ_{xx} ; (b) σ_{yy} .

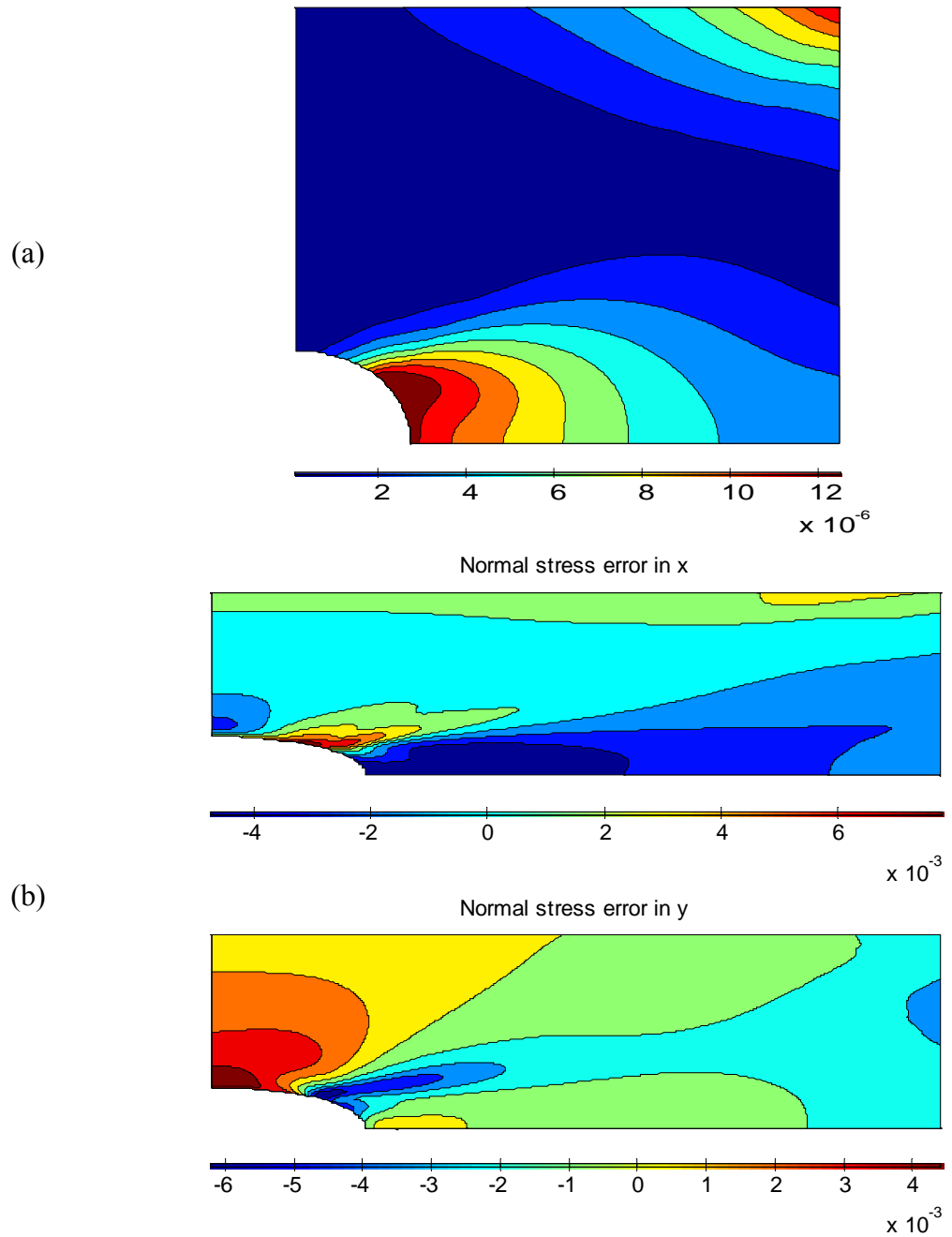


Figure 4.28. Contour plots of solutions for the infinite plate with a hole using n CS-FEM. (a) the error in displacement u ; (b) the normal stress errors σ_{xx} and σ_{yy} (N/m^2).

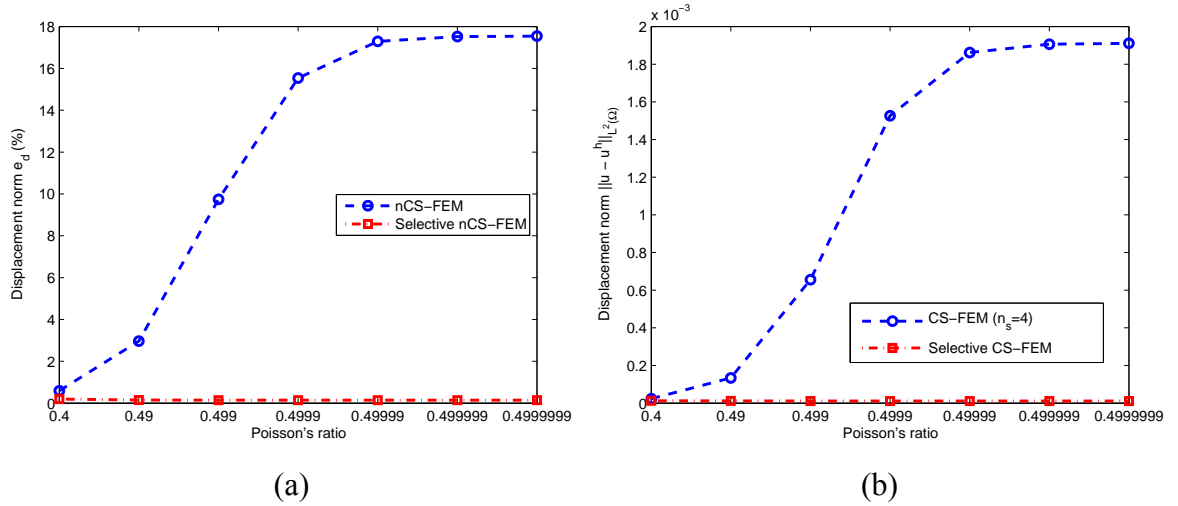


Figure 4.29. Error in displacement norm versus different Poisson's ratios of the infinite plate with a hole. (a) n -sided polygonal elements (451 nodes); (b) 4-node quadrilateral elements (289 nodes)

Chapter 5

Node-based Smoothed FEM (NS-FEM)

5.1 Introduction

In order to determine the error in numerical solutions of complicated problems without knowing the exact solution or to analyze the so-called duality in the FEM [4, 38, 151], it is practical to use two numerical models: one gives a lower bound and the other gives an upper bound of the unknown exact solution. This chapter discusses an S-FEM model that can be used for such a purpose. For the convenience in discussion, we focus on the so-called “force-driven” solid mechanics problems: boundary value problems with homogeneous Dirichlet (or essential) boundary conditions. For all the other types of problems, we will discuss in the conclusion section, after all these matters are settled.

For the above-mentioned force-driven problems, the most popular models giving a lower bound in term of strain energy are the compatible displacement FEM models which are widely used in solving complicated engineering problems. Obtaining an upper bound solution is, on the other hand, usually much more difficult, and many efforts have been made so far to overcome the difficulty. Currently, the model that can give an upper bound can be one of the following four models:

- (1) Model-1: the stress equilibrium FEM model [151];
- (2) Model-2: the recovery model using a statically admissible stress field from displacement FEM solution [32, 65, 66];

(3) Model-3: some hybrid equilibrium FEM models [3, 118];

(4) Model-4: Node-based S-FEM models [78, 83, 86].

Three first models, however, are known to have some major disadvantages. For Model-1, there are three main drawbacks: (1) the equilibrium approach is mathematically much more complicated and hence difficult to implement and more expensive computationally; (2) spurious modes often occur because tractions cannot be equilibrated by the approximated stress field; (3) it is complicated in solving an integral equation to obtain the displacement field from the stress solutions. For Model-2, there are two main drawbacks: (1) the procedure is complicated and expensive computationally; (2) it is difficult to obtain the desirable global errors due to the instability of the recovery upper bound solutions. For Model-3, there are three main drawbacks: (1) procedure is complicated and expensive computationally; (2) additional degrees of freedom are often required due to using both approximated displacement and stress variables; (3) there exist spurious modes in the hybrid models. Due to such drawbacks, three first models are not widely used in practical applications. It is still confined in the area of academic research.

Model-4 is considered the most simple, robust and practical techniques for obtain upper bounds for problems of all dimensions and of arbitrary complexity as long as triangular/tetrahedral types of mesh can be created. The development in this new direction originated from the recently discovery of the LC-PIM [83, 86] can produce upper bound solutions in strain energy for force-driven problems. The similar properties were later also found in the node-based S-FEM (NS-FEM) model using different types of elements [78]. This chapter is therefore devoted to the NS-FEM that is initially proposed in [78].

Apart from the important upper bound property in strain energy, the NS-FEM possesses also many other interesting properties that are similar to an equilibrium model such as the natural immunization from the volumetric locking, the ultra-accuracy and

super-convergence of stress solution. In addition, the NS-FEM works well with triangular and tetrahedral types of elements that can be generated automatically for 2D and 3D complicated geometries.

The formulation of the NS-FEM given in this chapter is first performed for 2D problems using in general arbitrary n -sided polygonal elements, and then in particular the triangular elements for 2D problems, and the tetrahedral elements for 3D problems. Finally, numerical examples will be presented to confirm the theory and to demonstrate the properties of the NS-FEM.

5.2 Creation of the node-based smoothing domains

In the NS-FEM, the domain is discretized using elements, as in the FEM, but the elements can be general polygons with arbitrary number of sides. On top of the element mesh, a set of non-overlap no-gap smoothing domains are then created associated with nodes, such that $\Omega = \sum_{k=1}^{N_n} \Omega_k^s$ and $\Omega_i^s \cap \Omega_j^s = \emptyset$, $i \neq j$, in which N_n is the total number of nodes in the element mesh. In this case, the number of smoothing domains are the same as the number of nodes: $N_s = N_n$, which satisfies the requirement of minimum number of smoothing domains given in [Table 3.2](#). The strain smoothing technique [24] is used to generate a modified strain field using the node-based smoothing domains and the assumed displacement field constructed using the element mesh. For n -sided polygonal elements, the smoothing domain Ω_k^s associated with the node k is created by connecting sequentially the mid-edge-point to the central points of the surrounding n -sided polygonal elements of the node k , as shown in [Figure 5.1](#). As a result, each n -sided polygonal element will be divided into n quadrilateral sub-domains and each sub-domain is attached

to the nearest field node. The domain Ω_k^s associated with the node k can also be viewed as the combination of the sub-domains of all the elements surrounding node k .

5.3 Formulation of the NS-FEM

5.3.1 General formulation

Using the general formulation of the S-FEM models presented in [Chapter 3, Section 3.1](#), the linear system of equations of the NS-FEM has the form of

$$\bar{\mathbf{K}}^{\text{NS-FEM}} \bar{\mathbf{d}} = \mathbf{f} \quad (5.1)$$

where $\bar{\mathbf{K}}^{\text{NS-FEM}}$ is the *smoothed* stiffness matrix whose entries are given by

$$\bar{\mathbf{K}}_{IJ}^{\text{NS-FEM}} = \int_{\Omega} \bar{\mathbf{B}}_I^T \mathbf{D} \bar{\mathbf{B}}_J d\Omega = \sum_{k=1}^{N_n} \int_{\Omega_k^s} \bar{\mathbf{B}}_I^T \mathbf{D} \underbrace{\bar{\mathbf{B}}_J}_{\text{constant in } \Omega_k^s} d\Omega = \sum_{k=1}^{N_n} \bar{\mathbf{B}}_I^T \mathbf{D} \bar{\mathbf{B}}_J A_k^s \quad (5.2)$$

where $A_k^s = \int_{\Omega_k^s} d\Omega$ is the area of node-based smoothing domain Ω_k^s , and the smoothed strain-displacement matrix $\bar{\mathbf{B}}_I$ is computed using Eq. (3.10). Now we need only the shape function values to obtain the smoothed strain-displacement matrix $\bar{\mathbf{B}}_I$. For general n -sided polygonal elements, shape functions values are obtained following the procedure given in Section 5.4.

5.3.2 NS-FEM-T3 for 2D problems

In particular, when linear triangular elements (T3) are used for 2D problems, the smoothed strain matrix $\bar{\mathbf{B}}_I$ can be assembled by another simply way using [78]

$$\bar{\mathbf{B}}_I(\mathbf{x}_k) = \frac{1}{A_k^s} \sum_{j=1}^{n_k^e} \frac{1}{3} A_j^e \mathbf{B}_j^e \quad (5.3)$$

where n_k^e is the number of elements around node k ; A_j^e is the area of the j^{th} triangular element around node k ; A_k^s is the area of the k^{th} smoothing domain and computed using

$$A_k^s = \int_{\Omega_k^s} d\Omega = \frac{1}{3} \sum_{j=1}^{n_k^e} A_j^e \quad (5.4)$$

In Eq. (5.3), matrix $\mathbf{B}_j^e = \sum_{I \in S_j^e} \mathbf{B}_I$ is the compatible strain-displacement matrix for the j^{th} triangular element around the node k . It is assembled from the compatible strain-displacement matrices $\mathbf{B}_I(\mathbf{x})$ of nodes in the set S_j^e which contains three nodes of the j^{th} triangular element. Matrix $\mathbf{B}_I(\mathbf{x})$ for the node I in triangular elements has the form of Eq. (2.48).

With this formulation, only the area and the usual compatible strain-displacement matrices \mathbf{B}_j^e of triangular elements are needed to calculate the system stiffness matrix for the NS-FEM-T3. The formulation is simple, but works only for triangular types of elements that use linear interpolation. For other NS-FEM models, the smoothed strain-displacement matrix $\bar{\mathbf{B}}_I$ has to be computed using the original Eq. (3.10), and the shape functions have to be evaluated in the way given in Section 5.4.

5.3.3 NS-FEM-T4 for 3D problems

The above formulation is quite straightforward to extend for 3D problems using 4-node tetrahedral elements (T4). The smoothed strain-displacement matrix $\bar{\mathbf{B}}_I(\mathbf{x}_k)$ for the NS-FEM-T4 is assembled using

$$\bar{\mathbf{B}}_I(\mathbf{x}_k) = \frac{1}{V_k^s} \sum_{j=1}^{n_k^e} \frac{1}{4} V_j^e \mathbf{B}_j^e \quad (5.5)$$

where V_j^e is the volume of the j^{th} tetrahedral element around the node k ; V_k^s is the volume of the k^{th} smoothing domain associated with node k , and is computed using

$$V_k^s = \int_{\Omega_k^s} d\Omega = \frac{1}{4} \sum_{j=1}^{n_k^e} V_j^e \quad (5.6)$$

In Eq. (5.5), matrix $\mathbf{B}_j^e = \sum_{I \in S_j^e} \mathbf{B}_I$ is the compatible strain-displacement matrix for the j^{th} tetrahedral element around the node k . It is assembled from the compatible strain-displacement matrices $\mathbf{B}_I(\mathbf{x})$ of nodes in the set S_j^e which contains four nodes of the j^{th} tetrahedral element. Matrix $\mathbf{B}_I(\mathbf{x})$ for the node I in tetrahedral elements has the form of

$$\mathbf{B}_I(\mathbf{x}) = \nabla_s \mathbf{N}_I(\mathbf{x}) = \begin{bmatrix} \frac{\partial N_I(\mathbf{x})}{\partial x} & 0 & 0 \\ 0 & \frac{\partial N_I(\mathbf{x})}{\partial y} & 0 \\ 0 & 0 & \frac{\partial N_I(\mathbf{x})}{\partial z} \\ \frac{\partial N_I(\mathbf{x})}{\partial y} & \frac{\partial N_I(\mathbf{x})}{\partial x} & 0 \\ 0 & \frac{\partial N_I(\mathbf{x})}{\partial z} & \frac{\partial N_I(\mathbf{x})}{\partial y} \\ \frac{\partial N_I(\mathbf{x})}{\partial z} & 0 & \frac{\partial N_I(\mathbf{x})}{\partial x} \end{bmatrix} \quad (5.7)$$

in which shape function $\mathbf{N}_I(\mathbf{x}) = \begin{bmatrix} N_I(\mathbf{x}) & 0 & 0 \\ 0 & N_I(\mathbf{x}) & 0 \\ 0 & 0 & N_I(\mathbf{x}) \end{bmatrix}$ satisfies the conditions (2.42).

With such a formulation, all we need is the volume and the usual compatible strain-displacement matrices \mathbf{B}_j^e of tetrahedral elements to compute the system stiffness matrix for the NS-FEM-T4. The formulation is simple, but works only for tetrahedral types of elements that use linear interpolation. For other NS-FEM models, the smoothed strain-displacement matrix $\bar{\mathbf{B}}_I$ has to be computed using the original Eq. (3.10), and the shape functions have to be evaluated in the way given in the next section.

5.4 Evaluation of the shape function values in the NS-FEM

For the NS-FEM using n -sided polygonal elements, the shape functions constructed in Chapter 3 (Section 3.2) can be used. When a linear compatible displacement field along

the boundary of the smoothing domains is used, the smoothed strain-displacement matrix $\bar{\mathbf{B}}_I$ can be computed using the shape function values at mid-segment-points (Gauss points) along segments $\Gamma_{k,p}^s \in \Gamma_k^s$ of the smoothing domains. The shape function values at each Gauss point are evaluated by averaging those of two related endpoints of the segment containing the Gauss point. For example, the values of the shape functions at point #a on the segment A-B shown in Figure 5.2, are evaluated as an average of those at two endpoints of the segment: points #A and #B. Therefore, in order to facilitate the evaluation of shape function values at Gauss points in the NS-FEM, we need first to evaluate the shape function values at the endpoints of segments such as mid-edge-points (#A, #C, #E, #G) and central points (#B, #D, #F, #H), as shown in Figure 5.2.

Figure 5.2 and Table 5.1 gives explicitly the shape function values at different points of the smoothing domain associated with node k . The number of support nodes for the smoothing domain is 11 including node k , and we have a total of 8 segments $\Gamma_{k,p}^s$ on Γ_k^s ($AB, BC, CD, DE, EF, FG, GH, HA$). Each segment needs only one Gauss point (due to linear interpolation), and therefore, there are a total of 8 Gauss points (a, b, c, d, e, f, g, h) used for the entire smoothing domain Ω_k^s , and the shape function values at these 8 Gauss points are tabulated in Table 5.1 by simple inspection.

It should be reminded that the purpose of introducing the central points and mid-edge-points is to facilitate the evaluation of the shape function values at these Gauss points. No extra degrees of freedom (DOFs) are associated with these points. In other words, these points carry no additional independent field variable. Therefore, the total DOFs of the NS-FEM will be exactly the same as those of the FEM using the same set of nodes.

It is easy to see that the bilinear and linear shape functions for 4-node quadrilateral and triangular elements of the standard FEM satisfy naturally the linear compatible property along the boundary of the smoothing domains. Hence, the NS-FEM can be applied easily

to the traditional 4-node quadrilateral or triangular elements. For the case of tetrahedral elements, the detailed formulation is given in Section 5.3.

5.5 Properties of the NS-FEM

The NS-FEM possesses some of the interesting properties of an equilibrium FEM model established based on the minimum complimentary energy principle [47].

Property 5.1: Upper bound property of the NS-FEM with respect to the exact solution

The numerical results have demonstrated that when a reasonably fine mesh is used to ensure sufficient smoothing effects to the model, the strain energy of numerical solution $\bar{E}_{\text{NS-FEM}}(\bar{\mathbf{d}})$ obtained from the NS-FEM solution has the following relationship with the total strain energy of exact solution E_{exact} .

$$\bar{E}_{\text{NS-FEM}}(\bar{\mathbf{d}}) \geq E_{\text{exact}}(\mathbf{u}) \quad (5.8)$$

where $\bar{\mathbf{d}}$ is the vector of the nodal displacements computed using an NS-FEM model; \mathbf{u} is the displacement of the exact solution of the same problem. The strain energy of the NS-FEM solution can be evaluated using

$$\bar{E}_{\text{NS-FEM}}(\bar{\mathbf{d}}) = \frac{1}{2} \bar{\mathbf{d}}^T \bar{\mathbf{K}}^{\text{NS-FEM}} \bar{\mathbf{d}} \quad (5.9)$$

where $\bar{\mathbf{K}}^{\text{NS-FEM}}$ is the system stiffness matrix of the NS-FEM. The strain energy of the exact solution can be computed using

$$E_{\text{exact}} = \int_{\Omega} (\boldsymbol{\varepsilon}(\mathbf{u}))^T \mathbf{D} \boldsymbol{\varepsilon}(\mathbf{u}) d\Omega = \frac{1}{2} \sum_{i=1}^{N_e} \int_{\Omega_i^e} (\boldsymbol{\varepsilon}_i^e)^T \mathbf{D} \boldsymbol{\varepsilon}_i^e d\Omega \quad (5.10)$$

where $\boldsymbol{\varepsilon}(\mathbf{u})$ is the exact strain field obtained using the exact displacement field \mathbf{u} , and $\boldsymbol{\varepsilon}_i^e$ is the exact strain solution of the i^{th} element.

A detailed discussion on the upper bound property, Eq. (5.8), for the general LC-PIM model can be found in Ref [83].

Property 5.2: The NS-FEM is naturally immune from the volumetric locking, and no special treatments are needed for solids of nearly incompressible materials.

Property 5.3: The recovery stress field constructed using the stresses at nodes are ultra-accurate and super-convergent. This continuous recovery stress field can be used as a representation of exact stress field in the adaptive analysis [105].

Property 5.4: The accuracy of displacement solutions in the NS-FEM is not particularly high. It is at the same level as that of the standard FEM using the same mesh.

5.6 Numerical implementation

5.6.1 Rank test for the stiffness matrix: stability analysis

Property 5.5: The NS-FEM possesses only “legal” zero energy modes that represents the rigid motions, and there exists no spurious zero-energy mode. This means that the NS-FEM is spatially stable.

This is ensured by the following key reasons:

- i) The NS-FEM satisfies the minimum number of smoothing domains N_s^{\min} for any problems presented in [Section 3.3](#). This can be easily confirmed, because $N_s = N_n$.
- ii) Even at the individual element level, the numerical integration used to evaluate Eq. (5.2) in the possible NS-FEM models satisfies the necessary condition to ensure the method to be stable as given in Table 5.2.
- iii) The shape functions used in the NS-FEM are of partitions of unity, ensuring a proper representation of rigid movements.
- iv) Because each of the smoothing domains are created for different node, they are linearly independent, which ensures linearly independent columns in the smoothed

strain matrix, and hence in the smoothed stiffness matrix. Hence the stiffness matrix in a NS-FEM model is SPD for stable materials, after the rigid motion is fixed.

Therefore, the NS-FEM will have proper number of zero eigenmodes representing the rigid body movements, and will not have any spurious zero-energy modes. In other words, any deformation (except the rigid motions) will result in strain energy in an NS-FEM model, implying that it will be stable.

Note that although the NS-FEM is spatially stable, this does not guarantee the *temporal* stability. In fact it can have nonzero-energy spurious modes, and can be temporally unstable, which will be discussed in more detail in [Chapter 6](#).

5.6.2 Standard 2D patch tests

In this standard 2D patch test, we use a square patch. The patch is first discretized by using 36 n -sided polygonal elements is shown in [Figure 4.6](#). We then create a set of smoothing domains following the procedure described in Section 5.2. The linear displacement field is then specified on all the boundaries of the patch using [Eq. \(4.13\)](#). The NS-FEM is used to solve this patch test problem for numerical solutions. The error norm in displacements [\(4.12\)](#) is used to examine the computed results. The material parameters are taken as $E = 100$, $\nu = 0.3$. It is found that the NS-FEM can pass the standard patch test within machine precision with the error norm in displacements of $e_d = 5.22 \text{ e-}13$ (%).

5.6.3 Standard 3D patch tests and a mesh sensitivity analysis

This 3D standard patch test is known also as the Irons first-order patch test. We perform this test using a cubic patch, and it is conducted together with a mesh sensitivity analysis. The patch is first discretized with a number of tetrahedral elements with N_n

nodes, in the same way as in the FEM. Linear displacements are imposed along all the exterior boundaries of the cubic patch with at least one interior node. Same as the 2D patch test, satisfaction of the patch test requires that the displacements of all the interior nodes follow “exactly” (to machine precision) the same linear function of the imposed displacements, and the constant strain/stress status in the 3D patch are reproduced.

The material parameters used in this patch test are $E = 6.895 \times 10^6 \text{ kPa}$, $\nu = 0.25$, and the linear displacement field is specified by

$$\begin{aligned} u &= 0.001 * (2x + y + z) / 2 \\ v &= 0.001 * (x + 2y + z) / 2 \\ w &= 0.001 * (x + y + 2z) / 2 \end{aligned} \quad (5.11)$$

The error norm in displacement (4.12) can be used to examine the computed results. For this 3D patch test, we use the energy error measure defined by

$$e_e = \left| \bar{E}_{\text{NS-FEM}} - E_{\text{exact}} \right| \quad (5.12)$$

where the total strain energy of the exact solution E_{exact} is evaluated using

$$E_{\text{exact}} = \frac{1}{2} \boldsymbol{\varepsilon}^T \mathbf{D} \boldsymbol{\varepsilon} V_{\text{cubic}} \quad (5.13)$$

in which the constant exact strains $\boldsymbol{\varepsilon}$ are used, and V_{cubic} is the volume of the cubic patch.

The total strain energy of the numerical solution $\bar{E}_{\text{NS-FEM}}$ can be evaluated using

$$\bar{E} = \frac{1}{2} \sum_{k=1}^{N_n} (\bar{\boldsymbol{\varepsilon}}_k)^T \mathbf{D} \bar{\boldsymbol{\varepsilon}}_k V_k^s \quad (5.14)$$

where $\bar{\boldsymbol{\varepsilon}}_k$ is the strain for the k^{th} node obtained using an NS-FEM model, and V_k^s is the volume of the k^{th} smoothing domain used in the patch.

Figure 5.3 shows the cubic patch with dimension of 10 by 10 by 10. The patch is discretized using 29 four-node tetrahedral elements and 15 nodes (including 8 nodes at the corners, 6 nodes at the center of 6 patch surfaces and 1 interior node), as shown in

Figure 5.3. In order to analyze the sensitivity of the results to mesh distortion, the interior node is moved randomly inside the cubic from the center point in the following fashion

$$\begin{aligned}x' &= x + \Delta x \cdot r_x \cdot \alpha_{ir} \\y' &= y + \Delta y \cdot r_y \cdot \alpha_{ir} \\z' &= z + \Delta z \cdot r_z \cdot \alpha_{ir}\end{aligned}\tag{5.15}$$

where x , y and z are the coordinates at the center point of the cubic patch; Δx , Δy and Δz are length of the cubic patch in x -, y - and z - directions, respectively; r_x , r_y and r_z are the computer-generated random numbers between -1.0 and 1.0 and α_{ir} is a prescribed irregularity factor chosen between 0.0 and 0.49. When $\alpha_{ir} = 0.0$, the interior node locates at the center point of the cubic patch, and when $\alpha_{ir} > 0.0$, the interior node moves randomly inside the cubic patch. The bigger the value of α_{ir} is, the more irregular the shape of elements is generated. At $\alpha_{ir} = 0.49$ the interior node is almost touching the surface.

It is found that the NS-FEM-T4 using tetrahedral elements can pass the Irons first-order patch test within machine precision regardless of the value α_{ir} used, as shown in Table 5.3. There is no accuracy loss due to the different choices of α_{ir} values: these errors are all within the machine precision. This shows that the NS-FEM-T4 can work well with severely distorted meshes.

5.7 Numerical examples

In this section, some example problems will be analyzed to demonstrate numerically the properties of the NS-FEM. For 2D problems, three kinds of elements are used: n -sided polygonal, 4-node quadrilateral and triangular elements. For 3D problems, only tetrahedral elements are used. In the discussions, the results of the NS-FEM using n -sided

polygonal elements (n NS-FEM) will be compared with those of the cell-based smoothed FEM using n -sided polygonal elements (n CS-FEM) that detailed in Chapter 4. The results of the NS-FEM using 4-node quadrilateral elements (NS-FEM-Q4) and triangular elements (NS-FEM-T3) will be compared with those of the standard FEM using quadrilateral elements (FEM-Q4), triangular elements (FEM-T3) and the CS-FEM using 4 smoothing domains for each element (CS-FEM-Q4). The results of the NS-FEM using tetrahedral elements (NS-FEM-T4) will be compared with those of the standard displacement FEM using 4-node tetrahedral elements (FEM-T4) and 8-node hexahedral elements (FEM-H8).

The error measure for the displacement and energy norms defined in Eqs. (4.18) and (4.19) will be used in the quantitative examination of the performance of these methods. In the calculation of Eq. (4.19) for the NS-FEM-Q4, NS-FEM-T3 and NS-FEM-T4, a computable recovery strain field $\bar{\boldsymbol{\epsilon}}^R$ will be used in place of the general numerical strain field $\tilde{\boldsymbol{\epsilon}}$. For the NS-FEM-Q4, the recovery strain field $\bar{\boldsymbol{\epsilon}}^R$ is defined in Eq. (4.20). For the NS-FEM-T3, $\bar{\boldsymbol{\epsilon}}^R$ is defined by

$$\bar{\boldsymbol{\epsilon}}^R = \sum_{j=1}^3 \mathbf{N}_j(\mathbf{x}) \bar{\boldsymbol{\epsilon}}(\mathbf{x}_j) \quad (5.16)$$

where $\mathbf{N}_j(\mathbf{x})$ are the same linear shape functions of triangular elements in the standard FEM, and $\bar{\boldsymbol{\epsilon}}(\mathbf{x}_j)$ is the smoothed strains at three nodes \mathbf{x}_j of the triangular element. For the NS-FEM-T4, $\bar{\boldsymbol{\epsilon}}^R$ is defined by

$$\bar{\boldsymbol{\epsilon}}^R = \sum_{j=1}^4 \mathbf{N}_j(\mathbf{x}) \bar{\boldsymbol{\epsilon}}(\mathbf{x}_j) \quad (5.17)$$

where $\mathbf{N}_j(\mathbf{x})$ are the linear shape functions of tetrahedral elements in the standard FEM, and $\bar{\boldsymbol{\epsilon}}(\mathbf{x}_j)$ is the smoothed strains at four nodes \mathbf{x}_j of the tetrahedral element.

Note that the convergence rates of the displacement and energy norms evaluated with respect to the ‘‘averaged’’ length of sides of elements. For the quadrilateral elements, the

average length of sides of elements is evaluated by Eq. (4.21). For the triangular elements, h is evaluated by

$$h = \sqrt{\frac{2A_{\Omega}}{N_e}} \quad (5.18)$$

For the tetrahedral elements, h is evaluated by

$$h = \sqrt[3]{\frac{6V_{\Omega}}{N_e}} \quad (5.19)$$

and for the hexahedral elements, h is evaluated by

$$h = \sqrt[3]{\frac{V_{\Omega}}{N_e}} \quad (5.20)$$

where V_{Ω} is the volume of the whole problem domain.

Note that the averaged lengths of sides of elements h by Eq. (4.21), (5.18), (5.19), (5.20) for the corresponding elements will also be used for all following chapters in this thesis as well.

5.7.1 A rectangular cantilever loaded at the end

The rectangular cantilever loaded at the end described in Example 4.10.1 is used again in this examination. The geometry and boundary conditions of the cantilever are plotted in Figure 4.7. The problem domain discretizations with n -sided polygonal, quadrilateral and triangular elements are shown in Figure 4.8 and Figure 5.4, respectively. The exact strain energy of the problem is known as 4.4746 Nm.

Figure 5.5 shows that the stresses computed using the NS-FEM-T3 and NS-FEM-Q4 agree well with the analytical solutions. Figure 5.6 shows the overall comparison of the stress distribution obtained using the n NS-FEM and the exact formulae. A very good agreement has been observed. The numerical results of strain energy are presented in Table 5.4, Table 5.5 and plotted in Figure 5.7 against the degrees of freedom, revealing the convergence of the solution of all models used. It can be found that the n NS-FEM, NS-FEM-Q4 and NS-FEM-T3 give upper bound solutions in the strain energy, i.e., the

strain energies of the n NS-FEM, NS-FEM-Q4 and NS-FEM-T3 are always bigger than the exact one and converge to it with the increase of degrees of freedom. In contrast, the n CS-FEM, FEM-Q4 and FEM-T3 produce the lower bound solutions in the strain energy. These results imply that we now have a very simple procedure to determine upper and lower bounds in strain energy of the exact solution, by using the NS-FEM together the CS-FEM or FEM using the same meshes.

Table 5.6 and Figure 5.8 compare the solution error in displacement norm obtained using the NS-FEM-T3 and NS-FEM-Q4, together with those of the FEM and CS-FEM-Q4. It is seen that the CS-FEM-Q4 stands out clearly. When the finest mesh ($h = 1$) is used, the error of the CS-FEM-Q4 is about $1/28$ of the FEM-T3 and $1/4$ of the FEM-Q4. The error of the NS-FEM-T3 is about $3/5$ of the FEM-T3. The error of the NS-FEM-Q4 is about 2 times of the FEM-Q4, but only $1/2$ of the NS-FEM-T3. In terms of convergence rate, all the models have a numerical rate slightly below the theoretical value of 2.0. All the S-FEM models performed generally only slightly better than the FEM counterparts.

Table 5.7 and Figure 5.9 compare the results of energy norm of the NS-FEM-T3 and NS-FEM-Q4, together with those of the FEM and CS-FEM-Q4. It is seen that the NS-FEM-T3 and NS-FEM-Q4 stand out clearly. When the finest mesh ($h = 1$) is used, the error of the NS-FEM-T3 solution is about $1/8$ of the FEM-T3 and even $1/3$ of the FEM-Q4. The NS-FEM-Q4 performed better than the NS-FEM-T3, but only by a small margin. In terms of convergence rate, all the S-FEM models performed much better than the FEM models, and all significantly above 1.0 that is the theoretical value of the weak formulation. This shows that the S-FEM models are super-convergent. The CS-FEM-Q4 stands out clearly with a rate of 1.5: a very strong super-convergence.

In overall, the CS-FEM-Q4 performed best for this problem. However, considering the mesh generation issues and accuracy in stress (measured by energy norm), the NS-FEM-

T3 is preferred, because it performed among the bests, but uses only triangular mesh. In addition, the NS-FEM-T3 delivers an upper bound solution.

From this example we also note that the NS-FEM-T3 and NS-FEM-Q4 possess three interesting properties similar to those of an equilibrium FEM model: (1) the strain energy is an upper bound of the exact solution; (2) the stress solutions are ultra-accurate and super-convergent; (3) the displacement solutions are not so significantly more accurate but are still better than that of FEM-T3.

5.7.2 Infinite plate with a circular hole

The infinite plate with a circular hole described in [Example 4.10.2](#) is used again to examine the NS-FEM models. The geometry and boundary conditions of the problem is plotted in [Figure 4.19](#). [Figure 4.20](#) and [Figure 5.10](#) give, respectively, the discretization of the domain using 4-node quadrilateral, n -sided polygonal and triangular elements. The exact strain energy of the problem is known as 1.1817×10^{-2} Nm.

The numerical results of strain energy have been presented in [Table 5.8](#), [Table 5.9](#) and plotted in [Figure 5.11](#) against the degrees of freedom, revealing the convergence of the solution of all models used. It again shows the upper bound property in the strain energy of the n NS-FEM, NS-FEM-Q4 and NS-FEM-T3, together with the lower bound property of the n CS-FEM, FEM-Q4 and FEM-T3. From [Figure 5.12](#) and [Figure 5.13](#), it is observed that all the computed displacements and stresses of the n NS-FEM using n -sided polygonal elements are all in a very good agreement with the analytical solutions. With the refinement of the mesh, the accuracy is getting higher and higher.

[Table 5.10](#) and [Figure 5.14](#) compare the results of displacement norm of the NS-FEM-T3 and NS-FEM-Q4 with those of the FEM and CS-FEM-Q4. It is again seen that the CS-FEM-Q4 stands out clearly. When the finest mesh ($h = 0.1969$) is used, the error of the CS-FEM-Q4 is about 1/5 of the FEM-T3 and 4/5 of the FEM-Q4. The NS-FEM-T3

performed better than the FEM-T3, but only by a small margin. The error of the NS-FEM-Q4 is about 3 times of the FEM-Q4, but only 4/5 of the NS-FEM-T3. In terms of convergence rate, except the FEM-T3, other models have a numerical rate slightly larger than the theoretical value of 2.0.

Table 5.11 and Figure 5.15 compare the results of energy norm of the NS-FEM-T3 and NS-FEM-Q4 with those of the FEM and CS-FEM-Q4. It is again seen that the NS-FEM-T3 and NS-FEM-Q4 stand out clearly. When the finest mesh ($h = 0.1969$) is used, the error of the NS-FEM-T3 is about 1/9 of the FEM-T3 and even 1/5 of the FEM-Q4. The NS-FEM-Q4 performed better than the NS-FEM-T3, but only by a small margin. In terms of convergence rate, all the S-FEM models performed much better than the FEM models, and all close to 2.0 and significantly above 1.0 that is the theoretical value of the weak formulation. This again shows that the S-FEM models are super-convergent. The NS-FEM-Q4 stands out clearly with a rate of 2.12: a very strong super-convergence.

Figure 5.16 plots the error in solution in displacement norm against Poisson's ratio changing from 0.4 to 0.4999999 obtained using FEM and NS-FEM models. Two types of element meshes are used in this study: n -sided polygonal elements (579 nodes) and for 4-node quadrilateral elements (mesh 16×16). In computing the displacement norm, we use Eq. (4.18) for the 4-node quadrilateral elements, and Eq. (4.27) for n -sided polygonal elements. The results show that the n NS-FEM and NS-FEM-Q4 is naturally immune from the volumetric locking: the error does not increase with the Poisson's ratio approaches to 0.5. The n CS-FEM and FEM-Q4 are subjected to volumetric locking resulting in a drastic accuracy lose in the numerical solutions, when the Poisson's ratio approaches 0.5.

In overall, it is again seen that NS-FEM models possess four interesting properties of an equilibrium FEM model: (1) the strain energy is an upper bound of the exact solution; (2) it is immune naturally from the volumetric locking; (3) the stress solutions are ultra-

accurate and super-convergent; (4) the displacement solutions are at the same level as that of FEM-T3 using the same distribution of nodes.

5.7.3 3-D Lamé problem (hollow sphere problem)

The 3-D Lamé problem consist of a hollow sphere with inner radius $a=1\text{m}$, outer radius $b=2\text{m}$ and subjected to internal pressure $P=100\text{N/m}^2$, as shown in Figure 5.17. The analytical solution of the benchmark problem is available in polar coordinate system [148]

$$u_r = \frac{Pa^3r}{E(b^3 - a^3)} \left[(1 - 2\nu) + (1 + \nu) \frac{b^3}{2r^3} \right] \quad (5.21)$$

$$\sigma_r = \frac{Pa^3(b^3 - r^3)}{r^3(a^3 - b^3)} \quad ; \quad \sigma_\theta = \frac{Pa^3(b^3 + 2r^3)}{2r^3(b^3 - a^3)} \quad (5.22)$$

where r is the radial distance from the centroid to the point of interest of the sphere.

As the problem is spherically symmetrical, only one-eighth of the sphere shown in Figure 5.17 is modeled, and the symmetry conditions are imposed on the three cutting symmetric planes. The material parameters of the problem are $E = 10^3 \text{N/m}^2$ and $\nu=0.3$.

From Figure 5.18, it is observed that all the computed displacements and stresses of the NS-FEM-T4 agree well with the analytical solutions. Table 5.12 and Figure 5.19 show the upper bound property in the strain energy of the NS-FEM-T4, while the FEM-T4 and FEM-H8 give the lower bounds.

Table 5.13 and Figure 5.20 compare the solution error in displacement norm obtained using the NS-FEM-T4, together with those of the FEM-T4 and FEM-H8. It is seen that the FEM-H8 stands out clearly. When the 3rd fine mesh for both T4 and H8 ($h \approx 0.156$) is used, the error of the FEM-H8 is about 1/3 of the NS-FEM-T4. The NS-FEM-T4 performed better than the FEM-T4, but only by a small margin. In terms of convergence rate, all the models have a numerical rate of around the theoretical value of 2.0.

Table 5.14 and Figure 5.21 compare the results of energy norm of the NS-FEM-T4, together with those of the FEM-T4 and FEM-H8. It is again seen that the NS-FEM-T4 stand out clearly. When the 3rd fine mesh for both T4 and H8 ($h \approx 0.156$) is used, the error of the NS-FEM-T4 is about 2/7 of the FEM-T4 and 2/5 of the FEM-H8. In terms of convergence rate, the NS-FEM-T4 stands out clearly with a rate of 1.34, while the rates of both FEM-T4 and FEM-H8 are slightly below the theoretical value of 1.0.

Figure 5.22 plots the error in displacement norm against Poisson's ratio changing from 0.4 to 0.4999999 by using tetrahedral elements (507 nodes). The results show that the NS-FEM-T4 is naturally immune from the volumetric locking, while the FEM-T4 is subjected to the volumetric locking resulting in a drastic accuracy lose in the numerical solutions.

In overall, it is again seen that the NS-FEM-T4 model also possesses four interesting properties that are similar to an equilibrium FEM model: (1) the strain energy is an upper bound of the exact solution; (2) it is immune naturally from the volumetric locking; (3) the stress solutions are ultra-accurate and super-convergent; (4) the displacement solutions are at the same level as that of FEM-T4 using the same mesh.

5.7.4 3D cubic cantilever: an analysis about the upper bound property

Consider a 3D cantilever of cubic shape, subjected to a uniform pressure on its upper face as shown in Figure 5.23. The exact solution of the problem is unknown. By incorporating the solutions of hexahedral super-element elements and the procedure of Richardson's extrapolation, Almeida Pereira [5] gave an approximation of the exact strain energy to be 0.950930. In addition, using standard FEM and a very fine mesh with 30,204 nodes and 20,675 ten-node tetrahedron elements, another reference solution of the strain energy is 0.9486. From this reference, the deflection at point A (1.0,1.0,-0.5) is 3.3912.

Table 5.15 and Figure 5.24 confirm the upper bound property on the strain energy of the NS-FEM-T4 and the lower bound property of the FEM-T4 and FEM-H8 for this 3D problem. Table 5.16 and Figure 5.25 show the convergence of deflection at point A (1.0,1.0,-0.5). The results also show the upper bound property for the displacement solution of the NS-FEM-T4 and the lower bound property of the FEM-T4 and FEM-H8.

5.7.5 A 3D L-shaped block: an analysis about the upper bound property

Consider the 3D square block with a cubic hole subjected to the surface traction q as shown in Figure 5.26. Due to the double symmetry of the problem, only a quarter of the domain is modeled, which becomes a 3D L-shaped block. The analysis is performed using input data: $q = 1$, $a = 1$, $E = 1$, $\nu = 0.3$. For this problem, the strain energy of 6.1999 given by Cugnon [34] is considered as the reference solution. In addition, using standard FEM and a very fine mesh with 33,641 nodes and 22,862 ten-node tetrahedron elements, another reference solution of the strain energy has been found to be 6.1916.

Again, Table 5.17 and Figure 5.27 confirm the upper bound property on the strain energy of the NS-FEM-T4 and the lower bound property of the FEM-T4 for 3D problems.

5.8 Remarks

In this chapter, a node-based S-FEM (NS-FEM) for upper bound solutions to solid mechanics problems is presented. Through the formulation, theoretical discussions, and numerical results, some conclusions can be drawn as follows:

- The NS-FEM allows the use of general polygonal elements with an arbitrary number of sides. The method can be applied easily to traditional 4-node quadrilateral or triangular elements. It works well with triangular elements for 2D problems, and with tetrahedral elements for 3D problems.

- In the NS-FEM, smoothed strain field are computed directly using only the shape functions at Gauss points along segments of boundary of the smoothing domains. The evaluation of shape function values for the discrete points can be performed in a simple manner for all types of meshes. The numerical implementation of the NS-FEM is straightforward and much simpler than that of equilibrium FEM models.
- The NS-FEM is a displacement model, using only displacements as unknowns. It, however, possesses interesting properties that are quite similar to those of an equilibrium FEM model such as: (1) the upper bound property of the strain energy, when a reasonably fine mesh is used for force driven problems; (2) natural immunization from the volumetric locking; (3) ultra-accuracy and super-convergence of stress solutions; (4) similar accuracy of displacement solutions compared to the standard FEM model. In fact, at any point in all these smoothing domains, the equilibrium equations are satisfied in an NS-FEM model. It is however not an equilibrium model because the stresses right on these interfaces of the smoothing domains are not in equilibrium. Therefore, it is said a quasi-equilibrium model. For *displacement driven* problems (zero external forces but nonzero prescribed displacement on the essential boundary), we expect the FEM and NS-FEM to swap their roles: the NS-FEM gives the lower bound and the FEM gives the upper bound. For general problems with mixed force and displacement boundary conditions, we can still expect these two models bound the exact solution from both sides, although which model is on which side will be problem dependent.
- From the upper bound property of the strain energy of the NS-FEM, a simple and practical procedure is proposed to determine both upper and lower bounds in the strain energy, by combining the NS-FEM with the FEM (for triangular, quadrilateral, or tetrahedral elements) or with the n CS-FEM (for n -sided polygonal elements).

*Table 5.1. Shape function values at different sites
on the smoothing domain boundary for node k (cf. Figure 5.2)*

Site	Node k	Node 1	Node 2	Node 3	Node 4	Node 5	Node 6	Node 7	Node 8	Node 9	Node 10	Description
k	1.0	0	0	0	0	0	0	0	0	0	0	Field node
1	0	1.0	0	0	0	0	0	0	0	0	0	Field node
2	0	0	1.0	0	0	0	0	0	0	0	0	Field node
3	0	0	0	1.0	0	0	0	0	0	0	0	Field node
4	0	0	0	0	1.0	0	0	0	0	0	0	Field node
5	0	0	0	0	0	1.0	0	0	0	0	0	Field node
6	0	0	0	0	0	0	1.0	0	0	0	0	Field node
7	0	0	0	0	0	0	0	1.0	0	0	0	Field node
8	0	0	0	0	0	0	0	0	1.0	0	0	Field node
9	0	0	0	0	0	0	0	0	0	1.0	0	Field node
10	0	0	0	0	0	0	0	0	0	0	1.0	Field node
A	1/2	1/2	0	0	0	0	0	0	0	0	0	Mid-edge
B	1/3	1/3	1/3	0	0	0	0	0	0	0	0	Centroid of element
C	1/2	0	1/2	0	0	0	0	0	0	0	0	Mid-edge
D	1/4	0	1/4	1/4	1/4	0	0	0	0	0	0	Centroid of element
E	1/2	0	0	0	1/2	0	0	0	0	0	0	Mid-edge
F	1/6	0	0	0	1/6	1/6	1/6	1/6	1/6	0	0	Centroid of element
G	1/2	0	0	0	0	0	0	0	1/2	0	0	Mid-edge
H	1/5	1/5	0	0	0	0	0	0	1/5	1/5	1/5	Centroid of element
a	5/12	5/12	1/6	0	0	0	0	0	0	0	0	Mid-segment of $\Gamma_{k,p}^s$
b	5/12	1/6	5/12	0	0	0	0	0	0	0	0	Mid-segment of $\Gamma_{k,p}^s$
c	3/8	0	3/8	1/8	1/8	0	0	0	0	0	0	Mid-segment of $\Gamma_{k,p}^s$
d	3/8	0	1/8	1/8	3/8	0	0	0	0	0	0	Mid-segment of $\Gamma_{k,p}^s$
e	1/3	0	0	0	1/3	1/12	1/12	1/12	1/12	0	0	Mid-segment of $\Gamma_{k,p}^s$
f	1/3	0	0	0	1/12	1/12	1/12	1/12	1/3	0	0	Mid-segment of $\Gamma_{k,p}^s$
g	7/20	1/10	0	0	0	0	0	0	7/20	1/10	1/10	Mid-segment of $\Gamma_{k,p}^s$
h	7/10	7/10	0	0	0	0	0	0	1/10	1/10	1/10	Mid-segment of $\Gamma_{k,p}^s$

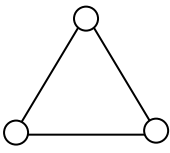
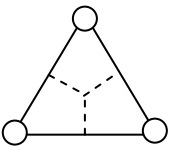
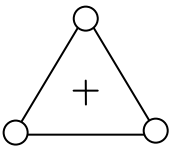
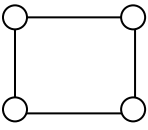
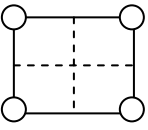
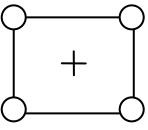
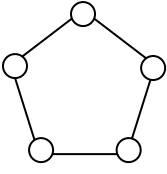
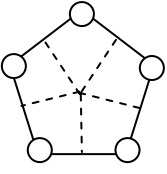
Table 5.2. Existence of spurious zero-energy modes in an individual element.		
Type of element	NS-FEM	FEM with reduced integration
 Triangle $N_R = 3$	 $n_Q = 3, N_Q = 3 \times n_Q = 9$ $n_t = 3, N_u = 2 \times n_t = 6$ $N_Q > N_u - N_R$ \Rightarrow spurious zero energy modes not possible	 $n_Q = 1, N_Q = 3 \times n_Q = 3$ $n_t = 3, N_u = 2 \times n_t = 6$ $N_Q = N_u - N_R$ \Rightarrow spurious zero energy modes not possible
 Quadrilateral $N_R = 3$	 $n_Q = 4, N_Q = 3 \times n_Q = 12$ $n_t = 4, N_u = 2 \times n_t = 8$ $N_Q > N_u - N_R$ \Rightarrow spurious zero energy modes not possible	 $n_Q = 1, N_Q = 3 \times n_Q = 3$ $n_t = 4, N_u = 2 \times n_t = 8$ $N_Q < N_u - N_R$ \Rightarrow spurious zero energy modes possible
 n -sided polygonal $(n > 4)$ $N_R = 3$	 $n_Q = n, N_Q = 3 \times n_Q = 3n$ $n_t = n, N_u = 2 \times n_t = 2n$ $N_Q > N_u - N_R$ \Rightarrow spurious zero energy modes not possible	Not applicable
Note: N_R : number of DOFs of rigid motion n_t : number of nodes n_Q : number of quadrature points/cells N_u : number of total DOFs N_Q : number of independent equations		

Table 5.3. Error in displacement norm and energy for the patch test.

	$\alpha_{ir} = 0.0$	$\alpha_{ir} = 0.1$	$\alpha_{ir} = 0.2$	$\alpha_{ir} = 0.3$	$\alpha_{ir} = 0.4$	$\alpha_{ir} = 0.49$
Disp. norm e_d (%)	2.25e-16	1.64e-15	3.42e-16	3.45e-15	1.34e-15	4.79e-15
Energy error e_e	0.0	4.56e-12	3.27e-11	4.25e-11	3.93e-12	1.56e-11

Mesh	16×4	24×6	32×8	40×10	48×12	Analytical sol.
DOFs	170	350	694	902	1274	
FEM-T3	3.7134	4.0973	4.2533	4.3301	4.3731	4.4747
FEM-Q4	4.3362	4.4118	4.4390	4.4518	4.4587	4.4747
CS-FEM-Q4	4.4310	4.4550	4.4635	4.4675	4.4697	4.4747
NS-FEM-T3	4.9785	4.7031	4.6051	4.5591	4.5338	4.4747
NS-FEM-Q4	4.7176	4.5898	4.5415	4.5183	4.5053	4.4747
ES-FEM-T3 [76]	4.4097	4.4539	4.4654	4.4697	4.4717	4.4747
α FEM-T3 [74] ($\alpha_{exact} = 0.6$)	4.4071	4.4566	4.4681	4.4719	4.4734	4.4747

^(*): The numerical solutions of the methods, the ES-FEM-T3 [76] and the α FEM-T3 [74], presented in the following chapters, are also presented in this table for the easy reference.

	Mesh 1	Mesh 2	Mesh 3	Mesh 4	Mesh 5	Analytical sol.
DOFs	344	704	1192	1808	2552	
n CS-FEM	4.1879	4.3347	4.3928	4.4218	4.4369	4.4747
n NS-FEM	4.6017	4.5397	4.5149	4.4999	4.4922	4.4747
n ES-FEM [104]	4.3800	4.4388	4.4532	4.4616	4.4657	4.4747

^(*): The numerical solutions of the method n ES-FEM [104] presented in Chapter 6, are also presented in this table for the easy reference.

Mesh	16×4	24×6	32×8	40×10	48×12
h (m)	4.0	2.0	1.5	1.2	1.0
FEM-T3	1.78 e-02	8.80 e-03	5.16 e-03	3.36 e-03	2.36 e-03
FEM-Q4	2.97 e-03	1.35 e-03	7.63 e-04	4.90 e-04	3.41 e-04
CS-FEM-Q4	7.40 e-04	3.31 e-04	1.87 e-04	1.20 e-04	8.31 e-05
NS-FEM-T3	1.23 e-02	5.60 e-03	3.20 e-03	2.07 e-03	1.45 e-03
NS-FEM-Q4	6.15 e-03	2.91 e-03	1.68 e-03	1.10 e-03	7.71 e-04
ES-FEM-T3 [76]	1.32 e-03	3.74 e-04	1.47 e-04	6.94 e-05	3.68 e-05
α FEM-T3 [74] ($\alpha_{exact} = 0.6$)	1.26 e-03	2.65 e-04	6.86 e-05	2.69 e-05	2.48 e-05

^(*): The numerical solutions of the methods, the ES-FEM-T3 [76] and the α FEM-T3 [74], presented in the following Chapters, are also presented in this table for the easy reference.

Mesh	16×4	24×6	32×8	40×10	48×12
h (m)	4.0	2.0	1.5	1.2	1.0
FEM-T3	8.77 e-01	6.16 e-01	4.71 e-01	3.80 e-01	3.18 e-01
FEM-Q4	3.71 e-01	2.49 e-01	1.88 e-01	1.50 e-01	1.25 e-01
CS-FEM-Q4	2.38 e-01	1.30 e-01	8.46 e-02	6.05 e-02	4.60 e-02
NS-FEM-T3	1.44 e-01	9.45 e-02	6.71 e-02	5.06 e-02	3.99 e-02
NS-FEM-Q4	1.16 e-01	7.28 e-02	5.10 e-02	3.83 e-02	3.00 e-02
ES-FEM-T3 [76]	2.96 e-01	1.58 e-01	1.02 e-01	7.28 e-02	5.53 e-02
α FEM-T3 [74] ($\alpha_{exact} = 0.6$)	2.93 e-01	1.54 e-01	9.86 e-02	7.00 e-02	5.31 e-02

^(*): The numerical solutions of the methods, the ES-FEM-T3 [76] and the α FEM-T3 [74], presented in the following Chapters, are also presented in this table for the easy reference.

Mesh	12×12	16×16	20×20	24×24	Analytical sol.
DOFs	338	578	882	1250	
FEM-T3	1.1762	1.1786	1.1797	1.1803	1.1817
FEM-Q4	1.1794	1.1805	1.1810	1.1812	1.1817
CS-FEM-Q4	1.1798	1.1807	1.1811	1.1813	1.1817
NS-FEM-T3	1.1848	1.1834	1.1827	1.1824	1.1817
NS-FEM-Q4	1.1850	1.1835	1.1827	1.1823	1.1817
ES-FEM-T3 [76]	1.1804	1.1811	1.1814	1.1815	1.1817

^(*): The numerical solutions of the ES-FEM-T3 [76] presented in Chapter 6, are also presented in this table for the easy reference.

	Mesh 1	Mesh 2	Mesh 3	Mesh 4	Analytical sol.
DOFs	326	678	1158	1770	
n CS-FEM	1.1759	1.1791	1.1803	1.1808	1.1817
n NS-FEM	1.1820	1.1820	1.1820	1.1819	1.1817
n ES-FEM [104]	1.1785	1.1805	1.1812	1.1814	1.1817

^(*): The numerical solutions of the method n ES-FEM [104] presented in Chapter 6, are also presented in this table for the easy reference.

	Mesh 1	Mesh 2	Mesh 3	Mesh 4	Mesh 5
h (m)	0.5468	0.3786	0.2895	0.2343	0.1969
FEM-T3	2.80 e-04	1.42 e-04	8.45 e-05	5.61 e-05	4.01 e-05
FEM-Q4	1.08 e-04	4.46 e-05	2.40 e-05	1.50 e-05	1.03 e-05
CS-FEM-Q4	8.46 e-05	3.48 e-05	1.88 e-05	1.19 e-05	8.19 e-06
NS-FEM-T3	3.87 e-04	1.69 e-04	8.95 e-05	5.49 e-05	3.70 e-05
NS-FEM-Q4	2.73 e-04	1.29 e-04	7.04 e-05	4.35 e-05	2.94 e-05
ES-FEM-T3 [76]	8.03 e-05	2.95 e-05	1.63 e-05	1.06 e-05	7.46 e-06

(*): The numerical solutions of the ES-FEM-T3 [76] presented in Chapter 6, are also presented in this table for the easy reference.

	Mesh 1	Mesh 2	Mesh 3	Mesh 4	Mesh 5
h (m)	0.5468	0.3786	0.2895	0.2343	0.1969
FEM-T3	9.95 e-03	6.89 e-03	5.20 e-03	4.17 e-03	3.48 e-03
FEM-Q4	6.09 e-03	3.86 e-03	2.79 e-03	2.18 e-03	1.79 e-03
CS-FEM-Q4	5.12 e-03	2.70 e-03	1.61 e-03	1.06 e-03	7.41 e-04
NS-FEM-T3	3.08 e-03	1.50 e-03	8.52 e-04	5.39 e-04	3.68 e-04
NS-FEM-Q4	2.33 e-03	1.06 e-03	5.77 e-04	3.53 e-04	2.35 e-04
ES-FEM-T3 [76]	5.27 e-03	2.69 e-03	1.59 e-03	1.04 e-03	7.29 e-04

(*): The numerical solutions of the ES-FEM-T3 [76] presented in Chapter 6, are also presented in this table for the easy reference.

	Mesh 1	Mesh 2	Mesh 3	Mesh 4	Analytical sol.
DOFs (T4)	1521	2337	3825	5814	
DOFs (H8)	1092	2535	3906	6951	
FEM-T4	5.9131	5.9986	6.0929	6.1387	6.3060
NSFEM-T4	6.6227	5.5380	6.4580	6.4219	6.3060
FEM-H8	5.9827	6.1063	6.1668	6.2023	6.3060
FS-FEM-T4 [103]	6.0343	6.0955	6.1607	6.1906	6.3060
α FEM-T4 [74] ($\alpha_{exact} = 0.7$)	6.3081	6.3058	6.3059	6.3060	6.3060

(*): The numerical solutions of the methods, the FS-FEM-T4 [103] and the α FEM-T4 [74], presented in the following Chapters, are also presented in this table for the easy reference.

	Mesh 1	Mesh 2	Mesh 3	Mesh 4
h (T4)	0.2193	0.1878	0.1565	0.1342
h (H8)	0.2535	0.1840	0.1563	0.1267
FEM-T4	4.06 e-03	3.12 e-03	2.07 e-03	1.58 e-03
NSFEM-T4	3.68 e-03	2.76 e-03	1.88 e-03	1.48 e-03
FEM-H8	2.26 e-03	1.35 e-03	7.92 e-04	5.44 e-04
FS-FEM-T4 [103]	3.03 e-03	2.30 e-03	1.50 e-03	1.14 e-03
α FEM-T4 [74] ($\alpha_{exact} = 0.7$)	1.40 e-03	1.02 e-03	6.67 e-04	4.71 e-04

^(*): The numerical solutions of the methods, the FS-FEM-T4 [103] and the α FEM-T4 [74], presented in the following Chapters, are also presented in this table for the easy reference.

	Mesh 1	Mesh 2	Mesh 3	Mesh 4
h (T4)	0.2193	0.1878	0.1565	0.1342
h (H8)	0.2535	0.1840	0.1563	0.1267
FEM-T4	5.89 e-01	5.13 e-01	4.19 e-01	3.63 e-01
NSFEM-T4	2.09 e-01	1.73 e-01	1.26 e-01	1.08 e-01
FEM-H8	5.51 e-01	4.22 e-01	3.42 e-01	2.85 e-01
FS-FEM-T4 [103]	3.75 e-01	3.03 e-01	2.24 e-01	1.86 e-01
α FEM-T4 [74] ($\alpha_{exact} = 0.7$)	2.83 e-01	2.30 e-01	1.71 e-01	1.44 e-01

^(*): The numerical solutions of the methods, the FS-FEM-T4 [103] and the α FEM-T4 [74], presented in the following Chapters, are also presented in this table for the easy reference.

	Mesh 1	Mesh 2	Mesh 3	Mesh 4	Mesh 5	Reference sol. [5]
DOFs (T4)	714	1221	2073	2856	4782	
DOFs (H8)	648	1029	1536	2187	3993	
FEM-T4	0.8572	0.8818	0.8978	0.9088	0.9190	0.9509
NSFEM-T4	1.0059	0.9882	0.9808	0.9791	0.9704	0.9509
FEM-H8	0.8999	0.9116	0.9195	0.9251	0.9323	0.9509
FS-FEM-T4 [103]	0.8801	0.8989	0.9111	0.9206	0.9274	0.9509
α FEM-T4 [74] ($\alpha_{exact} = 0.62$)	0.9478	0.9478	0.9488	0.9518	0.9514	0.9509

^(*): The numerical solutions of the methods, the FS-FEM-T4 [103] and the α FEM-T4 [74], presented in the following Chapters, are also presented in this table for the easy reference.

	Mesh 1	Mesh 2	Mesh 3	Mesh 4	Mesh 5	Reference sol.
DOFs (T4)	714	1221	2073	2856	4782	
DOFs (H8)	648	1029	1536	2187	3993	
FEM-T4	3.0780	3.1752	3.2341	3.2732	3.3050	3.3912
NS-FEM-T4	3.5912	3.5418	3.4943	3.4818	3.4577	3.3912
FEM-H8	3.2523	3.2875	3.3107	3.3269	3.3474	3.3912
FS-FEM-T4 [103]	3.1669	3.2390	3.2800	3.3128	3.3324	3.3912
α FEM-T4 [74] ($\alpha_{exact} = 0.62$)	3.4064	3.4087	3.4031	3.4091	3.4053	3.3912

^(*): The numerical solutions of the methods, the FS-FEM-T4 [103] and the α FEM-T4 [74], presented in the following Chapters, are also presented in this table for the easy reference.

	Mesh 1	Mesh 2	Mesh 3	Mesh 4	Mesh 5	Reference sol.
DOFs	806	1284	2556	3834	4826	
FEM-T4	5.7164	5.8189	5.9524	6.0028	6.0305	6.1999
NSFEM-T4	6.6787	6.5454	6.4227	6.3897	6.3658	6.1999
FS-FEM-T4 [103]	5.8728	5.9532	6.0358	6.0731	6.0927	6.1999
α FEM-T4 [74] ($\alpha_{exact} = 0.7$)	6.1861	6.1824	6.1828	6.1808	6.1960	6.1999

^(*): The numerical solutions of the methods, the FS-FEM-T4 [103] and the α FEM-T4 [74], presented in the following Chapters, are also presented in this table for the easy reference.

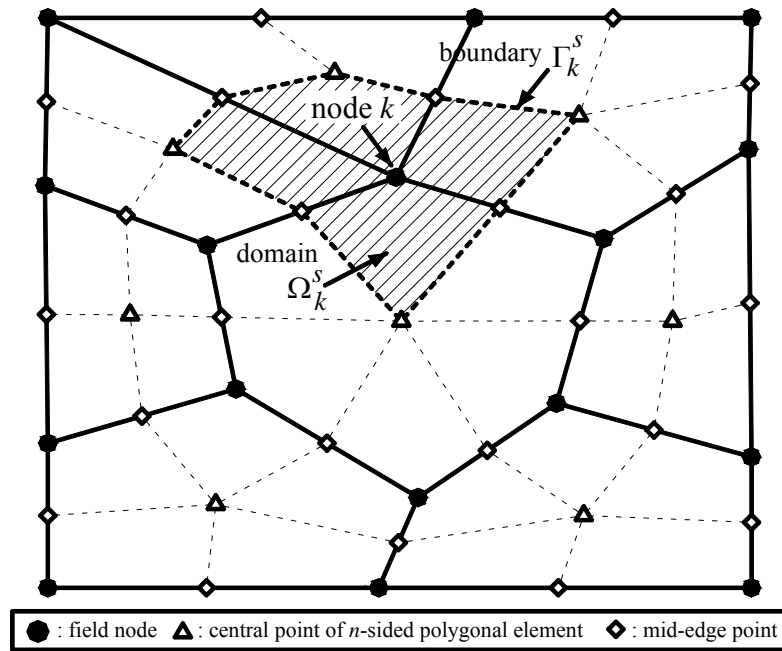


Figure 5.1. n -sided polygonal elements and the smoothing domains associated with nodes.

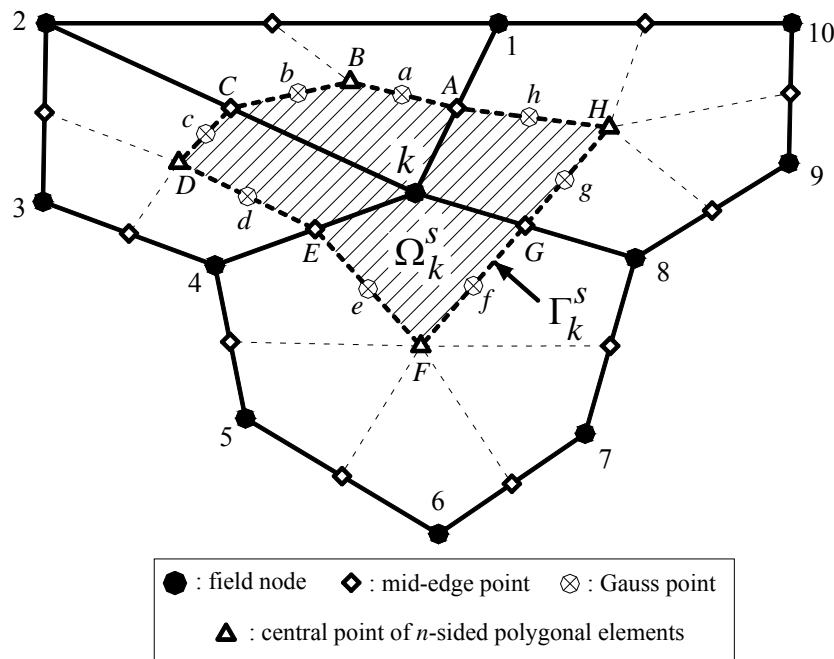


Figure 5.2. Position of Gauss points at mid-segment-points on the segments of smoothing domains associated with node k in a mesh of n -sided polygonal elements.

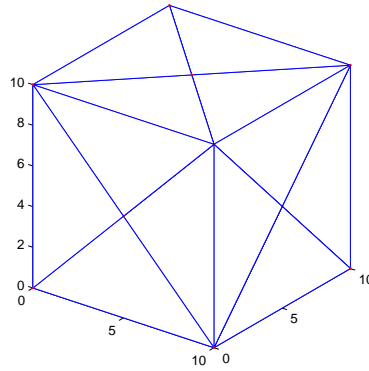


Figure 5.3. Domain discretization of a cubic patch with 4-node tetrahedral elements.

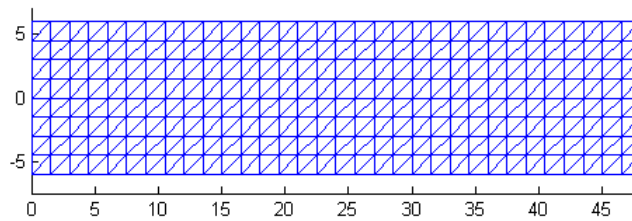


Figure 5.4. Domain discretization of the cantilever using triangular elements.

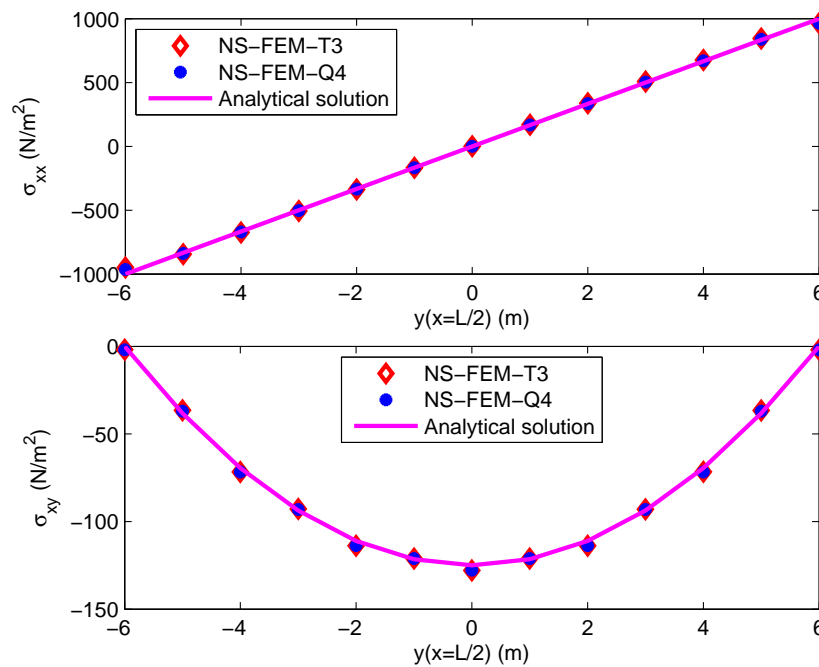


Figure 5.5. Comparison of the numerical results of NS-FEM models and analytical solutions for the cantilever loaded at the end. (a) Normal stress σ_{xx} ; (b) Shear stress τ_{xy} .

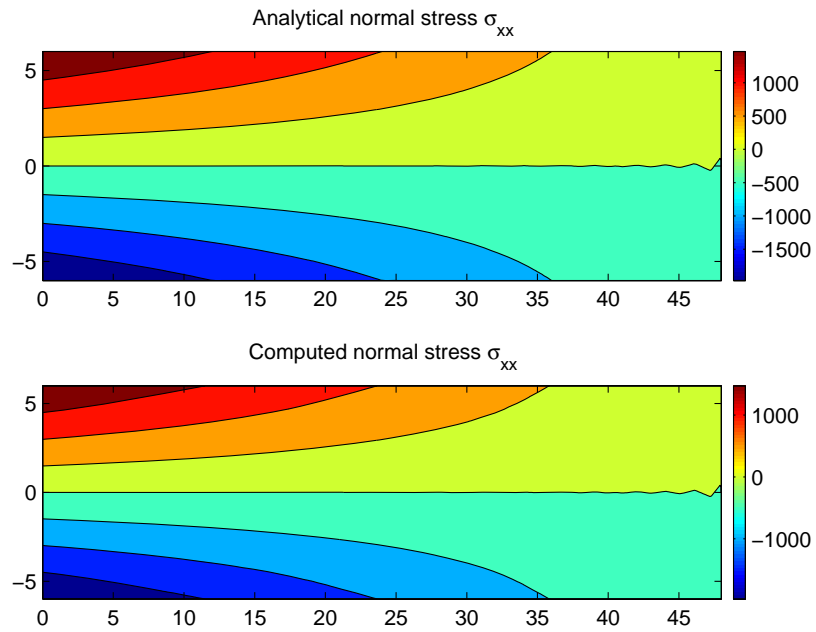


Figure 5.6. Contour of the analytical and the numerical normal stress σ_{xx} (N/m^2) for the cantilever obtained using the n NS-FEM.

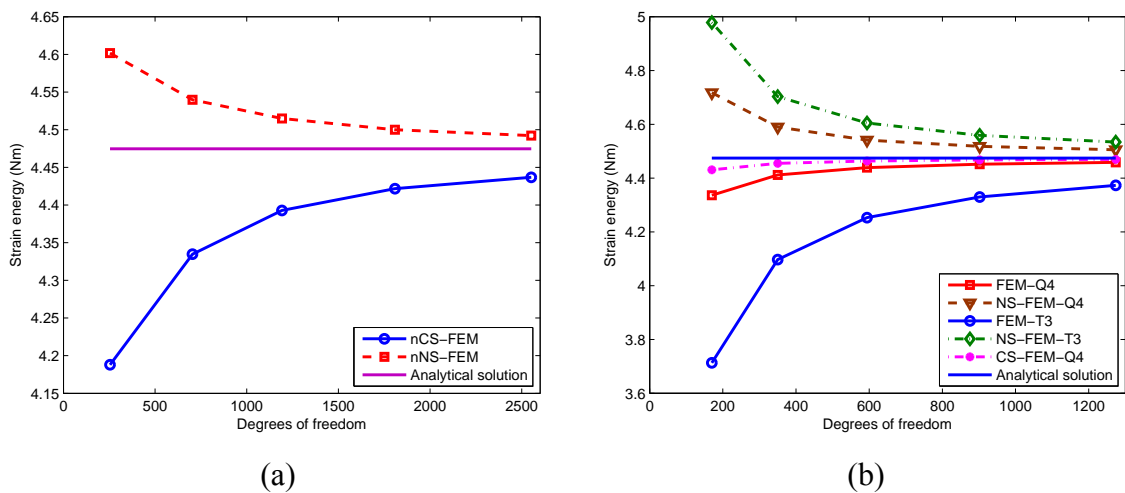


Figure 5.7. Convergence of the strain energy solution for the cantilever problem. (a) n -sided polygonal elements; (b) triangular and 4-node elements.

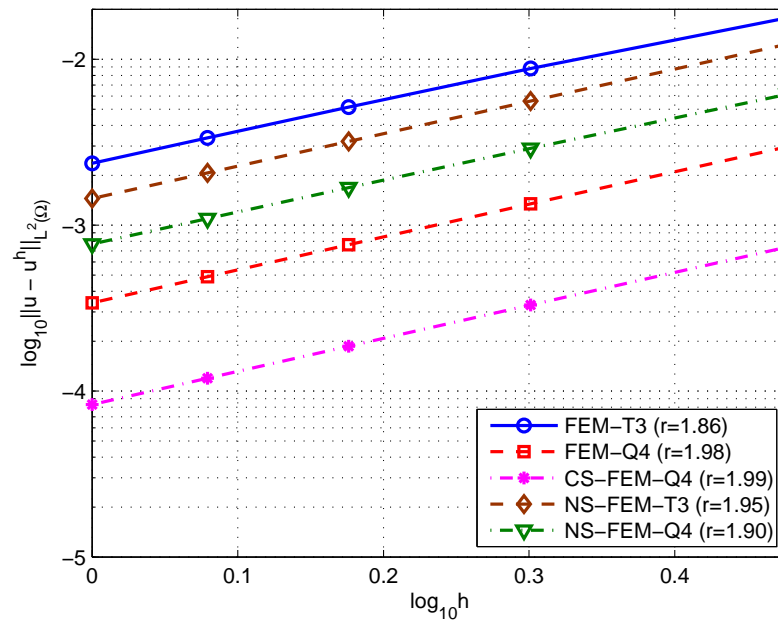


Figure 5.8. Error in displacement norm for the NS-FEM solution in comparison with that of other methods for the cantilever problem using the same distribution of nodes.

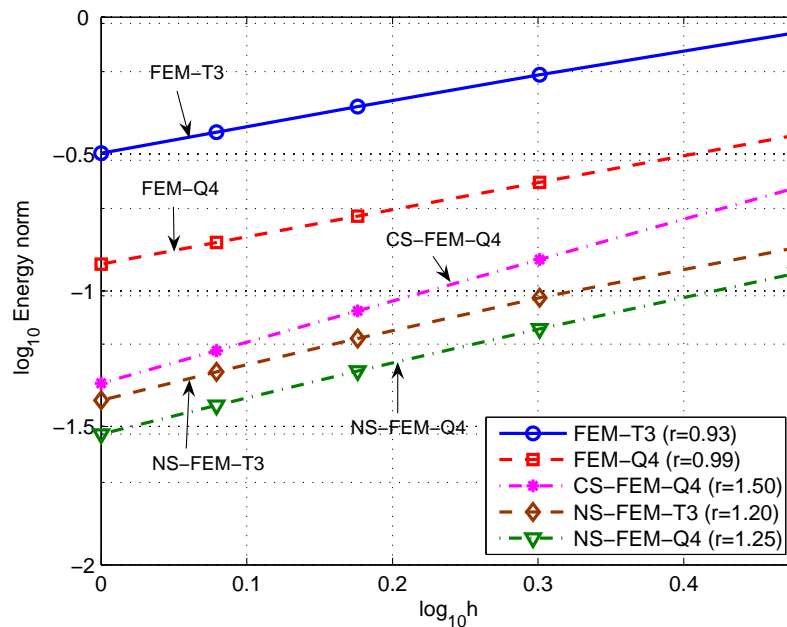


Figure 5.9. Error in energy norm for the NS-FEM solution in comparison with those of other methods for the cantilever problem using the same distribution of nodes.

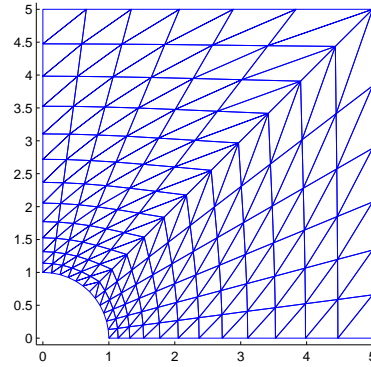


Figure 5.10. Domain discretization of the infinite plate with a circular hole using triangular elements.

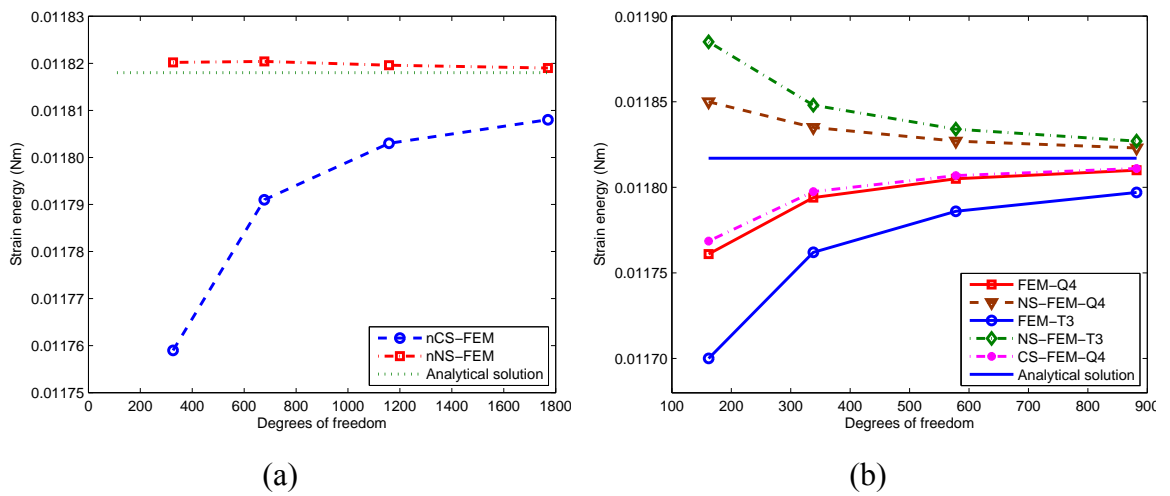


Figure 5.11. Convergence of the strain energy solution for the infinite plate with a circular hole. (a) n -sided polygonal elements; (b) triangular and quadrilateral elements.

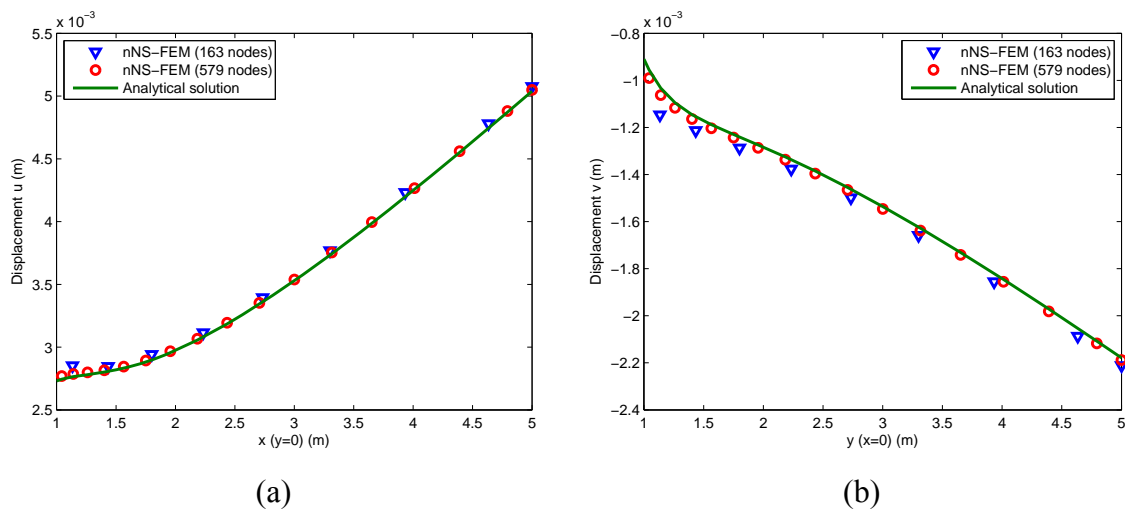


Figure 5.12. Computed and exact displacements of the n NS-FEM for the infinite plate with a circular hole. (a) displacement u (m) of nodes along bottom side; (b) displacement v (m) of nodes along left side.

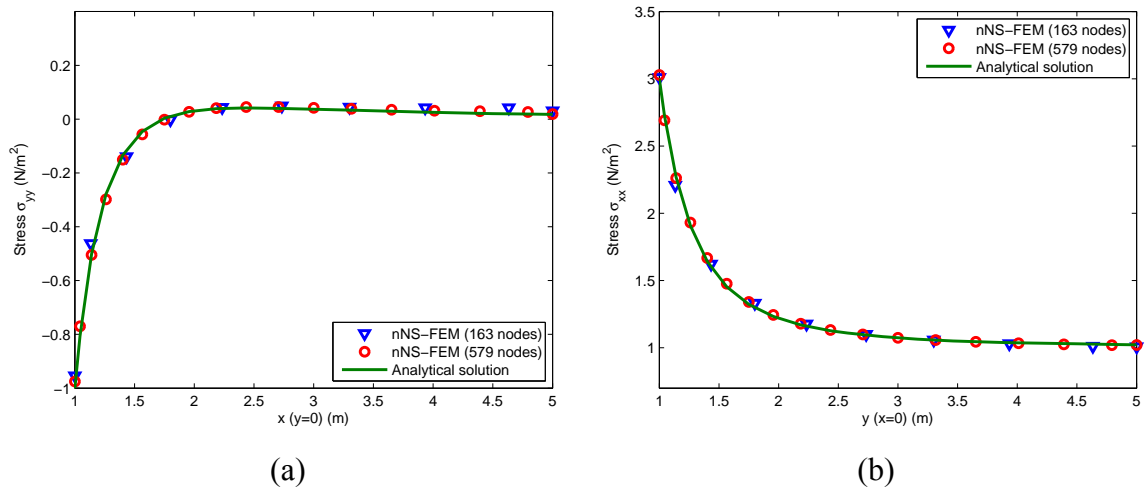


Figure 5.13. Exact and the numerical stresses using the n NS-FEM for the infinite plate with a circular hole. (a) stress σ_{yy} of nodes along bottom side; (b) stress σ_{xx} of nodes along left side.

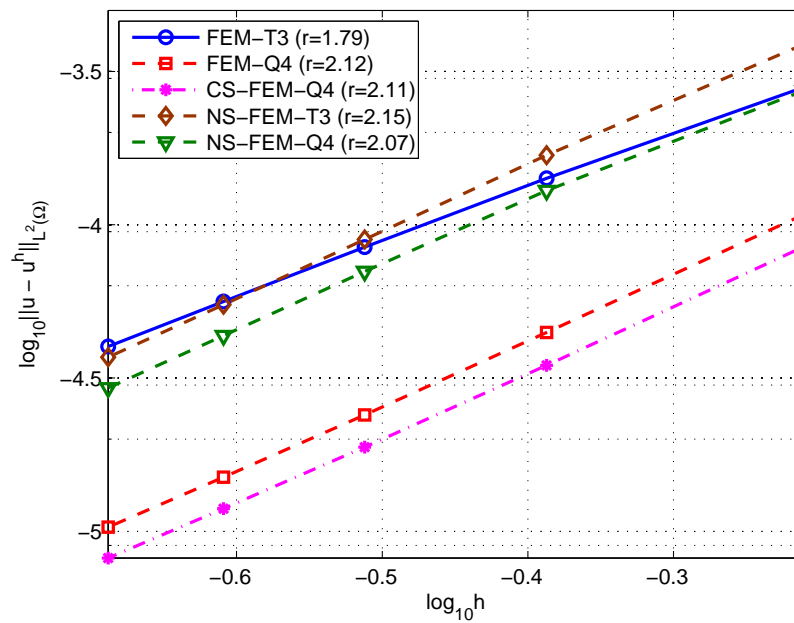


Figure 5.14. Error in displacement norm for NS-FEM in comparison with those of other methods for the infinite plate with a circular hole using the same distribution of nodes.

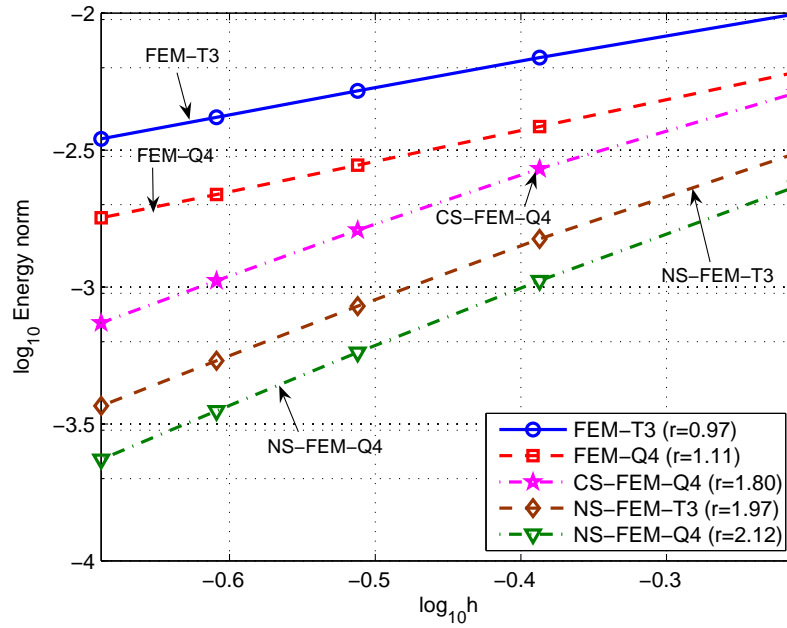


Figure 5.15. Error in energy norm for NS-FEM in comparison with those of other methods for the infinite plate with a circular hole using the same distribution of nodes.

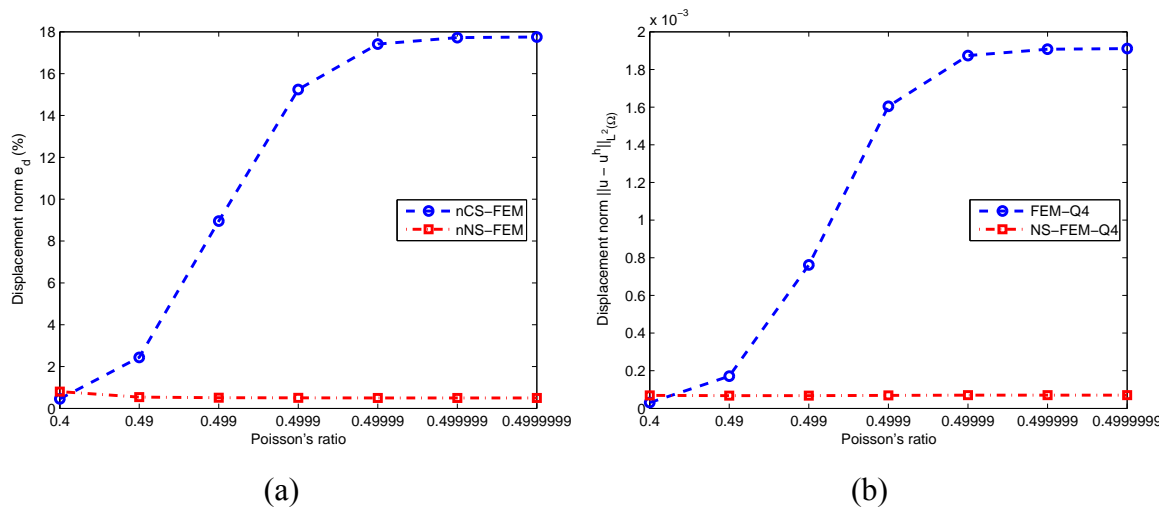


Figure 5.16. Error in displacement norm versus Poisson's ratios close to 0.5 for the infinite plate with a circular hole. (a) n -sided polygonal elements (579 nodes); (b) 4-node quadrilateral elements (289 nodes).

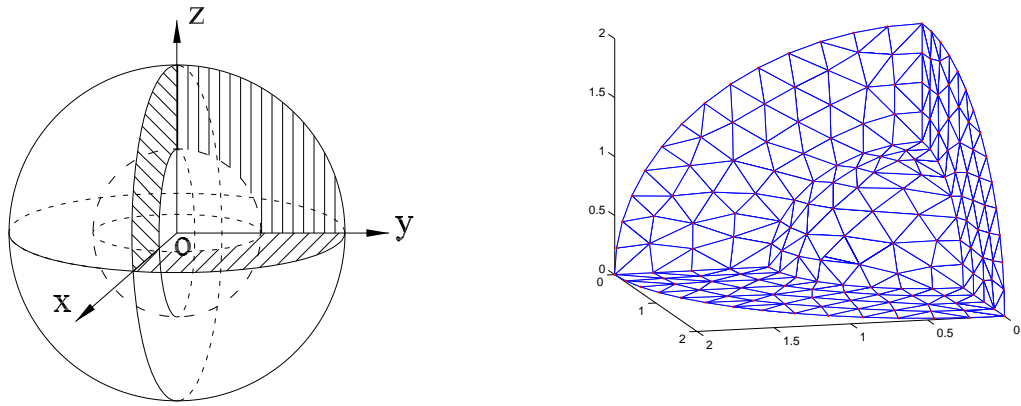


Figure 5.17. Hollow sphere problem setting and its one-eighth model discretized using 4-node tetrahedral elements.

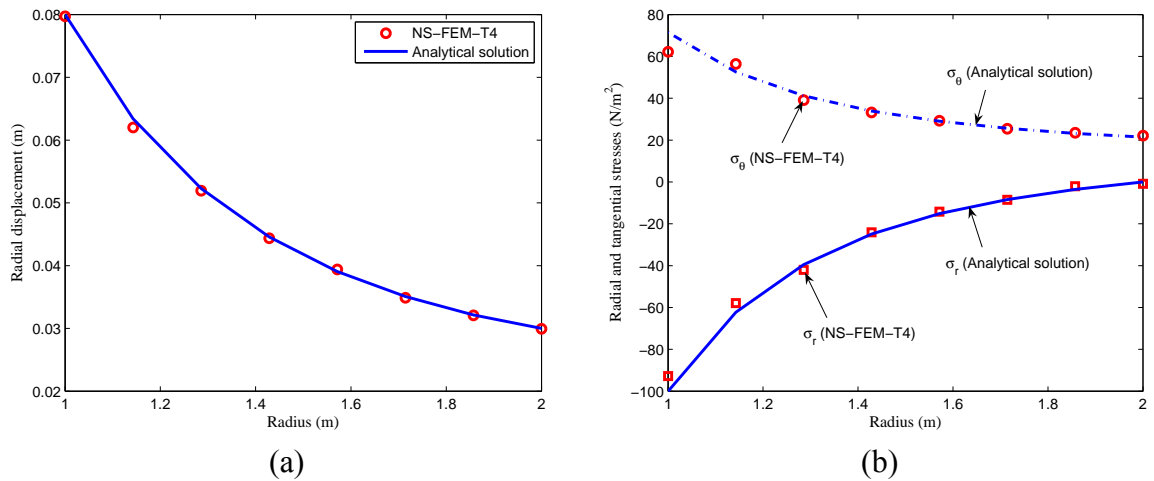


Figure 5.18. (a) Radial displacement v (m); (b) Radial and tangential stresses (N/m²) for the hollow sphere subjected to inner pressure.

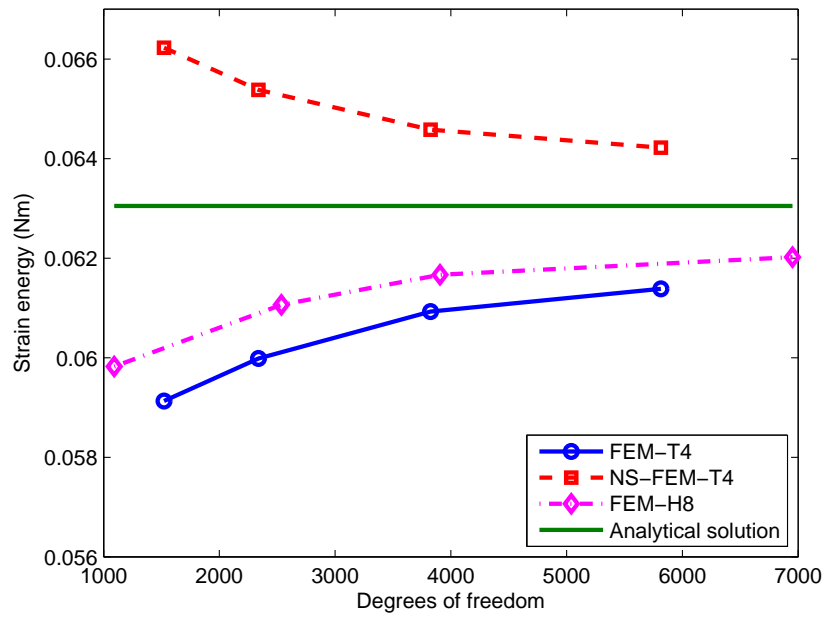


Figure 5.19. Convergence of the strain energy solution of the NS-FEM-T4 in comparison with other methods for the hollow sphere subjected to inner pressure.

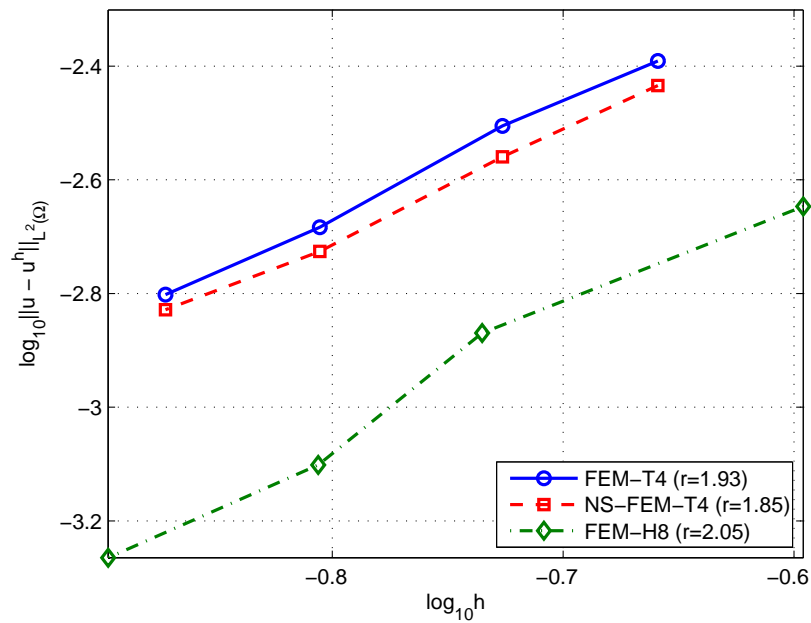


Figure 5.20. Error in displacement norm for the NS-FEM-T4 solution in comparison with those of other methods for the hollow sphere subjected to inner pressure.

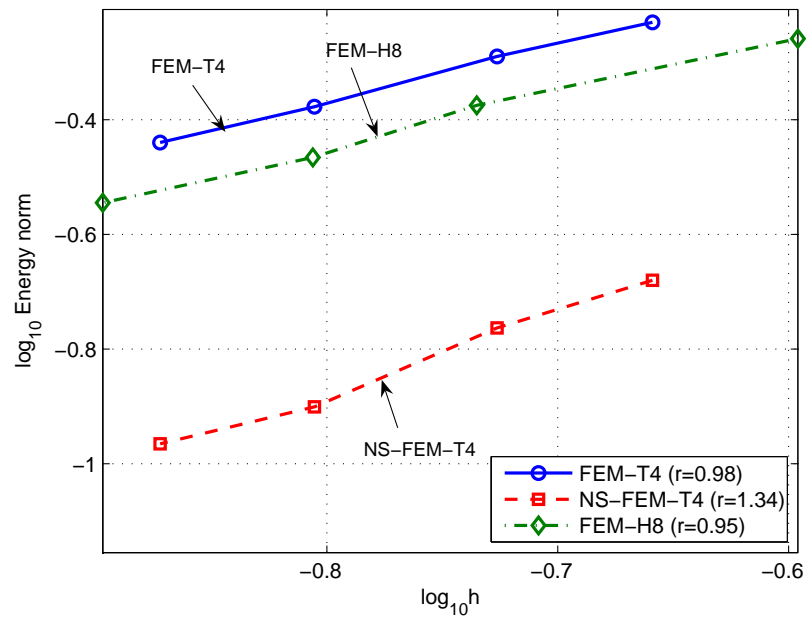


Figure 5.21. Error in energy norm for the NS-FEM-T4 solution in comparison with those of other methods for the hollow sphere subjected to inner pressure.

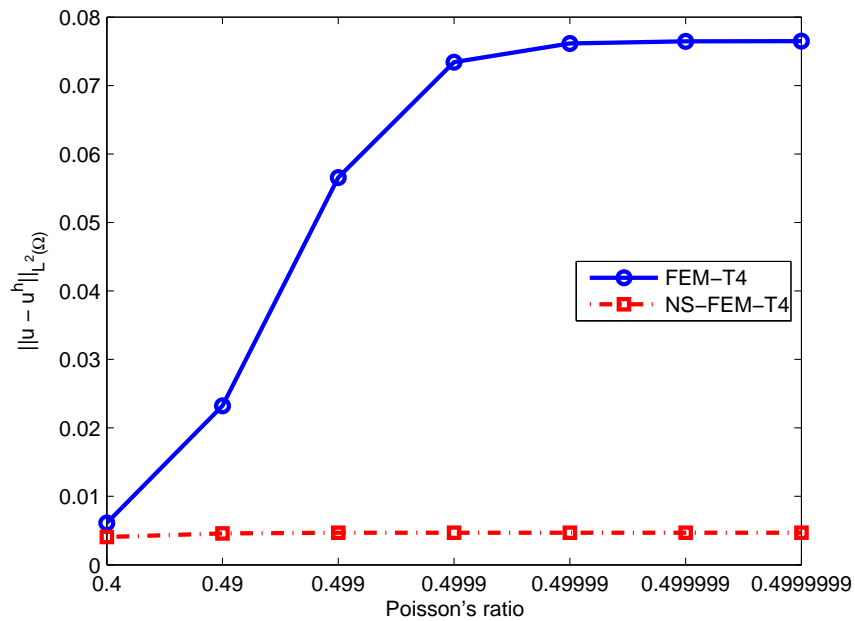


Figure 5.22. Displacement norm versus different Poisson's ratios for the hollow sphere subjected to inner pressure (507 nodes).

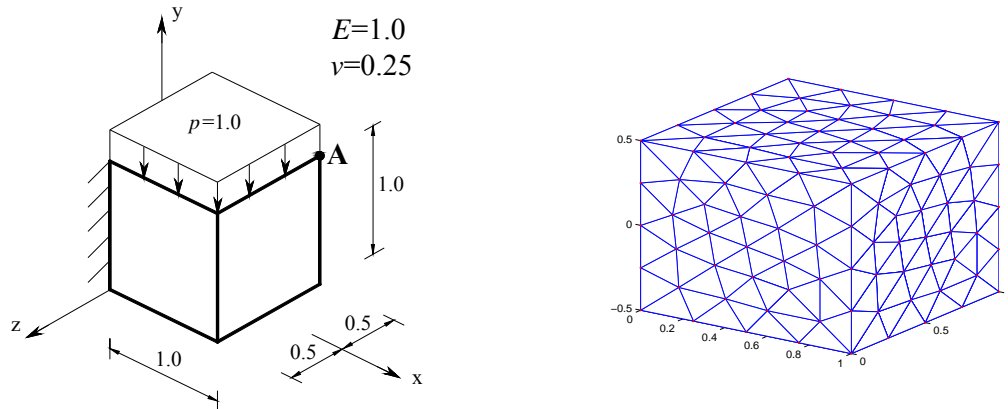


Figure 5.23. A 3D cubic cantilever subjected to a uniform pressure on the top surface, and a mesh with 4-node tetrahedral elements.

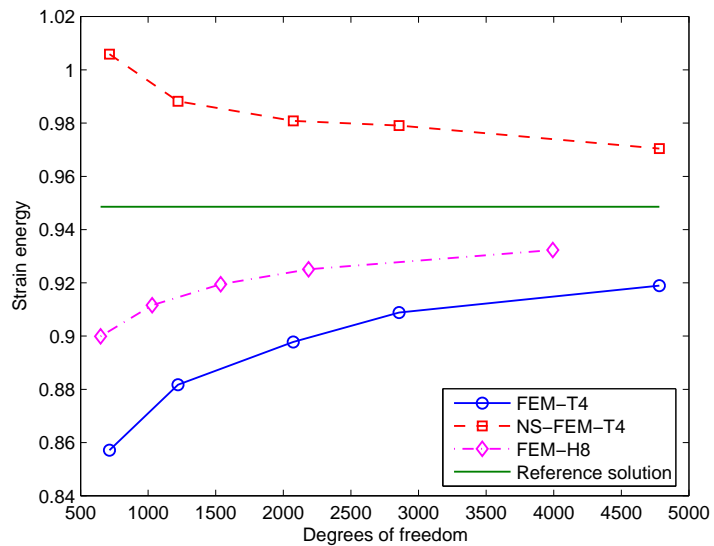


Figure 5.24. Convergence of the strain energy solution of the NS-FEM-T4 in comparison with other methods of the 3D cubic cantilever problem subjected to a uniform pressure.

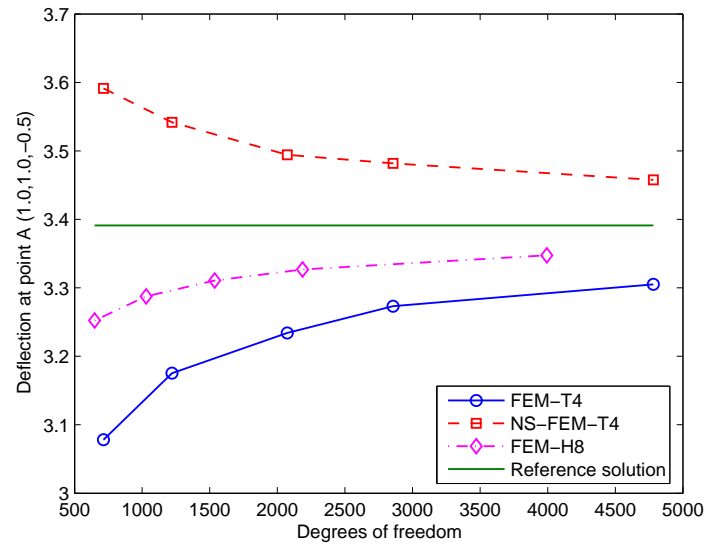


Figure 5.25. Convergence of the deflection solution at point A(1.0,1.0,-0.5) of the NS-FEM-T4 in comparison with other methods of the cubic cantilever subjected to a uniform pressure.

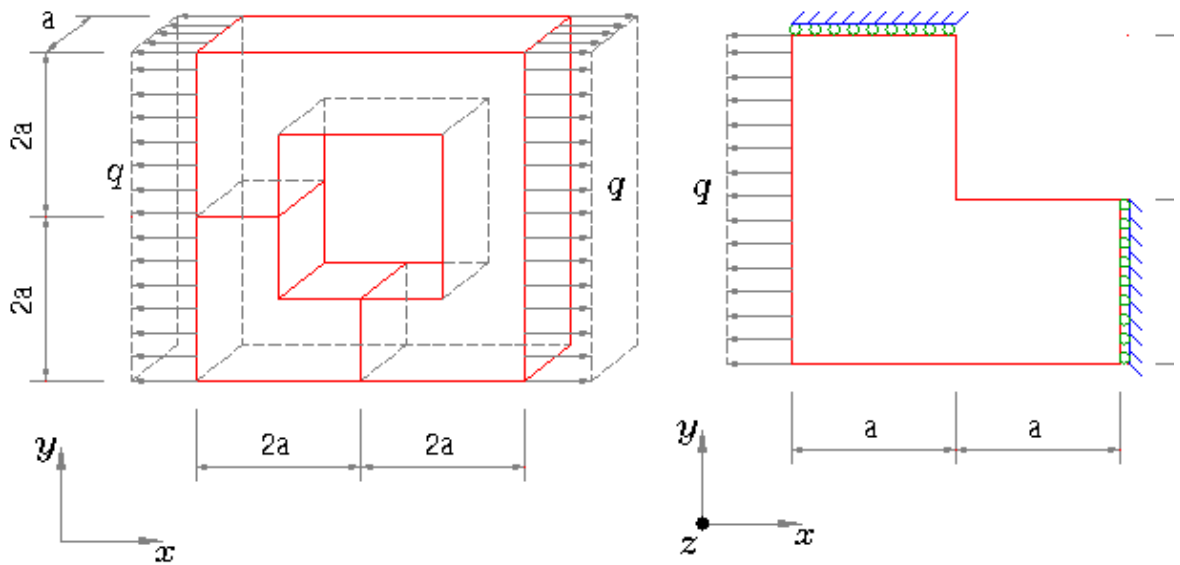


Figure 5.26. 3D block and an L-shaped quarter model.

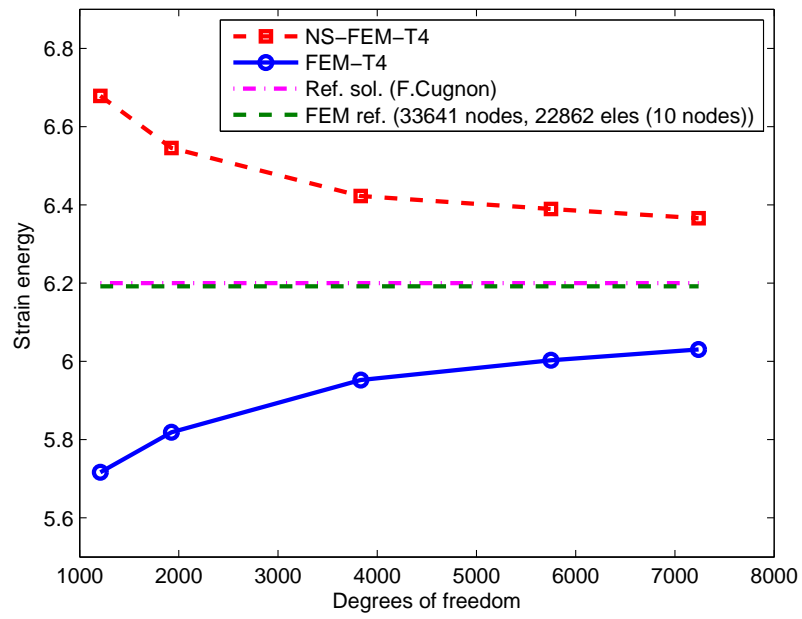


Figure 5.27. Convergence of the strain energy solution of the 3D *L*-shaped block problem.

Chapter 6

Edge-based Smoothed FEM (ES-FEM)

6.1 Introduction

Chapter 5 has presented the node-based S-FEM or NS-FEM [78], and it has proven via theoretical analysis and numerical examples that the NS-FEM is always spatially stable. In addition, the NS-FEM possesses interesting properties that are similar to those of an equilibrium FEM model such as: (1) the upper bound property of the strain energy for force-driven problems when a reasonably fine mesh is used; (2) natural immunization from the volumetric locking; (3) ultra-accuracy and super-convergence of stress solutions; and (4) same level of accuracy in displacement solutions as the FEM. It is, however, found that the NS-FEM behaves “overly-soft” resulted from the over-correction to the “overly-stiff” behavior of the compatible FEM [78]. Such an overly-soft behavior leads to “temporal” instability similar to those found in the equilibrium FEM models and in the nodal integration methods [99, 124, 125]. The temporal instability can be clearly observed when the NS-FEM is used for solving dynamic problems: (1) as spurious non-zero energy modes in free vibration analyses; and (2) numerical instability in the time marching in forced vibration analyses.

In this chapter, we therefore present a very outstanding S-FEM model: the edge-based S-FEM (ES-FEM) that is both spatially and temporally stable, and much more accurate

compared with many existing FEM models. The ES-FEM was originated in [76] to create models with close-to-exact stiffness, so that it can produce ultra-accurate results for solving static problems, and stable and accurate results for dynamic problems. In the ES-FEM, the strain smoothing domains are associated with edges of the element mesh, and hence the integration of the weak form becomes a simple summation over these edge-based smoothing domains. The ES-FEM works well, in general for a mesh of arbitrarily n -sided polygonal elements [104], and in particular for linear triangular elements [76]. In addition, a smoothing-domain-based selective ES/NS-FEM model has also been proposed that is immune from the volumetric locking, and works very well for solids of nearly incompressible materials [76, 104].

For the important mesh generation reasons, this chapter concentrates on the ES-FEM using linear triangular elements (ES-FEM-T3). In this case, the ES-FEM-T3 has been often found possessing the following excellent properties: (1) the results of the ES-FEM-T3 are often much more accurate than those of the FEM-T3 and often even more accurate than those of the FEM-Q4 with the same distribution of nodes. These results have been observed in static linear elastic problems; (2) No spurious non-zeros energy modes were found and hence the method is both spatially and temporally stable and hence works well for dynamic problems; (3) the implementation of the ES-FEM is straightforward: no penalty parameters or additional degrees of freedom are used; (4) The ES-FEM can easily be extended to 3D problems using tetrahedral elements [103]; and (5) the computational efficiency of the ES-FEM-T3 is the most superior among others compared numerical methods using the same distribution of nodes.

6.2 Creation of edge-based smoothing domains

In the ES-FEM, the domain discretization is still based on general polygonal elements with arbitrary number of sides, as in the NS-FEM. The element mesh will have a total

of N_{eg} edges located in the entire problem domain. On top of the element mesh, the problem domain Ω is divided into $N_s = N_{eg}$ non-overlap no-gap smoothing domains associated with the edges, such that $\Omega = \sum_{k=1}^{N_{eg}} \Omega_k^s$ and $\Omega_i^s \cap \Omega_j^s = \emptyset$, $i \neq j$. For a mesh of n -sided polygonal elements, the smoothing domain Ω_k^s associated with the edge k is created by connecting two endpoints of the edge to central points of adjacent elements as shown in Figure 6.1. For a mesh of triangular elements, an ES-FEM-T3 setting is shown in Figure 6.2. The strain smoothing technique [24] is used to create a smoothed strain field that is constant in each of the smoothing domains. The integration required in the weak form thus becomes a summation over all these edge-based smoothing domains.

6.3 Formulation of the ES-FEM

6.3.1 Static analyses

Using the general formulation for the static analysis of the S-FEM models presented in Chapter 3, Section 3.1, the linear system of equations of the ES-FEM has the form of

$$\bar{\mathbf{K}}^{\text{ES-FEM}} \bar{\mathbf{d}} = \mathbf{f} \quad (6.1)$$

where $\bar{\mathbf{K}}^{\text{ES-FEM}}$ is the *smoothed* stiffness matrix whose entries are given by

$$\bar{\mathbf{K}}_{IJ}^{\text{ES-FEM}} = \sum_{k=1}^{N_{eg}} \int_{\Omega_k^s} \bar{\mathbf{B}}_I^T \mathbf{D} \bar{\mathbf{B}}_J d\Omega = \sum_{k=1}^{N_{eg}} \bar{\mathbf{B}}_I^T \mathbf{D} \bar{\mathbf{B}}_J A_k^s \quad (6.2)$$

where $A_k^s = \int_{\Omega_k^s} d\Omega$ is the area of the edge-based smoothing domain Ω_k^s , and the smoothed strain-displacement matrix $\bar{\mathbf{B}}_I$ is computed by Eq. (3.10) using only shape function values on the boundaries of the smoothing domains.

In particular, when a mesh of linear triangular elements (ES-FEM-T3) are used, the smoothed strain-displacement matrix $\bar{\mathbf{B}}_I$ can be assembled by following simple equation

$$\bar{\mathbf{B}}_I(\mathbf{x}_k) = \frac{1}{A_k^s} \sum_{j=1}^{n_k^e} \frac{1}{3} A_j^e \mathbf{B}_j^e \quad (6.3)$$

where n_k^e is the number of elements attached to the edge k ($n_k^e = 1$ for the boundary edges and $n_k^e = 2$ for inner edges as shown in Figure 6.2); A_j^e is the area of the j^{th} element attached to the edge k ; and A_k^s is the area of the smoothing domain computed using

$$A_k^s = \int_{\Omega_k^s} d\Omega = \frac{1}{3} \sum_{j=1}^{n_k^e} A_j^e \quad (6.4)$$

In Eq. (6.3), matrix $\mathbf{B}_j^e = \sum_{I \in S_j^e} \mathbf{B}_I$ is the compatible strain-displacement matrix for the j^{th}

triangular element attached to the edge k . It is assembled by the compatible strain-displacement matrices $\mathbf{B}_I(\mathbf{x})$ of nodes in the set S_j^e which contains three nodes of the j^{th} triangular element. Matrix $\mathbf{B}_I(\mathbf{x})$ for the node I in triangular elements has the form of Eq. (2.48).

Note that with this formulation, only the area and the compatible strain-displacement matrices \mathbf{B}_j^e of triangular elements are needed to calculate the system stiffness matrix for the ES-FEM-T3. The formulation is simple, but works only for triangular types of elements that uses linear interpolation. For other ES-FEM models, the smoothed strain-displacement matrix $\bar{\mathbf{B}}_I$ has to be computed using the original Eq. (3.10), and the shape functions have to be evaluated in the way given in Section 6.4.

The above simple formulation is quite straightforward and can be easily extended for the 3D problems using tetrahedral elements [103], which will be presented in Chapter 7.

6.3.2 Dynamic analyses

Because the ES-FEM is both spatially and temporally stable [76], it suits well for dynamic problems, such as free and forced vibrations analyses. If the inertial and

damping forces are also considered in the dynamic equilibrium equations, the discretized system of equations in the ES-FEM can be expressed as a set of differential equations with respect to time:

$$\mathbf{M}\ddot{\bar{\mathbf{d}}} + \mathbf{C}\dot{\bar{\mathbf{d}}} + \bar{\mathbf{K}}^{\text{ES-FEM}}\bar{\mathbf{d}} = \mathbf{f} \quad (6.5)$$

where \mathbf{M} is the mass matrix and is computed using

$$\mathbf{M} = \int_{\Omega} \mathbf{N}^T \rho \mathbf{N} d\Omega \quad (6.6)$$

in which ρ is the mass density. The damping matrix \mathbf{C} is computed using

$$\mathbf{C} = \int_{\Omega} \mathbf{N}^T c \mathbf{N} d\Omega \quad (6.7)$$

where c is the damping coefficient.

For simplicity, the Rayleigh damping is used in this chapter, and the damping matrix \mathbf{C} is assumed to be a linear combination of \mathbf{M} and $\bar{\mathbf{K}}^{\text{ES-FEM}}$,

$$\mathbf{C} = \alpha \mathbf{M} + \beta \bar{\mathbf{K}}^{\text{ES-FEM}} \quad (6.8)$$

where α and β are the Rayleigh damping coefficients.

Many existing standard schemes can be used to solve the second-order time dependent problems, such as the Newmark method, Crank-Nicholson method, etc. [141]. In this chapter, the Newmark method is used. When the current state at $t = t_0$ is known as $(\bar{\mathbf{d}}_0, \dot{\bar{\mathbf{d}}}_0, \ddot{\bar{\mathbf{d}}}_0)$, we aim to find a new state $(\bar{\mathbf{d}}_1, \dot{\bar{\mathbf{d}}}_1, \ddot{\bar{\mathbf{d}}}_1)$ at $t_1 = t_0 + \theta \Delta t$ where $0.5 \leq \theta \leq 1$, using the following formulations:

$$\begin{aligned} \left[\left(\alpha + \frac{1}{\theta \Delta t} \right) \mathbf{M} + (\beta + \theta \Delta t) \bar{\mathbf{K}}^{\text{ES-FEM}} \right] \bar{\mathbf{d}}_1 &= \theta \Delta t \mathbf{f}_1 + (1 - \theta) \Delta t \mathbf{f}_0 \\ &+ \left(\alpha + \frac{1}{\theta \Delta t} \right) \mathbf{M} \bar{\mathbf{d}}_0 + \frac{1}{\theta} \mathbf{M} \dot{\bar{\mathbf{d}}}_0 + [\beta - (1 - \theta) \Delta t] \bar{\mathbf{K}}^{\text{ES-FEM}} \bar{\mathbf{d}}_0 \end{aligned} \quad (6.9)$$

$$\dot{\bar{\mathbf{d}}}_1 = \frac{1}{\theta \Delta t} (\bar{\mathbf{d}}_1 - \bar{\mathbf{d}}_0) - \frac{1 - \theta}{\theta} \dot{\bar{\mathbf{d}}}_0 \quad (6.10)$$

$$\ddot{\bar{\mathbf{d}}}_1 = \frac{1}{\theta \Delta t} (\dot{\bar{\mathbf{d}}}_1 - \dot{\bar{\mathbf{d}}}_0) - \frac{1 - \theta}{\theta} \ddot{\bar{\mathbf{d}}}_0 \quad (6.11)$$

Without the damping and forcing terms, Eq. (6.5) is reduced to a homogenous differential equation:

$$\mathbf{M}\ddot{\bar{\mathbf{d}}} + \bar{\mathbf{K}}^{\text{ES-FEM}}\bar{\mathbf{d}} = \mathbf{0} \quad (6.12)$$

A general solution of such a homogenous equation can be written as

$$\bar{\mathbf{d}} = \tilde{\mathbf{d}} \exp(i\omega t) \quad (6.13)$$

where t indicates time, $\tilde{\mathbf{d}}$ is the amplitude of the sinusoidal displacements and ω is the natural frequency. On its substitution into Eq. (6.12), the natural frequency ω can be found by solving the following eigenvalue equation.

$$\left(-\omega^2 \mathbf{M} + \bar{\mathbf{K}}^{\text{ES-FEM}}\right) \tilde{\mathbf{d}} = \mathbf{0} \quad (6.14)$$

Finally, we note that the trial function used in an ES-FEM model is the same as that in the standard FEM. Therefore the force vector \mathbf{f} , mass matrix \mathbf{M} and damping matrix \mathbf{C} in the ES-FEM are also computed in exactly the same way as in the FEM. In other words, the ES-FEM changes only the stiffness matrix.

6.4 Evaluation of the shape function values in the ES-FEM

As presented generally in [Chapter 3](#), when a linear compatible displacement field along the boundary of the smoothing domains is used, the smoothed strain-displacement matrix $\bar{\mathbf{B}}_l$ can be computed using Eq. (3.10) with only shape function values at mid-segment-points (Gauss points) along segments $\Gamma_{k,p}^s \in \Gamma_k^s$ of smoothing domains. The shape function value at each Gauss point is evaluated by a simple average using those of the two related endpoints that bound the segment containing that Gauss point. For example, the values of the shape functions at point #g1 on the segment 1-A shown in Figure 6.3 are evaluated by averaging the values of shape functions of two related nodes on the segment: points #1 and #A. Therefore, in order to facilitate the evaluation of shape function values at Gauss points in the ES-FEM, we first need to evaluate the shape

function values at the endpoints of segments such as field nodes (#1, #6, etc) and central points (#A, #B, etc) shown in Figure 6.3.

For an ES-FEM model using n -sided polygonal elements, the shape function constructed in Section 3.2 is used. These shape functions are obviously linear compatible along the boundary of smoothing domains associated with edges. The evaluation of the shape function values at the endpoints of segments shown in Figure 6.3 is quite straightforward.

Figure 6.3 and Table 6.1 give explicitly the shape function values at different points of the smoothing domain associated with the edge 1-6. The number of support nodes for the smoothing domain is 9 (from #1 to #9). We have 4 segments $\Gamma_{k,p}^s$ on Γ_k^s (1A, A6, 6B, B1). Each segment needs only one Gauss point, and therefore, there are a total of 4 Gauss points (g_1, g_2, g_3, g_4) used for the entire smoothing domain Ω_k^s associated with edge k , and the shape function values at these 4 Gauss points can be tabulated in Table 6.1 by simple inspection.

It may be again mentioned that no extra degrees of freedom are associated with these points. In other words, these points carry no additional field variables. For the linear triangular elements, the smoothed strain-displacement matrix $\bar{\mathbf{B}}_l$ can be computed by one of two ways: Eq. (3.10) or Eq. (6.3).

6.5 A smoothing-domain-based selective ES/NS-FEM

The ES-FEM models formulated above is subjected to the volumetric locking. Therefore, it can not be used directly to solve problems with nearly incompressible materials with the Poisson's ratio close to 0.5. On the other hand, we know that the NS-FEM formulated in Chapter 5 is naturally immune from the volume locking [78]. It is therefore making a good sense to combine the NS- and ES-FEM formulations to construct

a smoothing-domain-based selective ES/NS-FEM that can overcome the volumetric locking problem and yet with good performance.

In this section, such a smoothing-domain-based selective scheme will be used in the combined formulation of ES/NS-FEM. We apply two different types of smoothing domains selectively for the two different material “parts” (μ -part and λ -part). Since the node-based smoothing domains used in the NS-FEM were found effectively in overcoming volumetric locking, and the λ -part is known as the culprit of the volumetric locking, we simply use the node-based domains for the λ -part. Because the volumetric locking has nothing to do with the μ -part, we use the edge-based domains (ES-FEM) for the μ -part. Such a procedure is simple and easy to implement, and the stiffness matrix of the smoothing-domain-based selective ES/NS-FEM model can be simply written as

$$\bar{\mathbf{K}} = \underbrace{\sum_{i=1}^{N_{eg}} (\bar{\mathbf{B}}_{1,i})^T \mathbf{D}_1 \bar{\mathbf{B}}_{1,i} A_{1,i}^s}_{\bar{\mathbf{K}}_1^{\text{ES-FEM}}} + \underbrace{\sum_{j=1}^{N_n} (\bar{\mathbf{B}}_{2,j})^T \mathbf{D}_2 \bar{\mathbf{B}}_{2,j} A_{2,j}^s}_{\bar{\mathbf{K}}_2^{\text{NS-FEM}}} \quad (6.15)$$

where $\bar{\mathbf{B}}_{1,i}$ and $A_{1,i}^s$ are the smoothed strain-displacement matrix and area of the smoothing domain $\Omega_{1,i}^s$ associated with edge i ; $\bar{\mathbf{B}}_{2,j}$ and $A_{2,j}^s$ are the smoothed strain-displacement matrix and area of the smoothing domain $\Omega_{2,j}^s$ associated with node j ; \mathbf{D}_1 and \mathbf{D}_2 are the component material matrices decomposed from the material matrix \mathbf{D} as presented by Eqs. (4.15) and (4.16); and N_n is the total number of nodes of the whole problem domain. The formulation of $\bar{\mathbf{K}}_1^{\text{ES-FEM}}$ follows simply Eq. (6.2), and that of $\bar{\mathbf{K}}_2^{\text{NS-FEM}}$ following Eq. (5.2).

6.6 Numerical implementation

In the numerical implementation of the ES-FEM, the value of strains (or stresses) at the node i will be the averaged value of strains (or stresses) of the smoothing domains Ω_k^s associated with edges k around node i , and are computed numerically by

$$\bar{\boldsymbol{\varepsilon}}_i = \frac{1}{A_{eg}^i} \sum_{k=1}^{n_{eg}^i} \bar{\boldsymbol{\varepsilon}}_k A_k^s \quad (6.16)$$

where n_{eg}^i is the total number of edges connecting directly to node i ; $A_{eg}^i = \sum_{k=1}^{n_{eg}^i} A_k^s$ is the total area of all smoothing domains Ω_k^s associated with edge k around the node i ; and $\bar{\boldsymbol{\varepsilon}}_k$ and A_k^s are, respectively, the smoothing strain and the area of the smoothing domain Ω_k^s associated with edge k around node i .

Note that because linear elements are used, the strains in the elements are constants, we can use the same methods for the evaluation of the strains (or stresses) at nodes by the FEM, which give the identical results as those of Eq. (6.16) by the ES-FEM.

6.6.1 Rank analysis for the ES-FEM stiffness matrix

Property 6.1 (Spatial stability): the ES-FEM with n -sided polygonal elements possesses only “legal” zero energy modes that represent the rigid motions, and there exists no spurious zero-energy mode. Therefore, it is spatially stable.

The spatial stability of the ES-FEM is ensured by the following key reasons:

- i) The total number of edges is always bigger than that of nodes for any discretization.

Therefore the number of smoothing domains N_s is always much larger than the minimum number of smoothing domains N_s^{\min} presented in [Section 3.3](#).

- ii) The numerical integration used to evaluate Eq. (6.2) in the ES-FEM satisfies the necessary condition given in Section 6.1.3 in Ref [67]. This is true for all possible ES-FEM models, as detailed in Table 6.2.
- iii) The edge-based smoothing domains are independent with each other, and hence the strain smoothing operation ensures linearly independent columns (or rows) in the stiffness matrix [69].
- iv) The shape functions used in the ES-FEM are of partition of unity, which ensures a proper representation of the rigid motions.

Due to the above-mentioned reasons, no deformed zero-energy mode will exist in an ES-FEM. In other words, any deformation (except the rigid motions) will result in strain energy in an ES-FEM model (we assume, as always, the material is stable).

Note also that for any type of element mesh, the number of edges are always larger or equal the number of nodes. Therefore, the ES-FEM model is always “stiffer” than the NS-FEM for the same element mesh, which explains partially why the ES-FEM is temporally stable (more discussion later) and the NS-FEM is not.

6.6.2 Temporal stability of the ES-FEM-T3

Property 6.2 (Temporal stability): There exists no spurious non-zero energy modes in an ES-FEM-T3 model, and thus it is temporally stable.

In the standard FEM-T3, the shape functions are linear and hence the compatible strain field in an element is constant. Therefore, only one Gauss point is needed to perform the domain integration for the weak form for each element. This implies that the number of Gauss points used in the entire problem domain equals to the number of elements. Such an FEM-T3 model is known temporally stable in dynamic analysis and has no spurious non-zero energy modes.

In the ES-FEM using triangular meshes (ES-FEM-T3), the smoothing domains used are associated with edges of the elements and the strain (or stress) is constant over each smoothing domain. Hence, for stability considerations, each smoothing domain can be viewed equivalent to one Gauss point in terms of sampling the integrand in the weak form. Because the number of edges is always larger than the number of elements in any ES-FEM models, the number of samplings in an ES-FEM-T3 is always larger than that in the standard FEM-T3. Therefore, the ES-FEM-T3 must be stable temporally and should have no spurious non-zero energy modes, and is well suited for the dynamic analyses.

Note that, in the NS-FEM, smoothing domains associated with the node is employed to calculate the stiffness matrix. This works well for static problems. However, for vibration analysis, the NS-FEM is unstable because of the presence of spurious non-zero energy modes [78]. This is because the number of nodes is usually much smaller than the number of elements, and hence there is a chance for spurious modes to appear at a higher-energy level. This phenomena is quite similar to the under-integration of the weak form inherent in the nodal integration approach of meshfree methods. The temporal instability, therefore, has been one of the main concerns of NS-FEM and nodal integrated meshfree methods [99, 124, 125]. The simplest solution is to use the edge-based smoothing domains.

6.6.3 Standard patch test

Standard patch tests conducted in the NS-FEM, [Section 5.6.2](#), are now performed for n -sided polygonal and triangular elements as shown in Figure 6.4. The numerical results show that the ES-FEM models pass the standard patch test within machine precision.

6.6.4 Mass matrix for dynamic analysis

In dynamic analysis using the ES-FEM-T3, we can use the usual consistent mass matrix defined in Eq. (6.6). For computational efficiency purposes, the well-known lumped mass matrix for the linear triangular elements Ω_i^e can also be used.

$$[\mathbf{M}]_i^e = \frac{\rho t A_i^e}{3} [\mathbf{I}] \quad (6.17)$$

where $[\mathbf{I}]$ is the identity matrix of size 6 by 6, A_i^e is the area of the element, ρ and t are the mass density and the thickness of the element, respectively. The diagonal form of lumped mass matrix gives the superiority in terms of efficiency in computation over the consistent mass matrix in solving transient dynamics problems.

6.7 Numerical examples

In this section, some examples will be presented to demonstrate the properties of the ES-FEM models. For triangular elements, the ES-FEM-T3 results will be compared with those of the NS-FEM-T3, FEM-T3, FEM-Q4, CS-FEM-Q4 ($n_s = 4$) and FEM using 8-node quadratic elements (FEM-Q8). For the n -sided polygonal elements, the standard FEM model is not applicable, and hence the n ES-FEM results will be compared with those of n CS-FEM and n NS-FEM, using the same meshes.

For the triangular and 4-node quadrilateral elements, the displacement and energy norms are given by Eqs. (4.18) and (4.19), respectively. In the calculation of Eq. (4.19) for the ES-FEM-T3, recovery strain fields $\bar{\boldsymbol{\varepsilon}}^R$ defined in Eq. (5.16) is used as the final numerical strain field. For the n -sided polygonal elements, the displacement norm is given by Eq. (4.27), and the energy norm is given simply by

$$e_e = \left(\frac{1}{2} \sum_{k=1}^{N_s} (\boldsymbol{\varepsilon} - \bar{\boldsymbol{\varepsilon}}_k)^T \mathbf{D} (\boldsymbol{\varepsilon} - \bar{\boldsymbol{\varepsilon}}_k) A_k^s \right)^{1/2} \quad (6.18)$$

where $\bar{\boldsymbol{\varepsilon}}_k$ and A_k^s are the smoothing strain and the area of the smoothing domain Ω_k^s , respectively; $\boldsymbol{\varepsilon}$ is the analytical strain computed at the nodes (for comparison with the n NS-FEM), or at edge-mid-points (for comparison with the n ES-FEM), or at the central points of smoothing domains Ω_k^s (for comparison with the n CS-FEM); N_s is the total number of the smoothing domains.

6.7.1 A rectangular cantilever loaded at the end: a static analysis

The benchmarking problem of a rectangular cantilever loaded at the end described in [Example 4.10.1](#) is again used to examining the ES-FEM models. The geometry and boundary conditions of the cantilever is plotted in [Figure 4.7](#). The domain discretization with n -sided polygonal, quadrilateral and triangular elements are shown in [Figure 4.8](#) and [Figure 5.4](#), respectively. The exact strain energy of the problem is known as 4.4746 Nm.

[Figure 6.5](#) and [Figure 6.6](#) compare the results of displacements and relative errors of the ES-FEM-T3 with the FEM-T3, NS-FEM-T3 and FEM-Q4. It is shown that the FEM-T3 is very stiff, and the NS-FEM-T3 is very soft compared to the exact solution. The ES-FEM-T3 is stiffer than the NS-FEM-T3 and softer than the FEM-T3, and the ES-FEM-T3 solution is very close to the exact solution. Compared with all methods, the ES-FEM-T3 performs the best and even better than the FEM-Q4. [Figure 6.7](#) shows that all the computed stresses using the ES-FEM-T3 agree excellently with the analytical solutions.

The convergence of the strain energy is shown in [Table 5.4](#) and plotted in [Figure 6.8](#). It is seen that the FEM models behave overly-stiff and hence give lower bounds, and the NS-FEM-T3 behaves overly-soft and gives an upper bound. The solution of CS-FEM-Q4 is the most accurate. Although triangular elements are used, the ES-FEM-T3 result is as good as that of the CS-FEM-Q4.

The convergence of error in displacement norm is presented in [Table 5.6](#) and plotted in [Figure 6.9](#). It is seen that the ES-FEM-T3 stands out clearly. The error of displacement

norm of the ES-FEM-T3 is the smallest among all the compared models when the fine meshes are used. When the finest mesh ($h = 1$) is used, the error of the ES-FEM-T3 is about $1/64$ of the FEM-T3, $1/9$ of the FEM-Q4 and even $2/5$ of the CS-FEM-Q4. In terms of convergence rate, super-convergence is observed for the ES-FEM-T3 with a rate of 3.3 that is even much larger than the theoretical value of 2.0 for linear displacement models based on weak formulation. It is important to note that the super-convergence here is in terms of the displacement norm, which is very difficult to obtain for the compatible FEM models.

The convergence of the error in energy norm is presented in [Table 5.7](#) and plotted in [Figure 6.10](#). It is seen again that the S-FEM models stand out clearly. When the finest mesh ($h = 1$) is used, the solution accuracy of the ES-FEM-T3 is not as good as those of CS-FEM-Q4 and NS-FEM-T3, but it is still much better than that of the FEM-T3 and FEM-Q4. The solution error of the ES-FEM-T3 is about $1/6$ of the FEM-T3 and $2/5$ of the FEM-Q4. In terms of the convergence rate, super-convergence is observed for the ES-FEM-T3 with a rate of 1.52 that is much larger than the theoretical value of 1.0 for linear displacement models.

[Figure 6.11](#) compares the computation time of different methods using the same direct full-matrix solver. It is found that with the same distribution of nodes, the computation time of the ES-FEM-T3 is only shorter than that of the NS-FEM-T3. However, when the efficiency of computation (computation time for the same accuracy) in terms of both displacement and energy norms is considered as shown in [Figure 6.12](#) and [Figure 6.13](#), the ES-FEM-T3 model stands out clearly as a winner. Even though the ES-FEM-T3 uses triangular elements, it still wins by its super-convergence, as shown in [Figure 6.12](#). One can therefore expect that when finer mesh is used, the performance of ES-FEM-T3 will be even better. Because the ES-FEM-T3 works well with the triangular elements which are

very preferred in automated mesh generation, it has a clear advantage over the FEM-Q4 and CS-FEM-Q4 models in the development of adaptive and automatic solution tools.

For the n -sided polygonal elements, Figure 6.14 shows that all the computed stresses using the n ES-FEM agree well with the analytical solutions. The convergence of the strain energy is shown in Table 5.5 and plotted in Figure 6.15. It is seen that the n ES-FEM is the most accurate, while the n CS-FEM model behaves overly-stiff and hence gives a lower bound, and n NS-FEM behaves overly-soft and gives an upper bound.

The convergence of displacement norm is presented in Table 6.3 and plotted in Figure 6.16. It is seen that the n ES-FEM stands out clearly. The error of displacement norm of the n ES-FEM is the smallest among all the three models. When the finest mesh ($h = 1$) is used, the error of the n ES-FEM is about 1/4 of the n CS-FEM and 1/2 of the n NS-FEM. In terms of convergence rate, the n CS-FEM ($r = 1.85$) and n NS-FEM ($r = 1.71$) have a numerical rate smaller than the theoretical value of 2.0, while the rate of the n ES-FEM is $r = 2.16$, larger than the theoretical value.

The convergence of the error in energy norm is presented in Table 6.4 and plotted in Figure 6.17. Again, it is seen that the n ES-FEM stands out clearly. The error of energy norm of the n ES-FEM is the smallest among three models. When the finest mesh ($h = 1$) is used, the error of the n ES-FEM is about 2/5 of the n CS-FEM and 3/4 of the n NS-FEM. In terms of convergence rate, the n CS-FEM ($r = 0.93$) and n NS-FEM ($r = 0.94$) have a numerical rate smaller than the theoretical value of 1.0, while the rate of the n ES-FEM is larger with $r = 1.01$.

6.7.2 Infinite plate with a circular hole: a static analysis

The infinite plate with a circular hole described in Example 4.10.2 is used here to examine the ES-FEM models. The geometry and boundary conditions of the problem is

plotted in Figure 4.19. Figure 4.24 and Figure 5.10 give the discretization of the domain using 4-node quadrilateral, n -sided polygonal and triangular elements, respectively. The exact strain energy of the problem is known as 1.1817×10^{-2} Nm.

Figure 6.18 and Figure 6.19 show the comparison of displacements of the ES-FEM-T3 with the FEM-T3, NS-FEM-T3 and FEM-Q4. It is again seen that the FEM-T3 model is very stiff while the NS-FEM-T3 model is very soft compared to the exact model. The results of the ES-FEM-T3 are best and even better than those of the FEM-Q4. From Figure 6.20, it is observed that all the computed stresses using the ES-FEM-T3 agree well with the analytical solutions.

The convergence of the strain energy is shown in Table 5.8 and plotted in Figure 6.21. It is seen that the FEM models give lower bounds, the NS-FEM-T3 gives an upper bound, and the ES-FEM-T3 is the most accurate and even better than the CS-FEM-Q4.

The convergence of the error in displacement norm is shown in Table 5.10 and plotted in Figure 6.22. It is again seen that the ES-FEM-T3 stands out clearly. The error of displacement norm of the ES-FEM-T3 is the smallest among all the compared models. When the finest mesh ($h = 0.1969$) is used, the error of the ES-FEM-T3 is about 1/5 of the FEM-T3, 3/4 of the FEM-Q4 and even a little smaller than that of the CS-FEM-Q4. In terms of convergence rate, the rates of all methods, except the FEM-T3, are slightly larger than the theoretical value of 2.0.

The convergence of the error in energy norm is shown in Table 5.11 and plotted in Figure 6.23. It is seen that the S-FEM models stand out clearly. When the finest mesh ($h = 0.1969$) is used, the error of the ES-FEM-T3 is only worse than that of the NS-FEM-T3. This error is almost equal that of the CS-FEM-Q4, and is much better than that of the FEM-T3 and FEM-Q4. It is about 1/5 of the FEM-T3 and 2/5 of the FEM-Q4. In terms of convergence rate, the super-convergence is again observed for the ES-FEM-T3 with a rate

of 1.83 that is quite close to the optimal rate of 2.0 for equilibrium model, and much larger than the theoretical value of 1.0.

Figure 6.24 and Figure 6.25 plot the results obtained using n -sided polygonal elements. It is observed that all the computed displacements and stresses agree well with the analytical solutions. The convergence of the strain energy is shown in Table 5.9 and plotted in Figure 6.26. Again the n ES-FEM is found most accurate, while the n CS-FEM model gives a lower bound and n NS-FEM gives an upper bound.

The error in displacement norm is shown in Table 6.5 and plotted in Figure 6.27. In term of accuracy, it is seen that the n ES-FEM stands out clearly. The error of displacement norm of the n ES-FEM is the smallest among three models. When the finest mesh ($h = 0.1969$) is used, the error of the n ES-FEM is about 1/8 of the n NS-FEM and 1/2 of the n CS-FEM. In terms of convergence rate, the n ES-FEM ($r = 1.69$) is less than that of the n CS-FEM ($r = 2.04$) but still larger than that of the n NS-FEM ($r = 1.32$).

The convergence of the error in energy norm is presented in Table 6.6 are plotted in Figure 6.28. Again, it is seen that the n ES-FEM stands out clearly. The error of energy norm of the n ES-FEM is the smallest among three models. When the finest mesh ($h = 0.1969$) is used, the error of the n ES-FEM is about 1/4 of the n CS-FEM and 1/3 of the n NS-FEM. In terms of convergence rate, the super-convergence is again observed for the n ES-FEM with a rate of 1.98 that is almost the optimal rate of 2.0 for equilibrium model, and twice of the theoretical value of 1.0 for linear displacement models based on weak formulations.

Figure 6.29 shows the displacement norm against Poisson's ratio changing from 0.4 to 0.4999999. The results show that the smoothing-domain-based selective n ES/NS-FEM and ES-/NS-FEM-T3 models detailed in Section 6.5 can overcome the volumetric locking for nearly incompressible materials. Although the n NS-FEM and NS-FEM-T3 models are

also immune for the volumetric locking, the smoothing-domain-based selective n ES/NS-FEM and ES-/NS-FEM-T3 models give better results than those of the n NS-FEM and NS-FEM-T3, due to the contribution from the n ES-FEM and ES-FEM-T3 formulations.

Compared to the results given in Figure 5.16, it is observed that the ES-FEM model locks at the Poisson's ratio of 0.49, while the FEM model locks at the Poisson's ratio of 0.40. This shows that the smoothing operation used in the ES-FEM helps to reduce quite significantly the volumetric locking. To avoid the volumetric locking entirely, the selective ES/NS-FEM models should be used.

6.7.3 A cylindrical pipe subjected to an inner pressure: a static analysis

Figure 6.30 shows a thick cylindrical pipe, with internal radius $a = 0.1\text{m}$, external radius $b = 0.2\text{m}$, subjected to an internal pressure $p = 600\text{kN/m}^2$. Because of the axis-symmetry, we model only one quarter of cylinder shown in Figure 6.30. Figure 6.31 and Figure 6.32 give, respectively, the discretization of the domain using 4-node quadrilateral, 3-node triangular and n -sided polygonal elements. Plane strain condition is considered with Young's modulus $E = 21000\text{kN/m}^2$, Poisson's ratio $\nu = 0.3$. Symmetric conditions are imposed on the left and bottom edges, and outer boundary is set traction free. The exact solution for the stress components is [148]

$$\sigma_r(r) = \frac{a^2 p}{b^2 - a^2} \left(1 - \frac{b^2}{r^2}\right) \quad ; \quad \sigma_\varphi(r) = \frac{a^2 p}{b^2 - a^2} \left(1 + \frac{b^2}{r^2}\right) \quad ; \quad \sigma_{r\varphi} = 0 \quad (6.19)$$

while the exact solution of radial and tangential displacements are given by

$$u_r(r) = \frac{(1+\nu)a^2 p}{E(b^2 - a^2)} \left[(1-2\nu)r + \frac{b^2}{r} \right] \quad ; \quad u_\varphi = 0 \quad (6.20)$$

where (r, φ) are the polar coordinates and φ is measured counter-clockwise from the positive x -axis.

From Figure 6.33 and Figure 6.34, it is observed that all the computed displacements and stresses using the ES-FEM-T3 agree very well with the analytical solutions. Table 6.7 and Figure 6.35 show the convergence of strain energy of ES-FEM-T3 in comparison with different methods. It is again seen that the FEM models give lower bounds, the NS-FEM-T3 gives an upper bound, and the ES-FEM-T3 is the most accurate and even better than the CS-FEM-Q4.

The convergence of the error in displacement norm is shown in Table 6.8 and plotted in Figure 6.36. When the finest mesh ($h = 0.009$) is used, the error of displacement norm of the ES-FEM-T3 is only worse than that of the CS-FEM-Q4. This error is much better than that of the FEM-T3 and even better than that of the FEM-Q4. It is about $1/6$ of the FEM-T3 and $4/5$ of the FEM-Q4. In term of the convergence rate, the super-convergence is again observed for the ES-FEM-T3 with a rate of 2.36 that is larger than the theoretical value of 2.0. This rate is also the highest rate among the compared methods.

The convergence of the error in energy norm is shown in Table 6.9 are plotted in Figure 6.37. It is seen that the S-FEM models stand out clearly. When the finest mesh ($h = 0.009$) is used, the error of the ES-FEM-T3 is only worse than that of the NS-FEM-T3. This error is almost equal that of the CS-FEM-Q4, and is much better than that of the FEM-T3 and FEM-Q4. It is about $3/10$ of the FEM-T3 and $1/2$ of the FEM-Q4. In terms of convergence rate, the super-convergence is again observed for the ES-FEM-T3 with a rate of 1.42 that is much larger than the theoretical value of 1.0.

Figure 6.38 plot the results obtained using n -sided polygonal elements. It is observed that all the computed displacements and stresses agree well with the analytical solutions. The convergence of the strain energy is shown in Table 6.10 and Figure 6.39. Again the n ES-FEM is found most accurate, while the n CS-FEM model gives a lower bound and n NS-FEM gives an upper bound.

The error in displacement norm is shown in Table 6.11 and plotted in Figure 6.40. In term of accuracy, it is seen that the n ES-FEM stands out clearly. The error of displacement norm of the n ES-FEM is the smallest among three models. When the finest mesh ($h = 0.0074$) is used, the error of the n ES-FEM is about $1/6$ of the n NS-FEM and $2/5$ of the n CS-FEM. In terms of convergence rate, the super-convergence is observed for the n ES-FEM with a rate of 2.63 that is much larger than the theoretical value of 2.0. This rate is also much larger than those of the n CS-FEM ($r = 1.84$) and n NS-FEM ($r = 1.89$).

The convergence of the error in energy norm is presented in Table 6.12 and plotted in Figure 6.41. Again, it is seen that the n ES-FEM stands out clearly. The error of energy norm of the n ES-FEM is the smallest among three models. When the finest mesh ($h = 0.0074$) is used, the error of the n ES-FEM is about $1/2$ of those of the n CS-FEM and the n NS-FEM. In terms of convergence rate, the weak super-convergence is observed for the n ES-FEM with a rate of 1.15. This rate is also much larger than those of the n CS-FEM ($r = 0.95$) and the n NS-FEM ($r = 0.99$).

Figure 6.42 shows the displacement norm against Poisson's ratio changing from 0.4 to 0.4999999. The results again show that the smoothing-domain-based selective n ES/NS-FEM and ES-/NS-FEM-T3 models in Section 6.5 can overcome the volumetric locking for nearly incompressible materials. Although the n NS-FEM and NS-FEM-T3 models are also immune for the volumetric locking, the smoothing-domain-based selective n ES/NS-FEM and ES-/NS-FEM-T3 models give better results than those of the n NS-FEM and NS-FEM-T3, due to the contribution from the n ES-FEM and ES-FEM-T3 formulations.

6.7.4 Free vibration analysis of a shear wall

In this example, a shear wall with four square openings (see Figure 6.43) is analyzed, which has been solved using the BEM by Brebbia *et al.* [21]. The bottom edge of the wall

is fully clamped. Plane stress case is considered with $E = 10,000$, $\nu = 0.2$, $t = 1.0$ and $\rho = 1.0^*$. Two types of meshes of triangular and quadrilateral elements are used as shown in Figure 6.44. Numerical results using the FEM-Q8 with 6104 nodes and 1922 elements for the same problem are computed and used as reference solutions, in place of the unavailable exact solutions.

Table 6.13 lists the first 12 natural frequencies, and the first 12 modes using the NS-FEM-T3 and ES-FEM-T3 are plotted in Figure 6.45 and Figure 6.46. It is observed that (1) the ES-FEM-T3 does not have any spurious non-zero energy modes and all modes are physical; (2) the NS-FEM-T3 produces non-physical spurious modes at high energy level; (3) the natural frequencies obtained using the ES-FEM-T3 is much larger than those of the FEM-T3 that is known overly-stiff; (4) the ES-FEM-T3 results are the closest to the reference solution, and they converge faster even than the FEM-Q4 with the same distribution of nodes used. This example confirms that the ES-FEM-T3 model possesses a very close-to-exact stiffness.

6.7.5 Free vibration analysis of a connecting rod

A free vibration analysis of a connecting rod shown in Figure 6.47 is performed. The plane stress problem is considered with material parameters of $E = 10 \times 10^9 \text{ N/m}^2$, $\nu = 0.3$, $\rho = 7.8 \times 10^3 \text{ kg/m}^3$. The nodes on the left inner circumference are fixed in two directions. Two types of meshes of triangular and quadrilateral elements are used, as shown in Figure 6.48. Numerical results using the FEM-Q4 and FEM-Q8 for the same problem are computed and used as reference solutions for comparison purposes.

The results are listed in Table 6.14. It is observed that the ES-FEM-T3 gives the

* In this thesis, we often choose to use non-dimensional parameters because the purpose of the examples is just to examine our numerical results, and no much physical implications. Any set of physical units is applicable to the results, as long as these units are consistent for all the inputs and outputs.

comparable results as those of the FEM-Q4 using more nodes than the ES-FEM-T3. Again, Figure 6.49 and Figure 6.50 show that the ES-FEM-T3 does not have any spurious non-zero energy modes, while the NS-FEM-T3 has. This example re-confirms the fact that the ES-FEM-T3 model is temporally stable, has a very close-to-exact stiffness, and is expected to perform well in transient vibration analysis.

6.7.6 Transient vibration analysis of a cantilever beam

A benchmark problem of a cantilever beam is investigated using the ES-FEM-T3 model with the Newmark method for time stepping. The beam is subjected to a tip harmonic loading $f(t) = \cos \omega_f t$ in y -direction. Plane strain problem is considered with non-dimensional parameters as $L=4.0$, $H=1.0$, $t=1.0$, $E=1.0$, $\nu=0.3$, $\rho=1.0$, $\alpha=0.005$, $\beta=0.272$, $\omega_f=0.05$, $\theta=0.5$. The domain of the beam is represented with 10×4 elements. Three FEM models of FEM-T3, FEM-Q4 and FEM-Q8 are also used in the analysis for comparison purposes. The time step for time integration is set at $\Delta t=1.57$. From the dynamic responses in Figure 6.51, it is seen that the amplitude of the ES-FEM-T3 is closer to that of the FEM-Q8 as compared to the FEM-Q4. This shows that the ES-FEM-T3 using triangular elements can be applied to transient vibration analysis to deliver results of excellent accuracy. This is partially due to the fact that the ES-FEM-T3 model has very close-to-exact stiffness, which we have observed in all these free vibration analyses examples.

6.7.7 Transient vibration analysis of a spherical shell

As shown in Figure 6.52, a spherical shell is studied that subjected to a concentrated time-dependent loading at its apex. Due to the symmetry, only half of the spherical shell is modeled, as shown in Figure 6.53. Two types of meshes of triangular and quadrilateral

elements are created for the half model. For the model of triangular elements, we deliberately made it asymmetric. Non-dimensional numerical parameters are used:

$$R=12, t=0.1, \phi = 10.9^\circ, \theta = 0.5, E=1.0, \nu=0.3, \text{ and } \rho=1.0.$$

The time-dependence of the loading is first specified in the harmonic form of $f(t) = \cos \omega_f t$ and its dynamic responses are plotted in Figure 6.54 for the case of $\omega_f = 0.05$ and time step $\Delta t = 5$. No damping effect is included in this case. Again, it is seen that the amplitude of the ES-FEM-T3 is much more accurate than that of the FEM-T3 model and comparable to that of the FEM-Q4 model with the same set of nodes.

Next, a Heaviside step load $f(t) = 1$ is added at apex since $t=0$. Without damping, it is seen from Figure 6.55 that the deflection at apex approaches in a oscillatory fashion a constant value with the increase in time. With an inclusion of damping ($\alpha = 0.005$, $\beta = 0.272$), the response is damped out with time as expected.

6.8 Remarks

In this chapter, an edge-based S-FEM (ES-FEM) model is presented for stable and accurate solutions to static and dynamic problems of 2D solids. Through the theoretical analyses, formulation and numerical examples, some conclusions can be drawn as follows:

- (a) The ES-FEM can use general n -sided polygonal elements including triangular elements, and is spatially stable. The extension of the method for 3D problems using tetrahedral elements is also straightforward, and will be done in the next chapter.
- (b) In the ES-FEM using n -sided polygonal elements, field gradients are computed directly using only shape functions themselves at some particular points along segments of boundary of the smoothing domains. The values of shape functions for

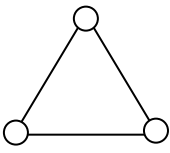
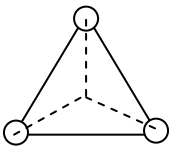
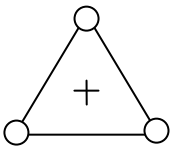
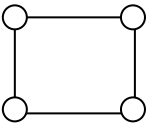
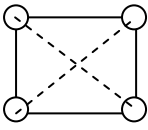
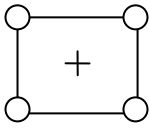
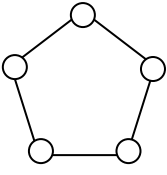
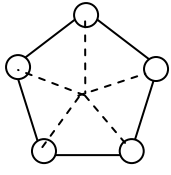
the discrete points of an n -sided polygonal element are defined in a simple linear interpolation and averaging manner.

- (c) The ES-FEM-T3 using triangular elements is stable and accurate without using any parameter for stabilization. The formulation is straightforward and the implementation is as easy as the FEM, without the increase of degrees of freedom. The ES-FEM-T3 often shows super-convergence behavior with ultra-accurate results: the numerical results of the ES-FEM-T3 using triangular elements are found even more accurate in both displacement and energy norms than the FEM using quadrilateral elements with the same distribution of nodes.
- (d) With the same distribution of nodes and the same direct solver, the computation time of the ES-FEM-T3 is longer than that of the FEM-Q4. However, when the computational efficiency (computation time for the same accuracy) and convergence rates in both displacement and energy norms are considered, the ES-FEM-T3 is the most superior.
- (e) Because the rates of convergence of the solution of the ES-FEM models are higher than the FEM counterparts, the computational efficiency of the ES-FEM becomes more significant when the mesh is refined.
- (f) A smoothing-domain-based selective ES/NS-FEM is effective in overcoming the volumetric locking for problems of nearly incompressible materials.
- (g) For the free vibration analysis, the ES-FEM-T3 using triangular elements gives the more accurate results and higher convergence rate than the FEM-Q4. No spurious non-zero energy modes were found in vibration analysis and hence the ES-FEM-T3 is found stable temporally for all these examples studied.

- (h) For the forced vibration analysis, vibration period obtained using the ES-FEM-T3 using triangular elements is more accurate compared to the FEM-Q4, and the vibration amplitude is closer to that of the higher-order FEM-Q8.
- (i) For n -sided polygonal elements, results of the n ES-FEM found agree well with exact solutions and often much better than those of others existing methods.

The ES-FEM has been developed for 2D piezoelectric [112], 2D visco-elastoplastic [106], plate [113] adaptive [26], and primal-dual shakedown analyses [149]. More general models based on meshfree settings, such as the ES-PIM can be found in [84].

Site	Node 1	Node 2	Node 3	Node 4	Node 5	Node 6	Node 7	Node 8	Node 9	Description
1	1.0	0	0	0	0	0	0	0	0	Field node
2	0	1.0	0	0	0	0	0	0	0	Field node
3	0	0	1.0	0	0	0	0	0	0	Field node
4	0	0	0	1.0	0	0	0	0	0	Field node
5	0	0	0	0	1.0	0	0	0	0	Field node
6	0	0	0	0	0	1.0	0	0	0	Field node
7	0	0	0	0	0	0	1.0	0	0	Field node
8	0	0	0	0	0	0	0	1.0	0	Field node
9	0	0	0	0	0	0	0	0	1.0	Field node
<i>A</i>	1/6	1/6	1/6	1/6	1/6	1/6	0	0	0	Centroid of element
<i>B</i>	1/5	0	0	0	0	1/5	1/5	1/5	1/5	Centroid of element
<i>g1</i>	7/12	1/12	1/12	1/12	1/12	1/12	0	0	0	Mid-segment of $\Gamma_{k,p}^s$
<i>g2</i>	1/12	1/12	1/12	1/12	1/12	7/12	0	0	0	Mid-segment of $\Gamma_{k,p}^s$
<i>g3</i>	1/10	0	0	0	0	6/10	1/10	1/10	1/10	Mid-segment of $\Gamma_{k,p}^s$
<i>g4</i>	6/10	0	0	0	0	1/10	1/10	1/10	1/10	Mid-segment of $\Gamma_{k,p}^s$

Table 6.2. Existence of spurious zero energy modes in an element.		
Type of element	ES-FEM	FEM with reduced integration
 <p>Triangle $N_R = 3$</p>	 <p>$n_Q = 3, N_Q = 3 \times n_Q = 9$ $n_t = 3, N_u = 2 \times n_t = 6$ $N_Q > N_u - N_R$ \Rightarrow spurious zero energy modes not possible</p>	 <p>$n_Q = 1, N_Q = 3 \times n_Q = 3$ $n_t = 3, N_u = 2 \times n_t = 6$ $N_Q = N_u - N_R$ \Rightarrow spurious zero energy modes not possible</p>
 <p>Quadrilateral $N_R = 3$</p>	 <p>$n_Q = 4, N_Q = 3 \times n_Q = 12$ $n_t = 4, N_u = 2 \times n_t = 8$ $N_Q > N_u - N_R$ \Rightarrow spurious zero energy modes not possible</p>	 <p>$n_Q = 1, N_Q = 3 \times n_Q = 3$ $n_t = 4, N_u = 2 \times n_t = 8$ $N_Q < N_u - N_R$ \Rightarrow spurious zero energy modes possible</p>
 <p>n-sided polygonal ($n > 4$) $N_R = 3$</p>	 <p>$n_Q = n, N_Q = 3 \times n_Q = 3n$ $n_t = n, N_u = 2 \times n_t = 2n$ $N_Q > N_u - N_R$ \Rightarrow spurious zero energy modes not possible</p>	<p>Not applicable</p>
<p>Note: N_R: number of DOFs of rigid motion n_Q: number of quadrature points/cells N_Q: number of independent equations</p> <p>n_t: number of nodes N_u: number of total DOFs</p>		

Mesh	16×4	24×6	32×8	40×10	48×12
h (m)	4.0	2.0	1.5	1.2	1.0
n CS-FEM	6.21	3.01	1.76	1.13	0.81
n NS-FEM	3.06	1.55	0.98	0.60	0.44
n ES-FEM	2.10	0.77	0.46	0.27	0.19

Mesh	16×4	24×6	32×8	40×10	48×12
h (m)	4.0	2.0	1.5	1.2	1.0
n CS-FEM	0.4718	0.3326	0.2532	0.2025	0.1721
n NS-FEM	0.2588	0.1738	0.1296	0.1001	0.0897
n ES-FEM	0.1956	0.1413	0.1065	0.0782	0.0666

	Mesh 1	Mesh 2	Mesh 3	Mesh 4	Mesh 5
h (m)	0.5468	0.3786	0.2895	0.2343	0.1969
n CS-FEM	1.2895	0.6299	0.3638	0.2335	0.1628
n NS-FEM	2.2983	1.3538	0.9439	0.7201	0.5840
n ES-FEM	0.5015	0.2494	0.1537	0.1039	0.0744

	Mesh 1	Mesh 2	Mesh 3	Mesh 4	Mesh 5
h (m)	0.5468	0.3786	0.2895	0.2343	0.1969
n CS-FEM	5.0119	3.4427	2.5880	2.0613	1.7091
n NS-FEM	4.5090	2.9545	2.1723	1.7047	1.3964
n ES-FEM	3.2525	1.6328	0.9604	0.6242	0.4368

Mesh	6×12	8×16	10×20	12×24	Analytical sol.
DOFs	182	306	462	650	
FEM-T3	0.2531	0.2546	0.2554	0.2558	0.2567
FEM-Q4	0.2560	0.2563	0.2564	0.2565	0.2567
CS-FEM-Q4	0.2563	0.2565	0.2566	0.2566	0.2567
NS-FEM-T3	0.2623	0.2599	0.2588	0.2582	0.2567
ES-FEM-T3	0.2570	0.2569	0.2569	0.2568	0.2567

Mesh	4×8	6×12	8×16	10×20	12×24
h (m)	0.0271	0.0181	0.0136	0.0109	0.0090
FEM-T3	2.11 e-05	9.82 e-06	5.61 e-06	3.61 e-06	2.52 e-06
FEM-Q4	4.14 e-06	1.88 e-06	1.07 e-06	6.84 e-07	4.76 e-07
CS-FEM-Q4	2.79 e-06	1.27 e-06	7.17 e-07	4.60 e-07	3.20 e-07
NS-FEM-T3	2.39 e-05	1.11 e-05	6.39 e-06	4.13 e-06	2.89 e-06
ES-FEM-T3	5.28 e-06	1.88 e-06	9.60 e-07	5.84 e-07	3.94 e-07

Mesh	4×8	6×12	8×16	10×20	12×24
h (m)	0.0271	0.0181	0.0136	0.0109	0.0090
FEM-T3	9.62 e-02	6.57 e-02	4.98 e-02	4.00 e-02	3.35 e-02
FEM-Q4	5.77 e-02	3.87 e-02	2.91 e-02	2.33 e-02	1.94 e-02
CS-FEM-Q4	4.54 e-02	2.58 e-02	1.72 e-02	1.25 e-02	0.96 e-02
NS-FEM-T3	2.76 e-02	1.58 e-02	1.06 e-02	0.77 e-02	0.60 e-02
ES-FEM-T3	4.49 e-02	2.54 e-02	1.69 e-02	1.22 e-02	0.94 e-02

	Mesh 1	Mesh 2	Mesh 3	Mesh 4	Mesh 5	Analytical solution
DOFs	368	616	928	1304	1744	
n CS-FEM	0.2559	0.2562	0.2563	0.2564	0.2565	0.2567
n NS-FEM	0.2592	0.2582	0.2577	0.2574	0.2572	0.2567
n ES-FEM	0.2572	0.2570	0.2569	0.2568	0.2568	0.2567

	Mesh 1	Mesh 2	Mesh 3	Mesh 4	Mesh 5
h (m)	0.0161	0.0124	0.0101	0.0085	0.0074
n CS-FEM	0.3200	0.2154	0.1480	0.1061	0.0758
n NS-FEM	0.9070	0.5362	0.3631	0.2469	0.2063
n ES-FEM	0.2481	0.1127	0.0627	0.0409	0.0318

	Mesh 1	Mesh 2	Mesh 3	Mesh 4	Mesh 5
h (m)	0.0161	0.0124	0.0101	0.0085	0.0074
n CS-FEM	0.0293	0.0240	0.0198	0.0167	0.0140
n NS-FEM	0.0281	0.0210	0.0183	0.0144	0.0130
n ES-FEM	0.0165	0.0122	0.0094	0.0081	0.0067

Model	NS-FEM-T3	ES-FEM-T3	FEM-T3	FEM-Q4	Reference (FEM-Q8) (6104 nodes 1922 elements)	Reference (Brebbia et al. [21])
Nodes: 559 Elements: 476 4-node elements or 952 triangles	1.827	2.050	2.144	2.073	2.011	2.079
	6.511	7.038	7.319	7.096	6.952	7.181
	7.515	7.620	7.651	7.625	7.600	7.644
	10.183	11.743	12.554	11.938	11.471	11.833
	13.733	15.143	15.943	15.341	14.972	15.947
	14.709 (*)	18.214	18.763	18.345	18.066	18.644
	17.032	19.714	20.382	19.876	19.581	20.268
	17.104 (*)	21.994	22.676	22.210	21.872	22.765
	18.360	22.778	23.640	23.001	22.636	
	18.890 (*)	23.349	24.126	23.552	23.293	
	19.450 (*)	25.052	25.534	25.175	25.018	
	19.538 (*)	25.837	26.845	26.071	25.877	
Nodes: 2072 Elements: 1904 4-node elements or 3808 triangles	1.935	2.022	2.063	2.032	2.011	2.079
	6.776	6.976	7.087	6.999	6.952	7.181
	7.566	7.606	7.620	7.609	7.600	7.644
	10.895	11.551	11.880	11.625	11.471	11.833
	14.468	15.019	15.322	15.092	14.972	15.947
	15.324 (*)	18.108	18.317	18.158	18.066	18.644
	17.553	19.619	19.862	19.677	19.581	20.268
	17.834 (*)	21.908	22.197	21.987	21.872	22.765
	19.152	22.681	23.000	22.759	22.636	
	20.511 (*)	23.308	23.569	23.380	23.293	
	21.027 (*)	25.030	25.206	25.073	25.018	
	21.303 (*)	25.875	26.216	25.956	25.877	

(*) spurious non-zero energy modes

Model	NS-FEM-T3	ES-FEM-T3	FEM-T3	Reference (FEM-Q4) (537 nodes 429 eles)	Reference (FEM-Q4) (1455 nodes 1256 eles)	Reference (FEM-Q8) (10002 nodes 3125 eles)
Nodes: 373 Elements: 574 triangles	4.94	5.14	5.32	5.14		5.12
	20.81	22.06	22.94	22.05		21.84
	48.39	49.38	49.70	49.30		49.12
	48.49	52.04	54.06	52.23		51.40
	84.93	92.72	96.86	93.61		91.79
	97.68	109.59	114.31	108.59		106.15
	114.03	132.68	142.45	134.64		130.14
	123.32 (*)	158.24	163.97	159.45		156.14
	143.64 (*)	158.95	169.28	160.59		157.70
	144.66 (*)	201.38	204.58	203.52		200.06
	151.43	204.84	210.12	208.68		204.41
	161.95 (*)	209.28	210.74	209.02		204.99
Nodes: 1321 Elements: 2296 triangles	5.05	5.12	5.21		5.12	5.12
	21.49	21.88	22.27		21.91	21.84
	48.88	49.17	49.35		49.21	49.12
	50.40	51.52	52.49		51.66	51.40
	89.61	91.93	93.84		92.39	91.79
	92.65 (*)	106.85	109.28		107.51	106.15
	103.44	130.55	134.58		131.48	130.14
	125.65	156.35	159.74		157.51	156.14
	151.62 (*)	157.85	159.97		158.69	157.70
	152.01 (*)	200.90	203.35		201.69	200.06
	155.54	204.26	207.50		206.04	204.41
	188.59 (*)	206.53	209.18		209.92	204.99

(*) spurious non-zero energy modes

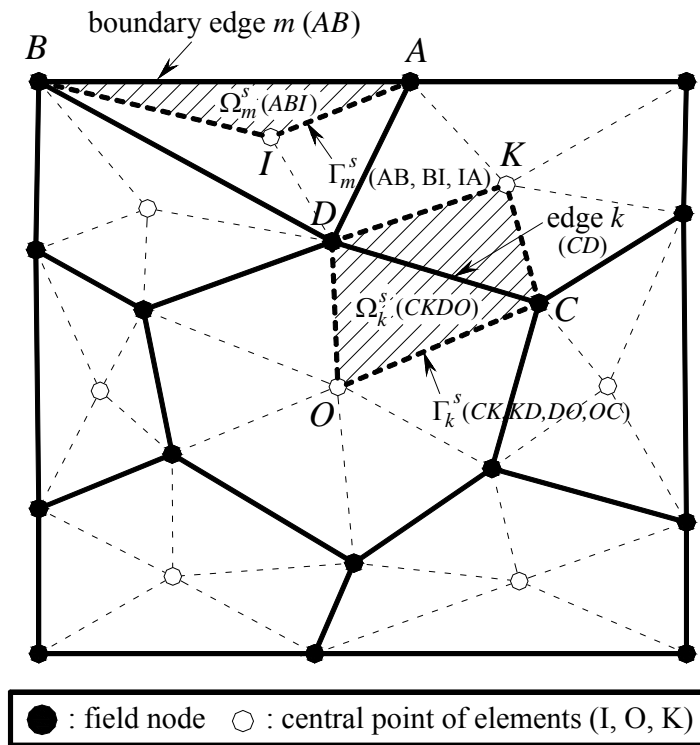


Figure 6.1. ES-FEM settings: domain discretization into arbitrary n -sided polygonal elements, and the smoothing domains created based on the edges of these elements.

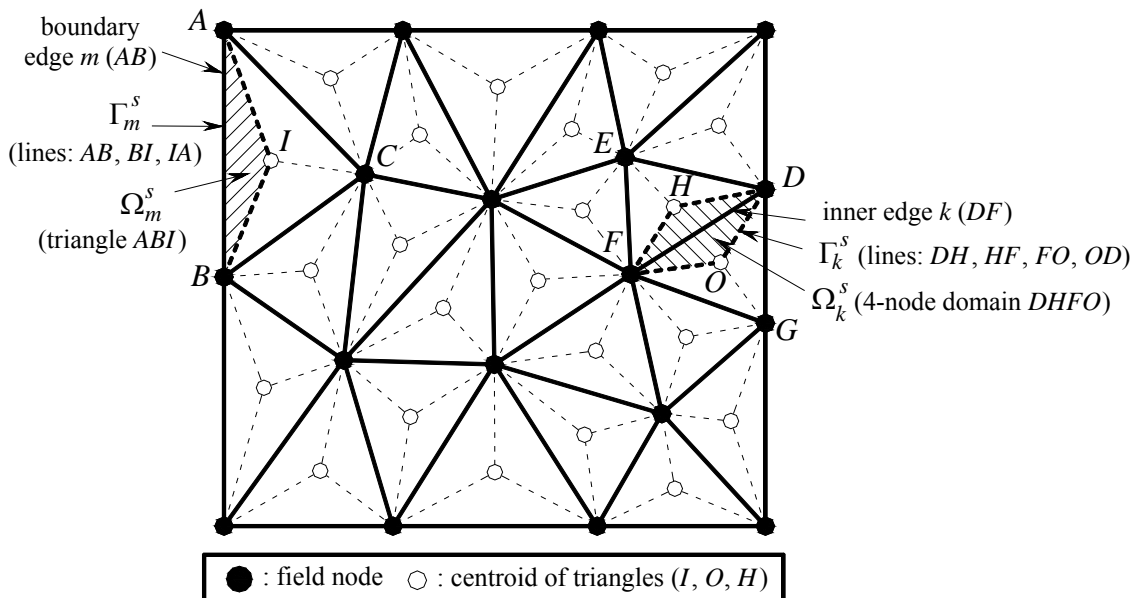


Figure 6.2. ES-FEM-T3 settings: triangular elements (solid lines) and the edge-based smoothing domains (shaded areas).

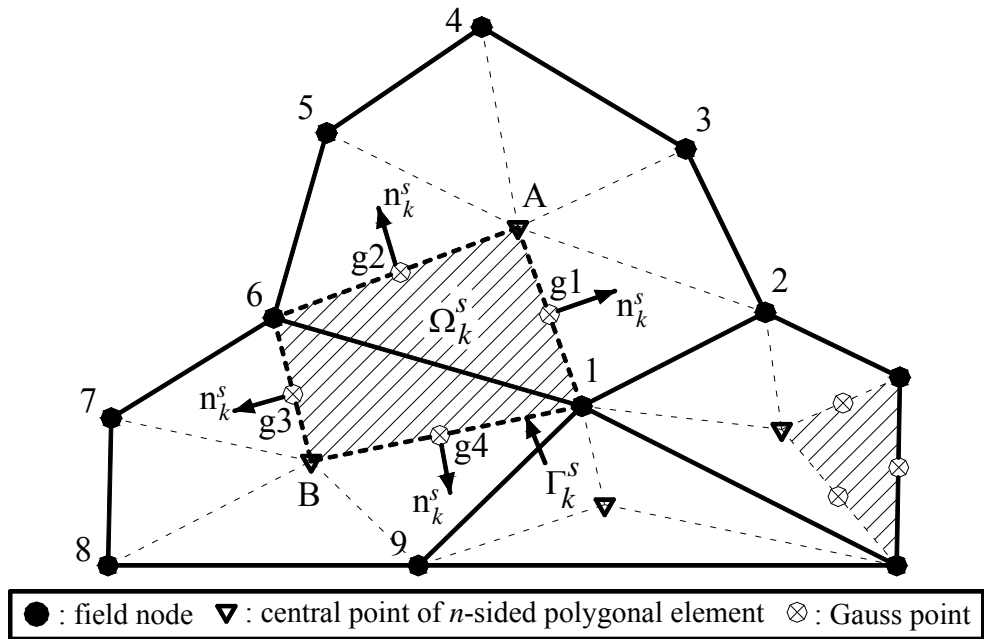


Figure 6.3. Gauss points of the smoothing domains associated with edges for n -sided polygonal elements in the ES-FEM.

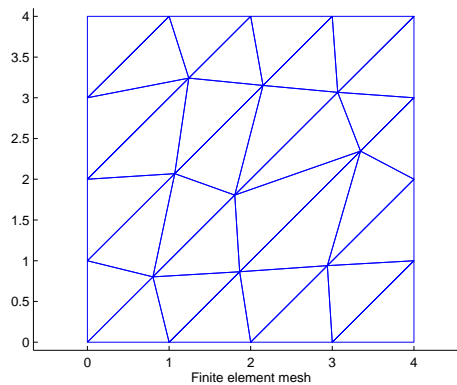


Figure 6.4. Mesh discretization using triangular elements for standard patch test.

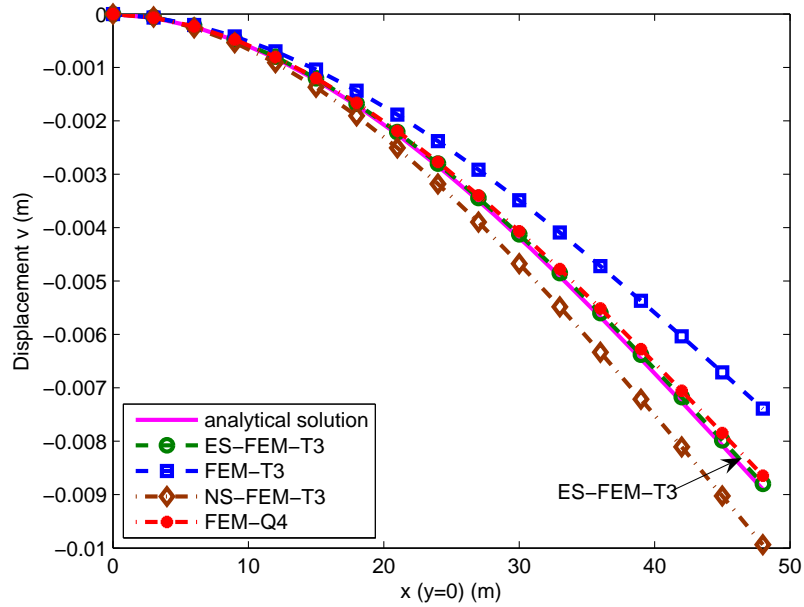


Figure 6.5. Distribution of displacement v along the horizontal middle axis of the cantilever subjected to a parabolic traction at the free end. The ES-FEM-T3 performs much better than FEM-T3 and even better than the FEM-Q4.

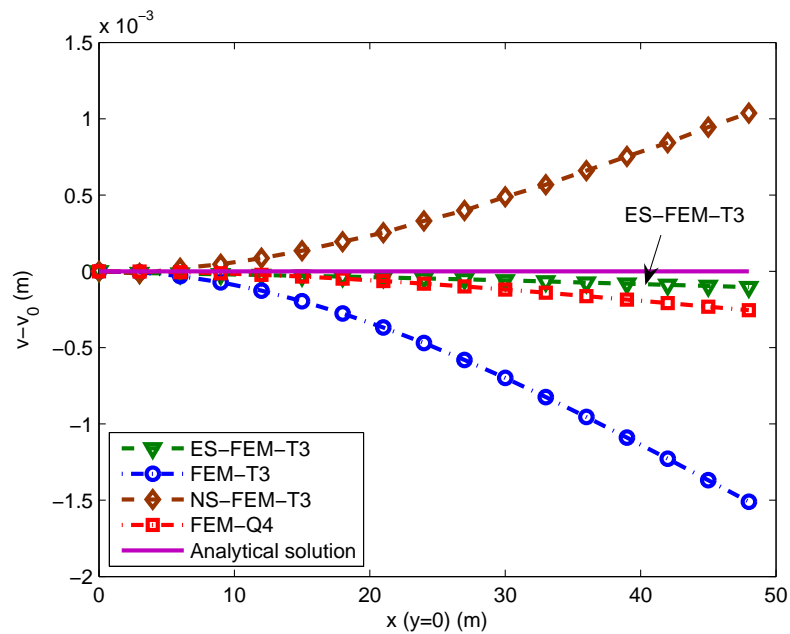


Figure 6.6. Relative error in displacement v along horizontal middle axis of the cantilever subjected to a parabolic traction at the free end. The ES-FEM-T3 solution is very close to the exact one.

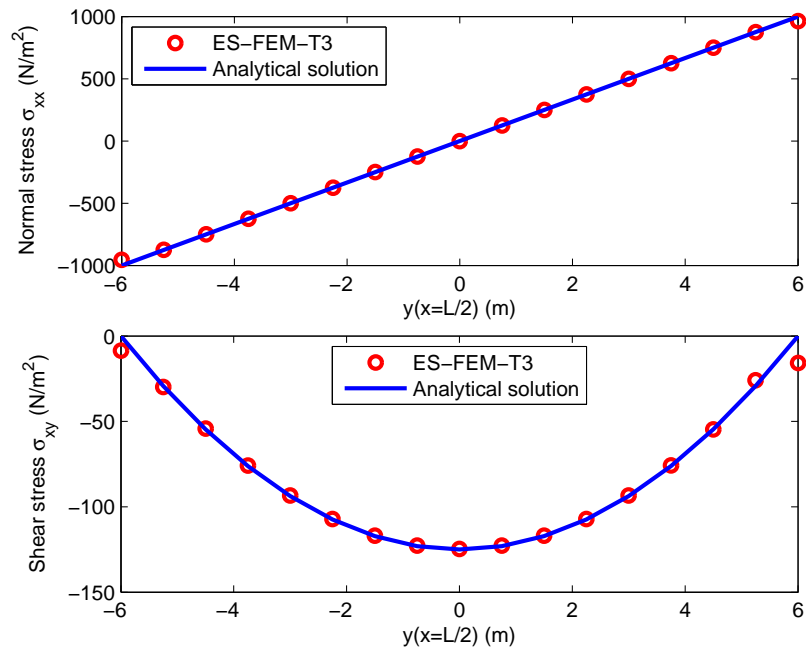


Figure 6.7. Normal stress σ_{xx} and shear stress σ_{xy} along the section of $x = L/2$ using the ES-FEM-T3 of the cantilever subjected to a parabolic traction at the free end.

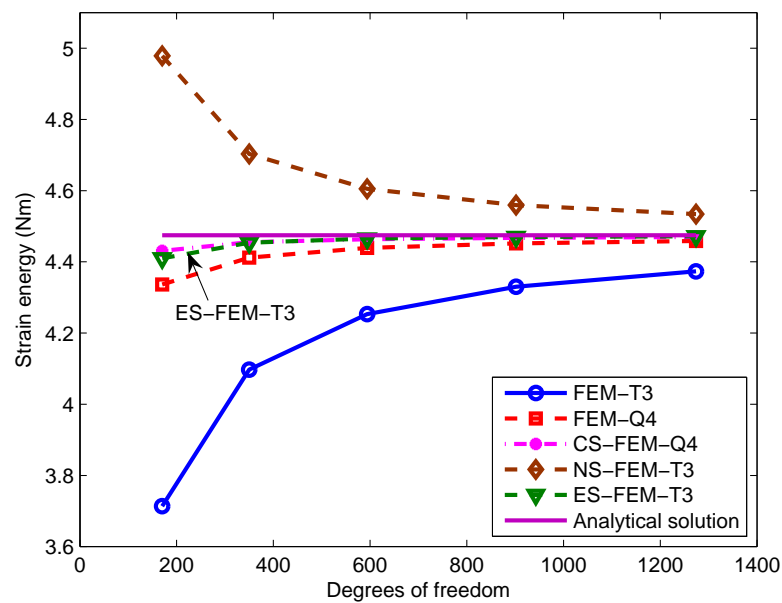


Figure 6.8. Convergence of the strain energy solution obtained using the ES-FEM-T3 in comparison with other methods for the cantilever subjected to a parabolic traction at the free end using the same distribution of nodes.

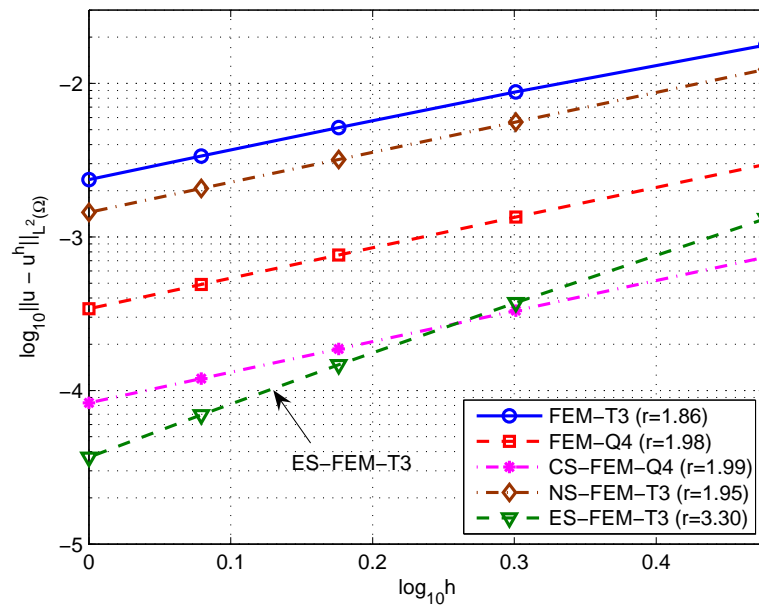


Figure 6.9. Error in displacement norm obtained using the ES-FEM-T3 in comparison with other methods for the cantilever subjected to a parabolic traction at the free end using the same distribution of nodes.

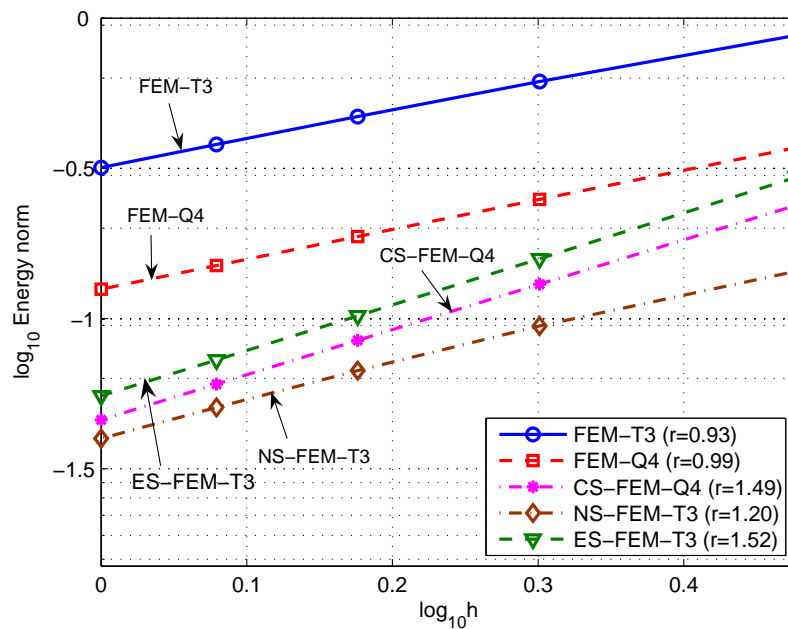


Figure 6.10. Error in energy norm obtained using the ES-FEM-T3 in comparison with other methods for the cantilever subjected to a parabolic traction at the free end using the same distribution of nodes.

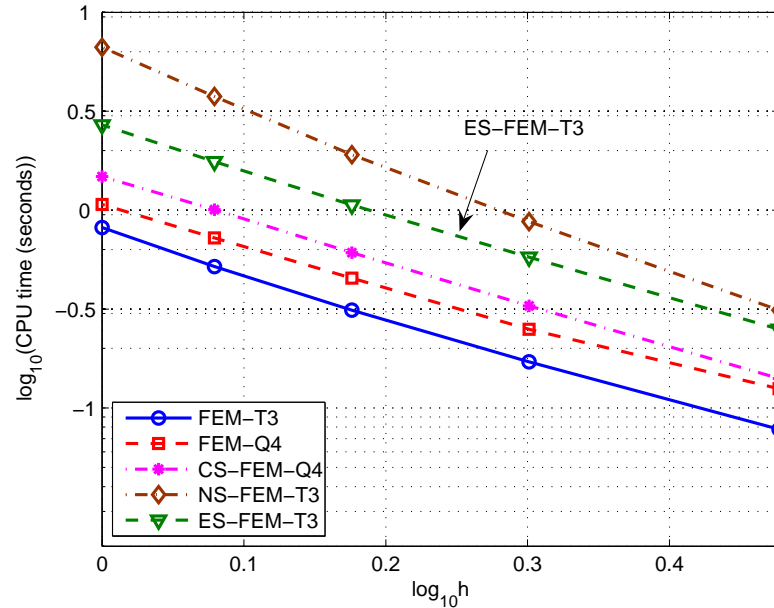


Figure 6.11. Comparison of the computation time of different methods for solving the cantilever subjected to a parabolic traction at the free end. For the same distribution of nodes, the FEM-T3 is the fastest to deliver the results.

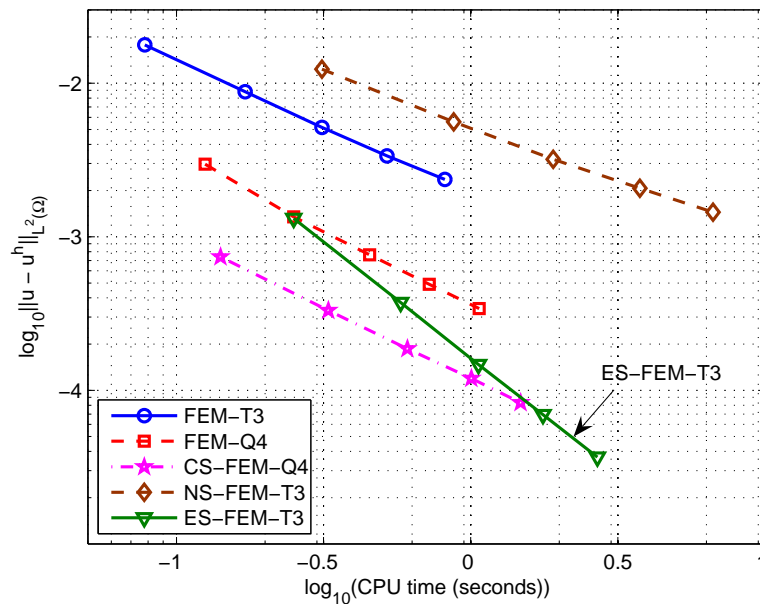


Figure 6.12. Comparison of the efficiency (computation time for the solutions of same accuracy measured in displacement norm) for solving the cantilever subjected to a parabolic traction at the free end. The ES-FEM-T3 stands out clearly as a winner, even though it uses triangular elements. It wins by its superiority in convergence rate.

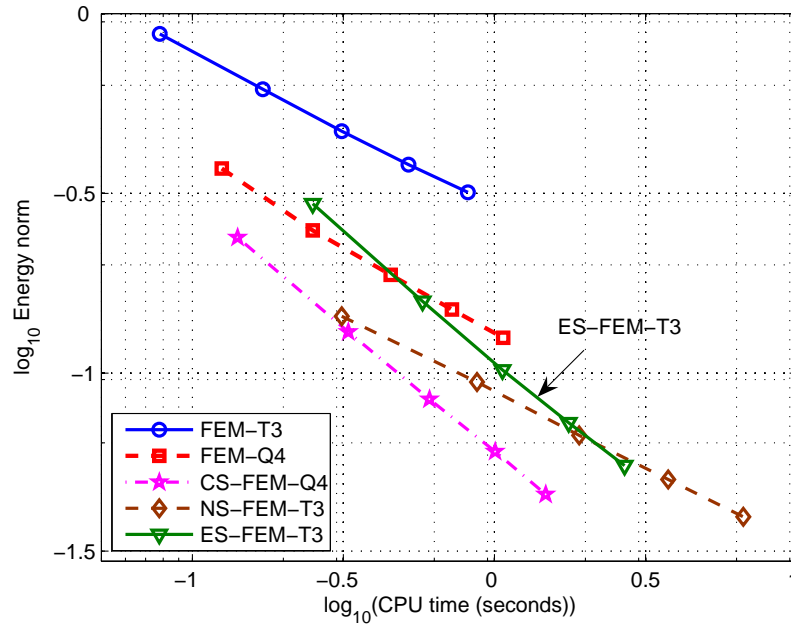


Figure 6.13. Comparison of the efficiency of computation time in terms of energy norm of the cantilever subjected to a parabolic traction at the free end. The CS-FEM-Q4 performed best, followed by the ES-FEM-T3 that uses triangular elements.

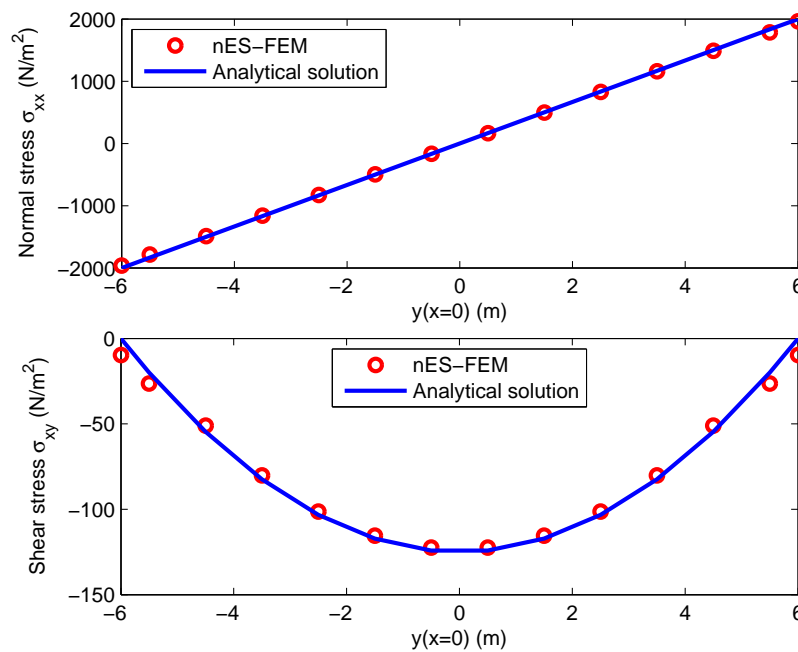


Figure 6.14. Normal stress σ_{xx} and shear stress σ_{xy} along the section of $x = 0$ using n ES-FEM of the cantilever subjected to a parabolic traction at the free end.

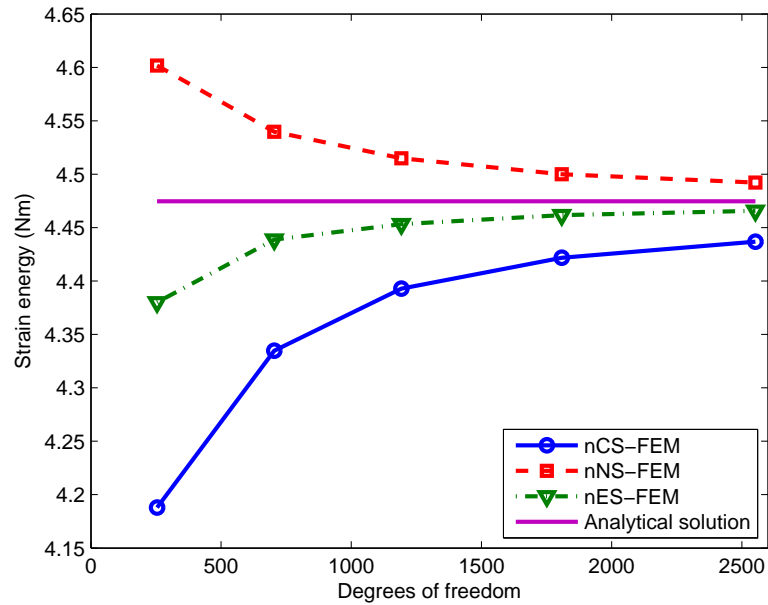


Figure 6.15. Convergence of the strain energy solution of n ES-FEM using n -sided polygonal elements in comparison with other methods for the cantilever subjected to a parabolic traction at the free end using the same meshes.

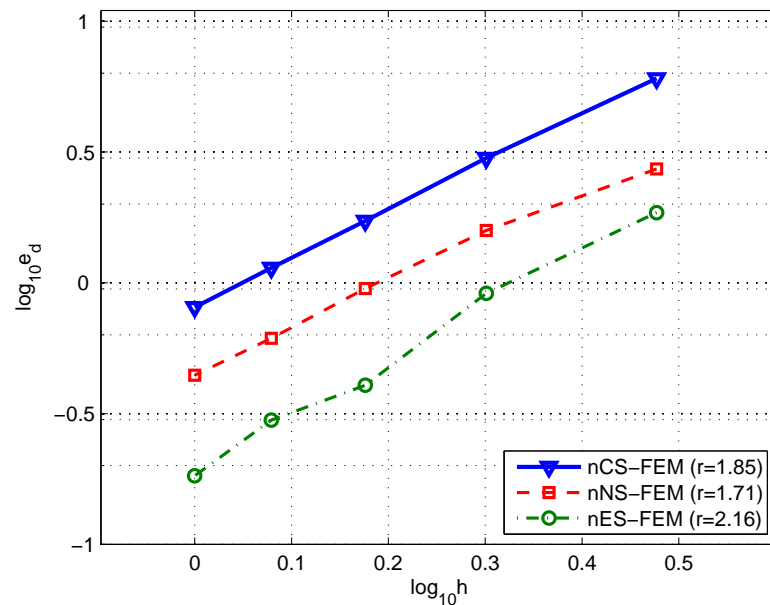


Figure 6.16. Error in displacement norm of n ES-FEM-T3 using n -sided polygonal elements in comparison with other methods for the cantilever subjected to a parabolic traction at the free end using the same meshes.

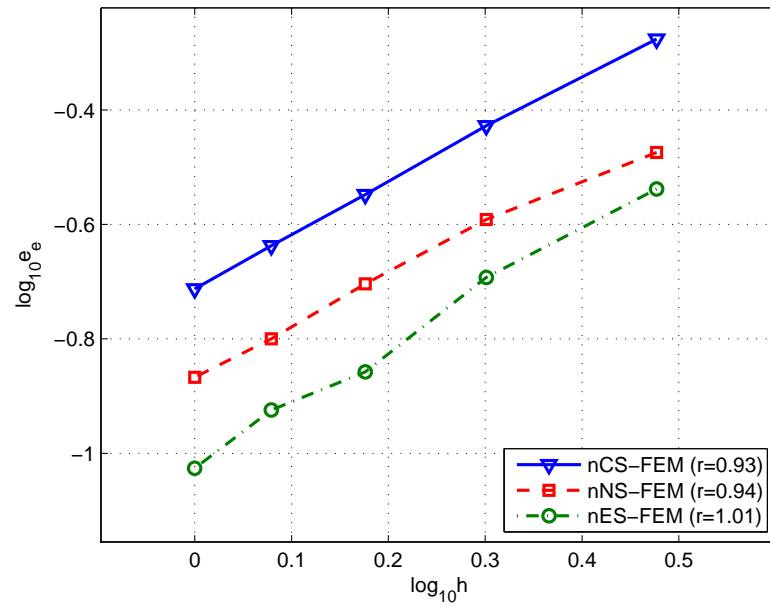


Figure 6.17. Error in energy norm of $nES-FEM-T3$ using n -sided polygonal elements in comparison with other methods for the cantilever subjected to a parabolic traction at the free end using the same meshes.

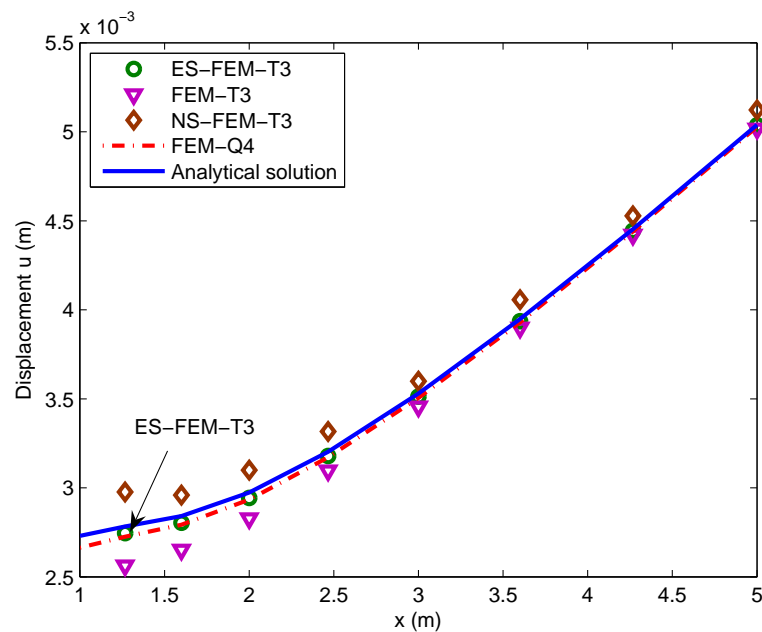


Figure 6.18. Distribution of displacement u along the bottom boundary of the infinite plate with a hole subjected to unidirectional tension.

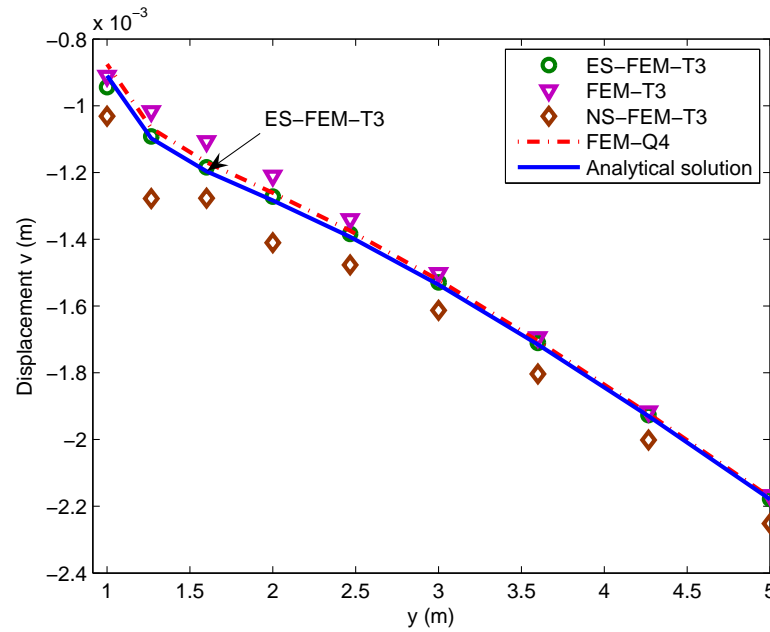


Figure 6.19. Distribution of displacement v along the left boundary of the infinite plate with a hole subjected to unidirectional tension.

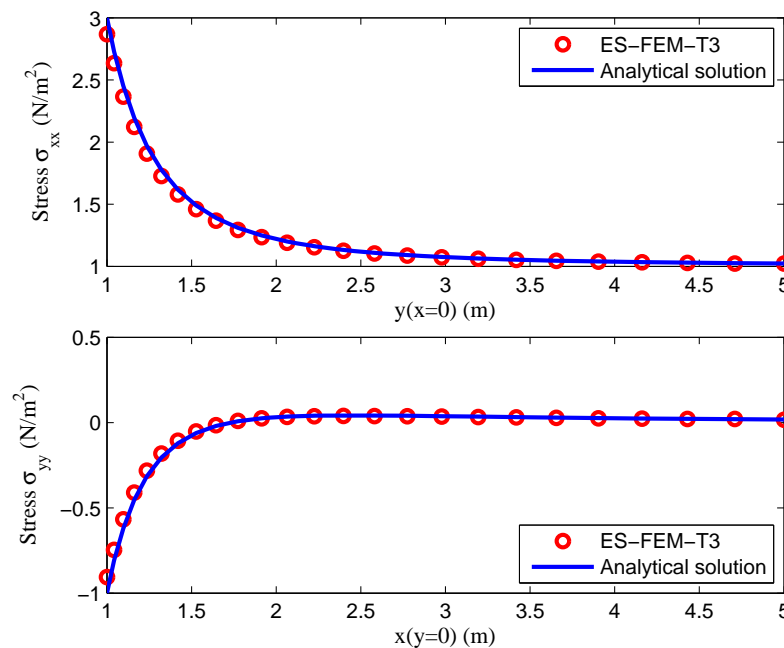


Figure 6.20. Stress σ_{xx} along the left boundary ($x = 0$) and stress σ_{yy} along the bottom boundary ($y = 0$) using the ES-FEM-T3 for the infinite plate with a hole subjected to unidirectional tension.

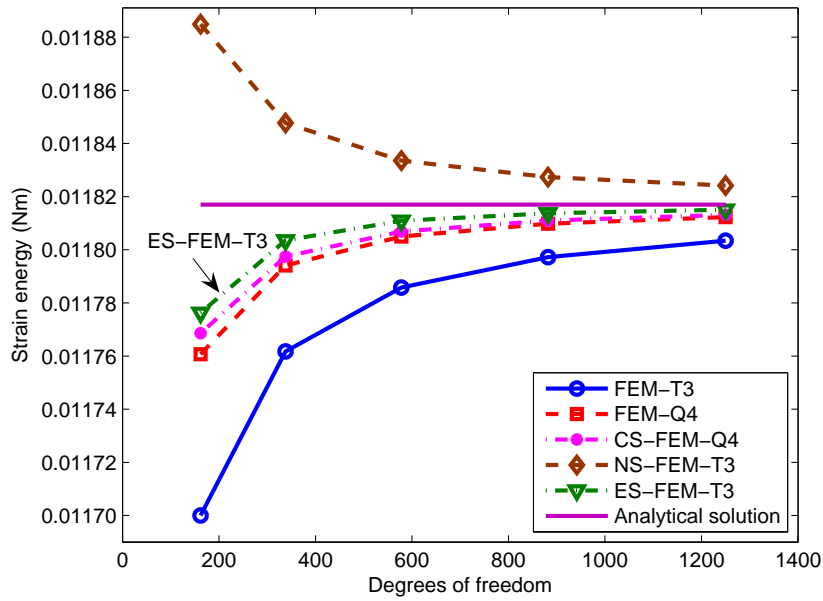


Figure 6.21. Convergence of the strain energy solution of ES-FEM-T3 in comparison with other methods for the infinite plate with a hole subjected to unidirectional tension using the same distribution of nodes.

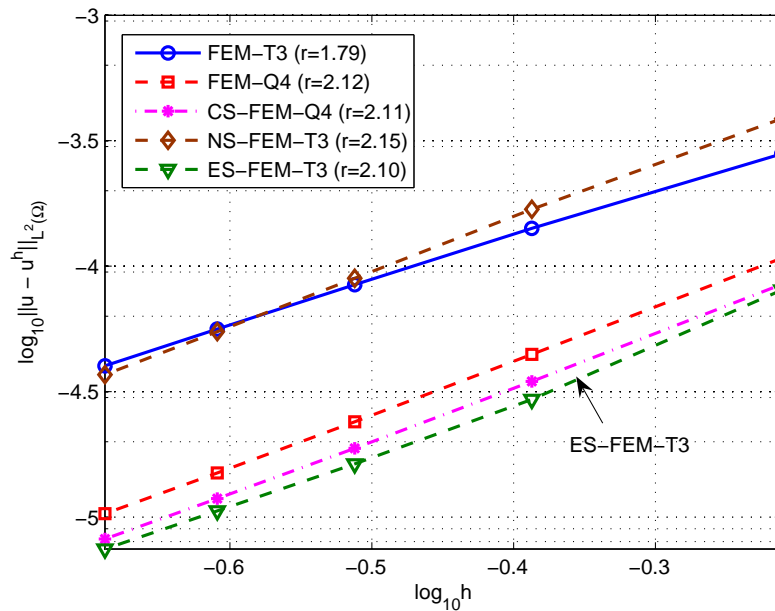


Figure 6.22. Error in displacement norm of the ES-FEM-T3 solution in comparison with other methods for the infinite plate with a hole subjected to unidirectional tension using the same distribution of nodes.

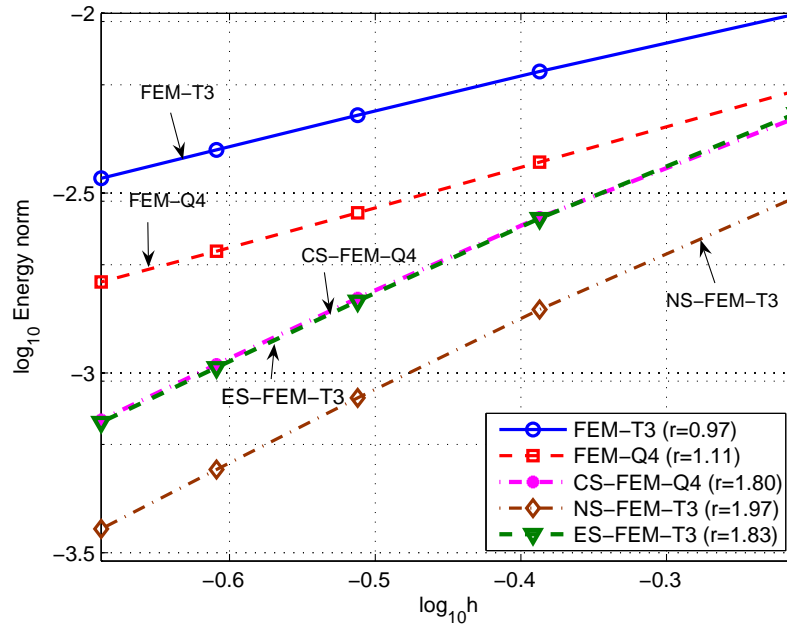


Figure 6.23. Error in energy norm of the ES-FEM-T3 solution in comparison with other methods for the infinite plate with a hole subjected to unidirectional tension using the same distribution of nodes.

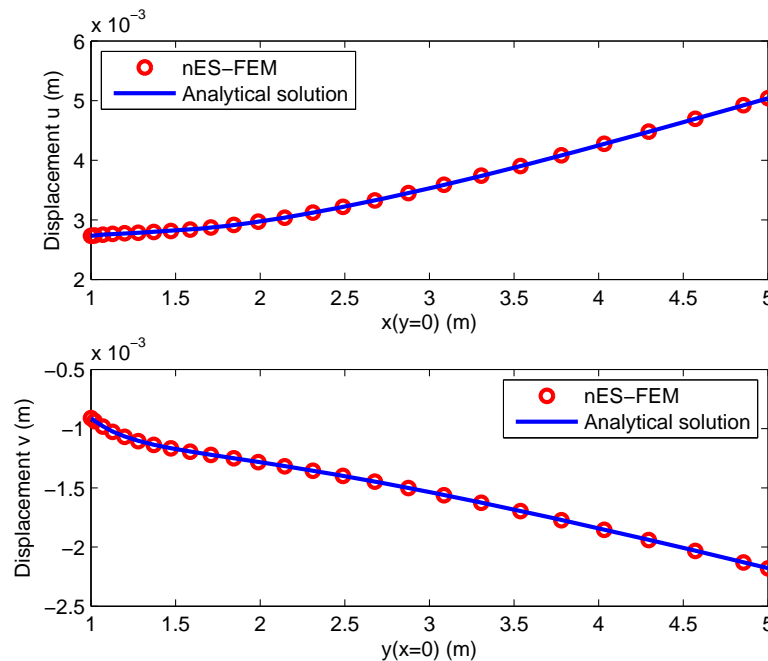


Figure 6.24. Displacement u along the bottom boundary and displacement v along the left boundary using n ES-FEM of the infinite plate with a hole subjected to unidirectional tension.

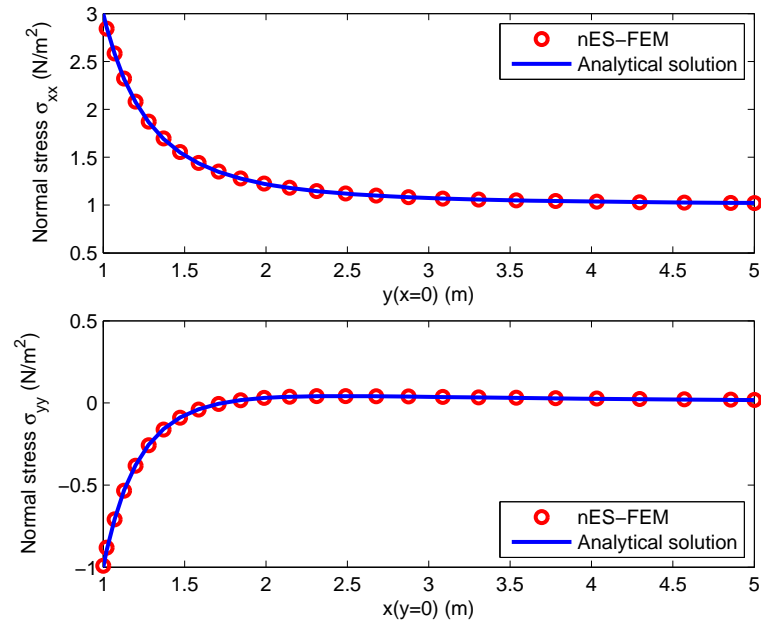


Figure 6.25. Stress σ_{xx} along the left boundary ($x=0$) and stress σ_{yy} along the bottom boundary ($y=0$) using n ES-FEM of the infinite plate with a hole subjected to unidirectional tension.

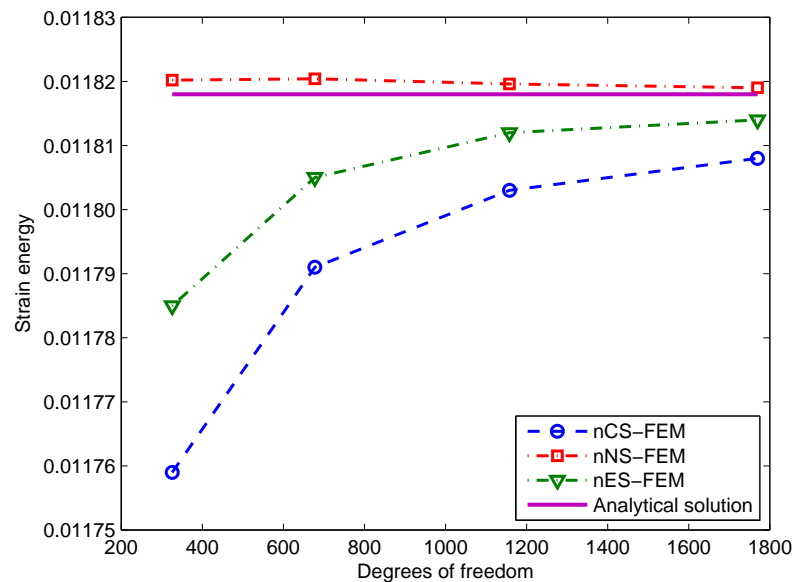


Figure 6.26. Convergence of the strain energy solution of n ES-FEM using n -sided polygonal elements in comparison with other methods for the infinite plate with a hole subjected to unidirectional tension using the same meshes.

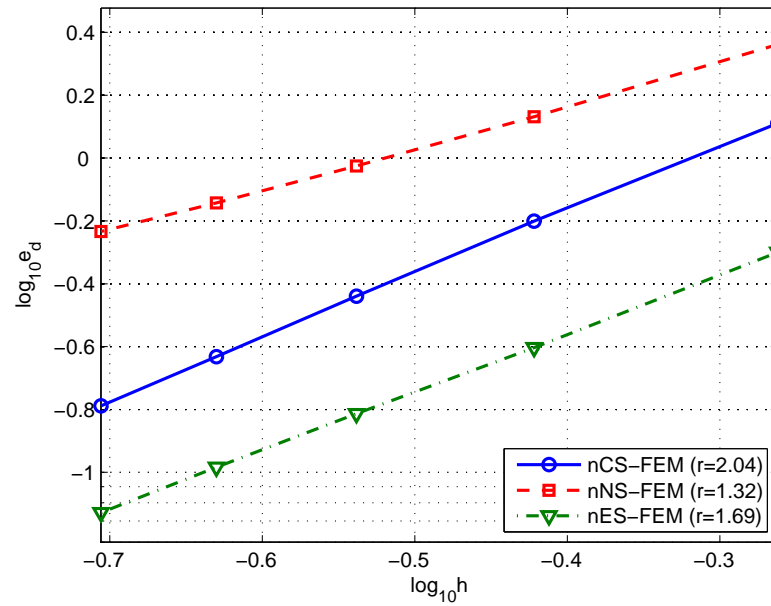


Figure 6.27. Error in displacement norm of n ES-FEM-T3 using n -sided polygonal elements in comparison with other methods for the infinite plate with a hole subjected to unidirectional tension using the same meshes.

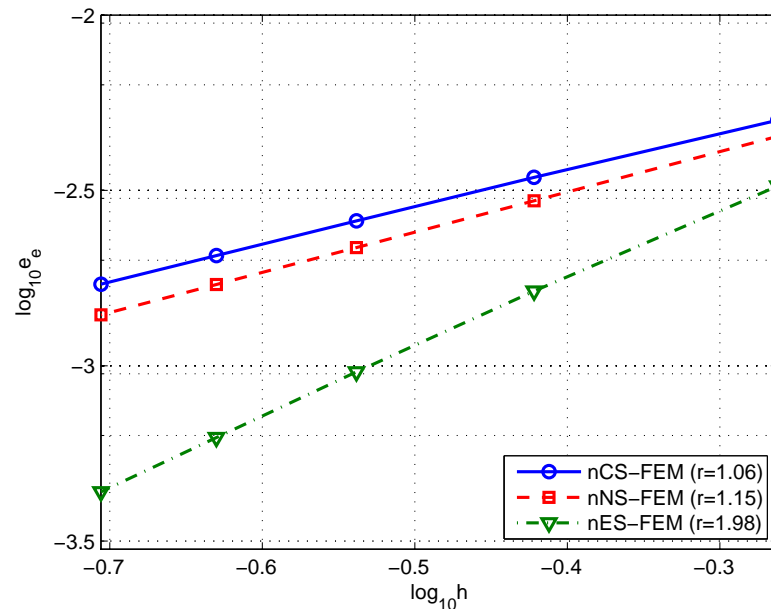


Figure 6.28. Error in energy norm of n ES-FEM-T3 using n -sided polygonal elements in comparison with other methods for the infinite plate with a hole subjected to unidirectional tension using the same meshes.

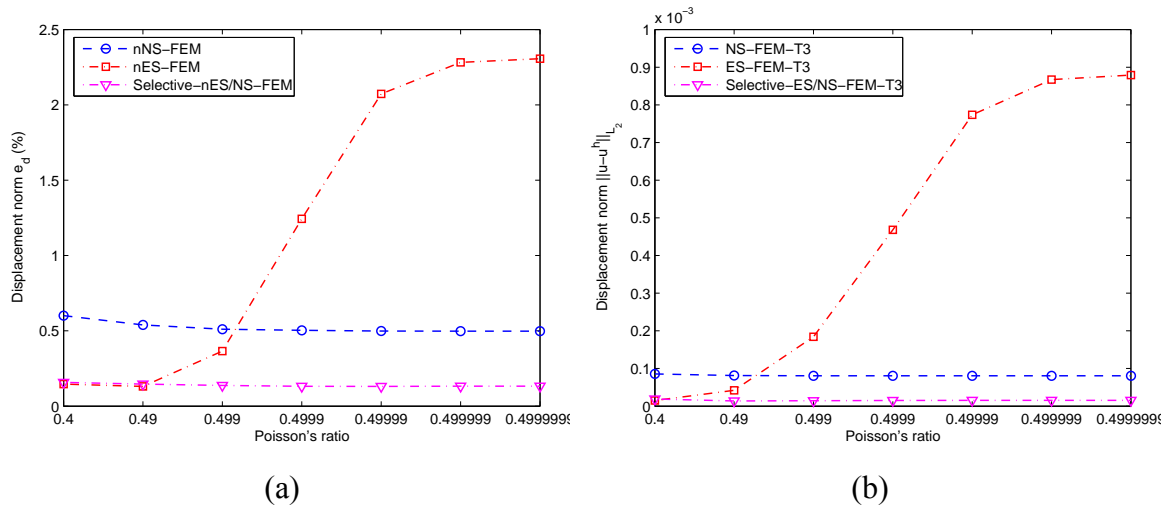


Figure 6.29. Displacement norm with different Poisson's ratios.
 (a) n -sided polygonal elements (579 nodes); (b) triangular elements (289 nodes).

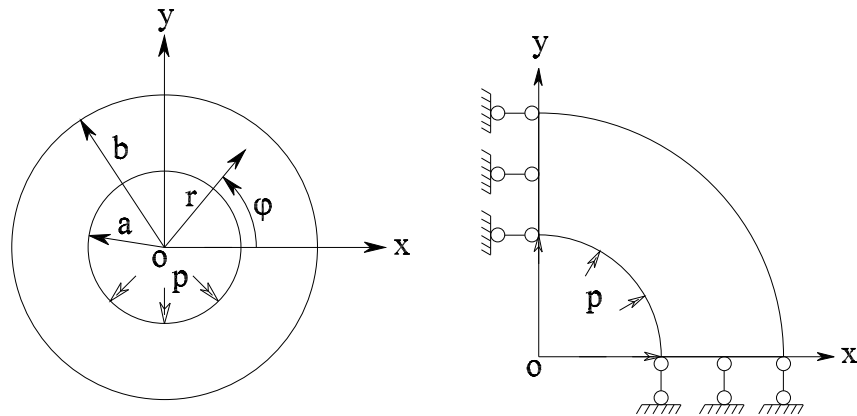


Figure 6.30. A thick cylindrical pipe subjected to an inner pressure and its quarter model.

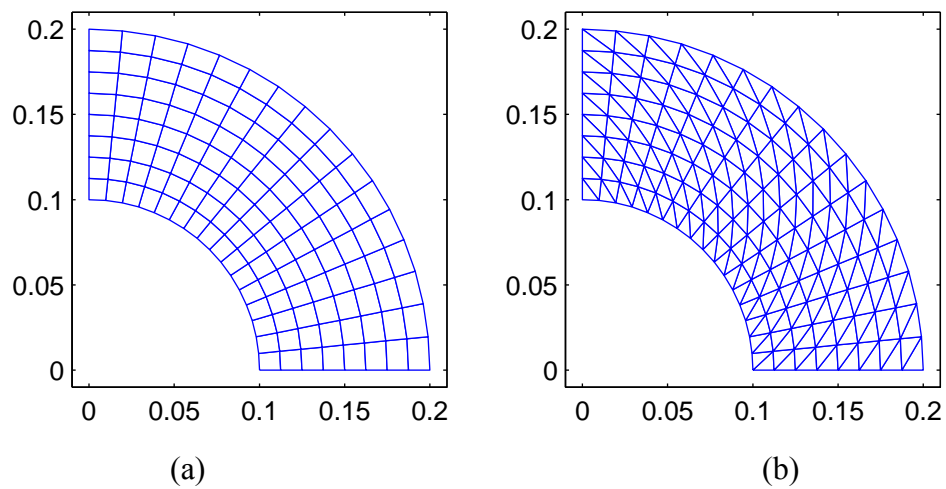


Figure 6.31. Discretization of the domain of the thick cylindrical pipe subjected to an inner pressure; (a) 4-node quadrilateral elements; (b) 3-node triangular elements.

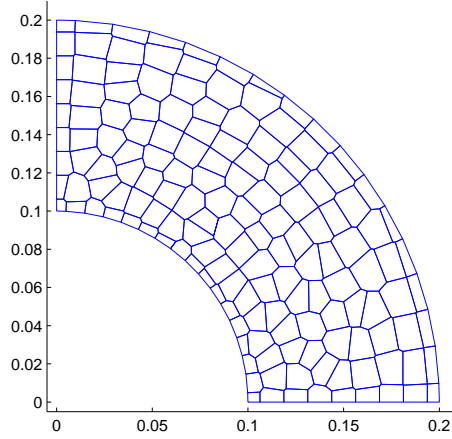


Figure 6.32. Discretization of the domain using n -sided polygonal elements of the thick cylindrical pipe subjected to an inner pressure.

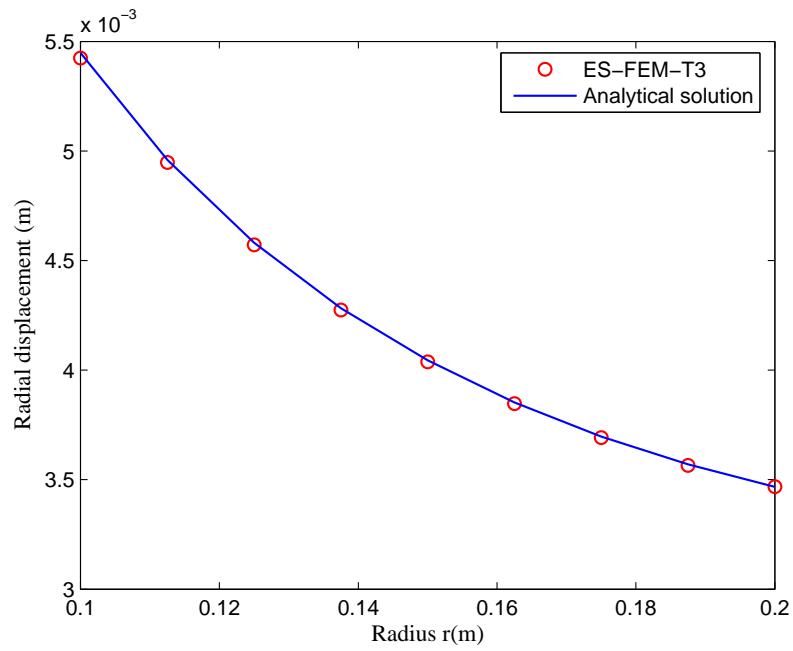


Figure 6.33. Distribution of the radial displacement of the cylindrical pipe subjected to an inner pressure using the ES-FEM-T3.

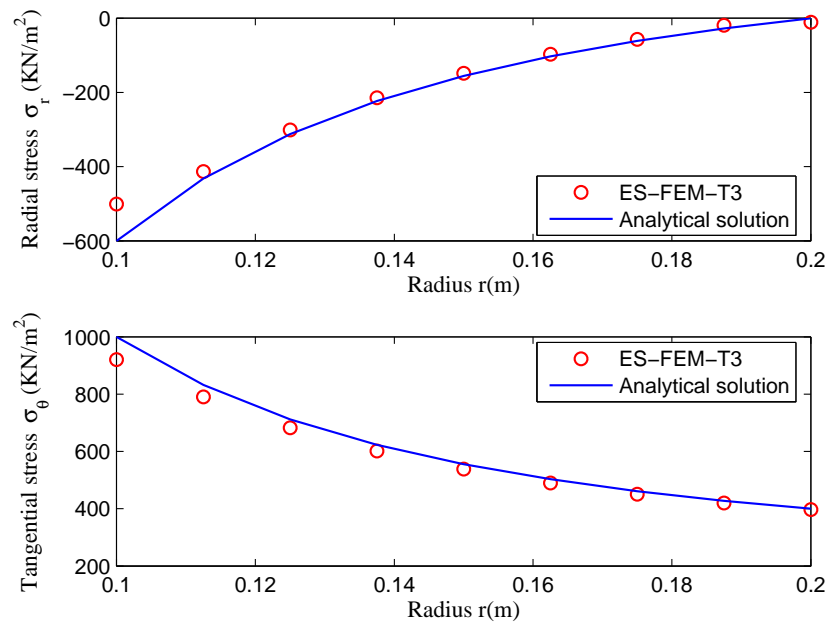


Figure 6.34. Distribution of the radial and tangential stresses of the cylindrical pipe subjected to an inner pressure using the ES-FEM-T3.

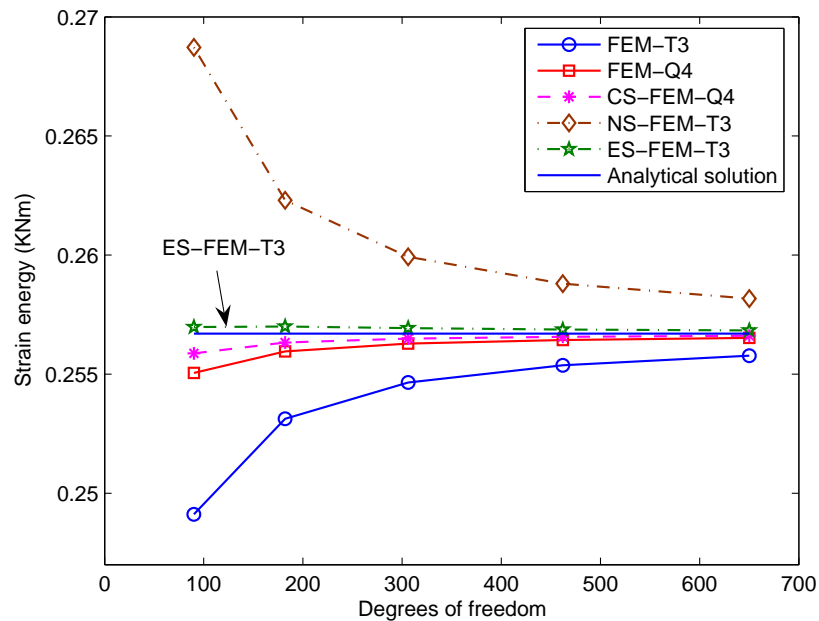


Figure 6.35. Convergence of strain energy of ES-FEM-T3 in comparison with other methods for the cylindrical pipe subjected to an inner pressure using the same distribution of nodes.

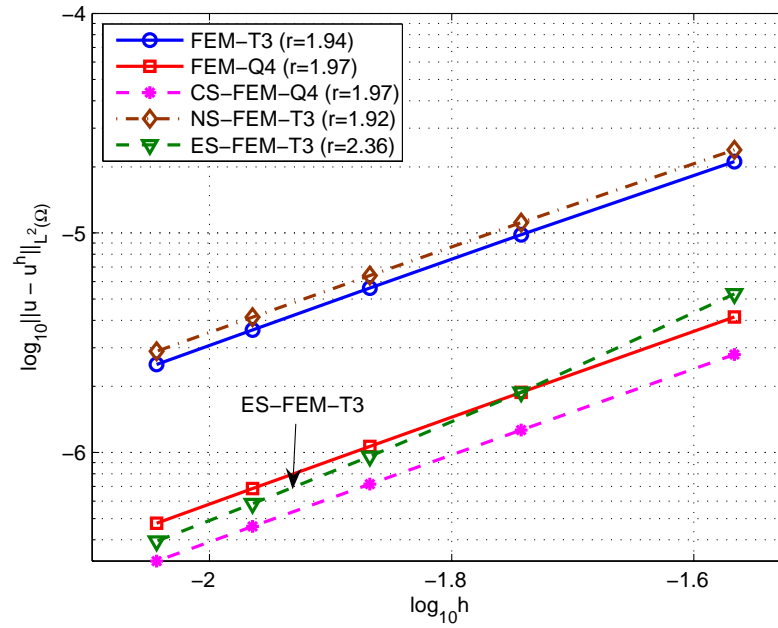


Figure 6.36. Error in displacement norm of ES-FEM-T3 in comparison with other methods for the cylindrical pipe subjected to an inner pressure using the same distribution of nodes.

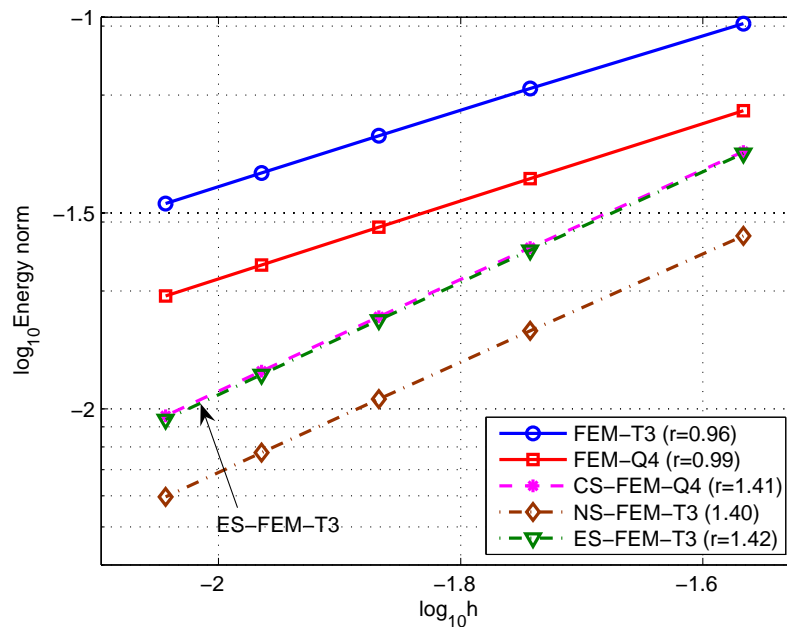


Figure 6.37. Error in energy norm of ES-FEM-T3 in comparison with other methods for the cylindrical pipe subjected to an inner pressure using the same distribution of nodes.

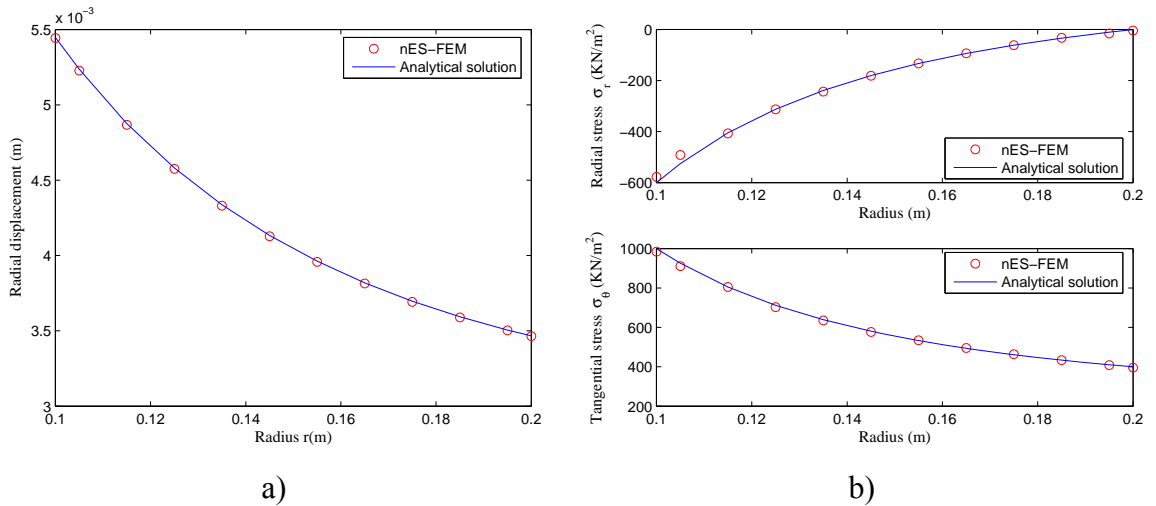


Figure 6.38. Computed and exact results of nodes along the radius of the thick cylindrical pipe subjected to an inner pressure using the n ES-FEM; (a) radial displacement u_r ; (b) radial stress σ_r and tangential stress σ_θ .

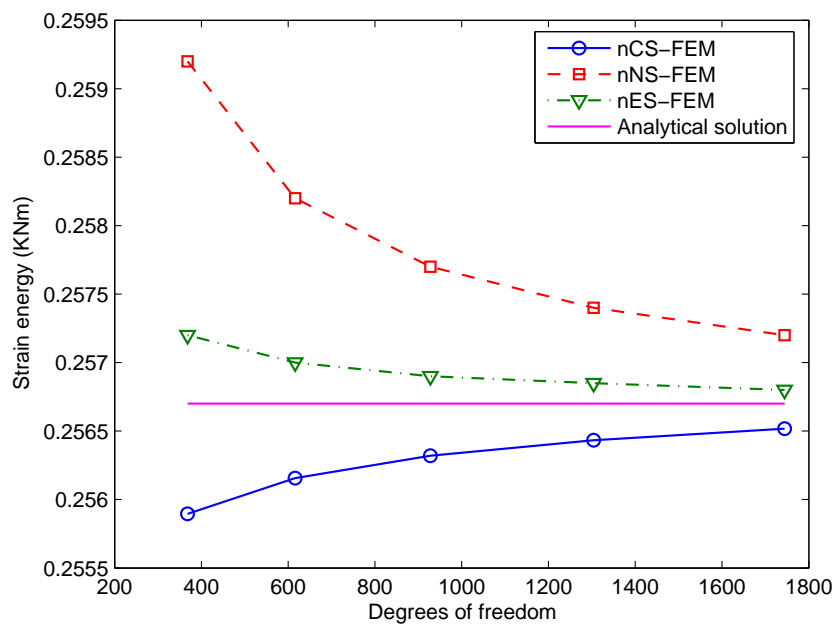


Figure 6.39. Convergence of the strain energy solution of n ES-FEM in comparison with other methods for the thick cylindrical pipe subjected to an inner pressure.

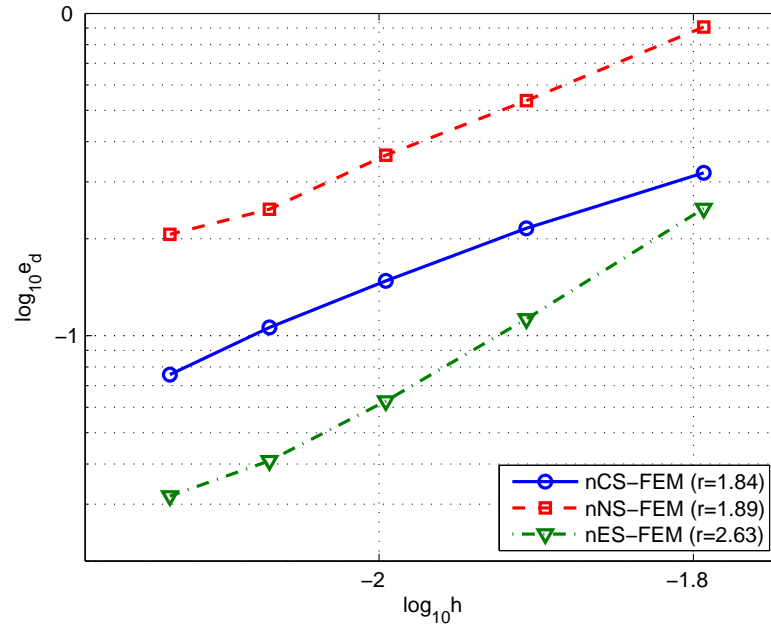


Figure 6.40. Error in displacement norm of n ES-FEM in comparison with other methods for the thick cylindrical pipe subjected to an inner pressure.

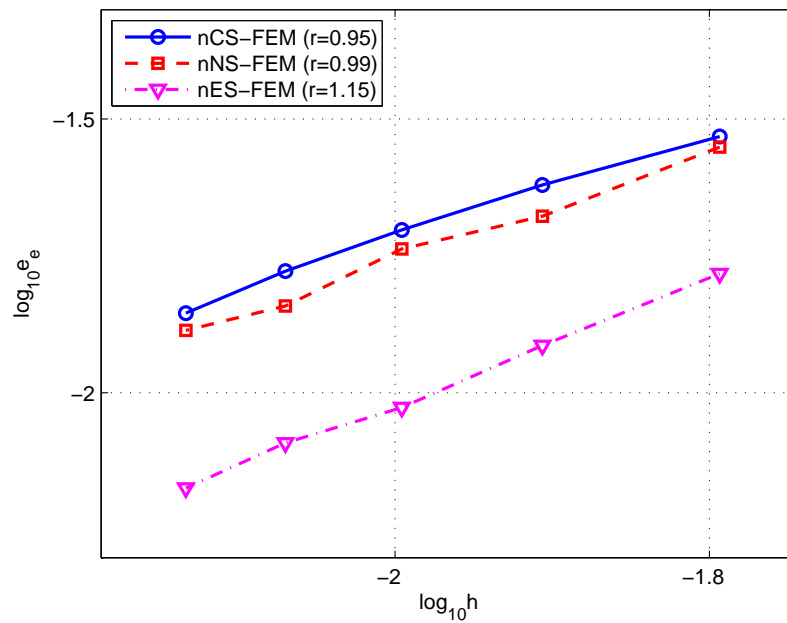


Figure 6.41. Error in energy norm of n ES-FEM in comparison with other methods for the thick cylindrical pipe subjected to an inner pressure.

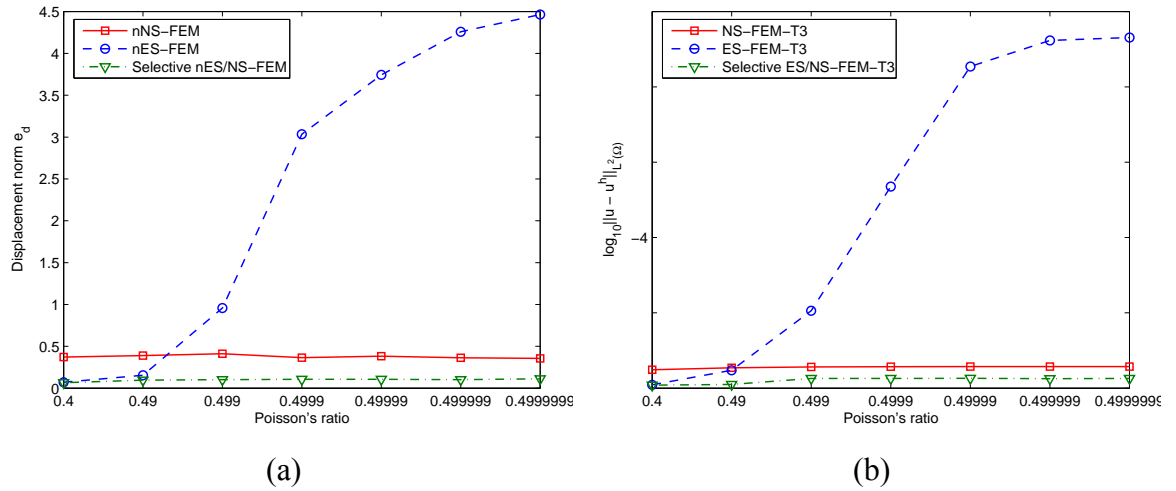


Figure 6.42. Displacement norm with different Poisson's ratios the thick cylindrical pipe subjected to an inner pressure; (a) n -sided polygonal elements (464 nodes); (b) triangular elements (91 nodes).

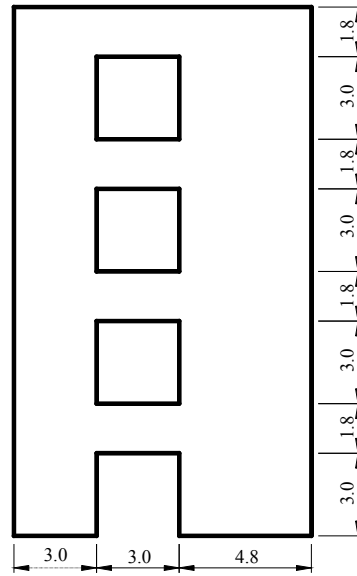


Figure 6.43. A shear wall with four square openings.

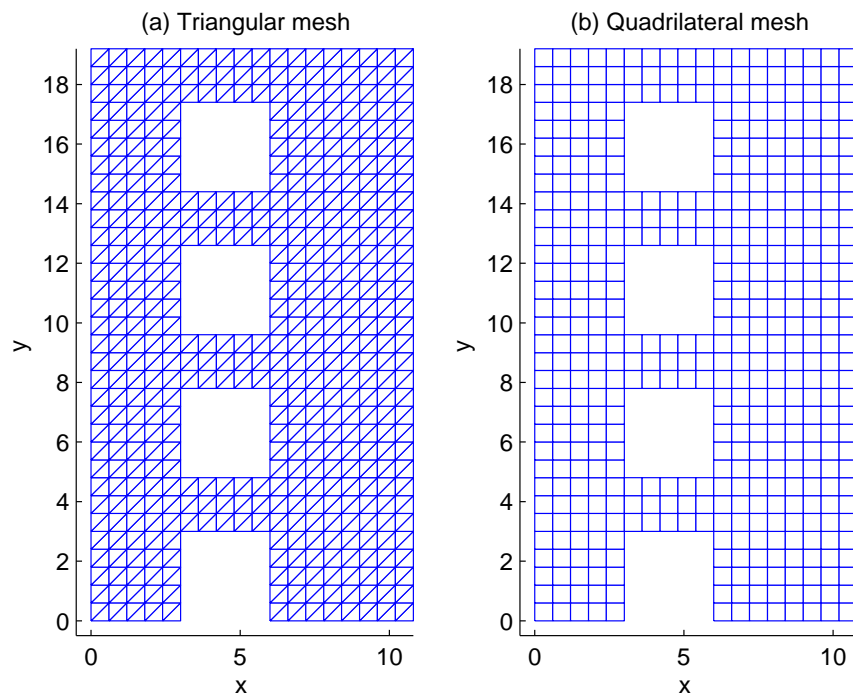
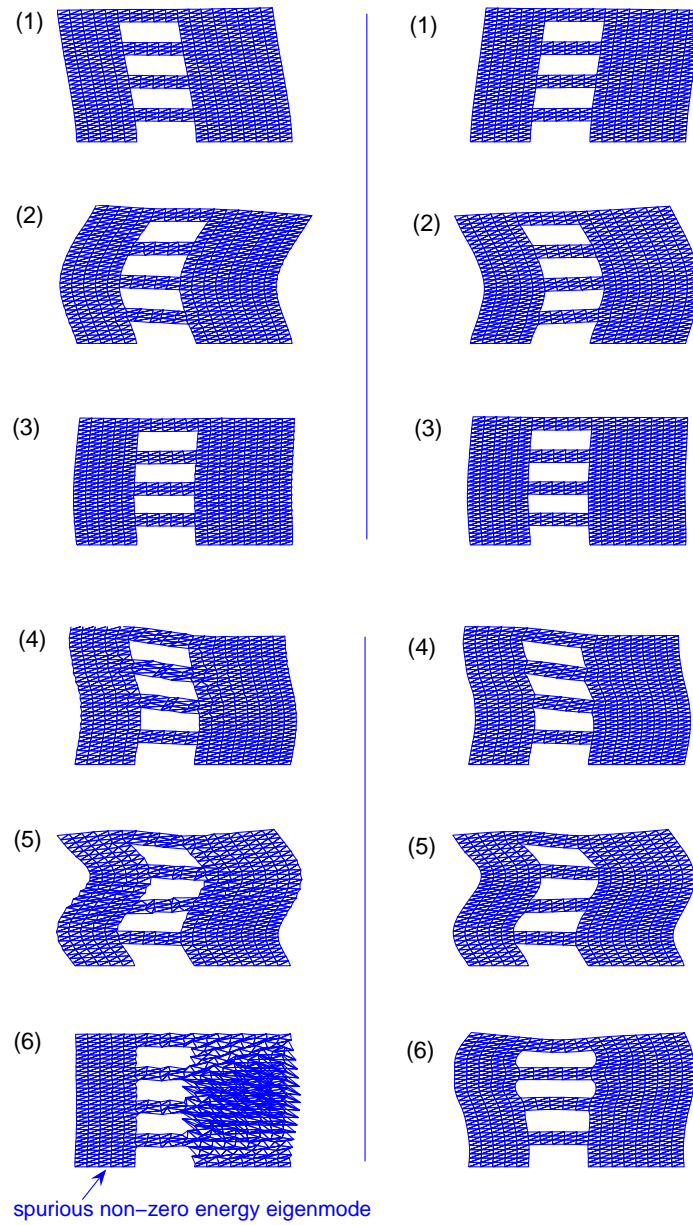


Figure 6.44. Domain discretization using triangular and 4-node quadrilateral elements of the shear wall with four openings.



(a) NS-FEM-T3

(b) ES-FEM-T3

Figure 6.45. 1st to 6th modes of the shear wall by the NS-FEM-T3 and ES-FEM-T3.

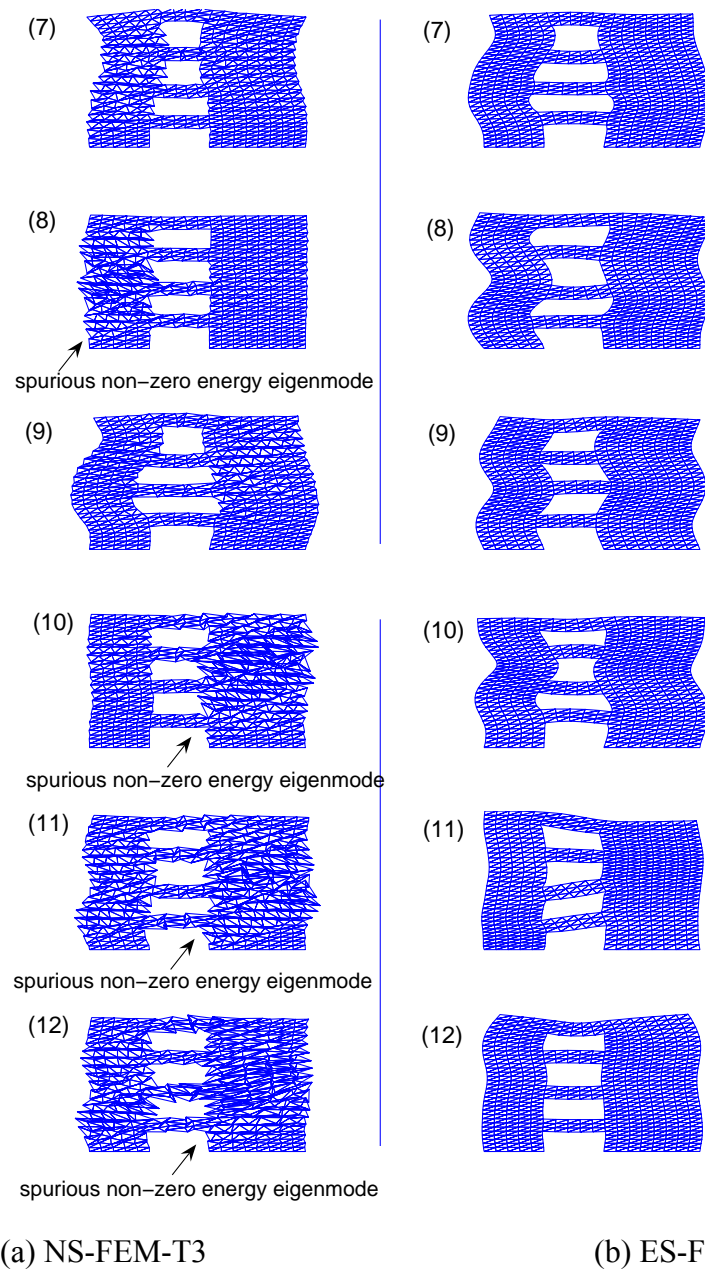


Figure 6.46. 7th to 12th modes of the shear wall by the NS-FEM-T3 and ES-FEM-T3.

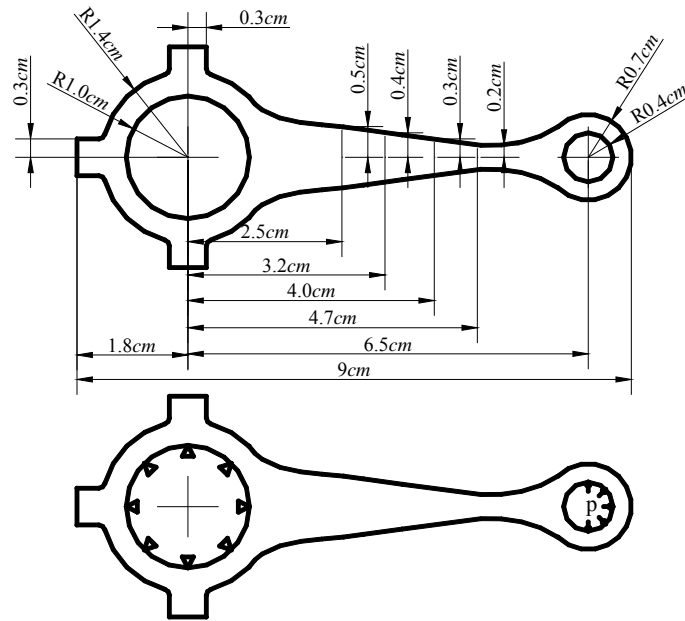


Figure 6.47. Geometric model, loading and boundary conditions of an automobile connecting bar.

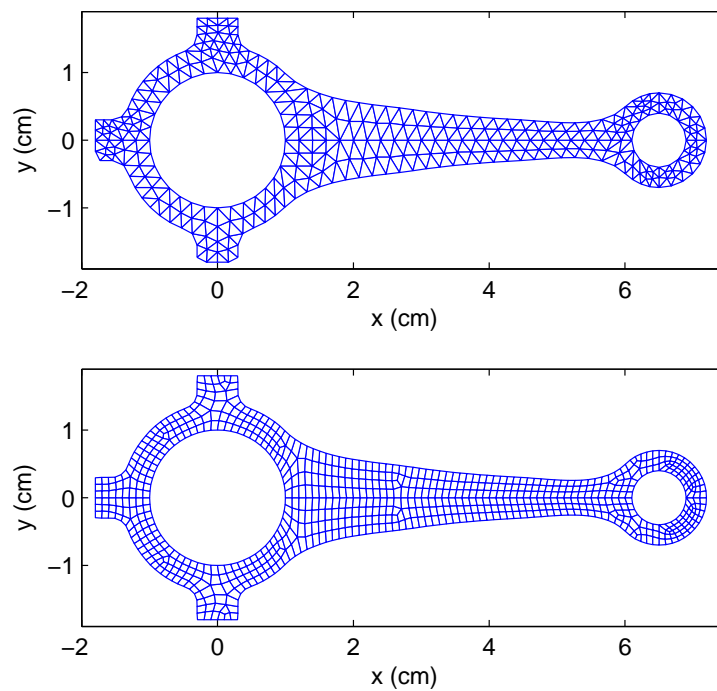


Figure 6.48. Domain discretization using triangular and 4-node quadrilateral elements of the automobile connecting bar.

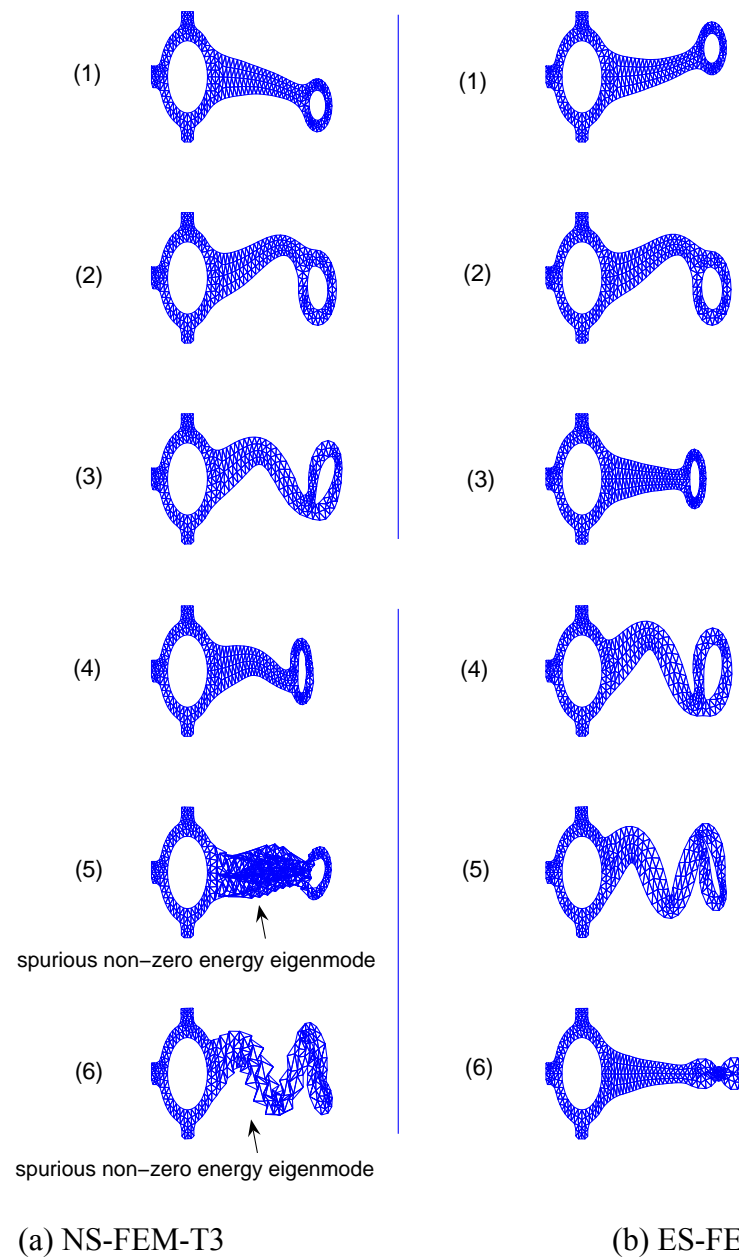


Figure 6.49. 1st to 6th modes of the connecting bar by NS-FEM-T3 and ES-FEM-T3.

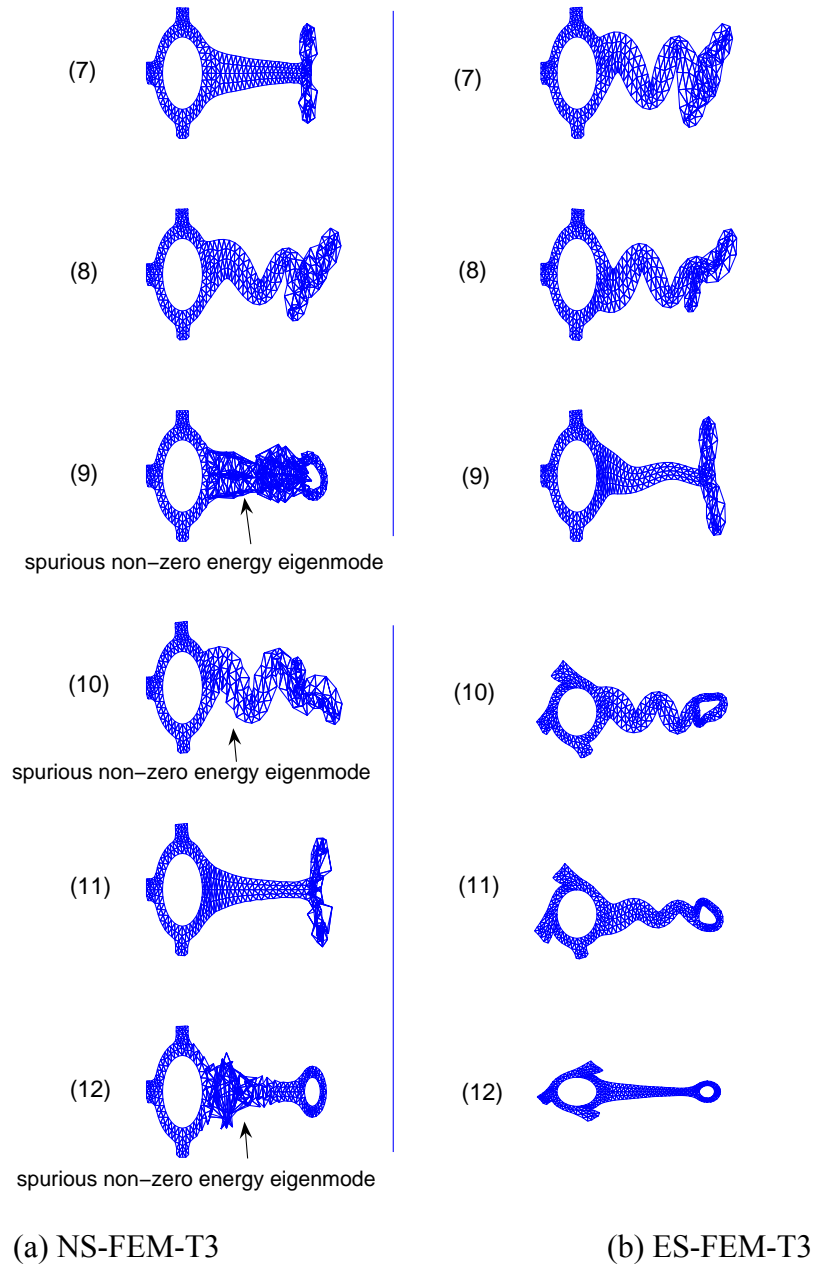


Figure 6.50. 7th to 12th modes of the connecting bar by NS-FEM-T3 and ES-FEM-T3.

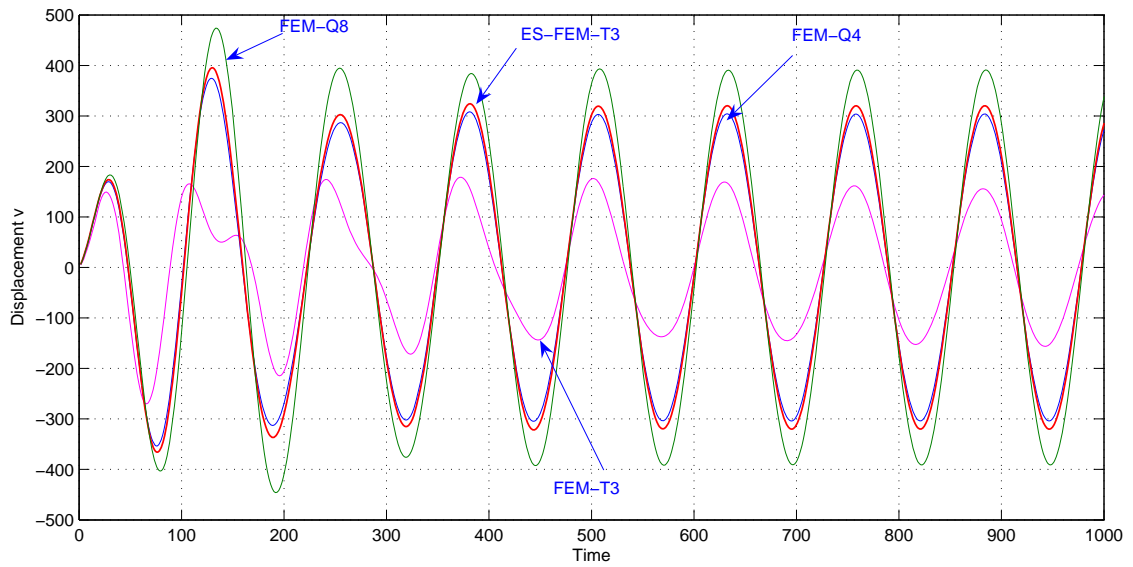


Figure 6.51. Transient responses for the cantilever beam subjected to a harmonic loading.

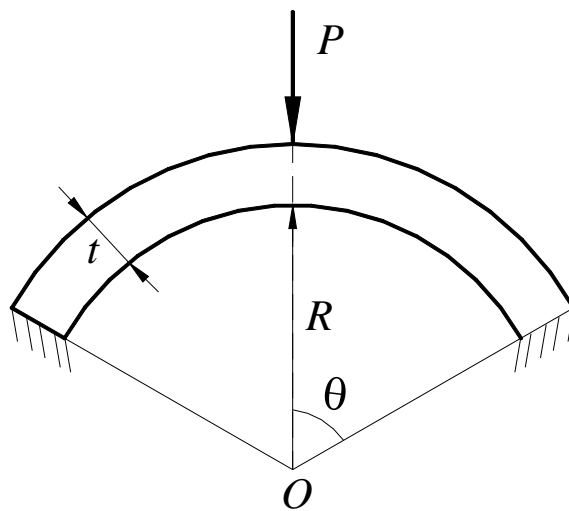


Figure 6.52. A spherical shell subjected to a concentrated loading at its apex.

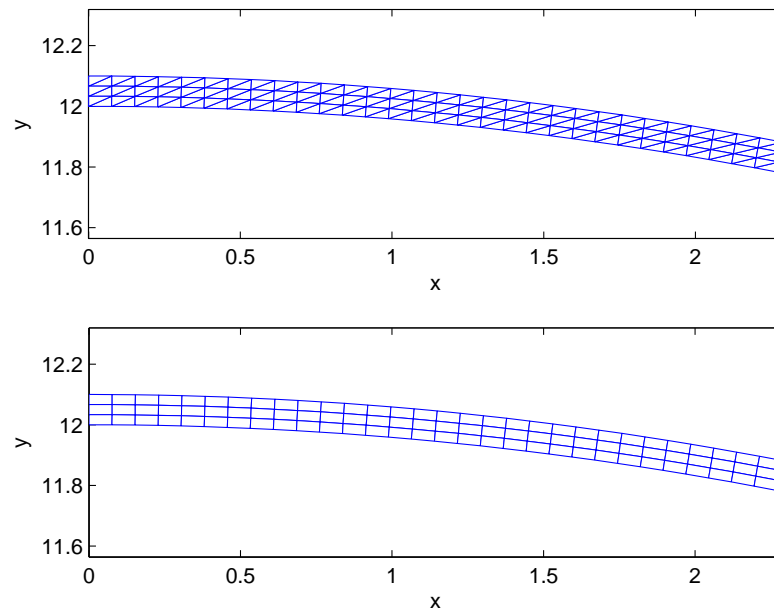


Figure 6.53. Domain discretization of half of the spherical shell using triangular and 4-node quadrilateral elements.

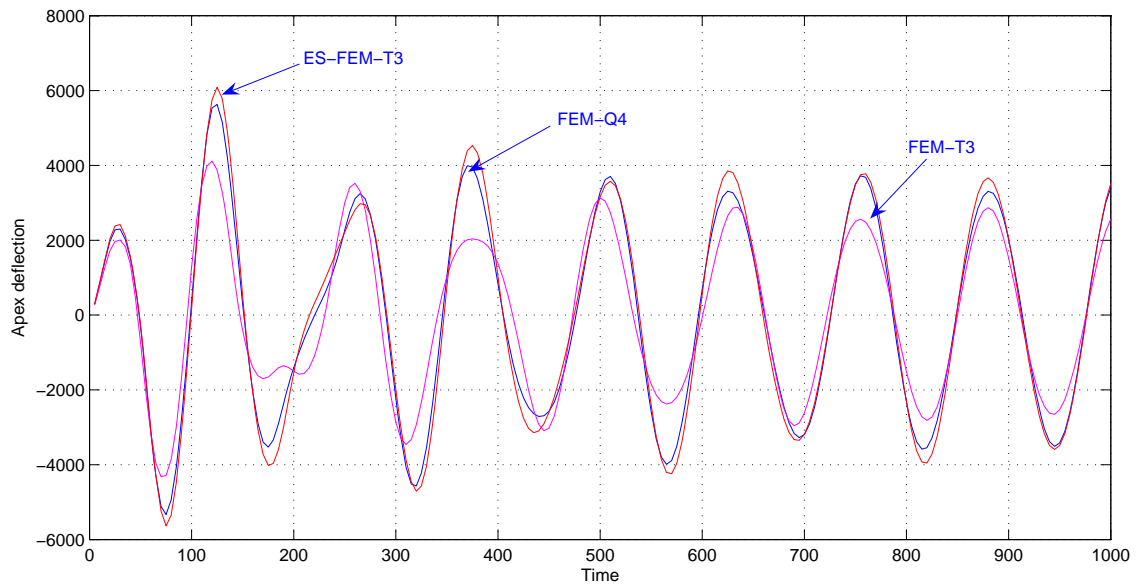


Figure 6.54. Transient responses for the spherical shell subjected to a harmonic loading.

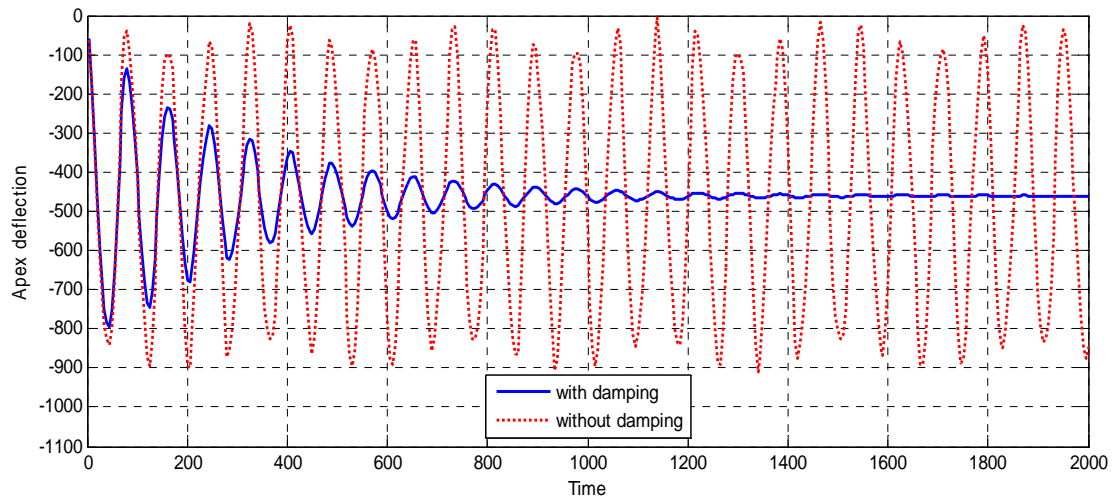


Figure 6.55. Transient responses obtained using the ES-FEM-T3 for the spherical shell subjected to a Heaviside step loading.

Chapter 7

Face-based Smoothed FEM (FS-FEM)

7.1 Introduction

The four-node tetrahedral element (T4) is often used to introduce the procedure of the finite element method (FEM-T4) for three dimensional (3D) problems, because of its simplicity in formulation: piecewise linear approximation of displacement field and constant strain field. Further more, most FEM codes use tetrahedral elements for adaptive analyses of 3D problems, due to the simple fact that tetrahedral meshes can be automatically generated and refined, even for complicated domains. The FEM-T4 is clearly superior at least for two counts: simplicity and adaptively.

However, the FEM-T4 also possesses crucial shortcomings for problems of solid mechanics. Three such shortcomings are the well-known overly-stiff behavior, poor stress solution, and volumetric locking in the nearly incompressible cases. In order to overcome these disadvantages, some new finite elements were proposed. Dohrmann *et al.* [40] presented a weighted least-squares approach in which a linear displacement field is fit to an element's nodal displacements. The method is claimed to be computationally efficient and avoids the volumetric locking problems. However more nodes are required on the element boundary to obtain a least square fitted linear displacement field. Dohrmann *et al.* [39] also proposed a nodal integration FEM in which each element is associated with a

single node and the linear interpolation functions of the original mesh are used. The method avoids the volumetric locking and performs better comparing to the FEM-T4 in term of stress solution for static problems. The nodal integration FEM can be viewed as a special linear case of the NS-FEM presented in [Chapter 5](#), and the LC-PIM [86, 157] formulated using the generalized gradient smoothing technique [68] and the point interpolation shape functions [67]. However, for dynamic problems, these types of node-based smoothed methods are known “overly soft” and unstable temporally due to the presence of spurious modes at higher energy levels. Therefore, a stabilization scheme such as the one proposed by Puso and Solberg [125] is required for dynamic problems.

In this chapter, in order to overcome the above-mentioned disadvantages of the FEM-T4 and the NS-FEM-T4 presented in [Chapter 5](#), we extend the idea of the ES-FEM-T3 for 3D problems. Instead of using the edge-based smoothing domains in 2D problems, we will now use the face-based smoothing domains for smoothed strain field construction. It is therefore termed as the face-based smoothed finite element method (FS-FEM) using T4 elements. In the FS-FEM-T4, the system stiffness matrix is computed using strains smoothed strains, and hence the FS-FEM-T4 model is found softer than that of the FEM-T4 using the same mesh. Some numerical results will be presented to demonstrate the efficiency and properties of the FS-FEM-T4 for both linear and geometrically nonlinear 3D problems. It will be shown that the implementation of the FS-FEM-T4 is straightforward and no penalty parameter or additional degrees of freedom is used, and the results are much better than those of the FEM-T4.

In addition, a smoothing-domain-based selective FS/NS-FEM-T4 is also formulated using combined face-based and node-based smoothing domains. The selective FS/NS-FEM-T4 is immune from volumetric locking for problems using nearly incompressible materials, due to the volumetric locking-free property inherited from the NS-FEM.

7.2 Creation of the face-based smoothing domains

In the FS-FEM-T4, the 3D problem domain is meshed into tetrahedral elements in the same way as in the standard FEM-T4. Since we only use T4 elements, the mesh generation can be done with easy for complicated geometries.

Consider now a 3D domain Ω discretized with N_e tetrahedral elements, such that

$\Omega = \sum_{i=1}^{N_e} \Omega_i^e$ and $\Omega_i^e \cap \Omega_j^e \neq \emptyset$, $i \neq j$, in which N_e is the total number of the elements in

the entire problem domain. The T4 element mesh shall have a total of N_f faces. On top of

the element mesh we now further create a set of 3D smoothing domains based on the N_f

faces of the element mesh, such that $\Omega = \sum_{k=1}^{N_f} \Omega_k^s$ and $\Omega_i^s \cap \Omega_j^s \neq \emptyset$, $i \neq j$. The smoothing

domain Ω_k^s associated with the face k is created by simply connecting three nodes of the

face to the centers of the adjacent elements as shown in Figure 7.1.

The procedure is simple, and can always be performed for a given T4 element mesh

without any technical difficulty. Strain smoothing operations [24] are then performed

over these smoothing domains for creating a piecewisely constant strain field that is then

used to establish the discretized system of equations.

7.3 Formulation of the FS-FEM-T4

7.3.1 Static analysis

Using the general formulation of the S-FEM models presented in [Chapter 3, Section 3.1](#), a linear system of equations of the FS-FEM-T4 for the static analysis has the form of

$$\bar{\mathbf{K}}^{\text{FS-FEM}} \bar{\mathbf{d}} = \mathbf{f} \quad (7.1)$$

where $\bar{\mathbf{K}}^{\text{FS-FEM}}$ is the *smoothed* stiffness matrix whose entries are given by

$$\bar{\mathbf{K}}_{II}^{\text{FS-FEM}} = \int_{\Omega} \bar{\mathbf{B}}_I^T \mathbf{D} \bar{\mathbf{B}}_J d\Omega = \sum_{k=1}^{N_f} \int_{\Omega_k^s} \bar{\mathbf{B}}_I^T \mathbf{D} \bar{\mathbf{B}}_J d\Omega = \sum_{k=1}^{N_f} \bar{\mathbf{B}}_I^T \mathbf{D} \bar{\mathbf{B}}_J V_k^s \quad (7.2)$$

where V_k^s is the volume of the face-based smoothing domain Ω_k^s and is computed by

$$V_k^s = \int_{\Omega_k^s} d\Omega = \frac{1}{4} \sum_{j=1}^{n_k^e} V_j^e \quad (7.3)$$

where n_k^e is the number of elements attached to the face k ($n_k^e = 1$ for the boundary faces and $n_k^e = 2$ for inner faces) and V_j^e is the volume of the j^{th} element attached to the face k .

In Eq. (7.2), the smoothed strain-displacement matrix $\bar{\mathbf{B}}_I$ on the domain Ω_k^s is computed numerically simply by an local *assembly* process similarly as in the FEM

$$\bar{\mathbf{B}}_I = \frac{1}{V_k^s} \sum_{j=1}^{n_k^e} \frac{1}{4} V_j^e \mathbf{B}_j^e \quad (7.4)$$

where $\mathbf{B}_j^e = \sum_{I \in S_j^e} \mathbf{B}_I$ is the compatible strain-displacement matrix for the j^{th} tetrahedral element attached to the face k . It is assembled from the compatible strain-displacement matrices $\mathbf{B}_I(\mathbf{x})$ of nodes in the set S_j^e which contains four nodes of the j^{th} tetrahedral element. Matrix $\mathbf{B}_I(\mathbf{x})$ for the node I in tetrahedral elements has the form of Eq. (5.7).

From Eq.(7.4), it is clear that the entries of matrix $\bar{\mathbf{B}}_I$ are constants over each smoothing domain. With this formulation, only the volume and the usual compatible strain-displacement matrices \mathbf{B}_j^e of the FEM-T4 elements are needed to compute the system stiffness matrix for the FS-FEM-T4.

The above formulation is simple, but works only for T4 elements that uses linear interpolation. In theory, the FS-FEM works also for other types of elements, as long as a continuous displacement field on the smoothing domain surface can be created. For these general FS-FEM models, the smoothed strain-displacement matrix $\bar{\mathbf{B}}_I$ has to be computed using the original Eq. (3.10).

7.3.2 Nonlinear analysis of large deformation

The extension of the FS-FEM-T4 to geometrically nonlinear problems of large deformation is straightforward, and the similar procedure used in the standard FEM can be adopted with minor changes. For isotropic linear elastic solids, the values of the strain gradient matrices and stresses at the face-based smoothing domains become the average values of those of the adjacent elements attached to the face. The formulation of the FS-FEM-T4 for geometrically nonlinear problems of large deformation based on the total Lagrange formulation [12, 128], and the discrete system equations can be expressed by:

$$\left(\bar{\mathbf{K}}_L^{\text{FS-FEM}} + \bar{\mathbf{K}}_{NL}^{\text{FS-FEM}}\right)\bar{\mathbf{d}} = \mathbf{f} - \bar{\mathbf{f}}_1 \quad (7.5)$$

where the stiffness matrix for the linearized portion can be written as

$$\bar{\mathbf{K}}_L^{\text{FS-FEM}} = \sum_{k=1}^{N_f} \bar{\mathbf{B}}_L^T \mathbf{D} \bar{\mathbf{B}}_L V_k^s \quad (7.6)$$

in which matrix $\bar{\mathbf{B}}_L$ is for the face-based smoothing domains, and is computed using

$$\bar{\mathbf{B}}_L = \frac{1}{V_k^s} \sum_{j=1}^{n_k^e} \frac{1}{4} V_j^e \mathbf{B}_{L,j}^e \quad (7.7)$$

In the forgoing equation, matrix \mathbf{B}_L^e for an element is given by

$$\mathbf{B}_L^e = \begin{bmatrix} F_{11}N_{1,1} & F_{21}N_{1,1} & F_{31}N_{1,1} \\ F_{12}N_{1,2} & F_{22}N_{1,2} & F_{13}N_{1,2} \\ F_{13}N_{1,3} & F_{23}N_{1,3} & F_{33}N_{1,3} \\ F_{11}N_{1,2} + F_{12}N_{1,1} & F_{21}N_{1,2} + F_{22}N_{1,1} & F_{31}N_{1,2} + F_{32}N_{1,1} \\ F_{12}N_{1,3} + F_{13}N_{1,2} & F_{22}N_{1,3} + F_{23}N_{1,2} & F_{32}N_{1,3} + F_{33}N_{1,2} \\ F_{11}N_{1,3} + F_{13}N_{1,1} & F_{21}N_{1,3} + F_{23}N_{1,1} & F_{31}N_{1,3} + F_{33}N_{1,1} \end{bmatrix} \quad (7.8)$$

$$\begin{bmatrix} F_{11}N_{2,1} & \cdots & F_{31}N_{4,1} \\ F_{12}N_{2,2} & \cdots & F_{13}N_{4,2} \\ F_{13}N_{2,3} & \cdots & F_{33}N_{4,3} \\ F_{11}N_{2,2} + F_{12}N_{2,1} & \cdots & F_{31}N_{4,2} + F_{32}N_{4,1} \\ F_{12}N_{2,3} + F_{13}N_{2,2} & \cdots & F_{32}N_{4,3} + F_{33}N_{4,2} \\ F_{11}N_{2,3} + F_{13}N_{2,1} & \cdots & F_{31}N_{4,3} + F_{33}N_{4,1} \end{bmatrix}$$

in which $N_{i,j} = \frac{\partial N_i}{\partial X_j}$, and F_{IJ} are entries of the deformation gradient tensor for the

element \mathbf{F}^e that is computed by

$$\mathbf{F}^e = \begin{bmatrix} F_{11} & F_{12} & F_{13} \\ F_{21} & F_{22} & F_{23} \\ F_{31} & F_{32} & F_{33} \end{bmatrix} = \left(\frac{\partial \mathbf{x}}{\partial \mathbf{X}} \right)^T = (\nabla_s \bar{\mathbf{d}} + \mathbf{I})^T \quad (7.9)$$

where \mathbf{I} is the third order unity matrix and $\nabla_s \bar{\mathbf{d}}$ is the conventional compatible strain.

The stiffness matrix for the non-linear portion in Eq. (7.5) can be written as

$$\bar{\mathbf{K}}_{NL}^{\text{FS-FEM}} = \sum_{k=1}^{N_f} \bar{\mathbf{B}}_{NL}^T \bar{\mathbf{S}} \bar{\mathbf{B}}_{NL} V_k^s \quad (7.10)$$

where matrix $\bar{\mathbf{B}}_{NL}$ is for the face-based smoothing domain, and is computed using

$$\bar{\mathbf{B}}_{NL} = \frac{1}{V_k^s} \sum_{j=1}^{n_k^e} \frac{1}{4} V_j^e \mathbf{B}_{NL,j}^e \quad (7.11)$$

In the forgoing equation, matrix \mathbf{B}_{NL}^e is for the element, and is given by

$$\mathbf{B}_{NL}^e = \begin{bmatrix} N_{1,1} & 0 & 0 & N_{2,1} & \cdots & 0 \\ N_{1,2} & 0 & 0 & N_{2,2} & \cdots & 0 \\ N_{1,3} & 0 & 0 & N_{2,3} & \cdots & 0 \\ 0 & N_{1,1} & 0 & 0 & \cdots & 0 \\ 0 & N_{1,2} & 0 & 0 & \cdots & 0 \\ 0 & N_{1,3} & 0 & 0 & \cdots & 0 \\ 0 & 0 & N_{1,1} & 0 & \cdots & N_{4,1} \\ 0 & 0 & N_{1,2} & 0 & \cdots & N_{4,2} \\ 0 & 0 & N_{1,3} & 0 & \cdots & N_{4,3} \end{bmatrix} \quad (7.12)$$

and matrix $\bar{\mathbf{S}}$ is for face-based smoothing domain, and is computed using

$$\bar{\mathbf{S}} = \frac{1}{V_k^s} \sum_{j=1}^{n_k^e} \frac{1}{4} V_j^e \mathbf{S}_j^e \quad \text{with } \mathbf{S}^e = \begin{bmatrix} S_{11} & S_{12} & S_{13} & 0 & 0 & 0 & 0 & 0 & 0 \\ S_{12} & S_{22} & S_{23} & 0 & 0 & 0 & 0 & 0 & 0 \\ S_{13} & S_{23} & S_{33} & 0 & 0 & 0 & 0 & 0 & 0 \\ 0 & 0 & 0 & S_{11} & S_{12} & S_{13} & 0 & 0 & 0 \\ 0 & 0 & 0 & S_{12} & S_{22} & S_{23} & 0 & 0 & 0 \\ 0 & 0 & 0 & S_{13} & S_{23} & S_{33} & 0 & 0 & 0 \\ 0 & 0 & 0 & 0 & 0 & 0 & S_{11} & S_{12} & S_{13} \\ 0 & 0 & 0 & 0 & 0 & 0 & S_{12} & S_{22} & S_{23} \\ 0 & 0 & 0 & 0 & 0 & 0 & S_{13} & S_{23} & S_{33} \end{bmatrix} \quad (7.13)$$

in which the entries S_{ll} of matrix \mathbf{S}^e are derived from the 2nd Piola-Kirchhoff stress tensor Ψ^e for the element by

$$\boldsymbol{\Psi}^e = \begin{bmatrix} S_{11} \\ S_{22} \\ S_{33} \\ S_{12} \\ S_{23} \\ S_{31} \end{bmatrix} = \mathbf{D} \begin{bmatrix} E_{11} \\ E_{22} \\ E_{33} \\ 2E_{12} \\ 2E_{23} \\ 2E_{31} \end{bmatrix} \quad (7.14)$$

The entries E_{IJ} in Eq. (7.14) is derived from the entries of the Green-Lagrange strain tensor \mathbf{E}^e for the element as

$$\mathbf{E}^e = \begin{bmatrix} E_{11} & E_{12} & E_{13} \\ E_{21} & E_{22} & E_{23} \\ E_{31} & E_{32} & E_{33} \end{bmatrix} = \frac{1}{2} \left((\mathbf{F}^e)^T \mathbf{F}^e - \mathbf{I} \right) \quad (7.15)$$

The “additional” force term caused by the nonlinearity in Eq. (7.5) becomes

$$\bar{\mathbf{f}}_1 = \sum_{k=1}^{N_f} \bar{\mathbf{B}}_L^T \bar{\boldsymbol{\Psi}} V_k^s \quad (7.16)$$

where

$$\bar{\boldsymbol{\Psi}} = \frac{1}{V_k^s} \sum_{j=1}^{n_k^e} \frac{1}{4} V_j^e \boldsymbol{\Psi}_{1,j}^e \quad (7.17)$$

7.4 A smoothing-domain-based selective FS/NS-FEM-T4 model

Similar to the ES/NS-FEM-T3 given in [Chapter 6, Section 6.5](#), this section presents a smoothing-domain-based selective ES/NS-FEM-T4 for 3D solids of incompressible materials. We use two different types of smoothing domains selectively for two different material “parts” (μ -part and λ -part). This scheme comes from the realization of two facts: 1) the node-based smoothing domains used in the NS-FEM-T4 were found effective in overcoming the volumetric locking [78]; and 2) the λ -part is known as the culprit of the volumetric locking. We therefore use the node-based smoothing domains for the λ -part and face-based smoothing domains for the μ -part. The stiffness matrix of the smoothing-domain-based selective FS/NS-FEM-T4 model becomes

$$\bar{\mathbf{K}} = \underbrace{\sum_{i=1}^{N_f} (\bar{\mathbf{B}}_{1,i})^T \mathbf{D}_1 \bar{\mathbf{B}}_{1,i} V_{1,i}}_{\bar{\mathbf{K}}_1^{\text{FS-FEM}}} + \underbrace{\sum_{j=1}^{N_n} (\bar{\mathbf{B}}_{2,j})^T \mathbf{D}_2 \bar{\mathbf{B}}_{2,j} V_{2,j}}_{\bar{\mathbf{K}}_2^{\text{NS-FEM}}} \quad (7.18)$$

where $\bar{\mathbf{B}}_{1,i}$ and $V_{1,i}$ are the smoothed strain-displacement matrix and volume of the smoothing domain associated with face i ; $\bar{\mathbf{B}}_{2,j}$ and $V_{2,j}$ are the smoothed strain-displacement matrix and volume of the smoothing domain associated with node j ; N_n is the total number of nodes in the entire problem domain; and matrices \mathbf{D}_1 and \mathbf{D}_2 are derived from the material constant matrix \mathbf{D} for 3D cases as follows

$$\mathbf{D} = \mu \underbrace{\begin{bmatrix} 2 & 0 & 0 & 0 & 0 & 0 \\ 0 & 2 & 0 & 0 & 0 & 0 \\ 0 & 0 & 2 & 0 & 0 & 0 \\ 0 & 0 & 0 & 1 & 0 & 0 \\ 0 & 0 & 0 & 0 & 1 & 0 \\ 0 & 0 & 0 & 0 & 0 & 1 \end{bmatrix}}_{\mathbf{D}_1} + \lambda \underbrace{\begin{bmatrix} 1 & 1 & 1 & 0 & 0 & 0 \\ 1 & 1 & 1 & 0 & 0 & 0 \\ 1 & 1 & 1 & 0 & 0 & 0 \\ 0 & 0 & 0 & 0 & 0 & 0 \\ 0 & 0 & 0 & 0 & 0 & 0 \\ 0 & 0 & 0 & 0 & 0 & 0 \end{bmatrix}}_{\mathbf{D}_2} = \mathbf{D}_1 + \mathbf{D}_2 \quad (7.19)$$

7.5 Stability of the FS-FEM-T4

Property 7.1: the FS-FEM-T4 possesses only “legal” zero energy modes that represents the rigid motions and hence the FS-FEM-T4 is spatially stable. There exist no spurious non-zero energy modes and thus the FS-FEM-T4 is also temporally stable.

In the standard FEM-T4 using linear shape functions, the integration of the weak form is based on elements. For each element, only one Gauss point is needed for the exact evaluation of the integrals. This implies that the number of Gauss points to calculate equals to the number of elements used in the problem domain. Such an FEM-T4 model is well known stable spatially and also temporally, and hence is widely used for dynamics analysis and has no spurious non-zero energy modes.

In the FS-FEM-T4, the smoothing domains used are associated with faces and the strain (or stress) on each domain is constant. Therefore, each smoothing domain can be

considered equivalent to one Gauss point sampling in evaluating the weak form. Because the number of faces is always larger than the number of elements in any T4 element meshes, the number of sampling points for the evaluation of the weak form in the FS-FEM-T4 is always larger than that in the FEM-T4. Therefore, the FS-FEM-T4 should be more stable than the FEM-T4 model, has no spurious non-zero energy modes, and is well suited for the dynamic analysis. This property of the FS-FEM-T4 is quite similar to that of the ES-FEM-T3 for dynamic analyses of 2D solid mechanics problems [76].

7.6 Irons first-order patch test and a mesh sensitivity analysis

The Irons first-order patch test presented in [Chapter 5, Section 5.6.3](#), is performed again for the FS-FEM-T4. The errors in displacement norm [\(4.12\)](#) and in energy norm [\(5.12\)](#) are used to examine quantitatively the computed results. An analysis of the sensitivity of the solution against highly distorted meshes is also considered.

The results of the patch test are listed in [Table 7.1](#) for meshes of different irregularities. It is found that the FS-FEM-T4 can pass the Irons first-order patch test within machine precision regardless of the irregularity factor α_{ir} used. There is no accuracy loss due to the choice of α_{ir} value. This shows that the FS-FEM-T4 can work well with the severely distorted meshes.

7.7 Numerical examples

In this section, some examples will be presented to demonstrate the properties of the FS-FEM-T4 model. To emphasize the advantages of the FS-FEM-T4, the results of the present method will be compared with those of the FEM using tetrahedral elements (FEM-T4), 8-node hexahedral elements (FEM-H8) and NS-FEM using tetrahedral

elements (NS-FEM-T4) [78]. The errors in displacement norm and energy norm defined in Eq. (4.18) and Eq. (4.19) are used in the analyses.

In the calculation of Eq. (4.19) for the FS-FEM-T4, a recovery strain field $\bar{\boldsymbol{\varepsilon}}^R$ defined in Eq.(5.17) will be used in the place of the general numerical strain field $\check{\boldsymbol{\varepsilon}}$. In the numerical implementation of the FS-FEM-T4, the value of strains (or stresses) at the node i will be the average value of the strains (or stresses) of the smoothing domains Ω_k^s around the node i , and are computed numerically using

$$\bar{\boldsymbol{\varepsilon}}_i = \frac{1}{V_f^i} \sum_{k=1}^{n_f^i} \bar{\boldsymbol{\varepsilon}}_k V_k^s \quad (7.20)$$

where n_f^i is the total number of the faces connecting directly to node i ; $V_f^i = \sum_{k=1}^{n_f^i} V_k^s$ is the total volume of the smoothing domain Ω_k^s around the node i ; and $\bar{\boldsymbol{\varepsilon}}_k$ and V_k^s are, respectively, the smoothing strain and the volume of the smoothing domain Ω_k^s .

Because linear elements are used, the strains in the elements are constants, we can use the same methods for the evaluation of the strains (or stresses) at nodes by the FEM-T4, which give the identical results as those of Eq. (7.20) by the FS-FEM-T4.

7.7.1 3D Lamé problem: a linear elasticity analysis

The 3D Lamé problem described in Example 5.7.3 is used again in the examination of the FS-FEM-T4. One-eighth of the sphere model is discretized as shown in Figure 5.17 and symmetry conditions are imposed properly on these three cutting symmetric planes. The exact strain energy of the problem is known as $E_{\text{exact}} = 6.306 \times 10^{-2} \text{ Nm}$.

Figure 7.2 and Figure 7.3 plot the distribution of the displacements and stresses obtained using the FS-FEM-T4, together with the analytical solution. It is seen clearly that these results agree very well. The convergence of the strain energy solution is

presented in Table 5.12 and plotted in Figure 7.4. It is seen that the results of NS-FEM-T4 is an upper bound solution, and that of FS-FEM-T4 is a lower bound solution, with respect to the exact solution. The results of FS-FEM-T4 are almost the same as those of the FEM-H8 and much more accurate than those of the FEM-T4.

The solution error in displacement norm obtained using the FS-FEM-T4 is presented in Table 5.13 and plotted in Figure 7.5, together with those of other methods. It is found that the result of FS-FEM-T4 is less accurate than that of FEM-H8 but more accurate than those of NS-FEM-T4 and FEM-T4. When the 3rd fine mesh for both T4 and H8 ($h \approx 0.156$) is used, the error of FS-FEM-T4 is about 3/4 of FEM-T4 and NS-FEM-T4. In terms of convergence rate, the rate of FS-FEM-T4 ($r = 1.99$) is also larger than those of FEM-T4 ($r = 1.93$) and NS-FEM-T4 ($r = 1.85$).

Table 5.14 and Figure 7.6 compared the solution error in energy norm obtained using the FS-FEM-T4, together with those of other methods using the same meshes. It is found that the results of FS-FEM-T4 is only less accurate than those of NS-FEM-T4 but more accurate than those of FEM-H8 and FEM-T4. When the 3rd fine mesh for both T4 and H8 ($h \approx 0.156$) is used, the error of FS-FEM-T4 is about 1/2 of FEM-T4 and 3/5 of FEM-H8. In terms of convergence rate, the FS-FEM-T4 stands out clearly with a rate of $r = 1.43$ which is much larger than the theoretical value of 1.0 and much higher even than those of the NS-FEM-T4 ($r = 1.34$) and FEM-H8 ($r = 0.95$). All the above results show that the FS-FEM-T4 is significantly more accurate than FEM-T4 and comparable with the FEM-H8 for 3D linear problems.

Figure 7.7 shows the solution error in displacement norm using the smoothing-domain-based selective FS/NS-FEM-T4 for nearly incompressible material when Poisson's ratio varies from 0.4 to 0.4999999. The results show that the smoothing-domain-based selective FS/NS-FEM-T4 model presented in Section 7.4 can overcome naturally the

volumetric locking for solids of nearly incompressible materials. This is due to the volumetric locking-free feature of the NS-FEM models discussed in [Chapter 5](#).

7.7.2 A 3D cubic cantilever: a linear elasticity analysis

The 3D cantilever of cubic shape subjected to a uniform pressure on its upper face described in [Example 5.7.4](#) is again studied, but using the FS-FEM-T4. The reference strain energy and deflection at point A (1.0,1.0,-0.5) from the solutions of the standard FEM using a very fine mesh with 30,204 nodes and 20,675 ten-node tetrahedron elements are 0.9486 and 3.3912, respectively.

The convergence of the strain energy solution obtained using the FS-FEM-T4 is presented in [Table 5.15](#) and plotted in [Figure 7.8](#), together with other methods. The convergence of the deflection at point A obtained using the FS-FEM-T4 is presented in [Table 5.16](#) and plotted in [Figure 7.9](#), together with other methods. It is found that the results of FS-FEM-T4 are less accurate than those of FEM-H8 but much more accurate than those of FEM-T4 for this problem. These results again show that the FS-FEM-T4 is significantly more accurate than the FEM-T4 for 3D linear elasticity problems.

7.7.3 A 3D cantilever beam: a geometrically nonlinear analysis

This example examines the use of the FS-FEM-T4 for the geometrically nonlinear analysis of large deformation for 3D solids. A 3D cantilever beam subjected to a uniformly distributed load is considered. The size of the beam is (10cm x 2cm x 2cm) and discretized using a mesh including 1322 nodes and 5802 tetrahedral elements as shown in [Figure 7.10](#). The related parameters are taken as $E = 3.0 \times 10^7$ KN/cm², $\nu = 0.3$.

First, a mesh sensitivity analysis using the FS-FEM-T4 and FEM-T4 is performed in the similar way as in the Iron first-order patch test. To create distorted meshes, the interior

nodes are intentionally moved randomly inside the cantilever beam from the original regular positions. The moved coordinates are computed using Eq. (5.15). In addition, the interior nodes of boundary faces are also moved randomly inside their original faces. Only the nodes located on the boundary sides of the cantilever beam are kept unchanged. Table 7.2 shows the relation between the tip deflection versus the prescribed irregularity factor α_{ir} chosen between 0.0 and 0.4, and Figure 7.11 plots a severely distorted mesh with $\alpha_{ir} = 0.4$. The results are computed using both the FS-FEM-T4 and FEM-T4 models with exactly the same meshes, and listed in Table 7.2. For easy analysis we use the result of the tip deflection $d = 2.5292$ obtained using the FEM-H8 with 2304 nodes as a reference solution. Table 7.2 shows that the FS-FEM-T4 produces more accurate and is less sensitive to the mesh distortion than those of FEM-T4. This finding implies that the FS-FEM-T4 is much more suitable than the FEM-T4 for geometrically nonlinear analysis of large deformation, where heavy mesh distortion are generally expected.

The geometrically nonlinear analysis based on the total Lagrange formulation that are often used in the FEM-T4 is carried out using 10 increment steps ($n=10$) with $\Delta f = 4\text{KN/cm}^2$ in each step. Figure 7.10 displays the initial and final configurations after 10 steps of increments of the deformation using the FS-FEM-T4. Table 7.3 and Figure 7.12 show the relation between the tip deflection and the load steps for different methods. The simulation result converges very rapidly in each load increment, only less than 5 times of iteration are needed. The results show that, the nonlinear effects make the cantilever beam behave stiffer compared to the linear solutions. In the geometrically nonlinear analysis, the results of FS-FEM-T4 are softer than those of FEM-T4 but stiffer than those of FEM-H8 using 1323 nodes. All these results suggest that the FS-FEM-T4 performs more accurately than the FEM-T4 for 3D geometrically nonlinear analysis of large deformation.

7.7.4 An axletree base: a geometrically nonlinear analysis

In this practical example, a geometrically nonlinear analysis of large deformation of an axletree base is studied using the FS-FEM-T4 method. As shown in Figure 7.13, the axletree base is symmetric about the y - z plane. A half model with 1342 nodes and 5124 tetrahedral elements is then created. The axletree base is subjected to a uniformly distributed force f on the concave annulus in the z -direction and fixed at the locations of four lower cylindrical holes and on the bottom plane. The related parameters are taken as $E = 3.0 \times 10^7 \text{ N/cm}^2$, $\nu = 0.3$. The analysis based on the total Lagrange formulation is carried out using 10 increment steps ($n=10$) with $\Delta f = 400 \text{ KN/cm}^2$ in each step.

Figure 7.14 displays the initial and final configurations viewed from the top of the 3D axletree base after 10 steps of simulation using the FS-FEM-T4. Table 7.4 and Figure 7.15 show the relation between the tip displacement (point A) in z -direction versus the load steps for different methods. The simulation converges in a rapid speed in each load increment, less than 9 iterations are needed. It can be seen that, the nonlinear effects make the axletree base behave stiffer compared to the linear solutions. In this geometrically nonlinear analysis, the results of FS-FEM-T4 are found softer than those of FEM-T4 and almost similar to that of the FEM-T4 using 2520 nodes. Note that for this problem, a discretization using 8-node hexahedral elements is impossible due to the complicity of the geometry of the problem, especially at points B, C or D shown in Figure 7.13. All these results again show that the FS-FEM-T4 performs more accurately than the FEM-T4 in 3D geometrically nonlinear analysis of large deformation.

7.8 Remarks

In this chapter, a face-based smoothed finite element method (FS-FEM-T4) is presented and applied to solve 3D solid mechanics problems. In the FS-FEM-T4, the system stiffness matrix is computed using the smoothed strains over the smoothing domains associated with the faces of the tetrahedral elements.

Through the theoretical analyses, formulations and numerical examples, it is found that the FS-FEM-T4 is significantly more accurate than the FEM-T4 using tetrahedral elements for both linear analysis and geometrically nonlinear analysis of large deformation. With the FS-FEM, we can now use tetrahedral elements with ease for accurate solutions for problems with complicated geometry.

In addition, a smoothing-domain-based selective FS/NS-FEM-T4 model is immune from volumetric locking, and hence it works well for solids of nearly incompressible materials. The implementation of the FS-FEM-T4 is straightforward and no additional degrees of freedom are used in the model.

	$\alpha_{ir} = 0.0$	$\alpha_{ir} = 0.1$	$\alpha_{ir} = 0.2$	$\alpha_{ir} = 0.3$	$\alpha_{ir} = 0.4$	$\alpha_{ir} = 0.49$
Displacement norm e_d (%)	3.95e-16	1.16e-15	7.73e-16	1.00e-15	1.53e-15	2.21e-15
Energy norm e_e	0.0	7.28e-12	1.82e-11	1.09e-11	7.28e-12	2.12e-11

	$\alpha_{ir} = 0.0$	$\alpha_{ir} = 0.1$	$\alpha_{ir} = 0.2$	$\alpha_{ir} = 0.3$	$\alpha_{ir} = 0.4$
FS-FEM-T4 (1322 nodes)	2.4429	2.4373 (0.23 %) ^(*)	2.4218 (0.86 %)	2.3888 (2.21 %)	2.3418 (4.14 %)
FEM-T4 (1322 nodes)	2.3639	2.3559 (0.34 %)	2.3349 (1.23 %)	2.2933 (2.99 %)	2.2141 (6.34 %)

^(*) The number in the bracket shows the relative error (%) between the numerical results at $\alpha_{ir} > 0$ and that at $\alpha_{ir} = 0.0$.

Load step	FEM-T4 (linear) (1322 nodes)	FEM-T4 (nonlinear) (1322 nodes)	FEM-H8 (nonlinear) (1323 nodes)	FS-FEM-T4 (nonlinear) (1322 nodes)
n = 1	0.2364	0.2295 (3) ^(*)	0.2421 (3)	0.2365 (3)
n = 2	0.4728	0.4314 (3)	0.4522 (3)	0.4430 (3)
n = 3	0.7092	0.6119 (3)	0.6405 (3)	0.6277 (3)
n = 4	0.9456	0.7831 (3)	0.8205 (3)	0.8038 (3)
n = 5	1.1819	0.9511 (3)	1.0022 (4)	0.9818 (4)
n = 6	1.4183	1.1210 (4)	1.1762 (4)	1.1516 (4)
n = 7	1.6547	1.2847 (4)	1.3495 (4)	1.3206 (4)
n = 8	1.8911	1.4479 (4)	1.5222 (4)	1.4891 (4)
n = 9	2.1275	1.6104 (4)	1.6943 (4)	1.6569 (4)
n = 10	2.3639	1.7724 (4)	1.8656 (4)	1.8242 (4)

^(*) The number in the bracket shows the number of iterations.

Table 7.4. Tip displacement (point A) (cm) in z -direction at load steps for the 3D axletree base using 4-node tetrahedral elements for the geometrically nonlinear analysis.				
Load step	FEM-T4 (linear) (1342 nodes)	FEM-T4 (nonlinear) (1342 nodes)	FEM-T4 (nonlinear) (2520 nodes)	FS-FEM-T4 (nonlinear) (1342 nodes)
$n = 1$	0.3534	0.3104 (3) ^(*)	0.3260 (3)	0.3274 (3)
$n = 2$	0.7068	0.5700 (4)	0.5990 (4)	0.6017 (4)
$n = 3$	1.0601	0.8120 (5)	0.8538 (5)	0.8577 (5)
$n = 4$	1.4135	1.0419 (5)	1.0963 (5)	1.1012 (5)
$n = 5$	1.7669	1.2568 (6)	1.3210 (6)	1.3268 (6)
$n = 6$	2.1203	1.4650 (6)	1.5393 (6)	1.5460 (6)
$n = 7$	2.4737	1.6652 (7)	1.7360 (7)	1.7434 (7)
$n = 8$	2.8271	1.8436 (7)	1.9340 (7)	1.9421 (7)
$n = 9$	3.1804	2.0269 (8)	2.1074 (8)	2.1161 (8)
$n = 10$	3.5338	2.1855 (8)	2.2901 (8)	2.2996 (8)

^(*) The number in the bracket shows the number of iterations.

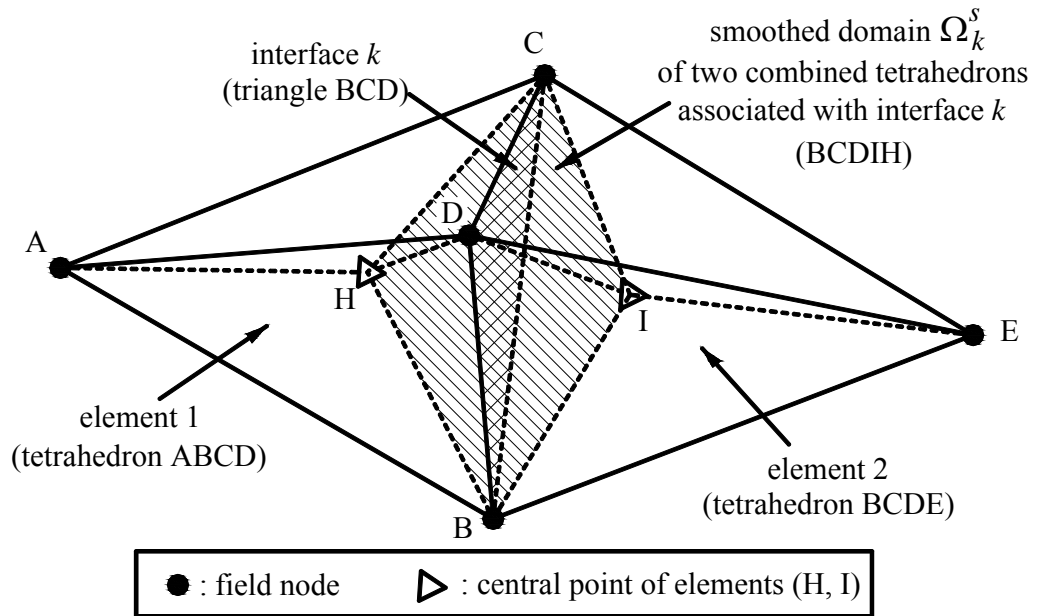


Figure 7.1. Two adjacent tetrahedral elements and the smoothing domain Ω_k^s (shaded domain) formed based on their interface k in the FS-FEM-T4.

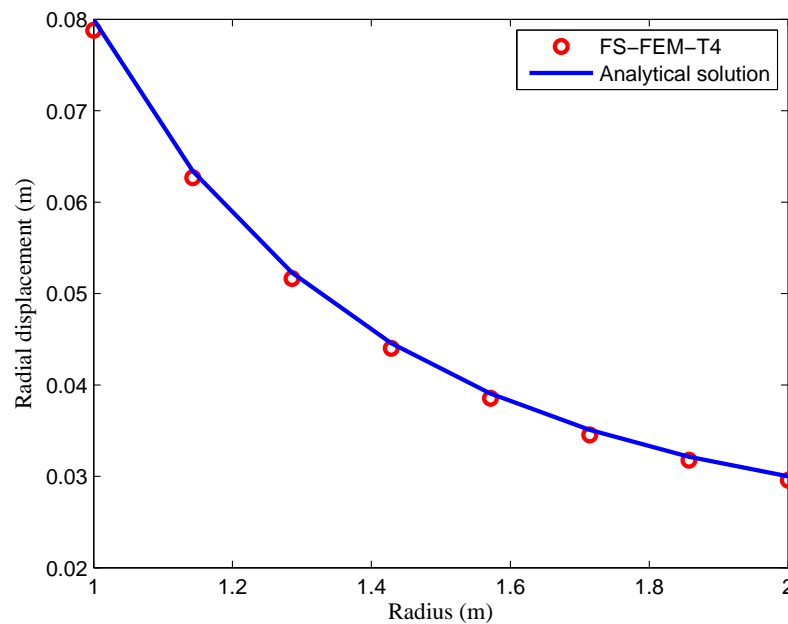


Figure 7.2. Distribution of the radial displacement in the hollow sphere subjected to an inner pressure using the FS-FEM-T4.

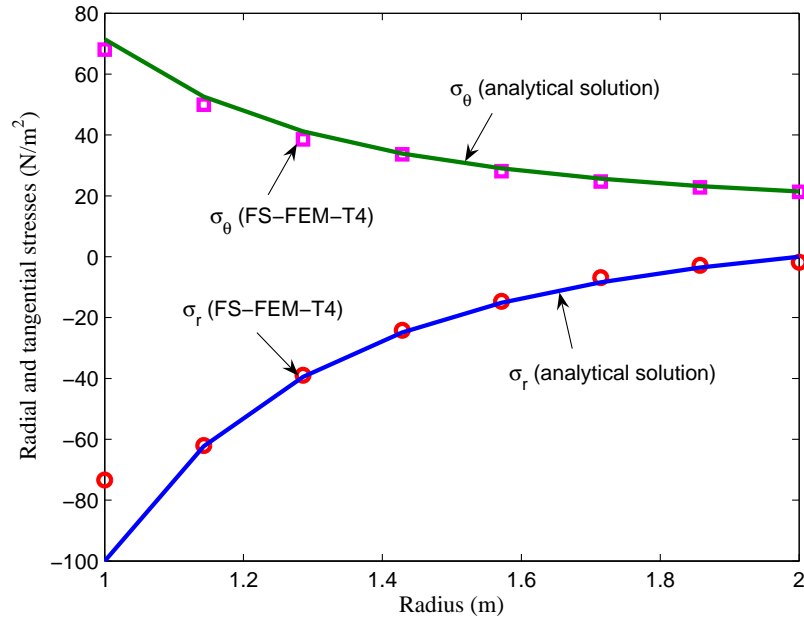


Figure 7.3. Distribution of the radial and tangential stresses in the hollow sphere subjected to an inner pressure using the FS-FEM-T4.

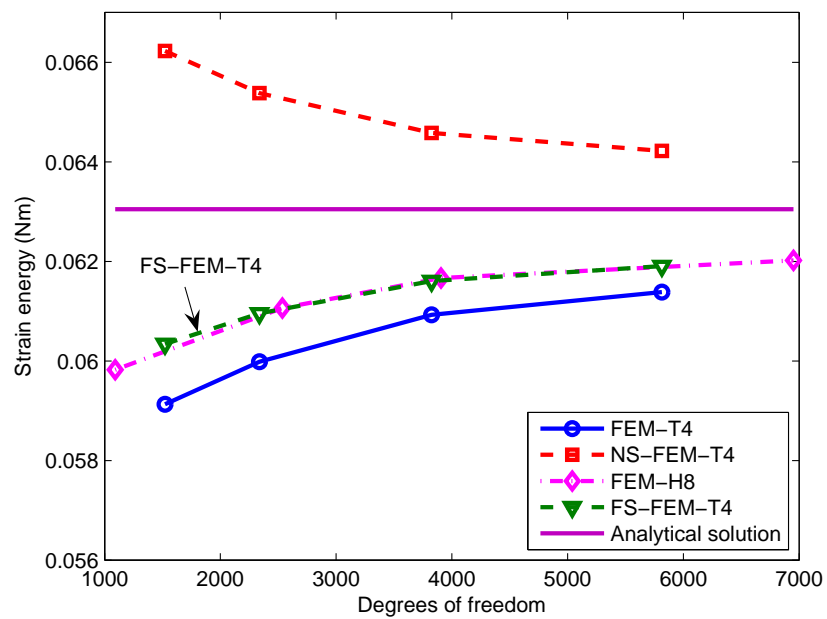


Figure 7.4. Convergence of strain energy solution of FS-FEM-T4 in comparison with other methods for the hollow sphere subjected to an inner pressure.

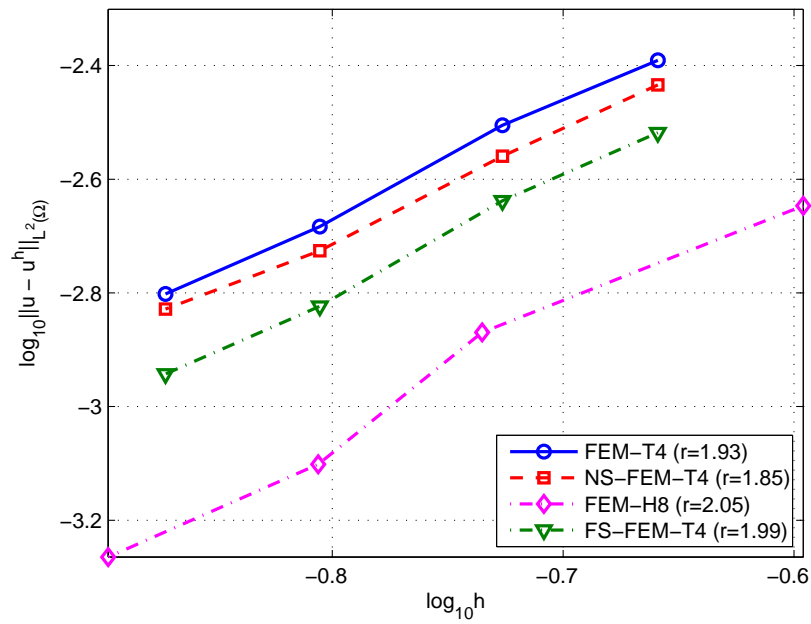


Figure 7.5. Error in displacement norm of FS-FEM-T4 in comparison with other methods for the hollow sphere subjected to an inner pressure.

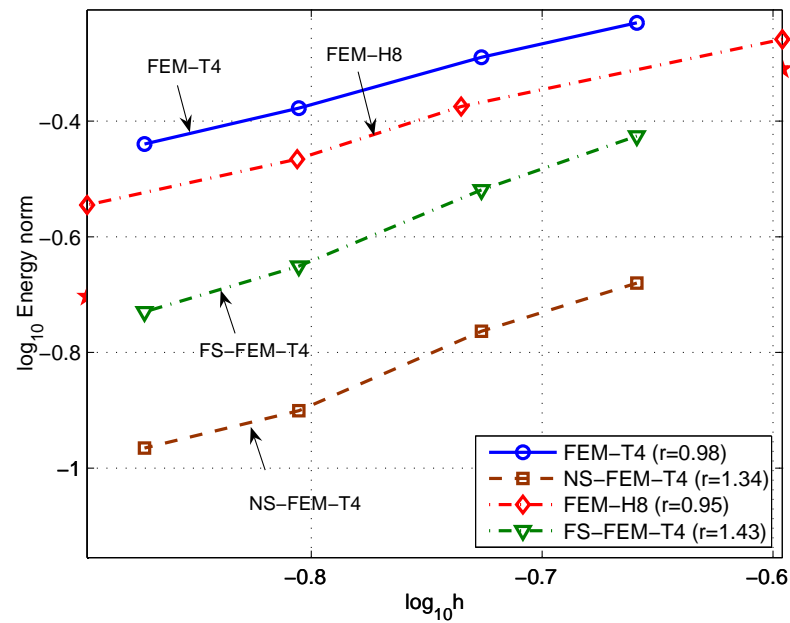


Figure 7.6. Error in energy norm of FS-FEM-T4 in comparison with other methods for the hollow sphere subjected to an inner pressure.

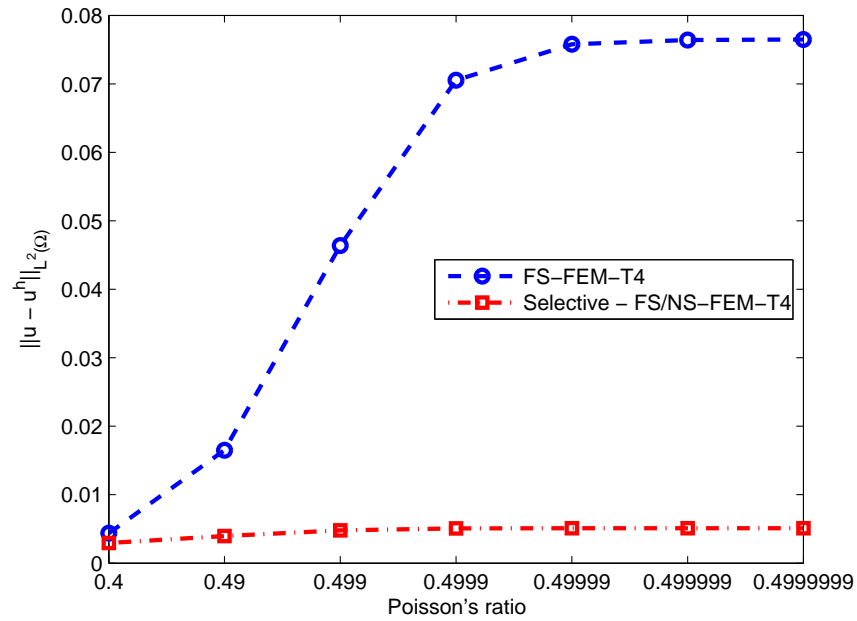


Figure 7.7. Error in displacement norm versus different Poisson's ratios of the hollow sphere subjected to an inner pressure.

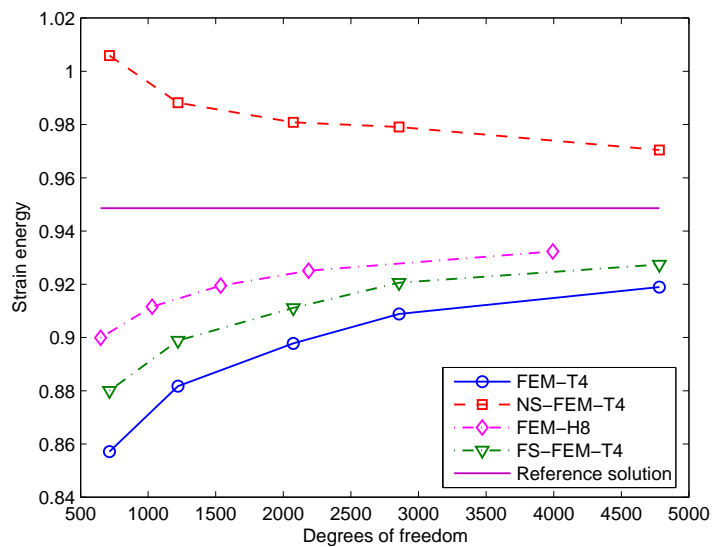


Figure 7.8. Convergence of the strain energy solution of FS-FEM-T4 in comparison with other methods for the cubic cantilever subjected to a uniform pressure on the top surface.

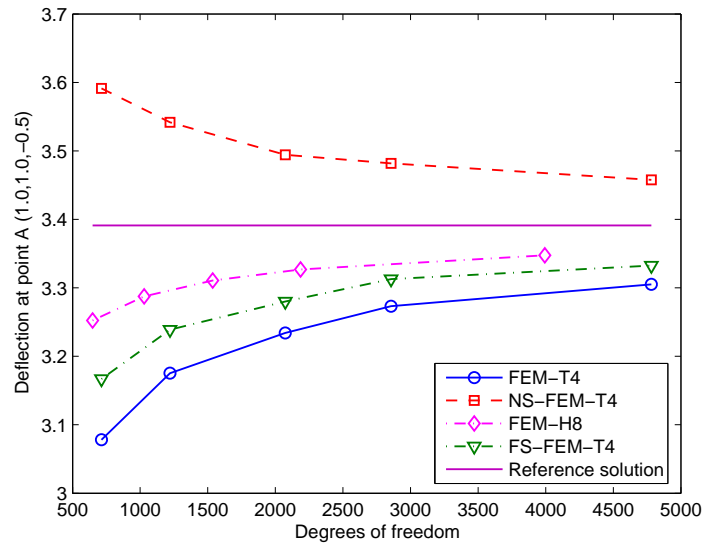


Figure 7.9. Convergence of the deflection at point A(1.0,1.0,-0.5) of FS-FEM-T4 in comparison with other methods for the cubic cantilever subjected to a uniform pressure.

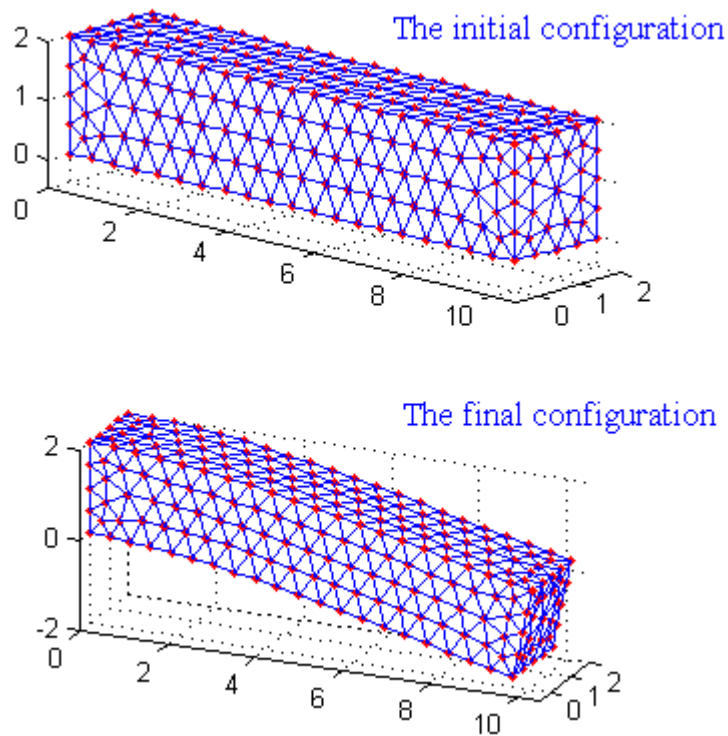


Figure 7.10. Initial and final configurations of the 3D cantilever beam subjected to a uniformly distributed load using the FS-FEM-T4 in the geometrically nonlinear analysis.

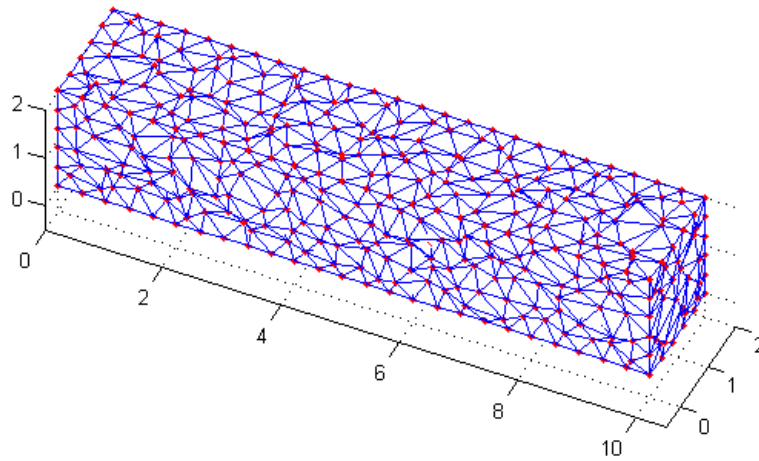


Figure 7.11. Domain discretization of the 3D cantilever beam subjected to a uniformly distributed load using severely distorted tetrahedral elements.

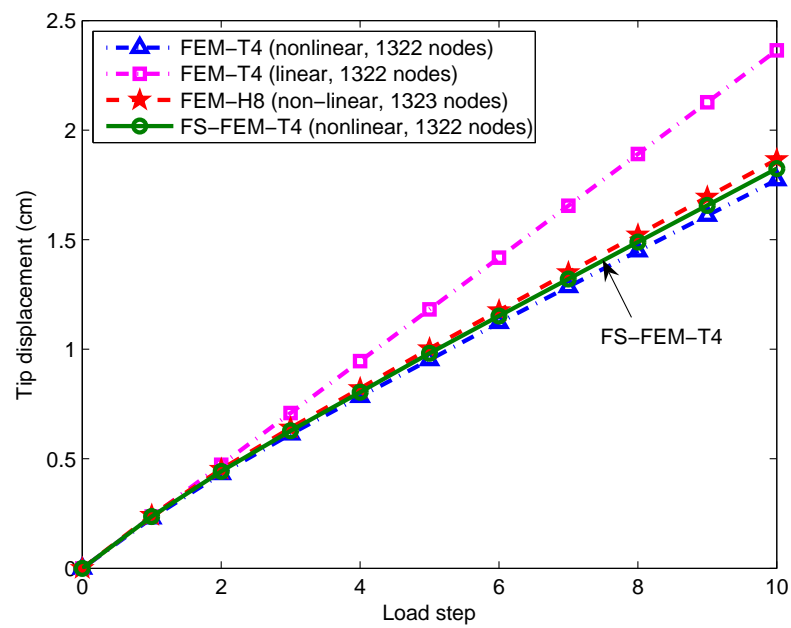


Figure 7.12. Tip deflection (*cm*) versus the load step of the 3D cantilever beam subjected to a uniformly distributed load in the geometrically nonlinear analysis.

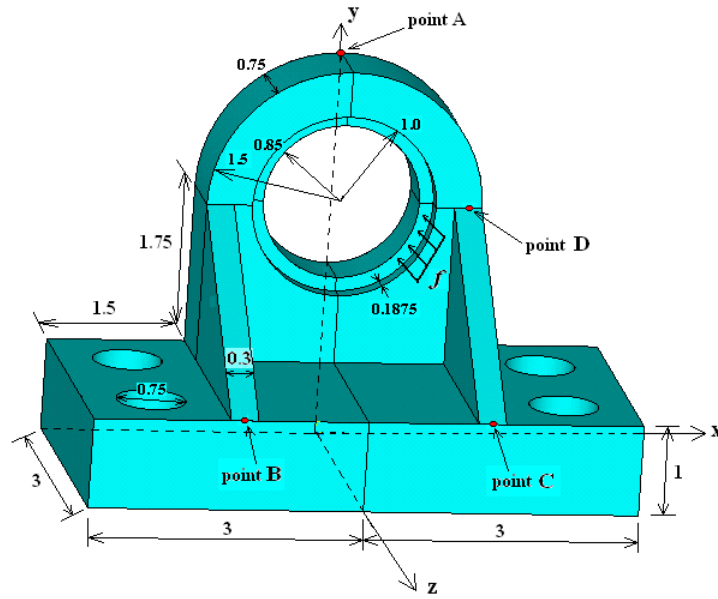


Figure 7.13. Axletree base model.

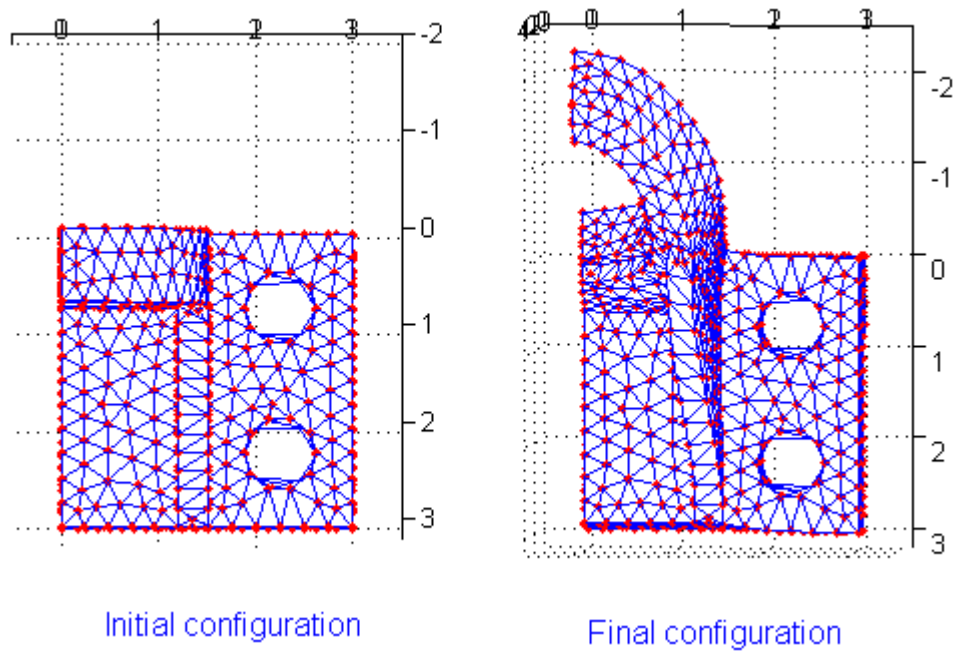


Figure 7.14. Initial and final configurations viewed from the top of an 3D axletree base using 4-node tetrahedral elements in the geometrically nonlinear analysis.

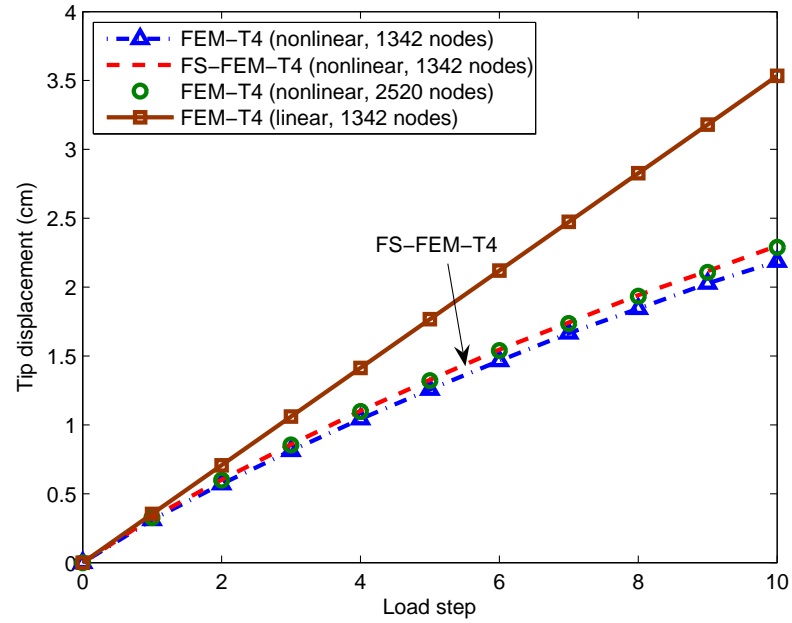


Figure 7.15. Tip displacement (point A) in z -direction versus the load step of an 3D axletree base using 4-node tetrahedral elements in the geometrically nonlinear analysis.

Chapter 8

Alpha FEM using triangular (α FEM-T3) and tetrahedral elements (α FEM-T4)

8.1 Introduction

Most of the existing mixed FEM models [9, 96, 131, 132] based on the mixed variational principles focusing mainly on the improvement of the accuracy of the solution. Obtaining exact solution (at least in a norm) using a numerical method is, however, an attractive idea in the area of computational methods. Hence, some interesting efforts have been made in recently in Liu's group aiming to obtain the exact solution in a norm using discrete models [75, 74]. The so-called alpha finite element method using 4-node quadrilateral elements (α FEM-Q4) has been developed for the purpose of finding a nearly exact solution in strain energy using coarse meshes [75]. The α FEM-Q4 gives a novel idea that works in the framework of FEM-Q4, by simply scaling the gradient of strains using a factor $\alpha \in [0, 1]$. Because the change needed is minor, the coding of the α FEM-Q4 is almost exactly the same as the standard FEM-Q4. In addition, the resultant strain energy function for the α FEM-Q4 model has a very simple polynomial form in terms of α . Based on such a simple function of strain energy curves, a general procedure of α FEM-Q4 has been suggested to obtain the nearly exact or best possible solution in strain

energy, using meshes with the same aspect ratio. An exact- α approach is devised for overestimation problems [75], and a stab- α approach for underestimation problems [75]. The α FEM-Q4 has clearly opened a new window of opportunity to obtain numerical solutions that are exact at least in a norm. However, the original α FEM-Q4 based on quadrilateral elements cannot provide exact solution to all elasticity problems. Furthermore, the use of 4-node quadrilateral elements in the α FEM-Q4 requires a quadrilateral mesh that cannot be generated in a fully automated manner for complicated domains.

Making use of the upper bound property of NS-FEM in [Chapter 5](#), the lower bound property of the standard FEM in strain energy, and the importance idea of α FEM-Q4, we introduce now a novel alpha finite element method using 3-node triangular (α FEM-T3) elements for 2D problems and 4-node tetrahedral elements (α FEM-T4) for 3D problems, which were originally presented in [74]. The essential idea of the method is to introduce a scale factor $\alpha \in [0,1]$ to establish a continuous function of strain energy that contains contributions from both the standard FEM and NS-FEM. This novel combined formulation of FEM and NS-FEM makes the best use of the upper bound property of the NS-FEM and the lower bound property of the standard FEM, and equipped with a free parameter for turning for special properties. Using meshes with the same aspect ratio, a unified approach has been proposed to obtain the nearly exact solution in strain energy for any given linear elasticity problem. The numerical results will confirm the interesting properties of the present method.

8.2 Idea of the α FEM-T3 and α FEM-T4

8.2.1 α FEM-T3 for 2D problems

The α FEM-T3 combines both the NS-FEM-T3 and the standard FEM-T3 by using the scale factor $\alpha \in [0,1]$. As presented in [Chapter 5](#), in the NS-FEM-T3, the domain Ω_i^e of

each triangular element is divided into three quadrilateral sub-domains of equal area, and each quadrilateral sub-domain contributes to the stiffness matrix of the node attached, as shown in Figure 8.1. In the α FEM-T3, the domain Ω_i^e of the triangular element is divided into four sub-domains with a scale factor α as shown in Figure 8.1: three quadrilateral sub-domains at the three corners are scaled down by $(1-\alpha^2)$ and are all having an equal area of $\frac{1-\alpha^2}{3} A_i^e$. The remaining Y -shaped sub-domain in the middle of the element has an area of $\alpha^2 A_i^e$. The same procedure in the NS-FEM-T3 is then used to compute the stiffness contributions of the three quadrilateral sub-domains at the three corners, while the usual procedure of the FEM-T3 is used to compute the stiffness contribution for the Y -shaped sub-domain, with the considerations of the area reductions. The entries in sub-matrices of the system stiffness matrix $\hat{\mathbf{K}}^{\alpha\text{FEM-T3}}$ will be assembled from the entries of those of NS-FEM-T3 and FEM-T3. The detailed formulation becomes

$$\hat{\mathbf{K}}_{IJ}^{\alpha\text{FEM-T3}} = \sum_{k=1}^{N_n} \bar{\mathbf{K}}_{IJ,k}^{\text{NS-FEM-T3}} + \sum_{i=1}^{N_e} \mathbf{K}_{IJ,i}^{\text{FEM}} \quad (8.1)$$

where N_n and N_e are, respectively, the total number of nodes and elements in the entire problem domain and

$$\bar{\mathbf{K}}_{IJ,k}^{\text{NS-FEM-T3}} = \int_{\Omega_{k,\alpha}^s} (\bar{\mathbf{B}}_I^\alpha(\mathbf{x}_k))^T \mathbf{D} \bar{\mathbf{B}}_J^\alpha(\mathbf{x}_k) d\Omega \quad (8.2)$$

$$\mathbf{K}_{IJ,i}^{\text{FEM}} = \int_{\Omega_{i,\alpha}^e} \mathbf{B}_I^T \mathbf{D} \mathbf{B}_J d\Omega = \mathbf{B}_I^T \mathbf{D} \mathbf{B}_J \alpha^2 A_i^e \quad (8.3)$$

in which the compatible strain-displacement matrix \mathbf{B}_I is computed using Eq. (2.48); $\Omega_{i,\alpha}^e$ is the Y -shape sub-domain in the triangular element; $\Omega_{k,\alpha}^s$ is the smoothing domain associated the node k and bounded by $\Gamma_{k,\alpha}^s$, as shown in Figure 8.2. The smoothed strain-displacement matrix $\bar{\mathbf{B}}_I^\alpha(\mathbf{x}_k)$ for $\Omega_{k,\alpha}^s$ is computed using

$$\bar{\mathbf{B}}_I^\alpha(\mathbf{x}_k) = \frac{1}{A_{k,\alpha}^s} \sum_{j=1}^{n_k^e} \frac{1}{3} (1-\alpha^2) A_j^e \mathbf{B}_{I,j} = \frac{1}{A_k^s} \sum_{j=1}^{n_k^e} \frac{1}{3} A_j^e \mathbf{B}_{I,j} = \bar{\mathbf{B}}_I(\mathbf{x}_k) \quad (8.4)$$

which implies that we can use the matrix $\bar{\mathbf{B}}_I(\mathbf{x}_k)$ defined in Eq. (5.3) for domain Ω_k^s instead the matrix $\bar{\mathbf{B}}_I^\alpha(\mathbf{x}_k)$ for domain $\Omega_{k,\alpha}^s$ in the computation. Note that to obtain Eq. (8.4), the following relation between the area $A_{k,\alpha}^s$ of the domain $\Omega_{k,\alpha}^s$ and the area A_k^s defined in Eq. (5.4) of the domain Ω_k^s is used:

$$A_{k,\alpha}^s = \int_{\Omega_{k,\alpha}^s} d\Omega = \sum_{j=1}^{n_k^e} \frac{1}{3} (1-\alpha^2) A_j^e = (1-\alpha^2) A_k^s \quad (8.5)$$

where n_k^e is the number of elements around the node k ; A_j^e is the area of the j^{th} element around the node k .

Using Eqs. (8.4) and (8.5), Eq. (8.2) now can be written as

$$\bar{\mathbf{K}}_{IJ,k}^{\text{NS-FEM-T3}} = (1-\alpha^2) \bar{\mathbf{B}}_I^T \mathbf{D} \bar{\mathbf{B}}_J A_k^s \quad (8.6)$$

which implies that we can simplify the procedure of coding program of α FEM-T3 by using the original NS-FEM-T3. Each triangle element is divided into three quadrilaterals of equal area to compute the contributions to the stiffness matrix with a scaling-down of $(1-\alpha^2)$.

To compute Eq. (8.3), the standard FEM using triangular elements (FEM-T3) is used to compute the contributions to the stiffness matrix with a simple scaling-down of α^2 .

The α FEM-T3 model is now equipped with a scaling factor α that acts as a ‘‘knob’’ controlling the contributions from portions of NS-FEM-T3 and FEM-T3. Since both NS-FEM-T3 and FEM-T3 models are spatially stable and convergent, when the factor α is ‘‘turned’’ from 0 to 1, a continuous function of solution in a norm can be expected from the solution of NS-FEM-T3 to that of FEM-T3.

8.2.2 α FEM-T4 for 3D problems

The extension from the α FEM-T3 to α FEM-T4 is straightforward. Following the same idea and concept of α FEM-T3 presented above, we can easily develop an α FEM-T4 model for 3D problems using tetrahedral elements. In this case, the (volumetric) domain Ω_i^e of each tetrahedral element will be divided into five sub-domains using a similar scaling factor α : four sub-domains at four corners will have an equal volume of $\frac{(1-\alpha^3)}{4}V_i^e$. The remaining sub-domain in the middle of the element will have a volume $\alpha^3V_i^e$. The NS-FEM-T4 is then used to compute for four corner sub-domains of equal volumes, while the FEM-T4 is used to compute for the remaining sub-domain in the middle, with a proper scaling. The system stiffness matrix $\hat{\mathbf{K}}^{\alpha\text{FEM-T4}}$ is computed using

$$\hat{\mathbf{K}}_{IJ}^{\alpha\text{FEM-T4}} = \sum_{k=1}^{N_n} \bar{\mathbf{K}}_{IJ,k}^{\text{NS-FEM-T4}} + \sum_{i=1}^{N_e} \mathbf{K}_{IJ,i}^{\text{FEM-T4}} \quad (8.7)$$

with the matrices $\bar{\mathbf{K}}_{IJ,k}^{\text{NS-FEM-T4}}$ and $\mathbf{K}_{IJ,i}^{\text{FEM-T4}}$ computed as follows:

$$\bar{\mathbf{K}}_{IJ,k}^{\text{NS-FEM-T4}} = (1-\alpha^3) \bar{\mathbf{B}}_I^T \mathbf{D} \bar{\mathbf{B}}_J V_k^s \quad (8.8)$$

$$\mathbf{K}_{IJ,i}^{\text{FEM-T4}} = \int_{\Omega_{i,\alpha}^e} \mathbf{B}_I^T \mathbf{D} \mathbf{B}_J d\Omega = \mathbf{B}_I^T \mathbf{D} \mathbf{B}_J \alpha^3 V_i^e \quad (8.9)$$

in which $\Omega_{i,\alpha}^e$ is the remaining sub-domain in the middle of the T4 element; the smoothed strain-displacement matrix $\bar{\mathbf{B}}_I$ is computed using Eq. (5.5), V_k^s is computed using Eq. (5.6) and the compatible strain-displacement matrix \mathbf{B}_I is computed using Eq. (5.7).

8.2.3 Properties of the α FEM-T3 and α FEM-T4

We now discuss the properties of α FEM-T3 and α FEM-T4 models. We consider linear elasticity problems with homogeneous essential boundary conditions. We first note:

Property 8.1 (displacement compatibility): The assumed displacement field is compatible (piecewisely-linear and continuous through out the domain) in the α FEM-T3 and α FEM-T4 models.

This property can be explicitly seen from the α FEM-T3 and α FEM-T4 formulation procedure: linear interpolation for displacement is used in all the elements in the entire problem domain. The α FEM-T3 and α FEM-T4 do not change in any way the assumed displacement field. This property (together with the spatial stability) ensures that the α FEM-T3 and α FEM-T4 for any $\alpha \in [0, 1]$ will be able to reproduce exactly the linear field. This will be further confirmed numerically in the patch tests given in Section 8.4.

Property 8.2 (variational consistence): The α FEM-T3 (or α FEM-T4) is variationally consistent.

Proof

In the α FEM-T3, the compatible strain $\boldsymbol{\varepsilon}^h = \nabla_s \mathbf{u}^h$ is used for the Y -shaped sub-domains $\Omega_{i,\alpha}^e$ of all the N_e elements, but the smoothed strain (3.4) is used for all the N_n smoothing domains $\Omega_{k,\alpha}^s$, the variational consistency thus needs to be examined. To this end, we start with the modified Hellinger-Reissner variational principle [122] with the assumed strain vector $\bar{\boldsymbol{\varepsilon}}$ and the assumed displacements \mathbf{u}^h as two independent field variables:

$$U(\mathbf{u}^h, \bar{\boldsymbol{\varepsilon}}) = - \int_{\Omega} \frac{1}{2} \bar{\boldsymbol{\varepsilon}}^T \mathbf{D} \bar{\boldsymbol{\varepsilon}} d\Omega + \int_{\Omega} (\mathbf{D} \bar{\boldsymbol{\varepsilon}})^T \nabla_s \mathbf{u}^h d\Omega - \int_{\Omega} (\mathbf{u}^h)^T \mathbf{b} d\Omega - \int_{\Gamma_t} (\mathbf{u}^h)^T \mathbf{t} d\Gamma \quad (8.10)$$

Note that in the N_e Y -shaped sub-domains $\Omega_{i,\alpha}^e$, the assumed strain is the compatible strain: $\bar{\boldsymbol{\varepsilon}} = \boldsymbol{\varepsilon}^h$. Performing the variation using the chain rule, we obtain

$$\begin{aligned} \delta U(\mathbf{u}^h, \bar{\boldsymbol{\varepsilon}}) = & - \int_{\Omega} \delta \bar{\boldsymbol{\varepsilon}}^T \mathbf{D} \bar{\boldsymbol{\varepsilon}} d\Omega + \int_{\Omega} \delta \bar{\boldsymbol{\varepsilon}}^T \mathbf{D} \nabla_s \mathbf{u}^h d\Omega + \int_{\Omega} \bar{\boldsymbol{\varepsilon}}^T \mathbf{D} \nabla_s \delta \mathbf{u}^h d\Omega - \\ & - \int_{\Omega} (\delta \mathbf{u}^h)^T \mathbf{b} d\Omega - \int_{\Gamma_i} (\delta \mathbf{u}^h)^T \mathbf{t} d\Gamma = 0 \end{aligned} \quad (8.11)$$

Discretize now the domain Ω into N_e triangles Ω_i^e with N_n smoothing cells $\Omega_{k,\alpha}^s$ associated with N_n nodes and N_e Y-shaped sub-domains $\Omega_{i,\alpha}^e$ corresponding to the N_e elements. Substituting the approximations (2.43) for \mathbf{u}^h and (3.9) for $\bar{\boldsymbol{\varepsilon}}$ into (8.11) and using the arbitrary property of variation, we obtain

$$\hat{\mathbf{K}}^{\text{two-field}} \hat{\mathbf{d}} = \mathbf{f} \quad (8.12)$$

where $\hat{\mathbf{K}}^{\text{two-field}}$ is the two-field stiffness matrix with entries of

$$\begin{aligned} \hat{\mathbf{K}}_{IJ}^{\text{two-field}} = & - \int_{\Omega} (\bar{\mathbf{B}}_I)^T \mathbf{D} \bar{\mathbf{B}}_J d\Omega + 2 \int_{\Omega} (\bar{\mathbf{B}}_I)^T \mathbf{D} \mathbf{B}_J d\Omega \\ = & - \sum_{k=1}^{N_n} \int_{\Omega_{k,\alpha}^s} (\bar{\mathbf{B}}_I^\alpha)^T \mathbf{D} \bar{\mathbf{B}}_J^\alpha d\Omega + 2 \sum_{k=1}^{N_n} \int_{\Omega_{k,\alpha}^s} (\bar{\mathbf{B}}_I^\alpha)^T \mathbf{D} \mathbf{B}_J d\Omega - \\ & - \sum_{i=1}^{N_e} \int_{\Omega_{i,\alpha}^e} (\bar{\mathbf{B}}_I^\alpha)^T \mathbf{D} \bar{\mathbf{B}}_J^\alpha d\Omega + 2 \sum_{i=1}^{N_e} \int_{\Omega_{i,\alpha}^e} (\bar{\mathbf{B}}_I^\alpha)^T \mathbf{D} \mathbf{B}_J d\Omega \end{aligned} \quad (8.13)$$

and \mathbf{f} is the load vector which is computed exactly in the same way as that in the standard FEM. In all N_e of Y-shaped sub-domains $\Omega_{i,\alpha}^e$ of elements, we have $\bar{\boldsymbol{\varepsilon}} = \boldsymbol{\varepsilon}^h$ and $\bar{\mathbf{B}}_I^\alpha \equiv \mathbf{B}_I$, Eq. (8.13) hence becomes

$$\begin{aligned} \hat{\mathbf{K}}_{IJ}^{\text{two-field}} = & - \sum_{k=1}^{N_n} \int_{\Omega_{k,\alpha}^s} (\bar{\mathbf{B}}_I^\alpha)^T \mathbf{D} \bar{\mathbf{B}}_J^\alpha d\Omega + 2 \sum_{k=1}^{N_n} \int_{\Omega_{k,\alpha}^s} (\bar{\mathbf{B}}_I^\alpha)^T \mathbf{D} \mathbf{B}_J d\Omega + \\ & + \sum_{i=1}^{N_e} \int_{\Omega_{i,\alpha}^e} \mathbf{B}_I^T \mathbf{D} \mathbf{B}_J d\Omega \end{aligned} \quad (8.14)$$

Using the smoothed matrices $\bar{\mathbf{B}}_I$ in Eq. (5.3) for N_n smoothing cells $\Omega_{k,\alpha}^s$, we have

$$\begin{aligned} \int_{\Omega_{k,\alpha}^s} \bar{\mathbf{B}}_I^T \mathbf{D} \mathbf{B}_J(\mathbf{x}) d\Omega = & \bar{\mathbf{B}}_I^T \mathbf{D} \int_{\Omega_{k,\alpha}^s} \mathbf{B}_J(\mathbf{x}) d\Omega = \bar{\mathbf{B}}_I^T \mathbf{D} A_{k,\alpha}^s \int_{\Omega_{k,\alpha}^s} \frac{\mathbf{B}_J(\mathbf{x})}{A_{k,\alpha}^s} d\Omega \\ = & \bar{\mathbf{B}}_I^T \mathbf{D} \bar{\mathbf{B}}_J A_{k,\alpha}^s = \int_{\Omega_{k,\alpha}^s} \bar{\mathbf{B}}_I^T \mathbf{D} \bar{\mathbf{B}}_J d\Omega \end{aligned} \quad (8.15)$$

which means that the following orthogonal condition is satisfied [137]

$$\int_{\Omega_{k,\alpha}^e} \bar{\mathbf{B}}_I^T \mathbf{D} \mathbf{B}_J(\mathbf{x}) d\Omega = \int_{\Omega_{k,\alpha}^e} \bar{\mathbf{B}}_I^T \mathbf{D} \bar{\mathbf{B}}_J d\Omega \quad (8.16)$$

Therefore, Eq. (8.14) becomes

$$\hat{\mathbf{K}}_{IJ}^{\text{two-field}} = \sum_{k=1}^{N_n} \int_{\Omega_{k,\alpha}^e} (\bar{\mathbf{B}}_I^\alpha)^T \mathbf{D} \bar{\mathbf{B}}_J^\alpha d\Omega + \sum_{i=1}^{N_e} \int_{\Omega_{i,\alpha}^e} \mathbf{B}_I^T \mathbf{D} \mathbf{B}_J d\Omega \quad (8.17)$$

Because the α FEM-T3 uses directly Eq. (8.17) to compute the stiffness matrix, it is “variationally consistent”, meaning that the formulation of α FEM-T3 follows exactly the modified Hellinger-Reissner variational principle. This proof is directly applicable also the same for the α FEM-T4. \square

We note that although the two-field Hellinger-Reissner principle is used, the α FEM-T3 and α FEM-T4 has only the displacements as unknowns. Therefore, it is very much different from the so-called mixed FEM formulation, where stresses (or strains) are usually also unknowns in addition to the displacement unknowns.

Property 8.2 can be understood intuitively in a very simple argument: because both FEM-T4 and NS-FEM-T4 are variationally consistent, the linear (area-weighted) combination of them must also be variationally consistent.

Property 8.3 (lower bound): When $\alpha = 1.0$, α FEM-T3/ α FEM-T4 become the standard FEM. The strain energy $\hat{E}(\alpha = 1)$ is an underestimation of the exact strain energy.

Property 8.4 (upper bound property): When $\alpha = 0.0$, α FEM-T3/ α FEM-T4 becomes the NS-FEM. The strain energy $\hat{E}(\alpha = 0)$ is an overestimation of the exact strain energy for sufficiently fine models with sufficient smoothing effects.

Property 8.5 (solution continuity property): When α changes from 0.0 to 1.0, the solutions of the α FEM-T3 and α FEM-T4 are continuous functions of α from the solution of the NS-FEM and that of the standard FEM.

Property 8.6 (exact solution property): The exact solution in strain energy exactly falls in the range of the solutions of the α FEM-T3 the α FEM-T4 with $\alpha \in [0, 1]$, as long as the corresponding NS-FEM model has sufficient smoothing effects. This means that the exact solution in strain energy can be obtained using the α FEM-T3 and α FEM-T4 with an $\alpha_{\text{exact}} \in [0, 1]$.

This property is a natural outcome of the Property 8.3-8.5. Based on Property 8.6, one can now devise the following procedure to compute a nearly exact solution in strain energy, by finding an approximate $\alpha_{\text{exact}} \in [0, 1]$.

The intensive numerical study has shown that using meshes of elements with the same aspect ratio, the strain energy curves $\hat{E}(\alpha)$ corresponding to these meshes will intersect approximately at a common point $(\alpha_{\text{exact}}, E_{\text{exact}})$ which gives a nearly exact strain energy of the problem. It is known that the solution which is the “best” in strain energy usually lead to a “very good” solution in displacement norm, because of the relation between the strain energy and displacement solution : $\hat{E}(\alpha) = \frac{1}{2} \hat{\mathbf{d}}^T \hat{\mathbf{K}}^{\alpha\text{FEM}} \hat{\mathbf{d}}$.

In the following analysis, the meshes with the same aspect ratio are defined in two ways: one for regular meshes and one for irregular meshes. Regular meshes are used only for the regular domains, and the ratio of number of elements discretized along coordinate directions has to be the same when the mesh is refined. For example, for the rectangular 2D meshes, three meshes (16×4) , (32×8) and (64×16) have the same aspect ratio of 4. Irregular meshes can used for any domains, the meshes with the same aspect ratio are obtained by dividing, in a nested manner, each element of the initial coarse mesh into 2^2 , 3^2 , 4^2 , etc. equal elements for triangular elements, and into 2^3 , 3^3 , 4^3 , etc. equal elements for tetrahedral elements. Such a refinement from the initial coarse mesh to

obtain finer meshes with the same aspect ratio is available in many automatic programs creating 3-node triangular and 4-node tetrahedral elements, and hence it can be done without any technical difficulty. Note that, we do not require the elements in a mesh to have the same aspect ratio. We require only the elements in two consequent meshes to have the same aspect ratio.

Property 8.7: The stiffness matrix of α FEM-T3 (or α FEM-T4) has the same dimension as the corresponding standard FEM using the same mesh. The unknowns of an α FEM-T3 (or α FEM-T4) model are only the displacements, and the number of unknowns is the same as that of the standard FEM using the same mesh.

Property 8.8: For the nearly incompressible materials (Poisson's ratio ν approaches to 0.5), the volumetric locking can be avoid by using $\alpha = 0$ or a very small $\alpha = 0.5 - \nu$ for the α FEM-T3 (or α FEM-T4) method, where ν is the Poisson's ratio that is smaller but very close to 0.5. Note that, for this kind of problems, we have to give up on obtaining the "exact" solution, and only focus on solving the volumetric locking issue.

From the above formulation of α FEM-T3, it is clear that only the area and the usual compatible strain-displacement matrices \mathbf{B}_T of triangular elements (and the factor α) are needed to compute the system stiffness matrix. Therefore, in the actual programming, the standard FEM and NS-FEM-T3 formulae are used directly to compute the entries of the stiffness matrices with scaling by α^2 and $(1 - \alpha^2)$, respectively, as shown in Eqs. (8.3) and (8.6) for the α FEM-T3. Similarly to the α FEM-T4, the scaling should be α^3 and $(1 - \alpha^3)$, respectively, as shown in Eqs. (8.8) and (8.9).

8.3 Nearly exact solution for linear elastic problems

A numerical procedure for computing a nearly exact solution for a linear elastic problem using the α FEM-T3 (or α FEM-T4) can be summarized as follows:

1. Discretize the domain Ω into two sets of coarse mesh of triangular elements (or tetrahedral elements for 3D problems) with the same aspect ratio.
2. Choose one array of $\alpha \in \overline{0:1}$, for example $\alpha = [0.0 \ 0.2 \ \dots \ 0.8 \ 1.0]^T$.
3. Loop over two sets of mesh created in step 1.
 4. Loop over the array of $\alpha \in \overline{0:1}$.
 5. Loop over all the elements using the standard FEM:
 - Compute and save the strain-displacement matrix \mathbf{B} for the elements.
 - Evaluate the stiffness matrix and force vector for the elements.
 - Multiply the stiffness matrix of the element with α^2 for triangular elements by Eq. (8.3) (or with α^3 for tetrahedral elements by Eq. (8.9)) and then assemble into the global stiffness matrix.
 - Assemble force vector into the global force vector.
 6. End the loop over all the elements
7. Loop over all the nodes using the NS-FEM:
 - Use the strain-displacement matrices \mathbf{B} of the element saved in step 5 to compute the strain-displacement matrix $\bar{\mathbf{B}}_I$ of the node by Eq. (5.3) for the triangular elements or by Eq. (5.5) for the tetrahedral elements.
 - Evaluate the smoothed stiffness matrix of the node by Eq. (5.2).
 - Multiply the smoothed stiffness matrix of the node with $(1-\alpha^2)$ for triangular elements by Eq. (8.6) (or $(1-\alpha^3)$ for tetrahedral elements by Eq. (8.8)) and then assemble into the global stiffness matrix.

8. End the loop over all the nodes
9. Implement essential boundary conditions.
10. Solve the system equations for the nodal displacements.
11. Evaluate strain, stress and save the global strain energy.
12. End the loop over the array containing $\alpha \in \overline{0:1}$.
13. End the loop over two sets of coarse meshes.
14. Interpolate the exact strain energy at α_{exact} from two arrays containing the strain energies saved at step 11.
15. Use α_{exact} and a finer mesh with the same aspect ratio as the two coarse meshes to compute the final solution through steps from 5 to 11.

As shown, obtaining α_{exact} requires additional effort, and hence we may want to avoid. Based on the theory presented, we know that in any case, the accuracy (in the strain energy or displacement norm) of an combined model is always better than either FEM or NS-FEM for any $\alpha \in (0,1)$. This gives us a guarantee that we can only get a better solution using any $\alpha \in (0,1)$. Therefore, if we only need to improve the accuracy of solution, we may simply using directly an $\alpha \in \overline{0.45:0.65}$ in 2D problems and $\alpha \in \overline{0.60:0.80}$ in 3D problems for any meshes without searching for the α_{exact} . This range of α is found preferable by numerical “experiments” on different linear problems using the α FEM-T3 and α FEM-T4. By this way, the α chosen will not be optimal and the solution may not be very close to the exact one, but the accuracy of the solution is often much better than the FEM using the same mesh.

8.4 Standard patch tests

8.4.1 Standard patch test for 2D problems

An irregular domain discretization of a square patch using three-node triangular elements is shown in [Figure 6.4](#). The displacement norm (4.12) is used to examine the results computed. The parameters are taken as $E=100$, $\nu=0.3$ and the linear displacement field is given by (4.13).

It is found that the α FEM-T3 can pass the standard patch test within machine precision regardless of the value of $\alpha \in [0,1]$ used as shown in Table 8.1. This example confirms Property 1 for 2D problems: the α FEM-T3 is displacement compatible, linearly conforming, capable producing exactly any linear displacement field for any $\alpha \in [0,1]$, and hence will always converge to any exact solution that can be approximated via a piecewisely linear interpolation.

8.4.2 Irons first-order patch test for 3D problems

The Irons first-order patch test as presented in [Chapter 5, Section 5.6.3](#) is gain used here but for testing the α FEM-T4. The displacement norm (4.12) is used to quantitatively examine the computed results, and the energy error is defined by

$$e_e(\alpha) = \left| \hat{E}(\alpha) - E_{exact} \right| \quad (8.18)$$

where the total strain energy of α FEM-T4 solution $\hat{E}(\alpha)$ is computed using

$$\begin{aligned} \hat{E}(\alpha) &= E^{FEM}(\alpha) + \bar{E}^{NS-FEM}(\alpha) \\ &= \frac{1}{2} \sum_{i=1}^{N_e} (\boldsymbol{\varepsilon}_i^h)^T \mathbf{D} \boldsymbol{\varepsilon}_i \alpha^3 V_i^e + \frac{1}{2} \sum_{k=1}^{N_n} (\bar{\boldsymbol{\varepsilon}}_k)^T \mathbf{D} \bar{\boldsymbol{\varepsilon}}_k (1 - \alpha^3) V_k^s \end{aligned} \quad (8.19)$$

where N_e is the total number of elements used in the problem domain, N_n is the total number of node of the model, $\boldsymbol{\varepsilon}_i^h$ is the compatible strain of the FEM solution of the i^{th} element, $\bar{\boldsymbol{\varepsilon}}_k$ is the smoothed strain of NS-FEM solution for the k^{th} node.

It is found that the α FEM-T4 can pass the standard first-order patch test within machine precision regardless of the value of $\alpha \in [0,1]$, as shown in Table 8.2 and Table 8.3. There is no accuracy loss due to the different choices of α values. This example confirms Property 1 for 3D problems.

8.5 Numerical examples

In order to study numerically the convergence rate of the present method, the displacement norm given by Eq. (4.18) and the energy norm given by (4.19) are used. In the computation of Eq. (4.19) for the α FEM-T3 and α FEM-T4, a recovery strain field $\hat{\boldsymbol{\varepsilon}}^R$ by (5.16) and (5.17), respectively, will be used in the place of the general numerical strain field $\tilde{\boldsymbol{\varepsilon}}$. Note that the strains at nodes $\hat{\boldsymbol{\varepsilon}}(\mathbf{x}_j)$ for the α FEM-T3 and α FEM-T4 are computed in the same way as those of NS-FEM-T3 and NS-FEM-T4, respectively.

8.5.1 A cantilever beam under a tip load: a convergence study

The cantilever loaded at the end described in Example 4.10.1 is tested again but using the α FEM-T3, in comparison with a number of other methods. The geometry and boundary conditions of the cantilever is plotted in Figure 4.7. The mesh of quadrilateral and triangular elements are shown in Figure 4.8 and Figure 5.4, respectively. The exact strain energy of the problem is known as 4.4746 Nm.

Following the procedures given in Section 8.3, we found $\alpha_{\text{exact}} = 0.6$ at the intersection of two strain energy curves using two meshes with the same aspect ratio (32×8 and 40×10), as shown in Figure 8.4.

Table 5.6 and Figure 8.5 compare the solution error in displacement norm obtained using the α FEM-T3 (at $\alpha_{\text{exact}} = 0.6$), together with other methods. It is seen that the α FEM-T3 stand out clearly. When the mesh with $h = 1.2$ is used, the error of the α FEM-T3 is about 1/18 of the FEM-Q4 and 2/9 of the CSFEM-Q4. In terms of convergence rate, the rate of the α FEM-T3 stands out clearly, $r = 4.2$, that is much larger than the theoretical value of 2.0.

Table 5.7 and Figure 8.6 compare the solution error in energy norm obtained using the α FEM-T3 (at $\alpha_{\text{exact}} = 0.6$), together with other methods. It is seen that the results of the α FEM-T3 is slightly more accurate than those of the ES-FEM-T3. It is, however, a little less accurate than NS-FEM-T3 and CS-FEM-Q4. In terms of convergence rate, the rate of the α FEM-T3 also stands out clearly, $r = 1.56$, that is much larger than the theoretical value of 1.0.

8.5.2 Cook's membrane: test for membrane elements

The Cook's membrane problem [30] is also a widely used benchmark problem for numerical methods. It is a clamped tapered panel subjected to an in-plane shearing load resulting in deformation dominated by a bending response, as shown in Figure 8.7. The material parameters used are Young's modulus $E = 1$, Poisson's ratio $\nu = 1/3$. Two discretizations of Cook's membrane problem using 4-node quadrilateral and 3-node triangular elements are also shown in Figure 8.7. The exact solution of the problem is unknown. Under plane stress conditions, the reference value of the vertical displacement at center tip section is 23.9642 [48] and the reference value of the strain energy is known

as 12.015 [30].

Using the α FEM-T3, and following the procedures given in Section 8.3, we found $\alpha_{\text{exact}} = 0.5085$ at the intersection of strain energy curves using meshes with the same aspect ratio as plotted in Figure 8.8. Table 8.4 and Figure 8.9 compares the result of the displacement at the tip center using the α FEM-T3 with six published 4-node quadrilateral elements: FEM-Q4, Qm6-modified Wilson element [147], FB-one Gauss point with hourglass stabilization [46], QBI-Quintessential bending/incompressible element [15], KF-one Gauss point with hourglass control [64] and Qnew - an improved stabilization technique for one-point quadrature integration method [48]. It can be seen that the α FEM-T3 with $\alpha_{\text{exact}} = 0.5085$ outperforms clearly all these methods.

In addition to the results shown in Figure 8.9, we make a more detailed comparison of α FEM-T3 with other elements for coarse meshes, and the results in number are listed in Table 8.5. It is again found that α FEM-T3 at $\alpha_{\text{exact}} = 0.5085$ gives the excellent performance compared to all these methods compared.

8.5.3 Semi-infinite plane: a convergence study

The semi-infinite plate subjected to a uniform pressure within a finite range ($-a \leq x \leq a$) shown in Figure 8.10 is studied. The plane strain condition is considered. The analytical stresses are given by [148]

$$\begin{aligned}\sigma_{11} &= \frac{P}{2\pi} [2(\theta_1 - \theta_2) - \sin 2\theta_1 + \sin 2\theta_2] \\ \sigma_{22} &= \frac{P}{2\pi} [2(\theta_1 - \theta_2) + \sin 2\theta_1 - \sin 2\theta_2] \\ \tau_{12} &= \frac{P}{2\pi} [\cos 2\theta_1 - \cos 2\theta_2]\end{aligned}\tag{8.20}$$

The directions of θ_1 and θ_2 are indicated in Figure 8.10. The corresponding displacements can be expressed as

$$\begin{aligned}
u_1 &= \frac{p(1-\nu^2)}{\pi E} \left[\frac{1-2\nu}{1-\nu} \left[(x+a)\theta_1 - (x-a)\theta_2 \right] + 2y \ln \frac{r_1}{r_2} \right] \\
u_2 &= \frac{p(1-\nu^2)}{\pi E} \left[\frac{1-2\nu}{1-\nu} \left[y(\theta_1 - \theta_2) + 2H \arctan \frac{1}{c} \right] + 2(x-a) \ln r_2 - \right. \\
&\quad \left. - 2(x+a) \ln r_1 + 4a \ln a + 2a \ln(1+c^2) \right]
\end{aligned} \tag{8.21}$$

where $H = ca$ is the distance from the origin to point O' , the vertical displacement is assumed to be zero and c is a coefficient.

Due to the symmetry about the y -axis, the problem is modeled with a $5a \times 5a$ square with $a = 0.2\text{m}$, $c = 100$ and $p = 1 \times 10^4 \text{N/m}^2$. The left and bottom sides are constrained using the exact displacements given by Eq. (8.21) while the right side is subjected to tractions computed from Eq. (8.20). Figure 8.11 gives the discretization of the domain using 4-node quadrilateral and triangular elements, respectively. The exact strain energy of the problem is known as 45.585 Nm.

Following the procedures given in Section 8.3, we found $\alpha_{\text{exact}} = 0.48$ at the intersection of strain energy curves using meshes with the same aspect ratio as shown in Figure 8.12. Table 8.6 and Figure 8.13 show the convergence of strain energy of α FEM-T3 (at $\alpha_{\text{exact}} = 0.48$) in comparison with different methods. It is seen that the results of α FEM-T3 are almost identical with the analytical solution, even with the coarse meshes. From Figure 8.14 and Figure 8.15, it is observed that all the computed displacements and stresses using α FEM-T3 (at $\alpha_{\text{exact}} = 0.48$) agree well with the analytical solutions.

Table 8.7 and Figure 8.16 compare the solution error in displacement norm obtained using the α FEM-T3 (at $\alpha_{\text{exact}} = 0.48$), together with other methods. In terms of accuracy, the α FEM-T3 and ES-FEM-T3 stand out clearly. When the finest mesh ($h = 0.0373$) is used, the error of the α FEM-T3 is about 2/7 of the FEM-T3 and 2/3 of the FEM-Q4. In terms of convergence rate, the rate of the α FEM-T3 is only larger than that of FEM-T3.

Table 8.8 and Figure 8.17 compare the solution error in energy norm obtained using the α FEM-T3 (at $\alpha_{\text{exact}} = 0.48$), together with other methods. In terms of accuracy, the results of the α FEM-T3 and NS-FEM-T3 stand out clearly. When the finest mesh ($h = 0.0373$) is used, the error of the α FEM-T3 is about $2/7$ of the FEM-T3 and $1/2$ of the FEM-Q4. In terms of convergence rate, the super-convergence is observed for the α FEM-T3 with a rate of 1.21 that is much larger than the theoretical value of 1.0.

Next, we test the α FEM-T3 for volumetric locking by varying the Poisson's ratio from 0.4 to 0.4999999. As presented in Property 8.8, it is recommended to use $\alpha = 0$ or a very small $\alpha = 0.5 - \nu$. Table 8.9 and Figure 8.18 show the displacement norm versus different Poisson's ratios for the α FEM-T3, FEM-T3 and FEM-Q4 (the mesh with 353 nodes and $h = 0.0559$ is used). The results show that the α FEM-T3 can avoid the volumetric locking, while the FEM-T3 and FEM-Q4 are clearly suffered from the volumetric locking. The results of α FEM-T3 using $\alpha = 0.5 - \nu$ are a little better than those simply using $\alpha = 0$, and hence are recommended by this paper. Note also that using $\alpha = 0.5 - \nu$ can also help to stabilize the solution for dynamic problems.

8.5.4 3D Lamé problem: a convergence study

The 3D Lamé problem described in Example 5.7.3 is used again in this examination, but for test α FEM-T4. As the problem is spherically symmetrical, and hence only one-eighth of the sphere model is shown in Figure 5.17 and symmetry conditions are imposed on the three symmetric planes. Following the procedures given in Section 8.3, we first compute the strain energy curves using different mesh of elements of the same aspect ratio, and the results are plotted in Figure 8.19. It is found that the strain energy curves versus $\alpha \in [0, 1]$ using three meshes intersect each other at $\alpha_{\text{exact}} = 0.7$. Figure 8.20 and

Figure 8.21 show that the distribution of the displacement and stresses using α FEM-T4 (at $\alpha_{\text{exact}} = 0.7$) agree very well with the analytical solution.

Table 5.12 and Figure 8.22 show the convergence of strain energy of α FEM-T4 (at $\alpha_{\text{exact}} = 0.7$) in comparison with different methods. It is again seen that the strain energies of α FEM-T4 are almost identical with the analytical solution ($E_{\text{exact}} = 6.305 \times 10^{-2}$ Nm), even with the coarse meshes.

Table 5.13 and Figure 8.23 compare the solution error in displacement norm obtained using the α FEM-T4 (at $\alpha_{\text{exact}} = 0.7$), together with other methods. It is seen that the α FEM-T4 stands out clearly. When the 3rd fine mesh for both T4 and H8 ($h \approx 0.156$) is used, the error of the α FEM-T4 is about 3/10 of the FEM-T4, and even 9/10 of the FEM-H8. In terms of convergence rate, the α FEM-T4 stands out clearly with a rate of $r = 2.22$ which is much larger than the theoretical value of 2.0 and much higher even than the FEM-H8 ($r = 2.05$).

Table 5.14 and Figure 8.24 compare the solution error in energy norm obtained using the α FEM-T4 (at $\alpha_{\text{exact}} = 0.7$), together with those of other methods. It is found that the results of α FEM-T4 is only less accurate than those of NS-FEM-T4 but more accurate than those of FEM-H8 and FEM-T4. When the 3rd fine mesh for both T4 and H8 ($h \approx 0.156$) is used, the error of α FEM-T4 is about 2/5 of FEM-T4 and 1/2 of FEM-H8. In terms of convergence rate, the rate of the α FEM-T4 stands out clearly, $r = 1.38$, that is much larger than the theoretical value of 1.0 and the rate of the FEM-H8 ($r = 0.95$).

8.5.5 3D cubic cantilever: accuracy study

The 3D cantilever of cubic shape subjected to a uniform pressure on its upper face described in Example 5.7.4 is again considered. The exact solution of the problem is

unknown. By incorporating the solutions of hexahedral super-element elements and the procedure of Richardson's extrapolation, Almeida Pereira [5] has given an approximately "exact" solution in strain energy to be 0.950930. In addition, using the standard FEM and a very fine mesh with 30,204 nodes and 20,675 ten-node tetrahedron elements, another reference solution of the strain energy is found to be $E = 0.9486$. This fine FEM model gives also a reference solution of 3.3912 for the deflection at point A (1.0,1.0,-0.5).

From Figure 8.25, it is found that the strain energy curves using three meshes with the same aspect ratio versus $\alpha \in [0, 1]$ intersect at $\alpha_{\text{exact}} = 0.62$. Table 5.15 and Figure 8.26 show the convergence of strain energy of α FEM-T4 ($\alpha_{\text{exact}} = 0.62$) in comparison with four different methods. It is again seen that the strain energies obtained using the α FEM-T4 are very close to the reference solution ($E_{\text{ref}} = 0.950930$), even when the coarse meshes are used.

Table 5.16 and Figure 8.27 show the convergence of the tip deflection at point A(1,1,-0.5) obtained using the α FEM-T4 (at $\alpha_{\text{exact}} = 0.62$), together with other different methods for comparison. It is again seen that the deflection solutions of α FEM-T4 are very close to the reference solution (3.3912), even using the coarse meshes.

8.5.6 A 3D L-shaped block: accuracy study

The 3D square block with a cubic hole subjected to a surface traction q described in Example 5.7.5 is again considered. Due to the double symmetry of the problem, only a quarter of the domain is modeled, which becomes a 3D L-shaped block as shown in Figure 5.26. The analysis is performed using dimensionless input data: $q = 1$, $a = 1$, $E = 1$, and $\nu = 0.3$. For this problem, the strain energy of 6.1999 given by Cugnon [34] is considered as the reference solution. In addition, using standard FEM and a very fine

mesh with 33,641 nodes and 22,862 ten-node tetrahedron elements, another reference solution of the strain energy has been found to be 6.1916.

From Figure 8.28, it is found that the strain energy curves using three meshes with the same aspect ratio versus $\alpha \in [0, 1]$ intersect at $\alpha_{\text{exact}} = 0.7$. Table 5.17 and Figure 8.29 show the convergence of strain energy of α FEM-T4 ($\alpha_{\text{exact}} = 0.7$) in comparison with three different methods. It is again seen that the strain energies obtained using the α FEM-T4 are very close to the reference solution, even when the coarse meshes are used.

8.6 Remarks

In this chapter, an alpha FEM with a scale factor α using triangular (α FEM-T3) and tetrahedral (α FEM-T4) elements is introduced. Through the theoretical study and numerical examples, the following major conclusions can be drawn:

- The α FEM-T3 and α FEM-T4 ensure the stability, variational consistence and the compatibility of the displacement field, and hence reproduce linear field exactly for any $\alpha \in [0, 1]$.
- The α FEM-T3 and α FEM-T4 are equipped with a scaling factor α that controls the contributions from the NS-FEM and FEM models. When the factor α varies from 0 to 1, a continuous solution function in the strain energy from the upper bound of the NS-FEM model to the lower bound of the FEM can be obtained.
- From the observed behavior of the numerical results, a unique approach has been proposed for the α FEM-T3 and α FEM-T4 to obtain the nearly exact solution in strain energy for linear elasticity problems. This approach uses two coarse meshes with the same aspect ratio to search for an approximate α_{exact} .

- The implementation of the α FEM-T3 (or α FEM-T4) in practical applications is relatively easy and quite similar to the standard FEM because of the following reasons; (1) automatic refinement from an initial coarse mesh to obtain the meshes with the same aspect ratio is available in many existing programs using creating 3-node triangular and 4-node tetrahedral elements; (2) the proposed methods only use the strain-displacement matrices \mathbf{B} of the standard FEM and area (or volume) of elements to compute the system stiffness matrix; (3) No new numerical integration is performed.
- For plane strain problems with nearly incompressible materials, we recommend the use of $\alpha = 0$ or a very small $\alpha = 0.5 - \nu$ to solve the volumetric locking problem.
- The obtained result from this study is very promising and the α FEM-T3 (or α FEM-T4) can be easily incorporated into the existing commercial software packages with a little modification.
- The α FEM-T3 (or α FEM-T4) is suitable also for adaptive analysis as it uses only triangular and tetrahedral elements that can be automatically generated for complicated domains.
- Searching for a good approximation of α_{exact} is still an open topic. If a more efficient scheme can be devised, the α FEM-T3 and α FEM-T4 can find much wider applications.

$\alpha = 0.0$ (NS-FEM-T3)	$\alpha = 0.2$	$\alpha = 0.4105^{(*)}$	$\alpha = 0.6038^{(*)}$	$\alpha = 0.8$	$\alpha = 1.0$ (FEM-T3)
0.2757 e-12	1.6029 e-12	1.4327 e-12	2.1737 e-12	0.7946 e-12	1.6499 e-12

(*) Arbitrarily generated number

	$\alpha = 0.0$ NS-FEM-T4	$\alpha = 0.2$	$\alpha = 0.4083^{(*)}$	$\alpha = 0.6149^{(*)}$	$\alpha = 0.8$	$\alpha = 1.0$ FEM-T4
e_d (%)	0.08 e-12	0.23 e-12	0.82 e-12	1.46 e-12	13.06 e-12	0.06 e-12

(*) Arbitrarily generated number

	$\alpha = 0.0$ NS-FEM-T4	$\alpha = 0.2$	$\alpha = 0.4083^{(*)}$	$\alpha = 0.6149^{(*)}$	$\alpha = 0.8$	$\alpha = 1.0$ FEM-T4
e_e	2.55 e-11	2.55 e-11	2.55 e-11	2.55 e-11	2.55 e-11	2.55 e-11

(*) Arbitrarily generated number

Mesh	4×4	8×8	16×16	32×32
FEM-Q4	18.3086	22.0710	23.4370	23.8204
Qm6 [147]	23.0056	23.7006	23.8923	23.9402
FB [46]	22.0950	23.4370	23.8204	23.9163
QBI [15]	20.4654	22.9098	23.6766	23.8923
KF [64]	19.8903	22.6941	23.6047	23.8683
Qnew [48]	23.0775	23.7006	23.8923	23.9402
α FEM-T3 ($\alpha_{\text{exact}} = 0.5085$)	23.7006	24.0322	24.0053	23.9777
Reference value	23.9642	23.9642	23.9642	23.9642

	Tip displacement			Strain energy		
	2×2	4×4	8×8	2×2	4×4	8×8
AT	19.67 (27) ^(*)	22.41 (75)	23.45 (243)	9.84	11.22	11.75
P-S	21.13 (18)	23.02 (50)	23.69 (162)	10.50	11.51	11.85
CH(0 – 1)	23.01 (18)	23.48 (50)	23.81 (162)	11.47	11.75	11.91
ECQ4/LQ6	23.05 (18)	23.48 (50)	23.81 (162)	11.48	11.75	11.91
HMQ/HQ4	21.35 (18)	23.04 (50)	23.69 (162)	10.61	11.52	11.85
FEMIXHB	22.81 (35)	23.52 (135)	23.92 (527)	11.27	11.79	11.97
AGQ6-I	23.07	23.68	23.87	--	--	--
AGQ6-II	25.92	24.37	24.04	--	--	--
QACM4	20.74	22.99	23.69	--	--	--
QACII6	25.92	24.37	24.04	--	--	--
α FEM-T3 ($\alpha_{\text{exact}} = 0.5085$)	--	23.56 (50)	23.99 (162)	--	11.77	12.00
Reference value	23.9642	23.9642	23.9642	12.015	12.015	12.015

(*) : Number of degrees of freedom denoted in parenthesis

	Mesh 1	Mesh 2	Mesh 3	Mesh 4	Mesh 5	Analytical solution
DOFs	194	410	706	1082	1538	
FEM-T3	43.0502	44.3177	44.8352	45.0938	45.2411	45.5850
FEM-Q4	44.6815	45.1768	45.3586	45.4452	45.4932	45.5850
CS-FEM-Q4	44.8423	45.2543	45.4043	45.4753	45.5146	45.5850
NS-FEM-T3	46.8508	46.2003	45.9577	45.8401	45.7739	45.5850
ES-FEM-T3	45.1151	45.4122	45.5056	45.5458	45.5665	45.5850
α FEM-T3 ($\alpha_{\text{exact}} = 0.48$)	45.5744	45.6290	45.6322	45.6291	45.6258	45.5850

Table 8.7. Error in displacement norm obtained using different methods for the semi-infinite plane subjected to a uniform pressure using the same distribution of nodes.

	Mesh 1	Mesh 2	Mesh 3	Mesh 4	Mesh 5
h (m)	0.1118	0.0745	0.0559	0.0447	0.0373
FEM-T3	7.94 e-04	4.07 e-04	2.46 e-04	1.64 e-04	1.17 e-04
FEM-Q4	3.77 e-04	1.76 e-04	1.01 e-04	6.56 e-05	4.60 e-05
CS-FEM-Q4	3.53 e-04	1.63 e-04	9.36 e-05	6.06 e-05	4.24 e-05
NS-FEM-T3	4.92 e-04	2.19 e-04	1.24 e-04	7.95 e-05	5.54 e-05
ES-FEM-T3	2.84 e-04	1.25 e-04	6.95 e-05	4.40 e-05	3.03 e-05
α FEM-T3 ($\alpha_{\text{exact}} = 0.48$)	2.53 e-04	1.20 e-04	7.00 e-05	4.57 e-05	3.21 e-05

Table 8.8. Error in energy norm obtained using different methods for the semi-infinite plane subjected to a uniform pressure using the same distribution of nodes.

	Mesh 1	Mesh 2	Mesh 3	Mesh 4	Mesh 5
h (m)	0.1118	0.0745	0.0559	0.0447	0.0373
FEM-T3	1.3498	0.9540	0.7372	0.6012	0.5081
FEM-Q4	0.8772	0.5946	0.4515	0.3648	0.3066
CS-FEM-Q4	0.6138	0.3631	0.2529	0.1924	0.1547
NS-FEM-T3	0.4284	0.2627	0.1883	0.1466	0.1200
ES-FEM-T3	0.5976	0.3585	0.2527	0.1941	0.1572
α FEM-T3 ($\alpha_{\text{exact}} = 0.48$)	0.5052	0.3035	0.2143	0.1649	0.1338

Table 8.9. Displacement norm versus different Poisson's ratios of the semi-infinite plane subjected to a uniform pressure ($\times 10^{-4}$).

Mesh	Poisson's ratios	α FEM-T3	α FEM-T3	FEM-T3	FEM-Q4
		$\alpha = 0$	$\alpha = 0.5 - \nu$		
12 \times 12	$\nu = 0.4$	1.24		3.34	1.12
12 \times 12	$\nu = 0.49$	1.25	1.21	14.28	4.43
12 \times 12	$\nu = 0.499$	1.29	1.28	33.09	19.62
12 \times 12	$\nu = 0.4999$	1.30	1.29	42.44	41.86
12 \times 12	$\nu = 0.49999$	1.30	1.30	45.78	54.65
12 \times 12	$\nu = 0.499999$	1.30	1.30	47.18	62.10
12 \times 12	$\nu = 0.4999999$	1.30	1.30	47.42	64.10

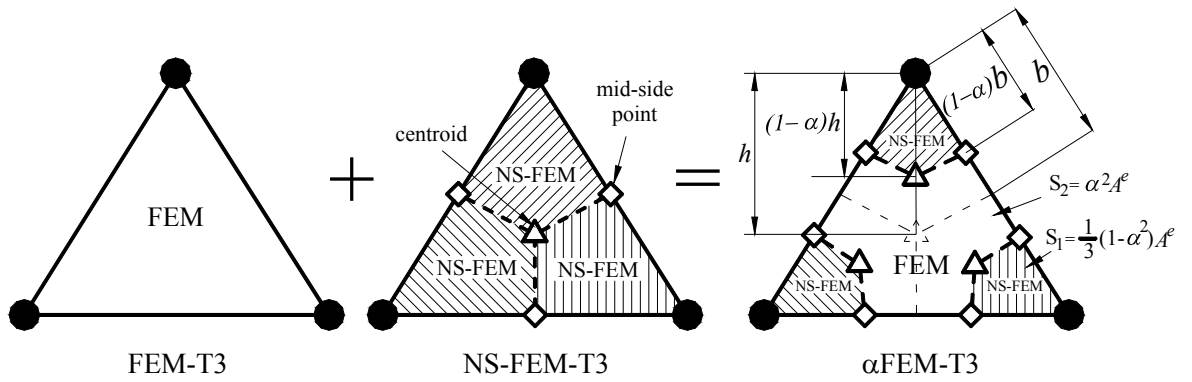


Figure 8.1. An α FEM-T3 element: combination of the triangular elements of FEM-T3 and NS-FEM-T3. The NS-FEM-T3 is used for three quadrilaterals sub-domain, and the FEM-T3 is used for the Y-shaped sub-domain in the center.

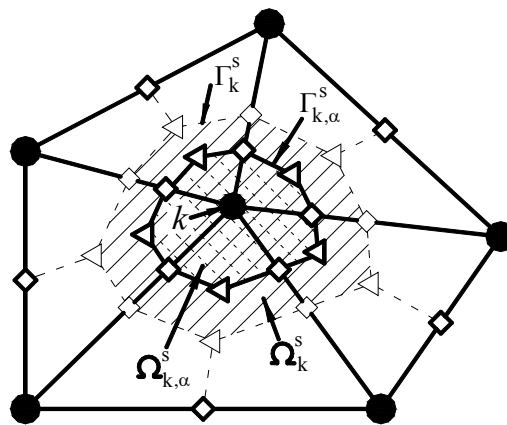


Figure 8.2. Smoothing domain associated with nodes for triangular elements in the α FEM-T3.

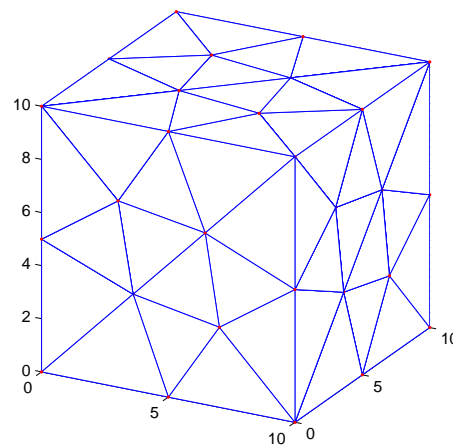


Figure 8.3. Domain discretization of a cubic patch using four-node tetrahedral elements.

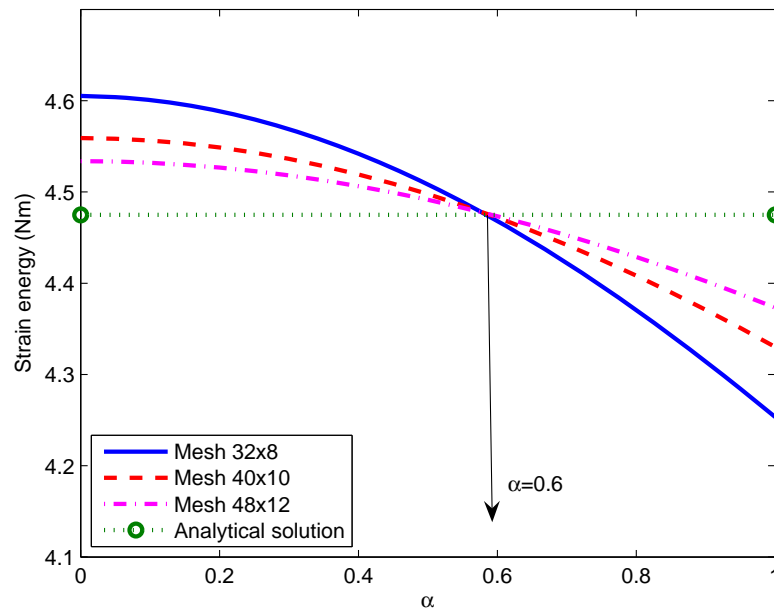


Figure 8.4. The strain energy curves of three meshes with the same aspect ratios intersect at $\alpha_{\text{exact}} = 0.6$ for the cantilever loaded at the end.

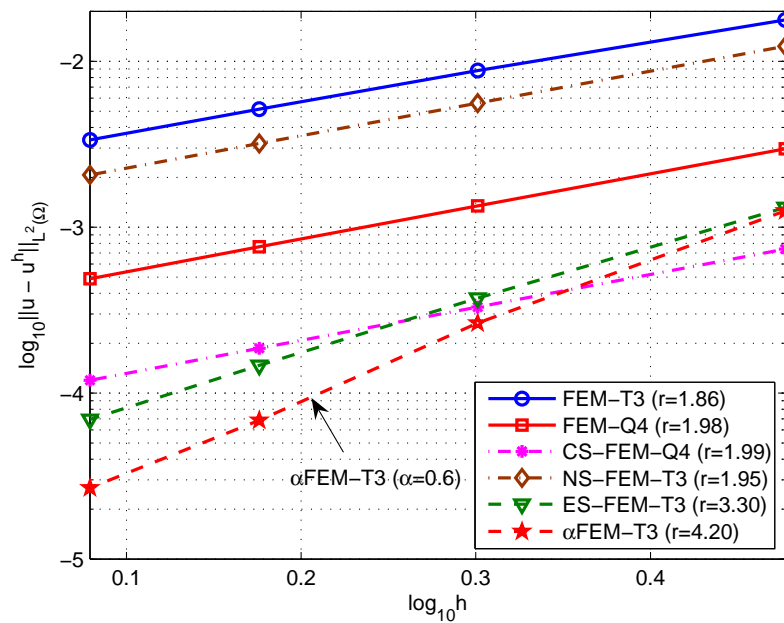


Figure 8.5. Error in displacement norm of α FEM-T3 ($\alpha_{\text{exact}} = 0.6$) in comparison with other methods for the cantilever loaded at the end using the same distribution of nodes.

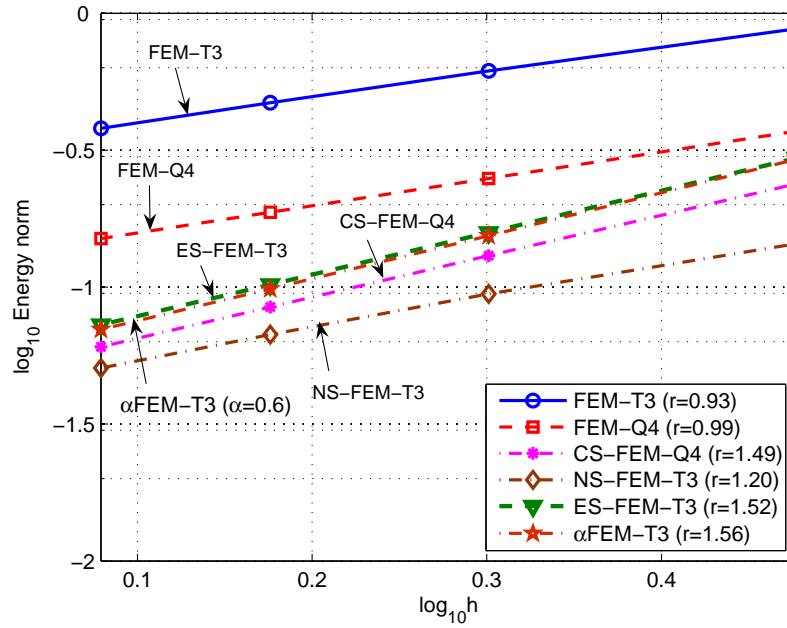


Figure 8.6. Error in energy norm of α FEM-T3 ($\alpha_{\text{exact}} = 0.6$) in comparison with other methods for the cantilever loaded at the end using the same distribution of nodes.

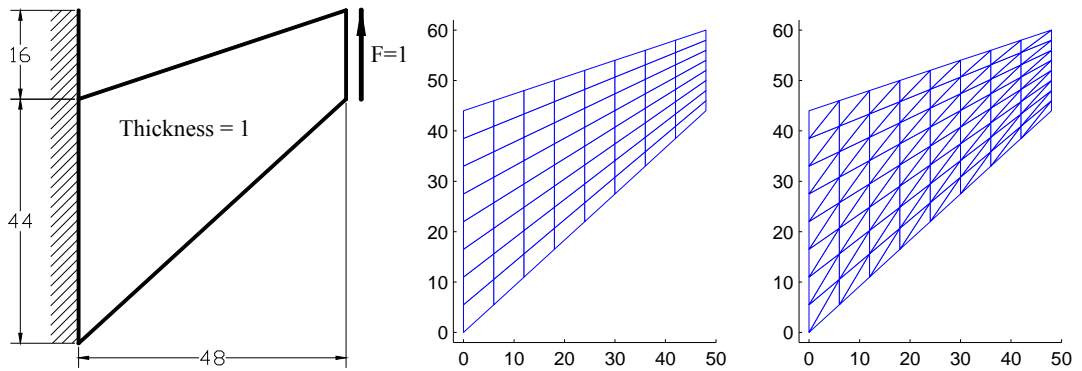


Figure 8.7. Cook's membrane problem and its discretizations using 4-node quadrilateral and 3-node triangular elements.

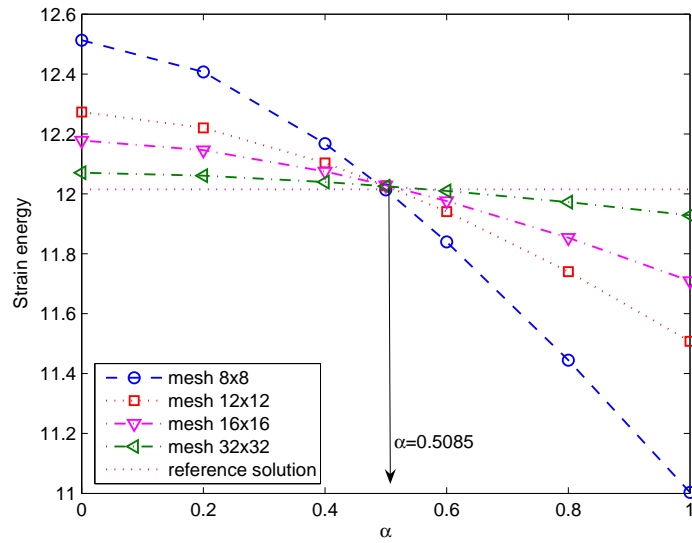


Figure 8.8. The strain energy curves of four meshes with the same aspect ratios intersect at $\alpha_{\text{exact}} = 0.5085$ for Cook's membrane problem.

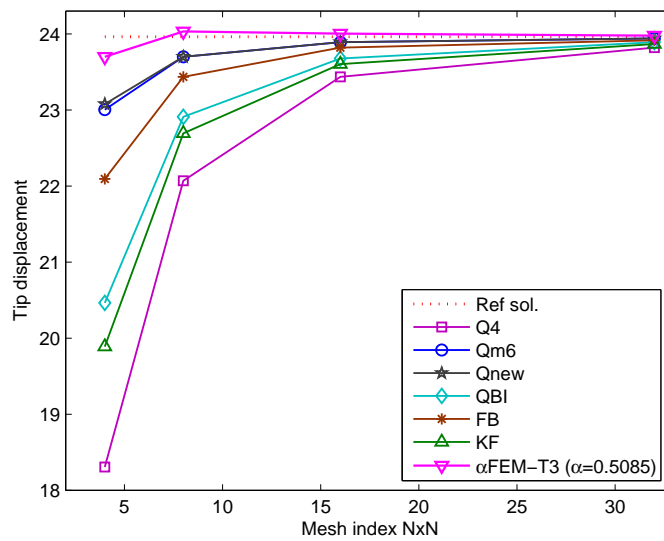


Figure 8.9. Convergence of tip displacement of α FEM-T3 ($\alpha_{\text{exact}} = 0.5085$) in comparison with other methods for Cook's membrane using the same distribution of nodes.

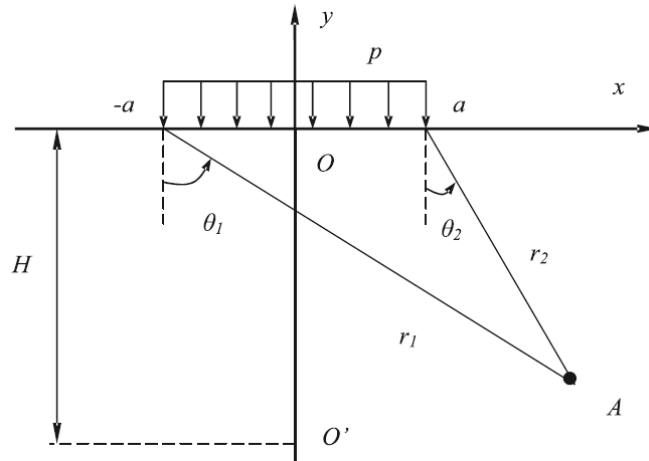


Figure 8.10. Semi-infinite plane subjected to a uniform pressure.

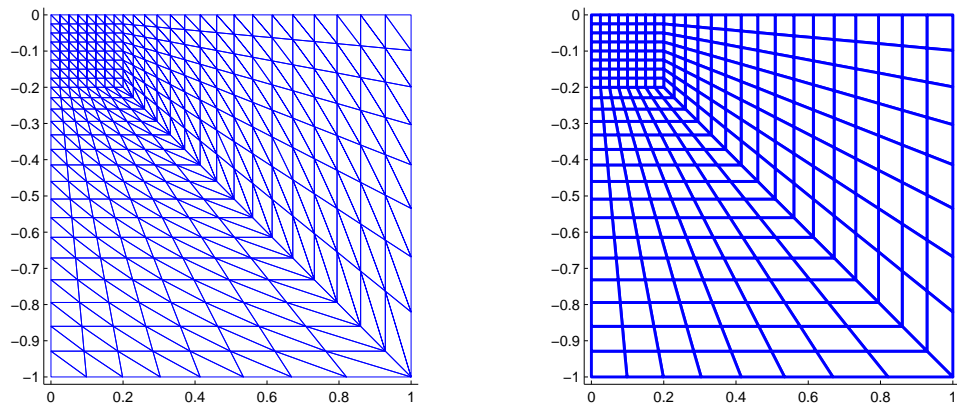


Figure 8.11. Domain discretization of the semi-infinite plane using 3-node triangular and 4-node quadrilateral elements.

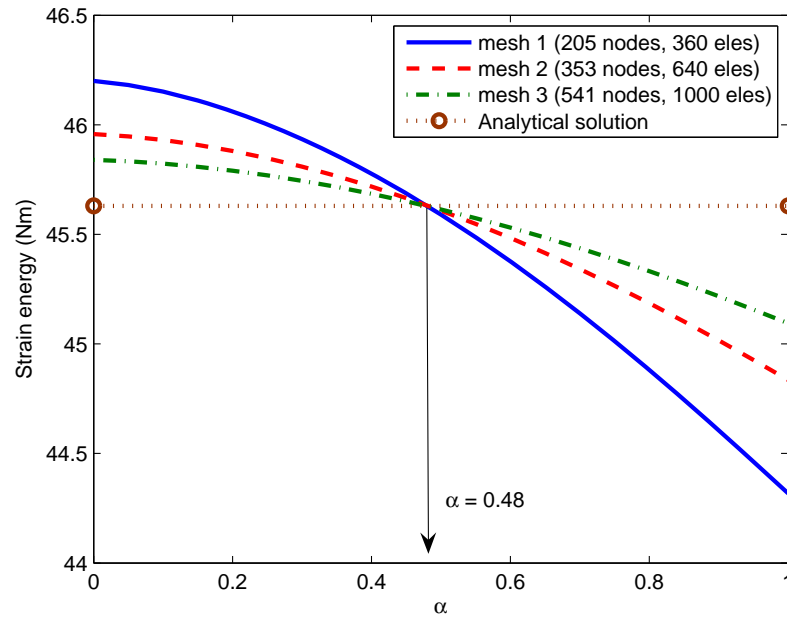


Figure 8.12. The strain energy curves of three meshes with the same aspect ratios intersect at $\alpha_{\text{exact}} = 0.48$ for the semi-infinite plane subjected to a uniform pressure.

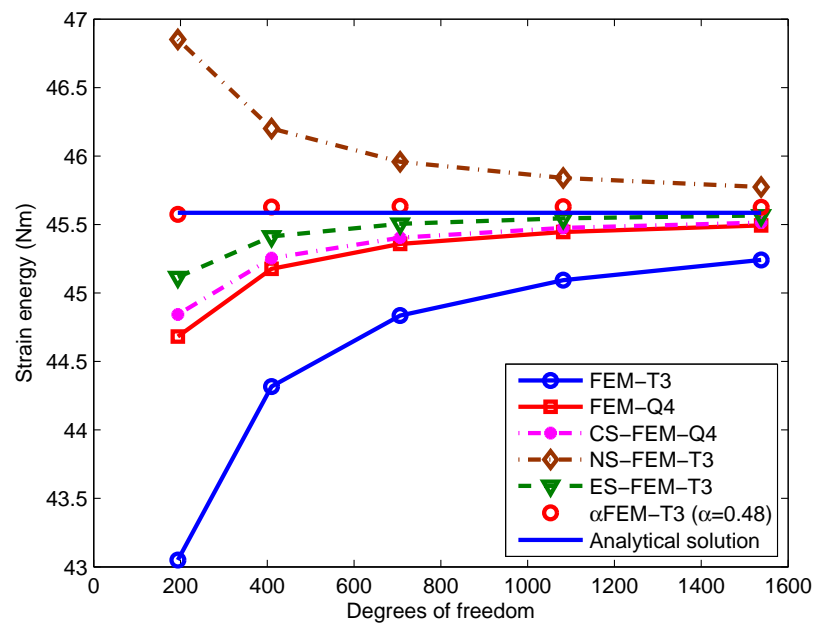


Figure 8.13. Convergence of strain energy of α FEM-T3 ($\alpha_{\text{exact}} = 0.48$) in comparison with other methods for the semi-infinite plane subjected to a uniform pressure.

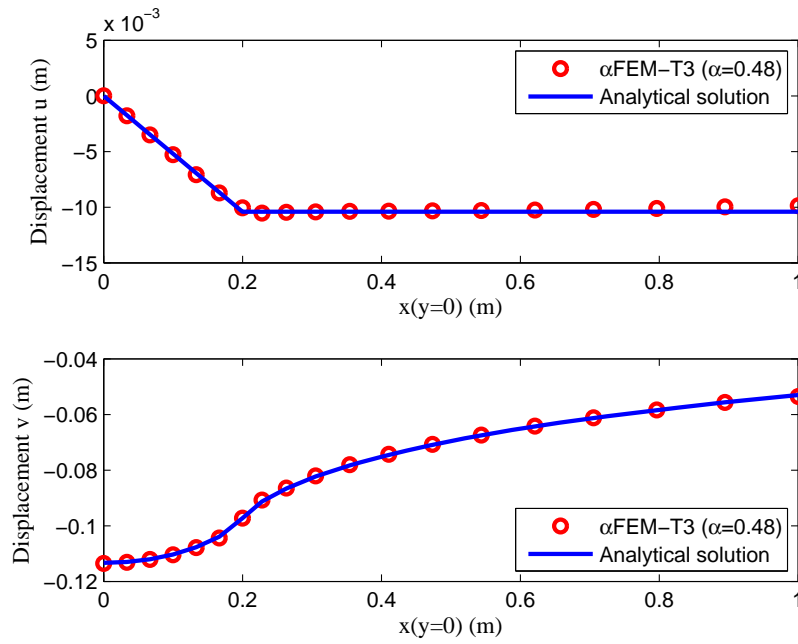


Figure 8.14. Computed and exact displacements of the semi-infinite plane subjected to a uniform pressure using the α FEM-T3 ($\alpha_{\text{exact}} = 0.48$).

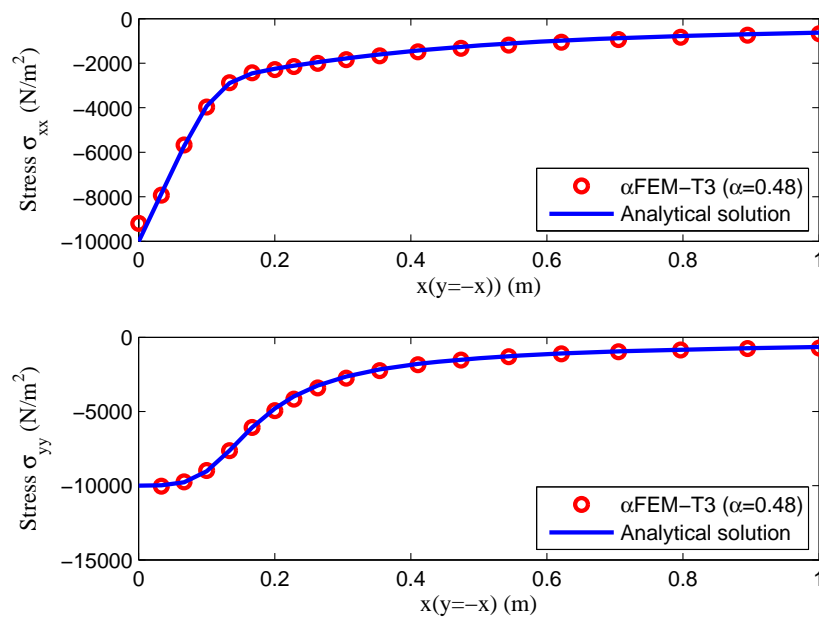


Figure 8.15. Computed and exact stresses of the semi-infinite plane subjected to a uniform pressure using the α FEM-T3 ($\alpha_{\text{exact}} = 0.48$).

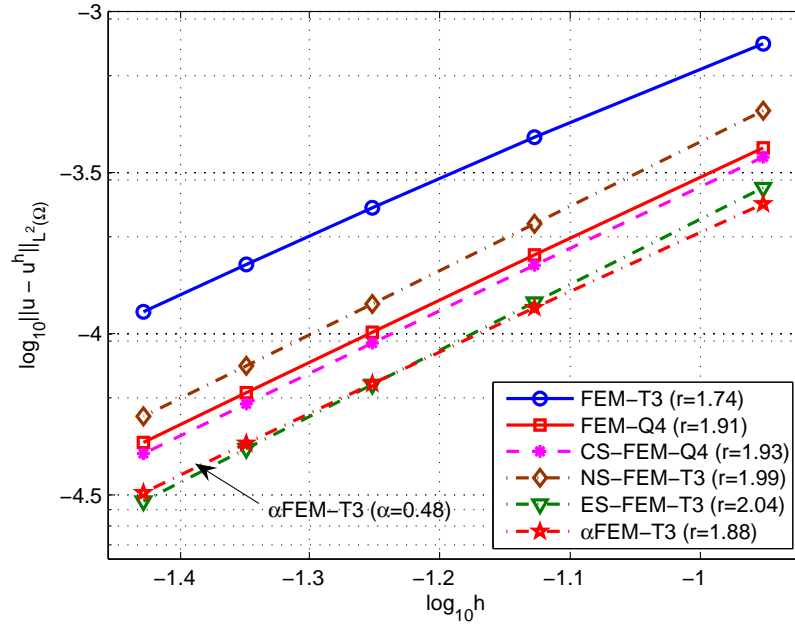


Figure 8.16. Error in displacement norm of α FEM-T3 ($\alpha_{\text{exact}} = 0.48$) in comparison with other methods for the semi-infinite plane subjected to a uniform pressure using the same distribution of nodes.

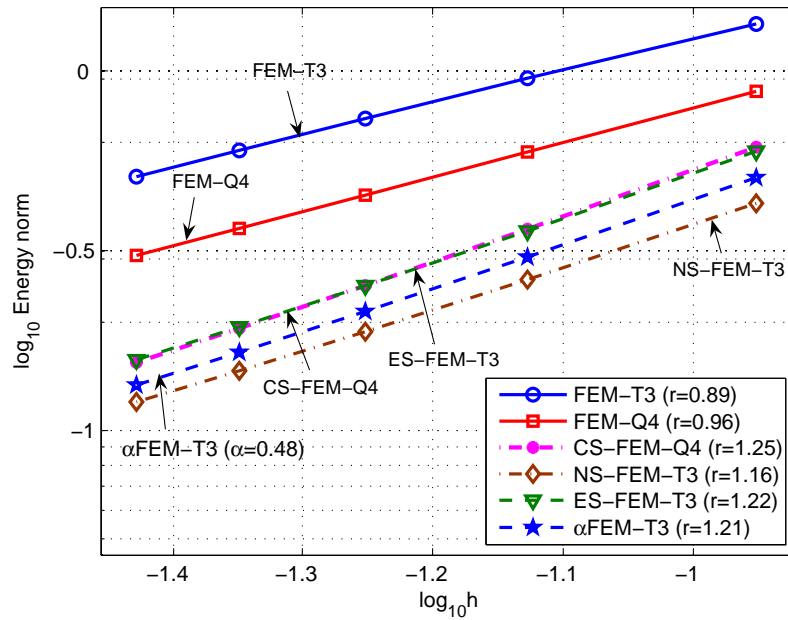


Figure 8.17. Error in energy norm of α FEM-T3 ($\alpha_{\text{exact}} = 0.48$) in comparison with other methods for the semi-infinite plane subjected to a uniform pressure using the same distribution of nodes.

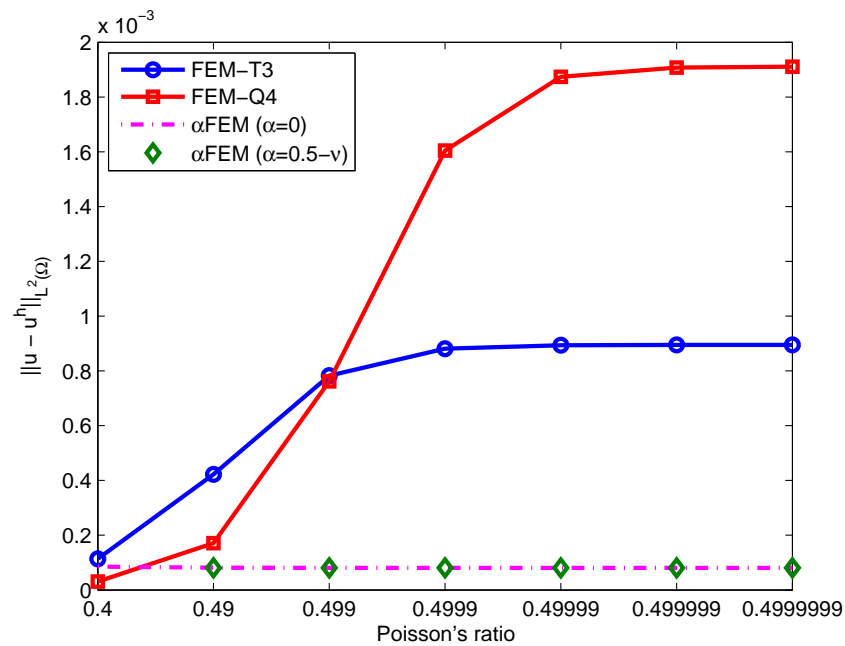


Figure 8.18. Displacement norm versus different Poisson's ratios of the material for the semi-infinite plane subjected to a uniform pressure (the mesh with 353 nodes and $h = 0.0559$ is used) .

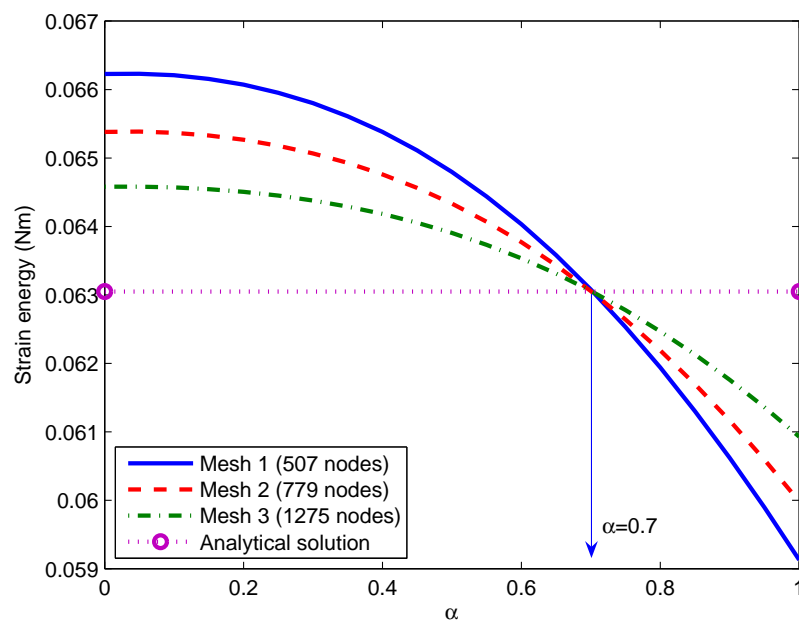


Figure 8.19. Using the strain energy curves of meshes with the same aspect ratios to find $\alpha_{\text{exact}} = 0.7$ for the hollow sphere subjected to inner pressure.

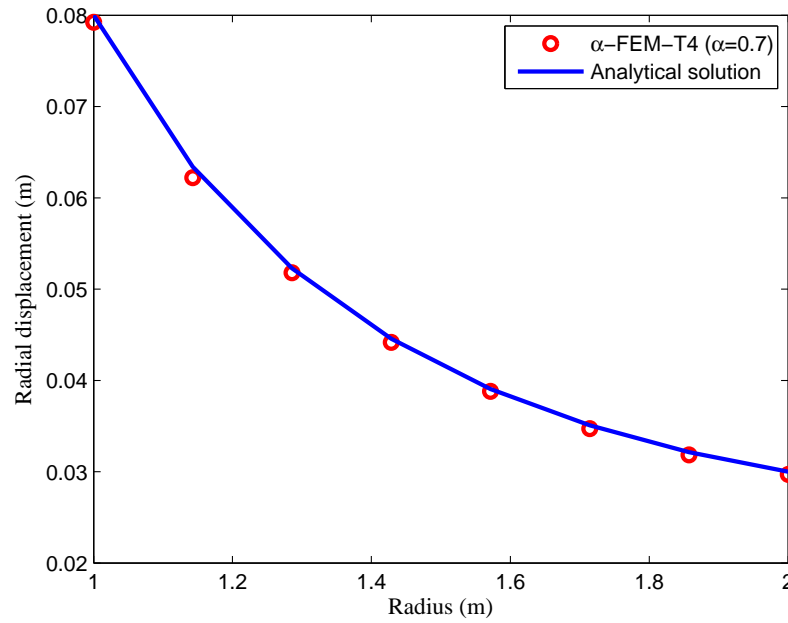


Figure 8.20. Distribution of the radial displacement of the hollow sphere subjected to inner pressure using α FEM-T4 ($\alpha_{\text{exact}} = 0.7$).

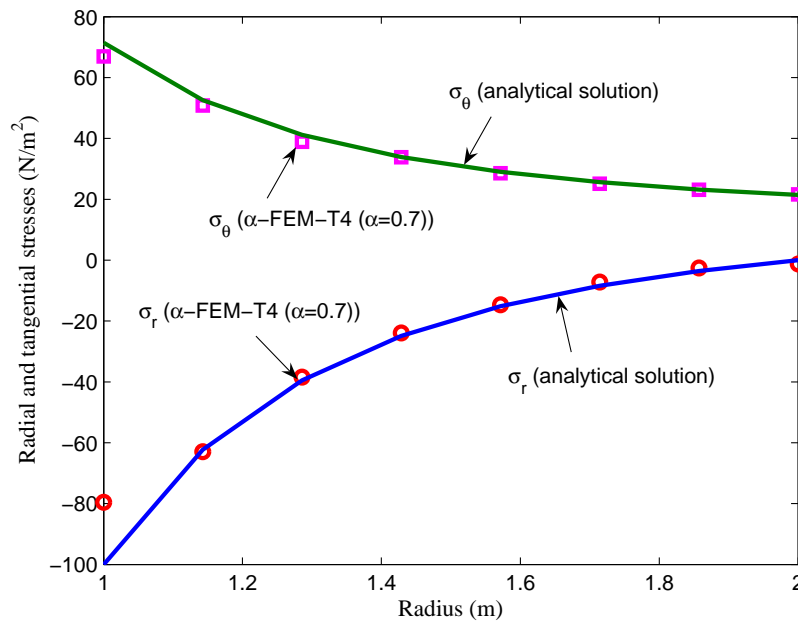


Figure 8.21. Distribution of the radial and tangential stresses of the hollow sphere subjected to inner pressure using α FEM-T4 ($\alpha_{\text{exact}} = 0.7$).

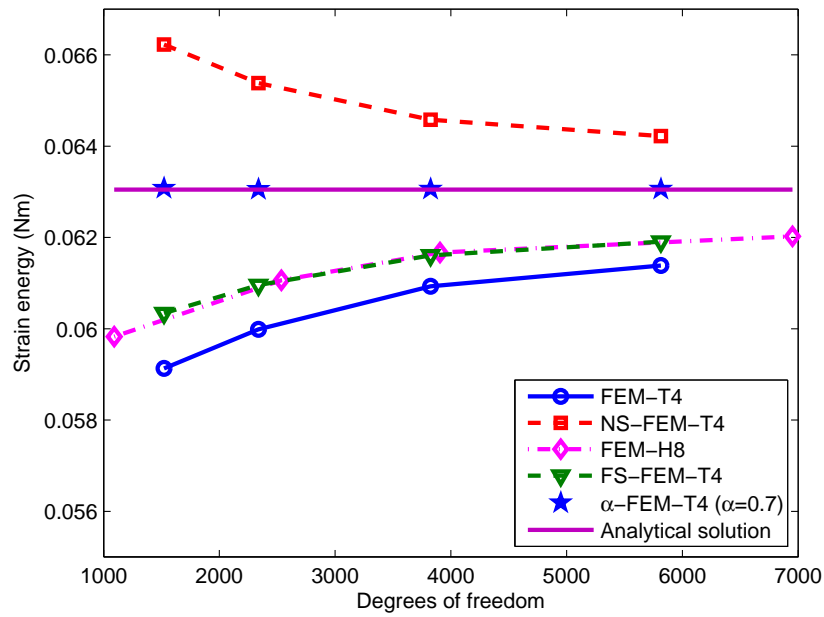


Figure 8.22. Convergence of strain energy solution of α FEM-T4 ($\alpha_{\text{exact}} = 0.7$) in comparison with others methods for the hollow sphere subjected to inner pressure.

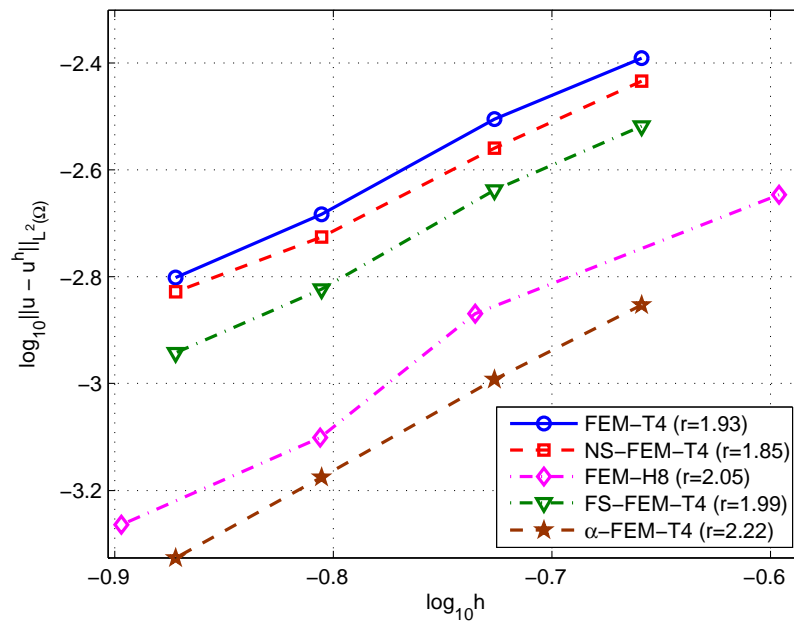


Figure 8.23. Error in displacement norm of α FEM-T4 ($\alpha_{\text{exact}} = 0.7$) in comparison with other methods for the hollow sphere subjected to inner pressure.

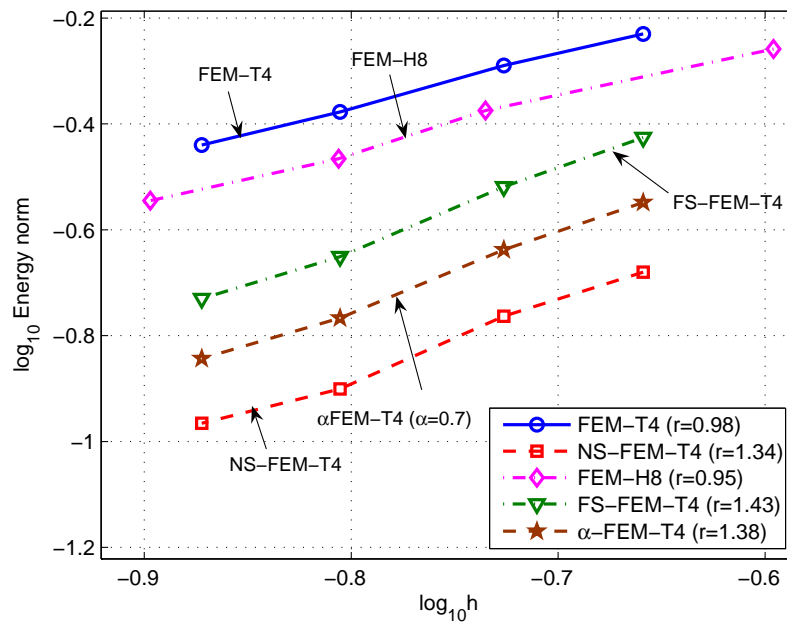


Figure 8.24. Error in energy norm of the solution obtained using α FEM-T4 ($\alpha_{\text{exact}} = 0.7$) in comparison with other methods for the hollow sphere subjected to inner.

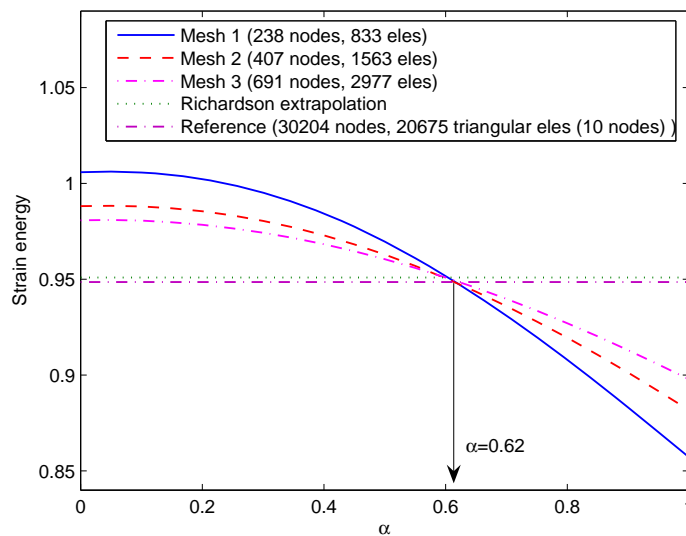


Figure 8.25. The strain energy curves of three meshes with the same aspect ratios to find $\alpha_{\text{exact}} = 0.62$ for the cubic cantilever.

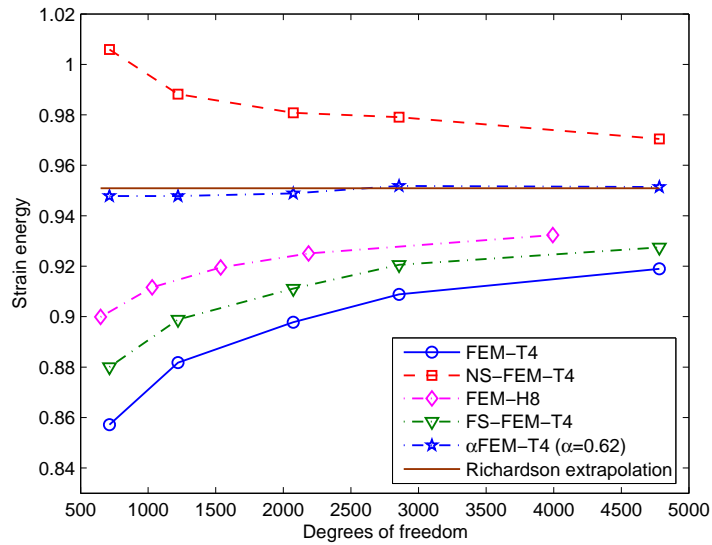


Figure 8.26. Convergence of the strain energy solutions of α FEM-T4 ($\alpha_{\text{exact}} = 0.62$) in comparison with other methods for the cubic cantilever subjected to a uniform pressure on the top surface.

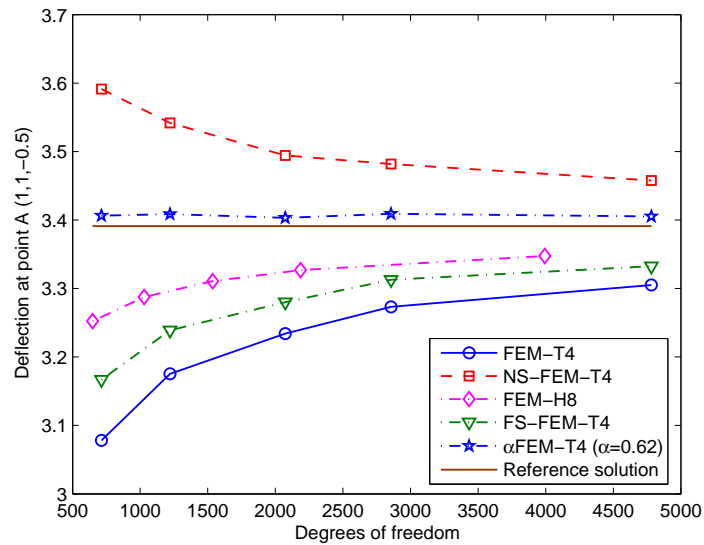


Figure 8.27. Convergence of the deflection at point A(1.0,1.0,-0.5) of α FEM-T4 ($\alpha_{\text{exact}} = 0.62$) in comparison with other methods for the cubic cantilever subjected to a uniform pressure on the top surface.

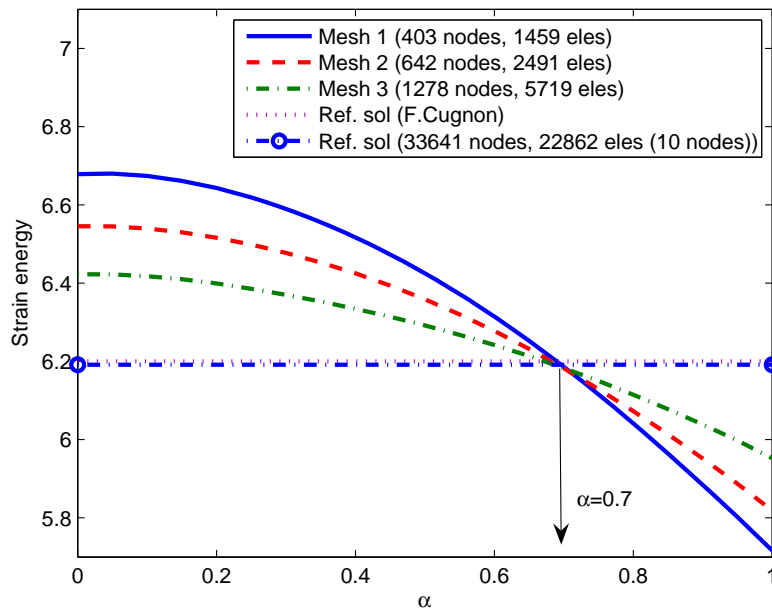


Figure 8.28. The strain energy curves of three meshes with the same aspect ratios to find $\alpha_{\text{exact}} = 0.7$ for the L -shaped 3D problem.

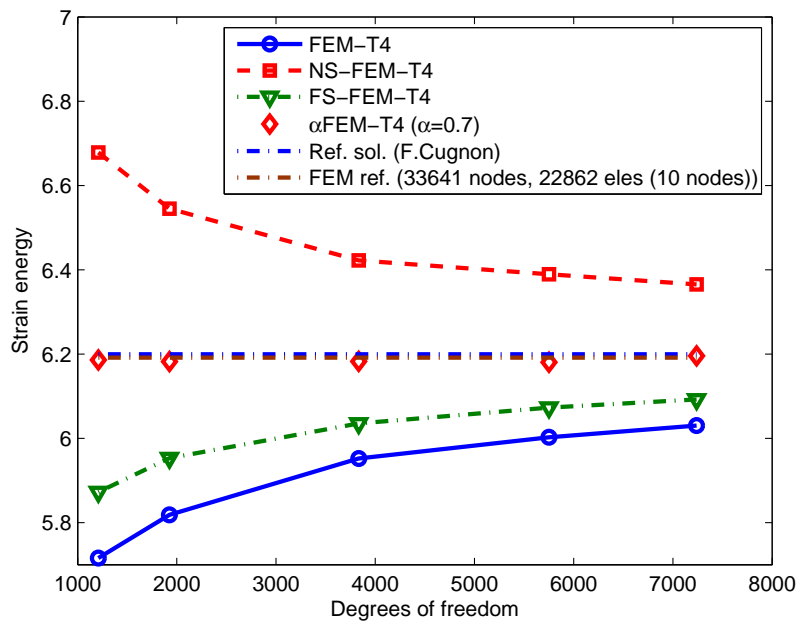


Figure 8.29. Convergence of the strain energy solutions of α FEM-T4 ($\alpha_{\text{exact}} = 0.7$) in comparison with other methods for L -shaped 3D problem.

Chapter 9

Conclusions and Recommendations

9.1 Conclusions Remarks

This thesis formulated and developed five new novel FEM models including four S-FEM models and one α FEM model scaled by an alpha variable. Chapter 3 presented the important foundational theories of the S-FEM models. In Chapters 4, 5, 6 and 7, based on four different entities including cells (elements), nodes, edges and faces, four different S-FEM models including the cell-based S-FEM (CS-FEM), node-based S-FEM (NS-FEM), edge-based S-FEM (ES-FEM) and face-based S-FEM (FS-FEM) were presented in more detail, respectively. In Chapter 8, by a rational combination of the NS-FEM and standard FEM with an alpha scaled variable, an alpha-FEM for triangular elements (α FEM-T3) and tetrahedral elements (α FEM-T4) is formulated to give nearly exact solutions in the strain energy for solid mechanics problems. The results of the research showed that the five new FEM models possess different characters and advantages compared to the standard FEM which can be listed sequentially as follows:

9.1.1 Original contributions

(1) The general formulation of the S-FEM models shows that four models, CS-FEM, NS-FEM, ES-FEM and FS-FEM, are variationally consistent and have the same unknowns of only the displacements at field nodes as those of the standard FEM model. However, the S-FEM models are “softer” than the standard FEM model. The strain energy of the S-FEM models hence becomes larger than that of the standard FEM model. In addition, the “softening” effect caused by the strain smoothing technique will be monotonically reduced with the increase of the number of smoothing domains (SD) in a nested manner. It is also shown that when the total number of SD of the whole problem domain approaches the infinity, $N_s \rightarrow \infty$, the solution of the S-FEM models will approach the solution of the standard FEM model, which also approaches the exact solution in the cases of NS-FEM, ES-FEM and FS-FEM.

The spatial and temporal stabilities of the ES-FEM and FS-FEM are always ensured because the total number of SD for whole problem domain, N_s , is always much larger than the minimum number of SD required, N_s^{\min} . The ES-FEM and FS-FEM hence work well for both static and dynamic problems. In the contrary, the NS-FEM only satisfies exactly the minimum number of SD required, N_s^{\min} . Therefore, the NS-FEM only works well for static problems. For dynamic analysis, the NS-FEM is unstable because of the presence of spurious non-zero energy modes. This is the same as the under-integration of the weak form inherent in the nodal integration approach of meshfree methods. For the CS-FEM, the stability of method is not ensured when the whole element is used as a SD for each element, because the minimum number of SD required, N_s^{\min} , may not be satisfied. In this case, the solution of CS-FEM has the same properties with those of FEM using reduced integration. The element stiffness matrix hence can contain spurious zeros

energy modes, and the system stiffness matrix after imposing essential boundary conditions can be singular depending on the setting of the problem. Therefore, the stability of CS-FEM is only ensured when more than one SD is used for each element.

Field gradients of four S-FEM models are computed directly only using shape functions themselves on the smoothing domain boundaries and no derivative of shape functions is needed. For the triangular and tetrahedral elements, the S-FEM models use the identical linear shape functions of the standard FEM. For n -sided polygonal elements, the S-FEM models use the general shape function constructed in Chapter 3. From these shape functions, the evaluation of the shape function values at points on the smoothing domain boundaries can be done with ease, using the simple point interpolation and/or averaging in a proper manner. The compatibility of the displacement field on the smoothing domain boundaries can always be ensured using such a point interpolation method, as long as the interpolation is based on the points on the smoothing domain boundaries.

Note that the shape function (or displacement field) constructed general for n -sided polygonal elements in Chapter 3 is implicit. We can not, in general, write out the exact forms of the displacement field explicitly. However, this is perfectly fine for the S-FEM models. Because we do not need to compute the derivatives of the displacement field and hence no explicit form is required. All we need in the S-FEM models is to evaluate the shape function values on the boundaries of the smoothing domains to compute the smoothed strain field. This evaluation is performed very easily from the available values of shape functions of field nodes.

Unlike the conventional FEM using isoparametric elements, as no coordinate transformation or mapping is performed in the S-FEM models, no limitation is imposed on the shape of elements used, and the integration of the weak form is performed on the

basis of physical smoothing domains, not by mapped elements. Domain discretization in the S-FEM models therefore is more flexible than FEM when even severely distorted or n -sided polygonal elements (for the CS-FEM, NS-FEM and ES-FEM) can be used.

In the S-FEM models using triangular, quadrilateral and tetrahedral elements, the trial function \mathbf{u}^h used is the same as that in the standard FEM model. Therefore the S-FEM models change only the system stiffness matrix $\bar{\mathbf{K}}$. The other matrices, such as mass matrix and damping matrix, and force vector which only used the trial function \mathbf{u}^h in computation, are computed in exactly the same way as in the standard FEM. In the S-FEM models, the system stiffness matrix $\bar{\mathbf{K}}$ is also symmetric positive definite (SPD) and the stiffness matrix of each smoothing domain $\bar{\mathbf{K}}_{IJ}$ needs to be computed only when nodes I and J share a same smoothing domain. Otherwise, it is zero. Hence, matrix $\bar{\mathbf{K}}$ will be also sparse for the S-FEM models and the discretized linear system of equations can be solved by using standard routines with ease.

Also note that matrix $\bar{\mathbf{K}}$ in the S-FEM models will be banded if the nodes are properly numbered, as that in the FEM. The bandwidth of $\bar{\mathbf{K}}$ will be determined by the largest difference of node numbers of the nodes associated with the smoothing domains. For the CS-FEM using smoothing domains located inside the elements, the bandwidth of $\bar{\mathbf{K}}$ will be same as that of \mathbf{K} in the FEM. It is because the number of nodes related to the smoothing domains is identical to that related to the elements. However, when the smoothing domains cover parts of adjacent elements such as in the NS-FEM, ES-FEM or FS-FEM, the bandwidth of $\bar{\mathbf{K}}$ will be larger than that of \mathbf{K} in the FEM. It is because the number of nodes supporting the smoothing domains is larger than that of the elements.

(2) The CS-FEM using the quadrilateral elements provided more accurate results than FEM-Q4 in terms of both displacement and energy error norms. In practical computation,

using $n_s = 4$ SD for each quadrilateral element in the CS-FEM is advised for all problems. The numerical solution of CS-FEM ($n_s = 4$) is always stable, accurate, much better than FEM-Q4, and often very close to the exact solutions. For the n -sided polygonal elements, the n CS-FEM using $n_{sc} = n$ triangular smoothing cells is always stable and gives good accuracy in computations. A selective integration scheme was also proposed to solve volumetric locking problems using nearly incompressible materials for both the CS-FEM and n CS-FEM.

(3) The NS-FEM is a displacement FEM model, using only displacements as unknowns. It, however, possesses interesting properties of an equilibrium FEM model such as: (i) the upper bound property of the strain energy, when a reasonably fine mesh is used for force driven problems; (ii) natural immunization from the volumetric locking; (iii) ultra-accuracy and super-convergence of stress solutions; (iv) similar accuracy of displacement solutions compared to the standard FEM model.

The NS-FEM can be applied for triangular, quadrilateral and n -sided polygonal elements in 2D problems, and for 4-node tetrahedral element in 3D problems. From the upper bound property of the strain energy of the NS-FEM, a simple and practical procedure is proposed to determine both upper and lower bounds in the strain energy, by combining the NS-FEM with CS-FEM (for n -sided polygonal elements) or with standard FEM (for triangular, 4-node quadrilateral and 4-node tetrahedral elements).

(4) The ES-FEM can use general n -sided polygonal elements (n ES-FEM) including triangular elements (ES-FEM-T3). A smoothing-domain-based selective ES/NS-FEM which is effective in overcoming the volumetric locking problems using nearly incompressible materials was proposed.

For n -sided polygonal elements, results of the n ES-FEM found agree well with exact solutions and often much better than those of others existing methods such as the n CS-FEM and n NS-FEM.

In particular for the triangular elements, the ES-FEM-T3 possesses many following excellent properties: (i) for the static elastic problems, the numerical results of ES-FEM-T3 are often found super-convergence and ultra-accurate: much more accurate than the FEM-T3 and even more accurate than those of FEM-Q4 with the same distribution of nodes; (ii) the ES-FEM-T3 is both spatially and temporally stable and hence works very well for dynamics analyses. The numerical results showed that the ES-FEM-T3 gives the more accurate results and higher convergence rates than the FEM-Q4 and (iii) the computational efficiency of ES-FEM-T3 is even better than the FEM-Q4 using the same distribution of nodes in term of CPU time for the same accuracy in both energy and displacement error norms.

(5) The FS-FEM, which is an extension of the ES-FEM, uses 4-node tetrahedral elements in 3D problems. The numerical results demonstrated that the FS-FEM is significantly more accurate than the FEM using tetrahedral elements (FEM-T4) for both linear analysis and geometrically nonlinear analysis of large deformation. In addition, a novel smoothing-domain-based selective scheme, which can overcome well the volumetric locking problems using nearly incompressible materials, is proposed. The computational efficiency of the FS-FEM was found better than that of FEM-T4 in term of CPU time for the same accuracy in both energy and displacement error norms.

(6) The α FEM using three-node triangular elements (α FEM-T3) and four-node tetrahedral elements (α FEM-T4) is applied for two-dimensional (2D) and three-

dimensional (3D) problems, respectively. The α FEM are equipped with a scaling factor α that controls the contributions from the NS-FEM and FEM models. When the factor α varies from 0 to 1, a continuous solution function in the strain energy from the upper bound of the NS-FEM model to the lower bound of the FEM can be obtained.

From the observed behavior of the numerical results, a unique approach has been proposed for the α FEM to obtain the nearly exact solution in strain energy for linear elasticity problems. This approach uses two coarse meshes with the same aspect ratio to search for an approximate α_{exact} . The α FEM with such an α_{exact} is capable to provide a “nearly exact” solution in strain energy using very coarse meshes. The α FEM can solve the volumetric locking problem with nearly incompressible materials.

9.1.2 Some insight comments

From the above results, it can be seen that the common effect of the strain smoothing technique is the reduction of the stiffness of the S-FEM models compared to the standard FEM model. This effect is called “softening effect” which contrasts with “stiffening effect” caused by the assumed displacement field of a compatible FEM model. Due to the softening effect, the strain energy of the S-FEM models becomes larger than that of FEM.

However, if compared to the exact strain energy, the strain energy of the S-FEM models can be larger or smaller, and further or closer depending on the number and associated entities (cells (elements), nodes, edges or faces) of smoothing domains (SD). Specifically, SD associated with nodes in the NS-FEM is larger than SD associated with edges in the ES-FEM (or with faces in the FS-FEM). In addition, almost of nodes in the problem domain in the NS-FEM are smoothed (except nodes at corners of problem domain), while only interior edges in the ES-FEM (or interior faces in the FS-FEM) are smoothed (the smoothing of boundary edges (or faces) is unaffected). As a result, the

softening effect in the NS-FEM is much stronger than that in the ES-FEM/FS-FEM. The strain energy obtained by the NS-FEM is therefore not only larger but also further than the exact strain energy, while the strain energy obtained by the ES-FEM/FS-FEM is smaller than that of the NS-FEM and is much closer to the exact strain energy. The solution in the strain energy (or displacement) of ES-FEM/FS-FEM is therefore much better than that obtained by the NS-FEM. This solution of ES-FEM is even more accurate than the FEM-Q4 with the same distribution of nodes used.

While it is clear to define the relative position of the strain energy obtained by the FEM or NS-FEM or ES-FEM/FS-FEM with the exact strain energy, it is indefinite for the case of the strain energy obtained by the CS-FEM. It may be larger or smaller, further or closer to the exact strain energy depending on the number of smoothing domains used in each element, n_s , and the problems solved.

Unlike the S-FEM models which use only the fixed smoothing domains to soften the stiffness, the α FEM even uses a continuous scale variable α to adjust the smoothing domain, and by using meshes with the same aspect ratio, the α FEM can even find α_{exact} which provides the nearly exact strain energy. In particular, this nearly exact strain energy can be obtained even with coarse discretizations of domain.

9.1.3 Crucial contributions

The above characters and advantages of five proposed new FEM models show four following crucial contributions:

First, the new FEM models, including four S-FEM models and the α FEM, are promising to provide more feasible options for numerical methods in terms of high accuracy, low computational cost, easy implementation, versatility and general applicability. The new FEM models can be applied especially effectively for 3-node

triangular (NS-FEM, ES-FEM, α FEM) and 4-node tetrahedral elements (NS-FEM, FS-FEM, α FEM). The new FEM models can be applied well for both compressible and nearly incompressible materials.

Second, in the S-FEM models, field gradients are computed directly only using shape functions themselves and no derivative of shape functions is needed. This is significant in numerical methods because it gives more the freedom and convenience in the construction of shape functions. Furthermore, the S-FEM models, which can use the severe distorted or n -sided polygonal elements (CS-FEM, NS-FEM and ES-FEM), remove the constrained conditions on the shape of elements of the standard FEM. This removal is important because it helps to overcome the difficulties related to the distortion of the shape of elements in analyzing the large deformation, crack and destruction problems, or in modeling continuum structured material by a set of discrete material points.

Third, the NS-FEM which possesses interesting properties of an equilibrium FEM model is promising to provide a much simpler tool to estimate the quality of the solution (the global error, bounds of solutions, convergence rates, etc) by combining itself with the standard compatible FEM. This has considerable impact on developing new quasi-equilibrium FEM elements and error estimation theories of the FEM. These new quasi-equilibrium FEM elements would be much simpler and more efficient than the existing complicated quasi-equilibrium FEM elements. At least, we now have a practical mean to obtain the upper and lower bounds of solutions in the strain energy without really worrying too much about where the exact solution is and use the approximated solution with confidence. In addition, how fine the mesh we should use can also be determined base on the gap (error) of these two bounds. As soon as the error is acceptable for our design purpose, we stop further refining the model. This know-where-to-stop requires

“certifying” the solution. It is very important because it give us confidence for the solution as well as preventing using unnecessarily large models in design and analysis, resulting in wastes of computational and manpower resources. The development of practical numerical methods for producing certified solutions will become more and more important to engineering design and analysis, and hence techniques that can provide upper bound solutions like the NS-FEM are very much in demand.

Fourth, the α FEM, which provides the nearly exact solution in the strain energy by only using the coarse meshes of 3-node triangular and 4-node tetrahedral elements, has a very meaningful contribution in providing more the reference solutions with high accuracy of new benchmark problems used to verify the accuracy, reliability and efficiency of numerical methods, especially in 3D problems or 2D problems with complicated geometry domains, or in many fields without having the analytical solutions such as fluid mechanics, solid mechanics, heat mechanics, etc.

9.2 Recommendations for future work

First, as one of the novel numerical methods, mathematical proofs about the characters and advantages of five proposed new novel numerical methods have not been explored comprehensively in this research. Some obtained results were mainly drawn from the numerical results which may restrict the general application of the methods to a certain degree. Further study is therefore needed to develop mathematical bases for these methods. This not only make five proposed new numerical methods more applicable to practical engineering problems with certain confidence, but also guide us on how to further improve the solutions. For instance, the interesting properties of an equilibrium FEM model in the NS-FEM and the existence of the α_{exact} in the α FEM models by using meshes with the same aspect ratio needs to be proved.

Second, it is now clearly necessary to establish a general theoretical framework to unify the formulation of all these newly developed FEM models. Some work has been performed by Liu [68, 69] recently to establish the new functional spaces containing the S-FEM models and S-PIM models. However, many theoretical aspects related to these spaces still need to be analyzed in detail in the coming time.

Third, it is important to further develop the analysis procedures (dual analysis, shakedown analysis, limit analysis, etc) to evaluate the quality of the solution (the global error, bounds of solutions, convergence rates, etc) or to evaluate the working limit of structures in the geometrical or material nonlinear problems by combining the analyses of both the standard compatible FEM and the NS-FEM. We also performed some research in this direction [149]. These are very promising research directions in the coming time.

Fourth, it is promising to apply five proposed new numerical methods in many different applied fields such as solid mechanics (plate, shell), smart materials (piezoelectric, composite, etc), fracture problems, fluid mechanics, fluid-structure interaction, contact problems, computational plasticity, heat conduction, petroleum engineering, wave propagation, etc. We now have extended five new numerical methods in many different applications and computations as listed in publications arising from the thesis. However, there are still a lot of things needed to be done to popularize the new methods in the community of researchers in computational mechanics.

References

1. Allman DJ (1984) A compatible triangular element including vertex rotations for plane elasticity analysis. *Computers and Structures*; 19(2): 1-8.
2. Allman DJ (1988) Evaluation of the constant strain triangle with drilling rotations. *International Journal for Numerical Methods in Engineering*; 26(12): 2645-2655.
3. Almeida JPM, Freitas JAT (1991) Alternative approach to the formulation of hybrid equilibrium finite elements. *Computers and structures*; 40:1043-1047.
4. Almeida JPM, Pereira OJBA (2006) Upper bounds of the error in local quantities using equilibrated and compatible finite element solutions for linear elastic problems. *Computer Methods in Applied Mechanics and Engineering*; 195:279-296.
5. Almeida Pereira OJB (2008) Hybrid equilibrium hexahedral elements and super-elements. *Communications in Numerical Methods in Engineering*; 24(2): 157-165.
6. Argyris JH (1954) Energy Theorems and Structural Analysis. *Aircraft Engineering: Part 1*; 26.
7. Argyris JH (1965) Continua and Discontinua, Proceedings, Conference on Matrix Methods in Structural Mechanics, Wright-Patterson AFB, Ohio: 11-189.
8. Argyris JH, Kelsey S (1954) Energy Theorems and Structural Analysis. *Aircraft Engineering: Part 2*; 27.
9. Arnold DN (1990) Mixed finite element methods for elliptic problems. *Computer Methods in Applied Mechanics and Engineering*; 82: 281-300.
10. Atluri SN (1973) On the hybrid stress finite element model in incremental analysis of large deflection problems. *International Journal of Solids and Structures*; 9: 1188-1191.
11. Atluri SN, Cazzani A (1995) Rotations in computational solid mechanics. *Archives of Computational Methods in Engineering*; 2: 49-138.
12. Bathe KJ (1996) *Finite element procedures*. Prentice Hall: Massachusetts (MIT).
13. Bathe KJ, Dvorkin E (1985) A four node plate bending element based on Reissner-Mindlin plates. *International Journal for Numerical Methods in Engineering*; 21: 367-383.

14. Beckers P, Zhong HG, Maunder E (1993) Numerical comparison of several a posteriori error estimators for 2D stress analysis. *European Journal of Finite Element Method*; 1: 165-178.
15. Belytschko T, Bachrach WE (1986) Efficient implementation of quadrilaterals with high coarse-mesh accuracy. *Computer Methods in Applied Mechanics and Engineering*; 54: 279-301.
16. Belytschko T, Ong JSJ (1984) Hourglass control in linear and nonlinear problems. *Computer Methods in Applied Mechanics and Engineering*; 43: 251-276.
17. Belytschko T, Tsay CS (1983) A stabilization procedure for the quadrilateral plate element with one-point quadrature. *International Journal for Numerical Methods in Engineering*; 19: 405-419.
18. Belytschko T, Tsay CS, Liu WK (1981) A stabilization matrix for the bilinear Mindlin plate element. *Computer methods in applied mechanics and engineering*; 29: 313-327.
19. Bergan PG, Felippa CA (1985) A triangular membrane element with rotational degrees of freedom. *Computer Methods in Applied Mechanics and Engineering*; 50: 25-69.
20. Bordas S, Rabczuk T, Nguyen-Xuan H, Nguyen-Vinh P, Natarajan S, Bog T, Do-Minh Q, Nguyen-Vinh H (2009) Strain smoothing in FEM and XFEM. *Computers and Structures*; doi:10.1016/j.compstruc.2008.07.006.
21. Brebbia CA, Telles JC, Wrobel LC (1984) *Boundary Element Techniques*. Springer: Berlin.
22. Brezzi F, Fortin M (1991) *Mixed and Hybrid finite element methods*. Springer-Verlag: New York.
23. Cen S, Chen XM, Fu XR (2007) Quadrilateral membrane element family formulated by the quadrilateral area coordinate method. *Computer Methods in Applied Mechanics and Engineering*; 196: 4337-4353.
24. Chen JS, Wu CT, Yoon S, You Y (2001) A stabilized conforming nodal integration for Galerkin meshfree method. *International Journal for Numerical Methods in Engineering*; 50: 435-466.
25. Chen JS, Wu CT, Belytschko T (2000) Regularization of material instabilities by meshfree approximations with intrinsic length scales. *International Journal for Numerical Methods in Engineering*; 47: 1303-1322.
26. Chen L, Nguyen-Xuan H, Nguyen-Thoi T, Wu SC (2009) Assessment of smoothed point interpolation methods (PIMs) for elastic mechanics. *Communications in Numerical Methods in Engineering*; in press, doi: 10.1002/cnm.1251.
27. Chen XM, Cen S, Fu XR, Long YQ (2007) A new quadrilateral area coordinate method (QACM-II) for developing quadrilateral finite element models. *International Journal for Numerical Methods in Engineering* (in press).

28. Chen XM, Cen S, Long YQ, Yao ZH (2004) Membrane elements insensitive to distortion using the quadrilateral area coordinate method. *Computers and Structures*; 82 (1): 35–54.
29. Clough RW (1960) The Finite Element Method in Plane Stress Analysis, *Proceedings, Second ASCE Conference on Electronic Computation, Pittsburgh, PA*: 345-378.
30. Cook R (1974) Improved two-dimensional finite element. *Journal of the Structural Division, ASCE* 100; ST6: 1851–1863.
31. Cook RD (1991) Modified formulations for nine-dof plane triangles that include vertex rotations. *International Journal for Numerical Methods in Engineering*; 31: 825-835.
32. Coorevits P, Ladeveze P, Pelle JP (1995) An automatic procedure with a control of accuracy for finite element analysis in 2D elasticity. *Computer Methods in Applied Mechanics and Engineering*; 121:91-121.
33. Courant R (1943) Variational Methods for the solution of Problems of Equilibrium and Vibrations. *Bulletin of the American Mathematical Society*; 49: 1-23.
34. Cugnon F (2000) Automatisation des calculs elements finis dans le cadre de la methode-p. *Universite de Lie, PhD thesis*.
35. Cui XY, Liu GR, Li GY, Zhao X, Nguyen-Thoi T, Sun GY (2008) A smoothed finite element method (SFEM) for linear and geometrically nonlinear analysis of plates and shells. *CMES-Computer Modeling in Engineering and Sciences*; 28(2): 109-125.
36. Dai KY, Liu GR (2007) Free and forced analysis using the smoothed finite element method (SFEM). *Journal of Sound and Vibration*; 301: 803-820.
37. Dai KY, Liu GR, Nguyen-Thoi T (2007) An n-sided polygonal smoothed finite element method (nSFEM) for solid mechanics. *Finite elements in analysis and design*; 43: 847-860.
38. Debongnie JF, Zhong HG, Beckers P (1995) Dual analysis with general boundary conditions. *Computer Methods in Applied Mechanics and Engineering*; 122: 183-192.
39. Dohrmann CR, Heinstein MW, Jung J, Key SW, Witkowski WR (2000) Node-based uniform strain elements for three-node triangular and four-node tetrahedral meshes. *International Journal for Numerical Methods in Engineering*; 47: 1549–1568.
40. Dohrmann CR, Key SW, Heinstein MW, Jung J (1998) A least squares approach for uniform strain triangular and tetrahedral finite elements. *International Journal for Numerical Methods in Engineering*; 42: 1181–1197.

41. Dolbow J, Moes N, Belytschko T (2000) Discontinuous enrichment in finite elements with a partition of unity method. *Finite Element in Analysis and Design*; 36: 235-260.
42. Dorfler W (1996) A convergent adaptive algorithm for Poisson's equation. *SIAM Journal on Numerical Analysis*; 33:1106-1124.
43. Eringen (1972) Nonlocal polar elastic continua, *Int. J. Eng. Sci.* 10, 1.
44. Felippa CA (1995) Parametric unification of matrix structural analysis: classical formulation and d-connected mixed elements. *Finite Elements in Analysis and Design*; 21: 45–74.
45. Felippa CA (2001) A historical outline of matrix structural analysis: A play in three acts. *Computers and Structures*; 79: 1313–1324.
46. Flanagan DP, Belytschko T (1981) A uniform strain hexahedron and quadrilateral with orthogonal hourglass control. *International Journal for Numerical Methods in Engineering*; 17: 679 –706.
47. Fraeijns de Veubeke BM (1965) Displacement and equilibrium models in the finite element method, In "Stress analysis", edit.Zienkiewicz O.C. Wiley, London.
48. Fredriksson M, Ottosen NS (2004) Fast and accurate 4-node quadrilateral. *International Journal for Numerical Methods in Engineering*; 61: 1809 –1834.
49. Ghosh S, Mallett RL (1994) Voronoi cell finite element. *Computers and Structures*; 50: 33-46.
50. Gruttmann F, Wanger W (2004) A stabilized one-point integrated quadrilateral Reissner-Mindlin plate element. *International Journal for Numerical Methods in Engineering*; 61: 2273-2295.
51. Gruttmann F, Wanger W, Wriggers (1992) A nonlinear quadrilateral shell element with drilling degrees of freedom. *Archive of Applied Mechanics*; 62, 474–486.
52. Hermann LR (1965) Elasticity equations for incompressible and nearly incompressible materials by a variational theorem. *AIAA Journal*; 3: 1896 –1900.
53. Hughes TJR (1980) Generalization of selective integration procedures to anisotropic and nonlinear media. *International Journal for Numerical Methods in Engineering*; 15: 1413-1418.
54. Hughes TJR (1987) *The Finite Element Method: Linear Static and Dynamic Finite Element Analysis*. Prentice-Hall: Englewood Cliffs, NJ.
55. Hughes TJR, Brezzi F (1989) On drilling degrees of freedom. *Computer Methods in Applied Mechanics and Engineering*; 72: 105-121.
56. Hughes TJR, Cohen M, Haroun M (1978) Reduced and selective integration techniques in finite element method of plates. *Nuclear Engineering Design*; 46: 203–222.

57. Hughes TJR, Cottrell JA, Bazilevs Y (2005) Isogeometric analysis: CAD, finite elements, NURBS, exact geometry and mesh refinement. *Computer Methods in Applied Mechanics and Engineering*; 194: 4135-4195.
58. Hughes TJR, Taylor RL, Kanoknukulchai W (1977) Simple and efficient element for plate bending. *International Journal for Numerical Methods in Engineering*; 11: 1529–1543.
59. Ibrahimbegovic A, Taylor RL, Wilson EL (1990) A robust quadrilateral membrane element with drilling degrees of freedom. *International Journal for Numerical Methods in Engineering*; 30: 445-457.
60. Iura M, Atluri SN (1992) Formulation of a membrane finite element with drilling degrees of freedom. *Computational Mechanics*; 9: 417-428.
61. Johnson C (1987) Numerical solution of partial differential equations by the finite element method. Cambridge University Press: New York.
62. Kelly DW (1980) Bounds on discretization error by special reduced integration of the Lagrange family of finite elements. *International Journal for Numerical Methods in Engineering*; 15: 1489-1506.
63. Korelc J, Wriggers P (1997) Improved enhanced strain four-node element with Taylor expansion of the shape functions. *International Journal for Numerical Methods in Engineering*; 40: 407-421.
64. Kosloff D, Frazier GA (1978) Treatment of hourglass patterns in low order finite element codes. *International Journal for Numerical and Analytical Methods in Geomechanics*; 2: 57-72.
65. Ladeveze P, Coffignal G, Pelle JP (1986) Accuracy of elastoplastic and dynamic analysis, in *Accuracy Estimates and Adaptive Refinements in Finite Element Computations*, Ch. 11, Babuska I, Zienkiewicz OC, Gago J, Oliveira ER (eds.). Wiley: New York.
66. Ladeveze P, Pelle JP, Rougeot P (1991) Error estimation and mesh optimisation for classical finite elements. *Engineering Computation*; 8: 69-80.
67. Liu GR (2002) *Meshfree methods: Moving Beyond the Finite Element Method*. CRC Press: Boca Raton, USA.
68. Liu GR (2008) A generalized gradient smoothing technique and the smoothed bilinear form for Galerkin formulation of a wide class of computational methods. *International journal of computational methods*; 5: 199-236.
69. Liu GR (2009) A G space theory and weakened weak (W2) form for a unified formulation of compatible and incompatible methods: Part I Theory, Part II Application to solid mechanics problems. *International Journal for Numerical Methods in Engineering*; accepted.
70. Liu GR, Dai KY, Nguyen-Thoi T (2007) A smoothed finite element method for mechanics problems. *Computational Mechanics*; 39: 859-877.

71. Liu GR, Li Y, Dai KY, Luan MT, Xue W (2006) A Linearly conforming radial point interpolation method for solid mechanics problems. *International Journal of Computational Methods*; 3(4): 401-428.
72. Liu GR, Liu MB (2003) *Smoothed particle Hydrodynamics-A Meshfree Particle Method*. World Scientific: Singapore.
73. Liu GR, Nguyen-Thoi T, Dai KY, Lam KY (2007) Theoretical aspects of the smoothed finite element method (SFEM). *International journal for numerical methods in Engineering*; 71: 902-930.
74. Liu GR, Nguyen-Thoi T, Lam KY (2008) A novel Alpha Finite Element Method (α FEM) for exact solution to mechanics problems using triangular and tetrahedral elements. *Computer Methods in Applied Mechanics and Engineering*; 197: 3883-3897.
75. Liu GR, Nguyen-Thoi T, Lam KY (2009) A novel FEM by scaling the gradient of strains with factor α (α FEM). *Computational Mechanics*; 43: 369-391.
76. Liu GR, Nguyen-Thoi T, Lam KY (2009) An edge-based smoothed finite element method (ES-FEM) for static, free and forced vibration analyses of solids. *Journal of Sound and Vibration*; 320: 1100-1130.
77. Liu GR, Nguyen-Thoi T, Nguyen-Xuan H, Dai KY, Lam KY (2009) On the essence and the evaluation of the shape functions for the smoothed finite element method (SFEM) (Letter to Editor). *International Journal for Numerical Methods in Engineering*; 77: 1863-1869.
78. Liu GR, Nguyen-Thoi T, Nguyen-Xuan H, Lam KY (2009) A node-based smoothed finite element method (NS-FEM) for upper bound solution to solid mechanics problems. *Computers and Structures*; 87: 14-26.
79. Liu GR, Nguyen-Xuan H, Nguyen-Thoi T (2009) A variationally consistent α FEM (VC α FEM) for solid mechanics problems. *International Journal for Numerical Methods in Engineering*; (revised).
80. Liu GR, Quek SS (2003) *The finite element method: a practical course*. Butterworth Heinemann: Oxford.
81. Liu GR, Xu XG (2008) A gradient smoothing method (GSM) for fluid dynamics problems. *International Journal for Numerical Methods in Fluids*; 58: 1101-1133.
82. Liu GR, Xu XG (2009) An Adaptive Gradient Smoothing Method (GSM) For Fluid Dynamics Problems. *International Journal for Numerical Methods in Fluids*; doi: 10.1002/flid.2032 .
83. Liu GR, Zhang GY (2008) Upper bound to elasticity problems using the linearly conforming point interpolation method (LC-PIM). *International Journal for Numerical Methods in Engineering*; 74: 1128-1161.
84. Liu GR, Zhang GR (2008) Edge-based Smoothed Point Interpolation Methods. *International Journal of Computational Methods*; 5(4): 621-646.

85. Liu GR, Zhang GY (2009) A normed G space and a cell-based smoothed point interpolation method. *International Journal of Computational Methods*, 6(1): 147-179.
86. Liu GR, Zhang GY, Dai KY, Wang YY, Zhong ZH, Li GY, Han X (2005) A linearly conforming point interpolation method (LC-PIM) for 2D solid mechanics problems. *International Journal of Computational Methods*; 2(4): 645-665.
87. Liu GR, Zhang J, Lam KY (2008) A gradient smoothing method (GSM) with directional correction for solid mechanics problems. *Computational Mechanics*; 41: 457-472.
88. Liu WK, Belytschko T (1984) Efficient linear and nonlinear heat conduction with a quadrilateral element. *International Journal for Numerical Methods in Engineering*; 20: 931-948.
89. Liu WK, Hu YK, Belytschko T (1994) Multiple quadrature underintegrated finite elements, *International Journal for Numerical Methods in Engineering* 37: 3263-3289.
90. Liu WK, Ong JSJ, Uras RA (1985) Finite element stabilization matrices—A unification approach. *Computer Methods in Applied Mechanics and Engineering*; 53: 13-46.
91. Lucy L (1977) A numerical approach to testing the fission hypothesis. *Astron. Journal*; 82: 1013–1024.
92. Lyly M, Stenberg R, Vihinen T (1993) A stable bilinear element for the Reissner-Mindlin plate model. *Computer Methods in Applied Mechanics and Engineering*; 110: 343-357.
93. Malkus DS, Hughes TJR (1978) Mixed Finite Element Methods – Reduced and Selective Integration Techniques: A Unification of Concepts. *Computer Methods in Applied Mechanics and Engineering*; 15: 63-81.
94. Mauder EAW, Alemeida JPM, Ramsay ACA (1996) A general formulation of equilibrium macro-elements with control of spurious kinematic modes. *International Journal for Numerical Methods in Engineering*; 39: 3175–3194.
95. Melenk JM, Babuska I (1996) The partition of unity finite element method: Basic theory and applications. *Computer Methods in Applied Mechanics and Engineering*; 139: 289–314.
96. Mijuca D, Berković M (1998) On the efficiency of the primal-mixed finite element scheme. *Advances in Computational Structured Mechanics*; Civil-Comp Press: 61–69.
97. Moes N, Dolbow J, Belytschko T (1999) A finite element method for crack growth without remeshing. *International Journal for Numerical Methods in Engineering*; 46: 131-150.

98. Monaghan JJ (1982) Why particle methods work. *Siam J. Sci. Stat. Comput.*; 3(4): 423–433.
99. Nagashima T (1999) Node-by-node meshless approach and its applications to structural analyses. *International Journal for Numerical Methods in Engineering*; 46: 341–385.
100. Natarajan S, Bordas S, Mahapatra DR (2009) Numerical integration over arbitrary polygonal domains based on Schwarz-Christoffel conformal mapping. *International Journal for Numerical Methods in Engineering*; doi: 10.1002/nme.
101. Nguyen-Thanh N, Rabczuk T, Nguyen-Xuan H, Bordas S (2008) A smoothed finite element method for shell analysis. *Computer Methods in Applied Mechanics and Engineering*; 198: 165-177.
102. Nguyen-Thoi T, Liu GR, Dai KY, Lam KY (2007) Selective Smoothed Finite Element Method. *Tsinghua Science and Technology*; 12(5): 497:508.
103. Nguyen-Thoi T, Liu GR, Lam KY, Zhang GY (2009) A Face-based Smoothed Finite Element Method (FS-FEM) for 3D linear and nonlinear solid mechanics problems using 4-node tetrahedral elements. *International Journal for Numerical Methods in Engineering*; 78: 324-353.
104. Nguyen-Thoi T, Liu GR, Nguyen-Xuan H (2009) An n-sided polygonal edge-based smoothed finite element method (nES-FEM) for solid mechanics. *Communications in Numerical Methods in Engineering*; (accepted)
105. Nguyen-Thoi T, Liu GR, Nguyen-Xuan H, Nguyen-Tran C (2009) Adaptive analysis using the node-based smoothed finite element method (NS-FEM). *Communications in Numerical Methods in engineering*; doi: 10.1002/cnm.1291.
106. Nguyen-Thoi T, Liu GR, Vu-Do HC, Nguyen-Xuan H (2009) An edge-based smoothed finite element method (ES-FEM) for visco-elastoplastic analyses in 2D solids using triangular mesh. *Computational Mechanics*; 45: 23-44.
107. Nguyen-Thoi T, Liu GR, Vu-Do HC, Nguyen-Xuan H (2009) A face-based smoothed finite element method (FS-FEM) for visco-elastoplastic analyses of 3D solids using tetrahedral mesh. *Computer Methods in Applied Mechanics and Engineering*; 198: 3479-3498.
108. Nguyen-Van H, Mai-Duy N, Tran-Cong T (2008) A smoothed four-node piezoelectric element for analysis of two-dimensional smart structures. *CMES-Computer Modeling in Engineering and Sciences*; 23(3): 209-222.
109. Nguyen Vinh Phu, Rabczuk Timon, Bordas Stéphane, Duflo Marc (2008) Meshless methods: A review and computer implementation aspects. *Mathematics and Computers in Simulation*; (in press) doi:10.1016/j.matcom.2008.01.003.
110. Nguyen-Xuan Hung, Bordas Stéphane, Nguyen-Dang Hung (2008) Smooth finite element methods: Convergence, accuracy and properties. *International Journal for Numerical Methods in Engineering*; 74: 175-208.

111. Nguyen-Xuan H, Bordas S, Nguyen-Dang H (2008) Addressing volumetric locking and instabilities by selective integration in smoothed finite elements. *Communications in Numerical Methods and Engineering*; 25: 19-34.
112. Nguyen-Xuan H, Liu GR, Nguyen-Thoi T, Nguyen-Tran C (2009) An edge-based smoothed finite element method (ES-FEM) for analysis of two-dimensional piezoelectric structures. *Smart Materials and Structures*; 18:065015 (12pp).
113. Nguyen-Xuan H, Liu GR, Thai-Hoang C, Nguyen-Thoi T (2009) An edge-based smoothed finite element method with stabilized discrete shear gap technique for analysis of Reissner-Mindlin plates. *Computer Methods in Applied Mechanics and Engineering*; 199: 471:489.
114. Nguyen-Xuan H, Nguyen-Thoi T (2009) A stabilized smoothed finite element method for free vibration analysis of Mindlin-Reissner plates. *Communications in Numerical Methods in Engineering*; 25: 882-906.
115. Nguyen-Xuan H, Rabczuk T, Bordas S, Debongnie JF (2008) A smoothed finite element method for plate analysis. *Computer Methods in Applied Mechanics and Engineering*; 197: 1184-1203.
116. Oliveira Eduardo R De Arantes E (1968) Theoretical Foundations of The Finite Element Method. *International Journal of Solids and Structures*. 4: 929-952.
117. Okabe A, Boots B, Sugihara K (1992) *Spatial Tessellations: Concepts and Applications of Voronoi Diagrams*. Wiley: Chichester.
118. Pereira OJBA, Almeida JPM, Maunder EAW (1999) Adaptive methods for hybrid equilibrium finite element models. *Computer Methods in Applied Mechanics and Engineering*; 176: 19-39.
119. Pian THH, Sumihara K (1984) Rational approach for assumed stress finite elements. *International Journal for Numerical Methods in Engineering*; 20: 1685 –1695.
120. Pian THH, Tong P (1969) Basis of finite elements for solids continua. *International Journal for Numerical Methods in Engineering*; 1: 3–28.
121. Pian THH, WU CC (1988) A rational approach for choosing stress term for hybrid finite element formulations; 26: 2331–2343.
122. Pian THH, Wu CC (2006) *Hybrid and Incompatible finite element methods*. CRC Press: Boca Raton.
123. Piltner R, Taylor RL (2000) Triangular finite elements with rotational degrees of freedom and enhanced strain modes. *Computers and Structures*; 75: 361- 368.
124. Puso MA, Chen JS, Zywicki E, Elmer W (2008) Meshfree and finite element nodal integration methods. *International Journal for Numerical Methods in Engineering*; 74: 416-446.

125. Puso MA, Solberg J (2006) A formulation and analysis of a stabilized nodally integrated tetrahedral. *International Journal for Numerical Methods in Engineering*; 67: 841–867.
126. Rabczuk T, Belytschko T, Xiao SP (2004) Stable particle methods based on Lagrangian kernels. *Computer Methods in Applied Mechanics and Engineering*; 193: 1035-1063.
127. Reddy BD (1998) *Introductory Functional Analysis*. Springer-Verlag: New York.
128. Reddy JN (2004) *An introduction to nonlinear finite element analysis*. Oxford University Press.
129. Reese S, Wriggers P (2000) A stabilization technique to avoid hourglassing in finite elasticity. *International Journal for Numerical Methods in Engineering*; 48: 79–109.
130. Richardson LF (1910) The approximate arithmetical solution by finite differences of physical problems, *Trans. Roy.Soc. (London) A210*: 307–357.
131. Rong TY, Lu AQ (2001) Generalized mixed variational principles and solutions for ill-conditioned problems in computational mechanics: Part I. Volumetric locking. *Computer Methods in Applied Mechanics and Engineering*; 191: 407-422.
132. Rong TY, Lu AQ (2003) Generalized mixed variational principles and solutions for ill-conditioned problems in computational mechanics: Part II. Shear locking. *Computer Methods in Applied Mechanics and Engineering*; 192: 4981-5000.
133. Sandhu RS, Singh KJ (1978) Reduced integration for improved accuracy of finite element approximations. *Computer Methods in Applied Mechanics and Engineering*; 14: 23-37.
134. Sevilla R, Fernandez-Mendez S, Huerta A (2008) NURBS-Enhanced Finite Element Method (NEFEM). *International Journal for Numerical Methods in Engineering*; 76: 56–83.
135. Sevilla R, Fernandez-Mendez S, Huerta A (2008) NURBS-enhanced finite element method for Euler equations. *International Journal for Numerical Methods in Fluids*; 57: 1051-1069.
136. Simo JC, Hughes TJR (1998) *Computational Inelasticity*. Springer-Verlag: New York.
137. Simo JC, Hughes TJR (1986) On the Variational Foundations of Assumed Strain Methods. *Journal of Applied Mechanics*; 53: 51-54.
138. Simo JC, Armero F (1992) Geometrically nonlinear enhanced mixed methods and the method of incompatible modes. *International Journal for Numerical Methods in Engineering*; 33: 1413-1449.
139. Simo JC, Armero F, Taylor RL (1993) Improved version of assumed enhanced strain tri-linear element for 3D finite deformation problems. *Computer Methods in Applied Mechanics and Engineering*; 110: 359-386.

140. Simo JC, Rifai MS (1990) A class of mixed assumed strain methods and the method of incompatible modes. *International Journal for Numerical Methods in Engineering*; 29: 1595 – 1638.
141. Smith IM, Griffiths DV (1998) *Programming the Finite Element Method*, third ed. Wiley: New York.
142. Sukumar N (2004) Construction of polygonal interpolants: a maximum entropy approach. *International Journal for Numerical Methods in Engineering*; 61: 2159-2181.
143. Sukumar N, Chopp DL, Moes N, Belytschko T (2001) Modeling holes and inclusions by level sets in the extended finite-element method. *Computer Methods in Applied Mechanics and Engineering*; 190: 6183-6200.
144. Sukumar N, Malsch EA (2006) Recent advances in the construction of polygonal finite element interpolants. *Archives of Computational Methods in Engineering*; 13(1): 129-163.
145. Sukumar N, Tabarraei A (2004) Conforming polygonal finite elements. *International Journal for Numerical Methods in Engineering*; 61: 2045-2066.
146. Synge JL (1957) *The Hypercircle in Mathematical Physics*. Cambridge University Press: London.
147. Taylor RL, Beresford PJ, Wilson EL (1976) A non-conforming element for stress analysis. *International Journal for Numerical Methods in Engineering*; 10: 1211–1219.
148. Timoshenko SP, Goodier JN (1970) *Theory of Elasticity* (3rd edn). McGraw-Hill: New York.
149. Tran Thanh Ngoc, Liu GR, Nguyen-Xuan H, Nguyen-Thoi T (2009) An edge-based smoothed finite element method for primal-dual shakedown analysis of structures. *International Journal for Numerical Methods in Engineering*; 10.1002/nme.2804.
150. Turner MJ, Clough RW, Martin HC, Topp LJ (1956) Stiffness and Deflection Analysis of Complex Structures. *Journal of the Aeronautical Sciences*; 23: 805-823.
151. Veubeke BF (1965) Displacement and equilibrium models in the finite element method. in *Stress analysis*, Zienkiewicz OC, Holister GS (eds). Wiley: London.
152. Wu HC (1982) *Variational Principle in Elasticity and Applications*. Scientific Press, Beijing.
153. Xie X (2005) An accurate hybrid macro-element with linear displacements. *Communications in Numerical Methods in Engineering*; 21: 1–12.
154. Xie X, Zhou T (2004) Optimization of stress modes by energy compatibility for 4-node hybrid quadrilaterals. *International Journal for Numerical Methods in Engineering*; 59: 293–313.

155. Xu GX, Liu GR, Lee KH (2009) Application of gradient smoothing method (GSM) for steady and unsteady incompressible flow problems using irregular triangles. *International Journal for Numerical Methods in Fluids* (submitted).
156. Yoo JW, Moran B and Chen JS (2004) Stabilized conforming nodal integration in the natural-element method. *International Journal for Numerical Methods in Engineering*; 60: 861-890.
157. Zhang GY, Liu GR, Wang YY, Huang HT, Zhong ZH, Li GY, Han X (2007) A linearly conforming point interpolation method (LC-PIM) for three-dimensional elasticity problems. *International Journal for Numerical Methods in Engineering*; 72: 1524-1543.
158. Zhou T, Nie Y (2001) A combined hybrid approach to finite element schemes of high performance. *International Journal for Numerical Methods in Engineering*; 51: 181–202.
159. Zienkiewicz OC, Cheung YK (1967) *The Finite Element Method in Structural and Continuum Mechanics*. McGraw-Hill (4th ed) Zienkiewicz OC, Taylor RL, Vols. 1 and 2, 1989/1990.
160. Zienkiewicz OC, Taylor RL (2000) *The finite element method* (5th ed). Butterworth Heinemann: Oxford.
161. Zienkiewicz OC, Taylor RL, Too JM (1971) Reduced integration technique in general analysis of plates and shells. *International Journal for Numerical Methods in Engineering*; 3: 275–290.
162. Zienkiewicz OC, Zhu JZ (1992) The superconvergence patch recovery and a posteriori error estimates. Part 1: The recovery techniques. *International Journal for Numerical Methods in Engineering*; 33: 1331-1364.
163. Zienkiewicz OC, Zhu JZ (1992) The superconvergence patch recovery and a posteriori error estimates. Part 2: Error estimates and adaptivity. *International Journal for Numerical Methods in Engineering*; 33: 1365-1382.

Publications arising from Thesis

International Books

1. G.R. Liu, **Nguyen Thoi Trung**. Smoothed Finite Element Methods. CRC Press: NewYork, 2010, in press (about 700 pages).

International Journals

1. Liu GR, Dai KY, **Nguyen-Thoi T** (2007) A smoothed finite element method for mechanics problems. Computational Mechanics; 39: 859-877.
2. Liu GR, **Nguyen-Thoi T**, Dai KY, Lam KY (2007) Theoretical aspects of the smoothed finite element method (SFEM). International journal for numerical methods in Engineering; 71: 902-930.
3. Dai KY, Liu GR, **Nguyen-Thoi T** (2007) An n-sided polygonal smoothed finite element method (nSFEM) for solid mechanics. Finite elements in analysis and design; 43: 847-860.
4. **Nguyen-Thoi T**, Liu GR, Dai KY, Lam KY (2007) Selective Smoothed Finite Element Method. Tsinghua Science and Technology; 12(5): 497-508.
5. Zhang GY, Liu GR, **Nguyen-Thoi T**, Song CX, Han X, Zhong ZH, Li GY (2007) The upper bound property for solid mechanics of the linearly conforming radial point interpolation method (LC-RPIM). International Journal of Computational Methods; 4(3): 521-541.
6. Liu GR, **Nguyen-Thoi T**, Lam KY (2008) A novel Alpha Finite Element Method (α FEM) for exact solution to mechanics problems using triangular and tetrahedral

- elements; *Computer Methods in Applied Mechanics and Engineering*; 197: 3883-3897.
7. Cui XY, Liu GR, Li GY, Zhao X, **Nguyen-Thoi T**, Sun GY (2008) A smoothed finite element method (SFEM) for linear and geometrically nonlinear analysis of plates and shells. *CMES-Computer Modeling in Engineering and Sciences*; 28(2): 109-125.
 8. Liu GR, **Nguyen-Thoi T**, Lam KY (2009) A novel FEM by scaling the gradient of strains with factor α (α FEM). *Computational Mechanics*; 43: 369-391.
 9. Liu GR, Xu X, Zhang GY, **Nguyen-Thoi T** (2009) A superconvergent point interpolation method (SC-PIM) with piecewise linear strain field using triangular mesh. *International journal for numerical methods in Engineering*; 77: 1439-1467.
 10. Liu GR, **Nguyen-Thoi T**, Nguyen-Xuan H, Lam KY (2009) A node-based smoothed finite element method (NS-FEM) for upper bound solution to solid mechanics problems; *Computers and Structures*; 87: 14-26.
 11. Liu GR, **Nguyen-Thoi T**, Lam KY (2009) An edge-based smoothed finite element method (ES-FEM) for static, free and forced vibration analyses in solids. *Journal of Sound and Vibration*; 320: 1100-1130.
 12. **Nguyen-Thoi T**, Liu GR, Lam KY, Zhang GY (2009) A Face-based Smoothed Finite Element Method (FS-FEM) for 3D linear and nonlinear solid mechanics problems using 4-node tetrahedral elements. *International Journal for Numerical Methods in Engineering*; 78: 324-353.
 13. Liu GR, **Nguyen-Thoi T**, Nguyen-Xuan H, Dai KY, Lam KY (2009) On the essence and the evaluation of the shape functions for the smoothed finite element method (SFEM) (Letter to Editor). *International Journal for Numerical Methods in Engineering*; 77: 1863-1869.
 14. Liu GR, Nguyen-Xuan H, **Nguyen-Thoi T**, Xu X (2009) A novel weak form and a superconvergent alpha finite element method ($S\alpha$ FEM) for mechanics problems using triangular meshes. *Journal of Computational Physics*; 228: 4055-4087.

15. Nguyen-Xuan H, Liu GR, **Nguyen-Thoi T**, Nguyen-Tran C (2009) An edge-based smoothed finite element method (ES-FEM) for analysis of two-dimensional piezoelectric structures. *Smart Materials and Structures*; 18:065015, 12pp.
16. Nguyen-Xuan H, **Nguyen-Thoi T** (2009) A stabilized smoothed finite element method for free vibration analysis of Mindlin-Reissner plates. *Communications in Numerical Methods in Engineering*; 25: 882-906.
17. **Nguyen-Thoi T**, Liu GR, Vu-Do HC, Nguyen-Xuan H (2009) A face-based smoothed finite element method (FS-FEM) for visco-elastoplastic analyses of 3D solids using tetrahedral mesh. *Computer Methods in Applied Mechanics and Engineering*; 198: 3479-3498.
18. **Nguyen-Thoi T**, Liu GR, Vu-Do HC, Nguyen-Xuan H (2009) An edge-based smoothed finite element method (ES-FEM) for visco-elastoplastic analyses of 2D solids using triangular mesh. *Computational Mechanics*; 45: 23-44.
19. Nguyen-Xuan H, Liu GR, Thai-Hoang C, **Nguyen-Thoi T** (2009) An edge-based smoothed finite element method with stabilized discrete shear gap technique for analysis of Reissner-Mindlin plates. *Computer Methods in Applied Mechanics and Engineering*; 199: 471:489.
20. Chen L, Nguyen-Xuan H, **Nguyen-Thoi T**, Wu SC (2009) Assessment of smoothed point interpolation methods (PIMs) for elastic mechanics. *Communications in Numerical Methods in Engineering*; in press, doi: 10.1002/cnm.1251.
21. **Nguyen-Thoi T**, Liu GR, Nguyen-Xuan H, Nguyen-Tran C (2009) Adaptive analysis using the node-based smoothed finite element method (NS-FEM). *Communications in Numerical Methods in Engineering*; in press, doi: 10.1002/cnm.1291.
22. **Nguyen-Thoi T**, Liu GR, Nguyen-Xuan H (2009) Additional properties of the node-based smoothed finite element method (NS-FEM) for solid mechanics problems. *International Journal of Computational Methods*, accepted.
23. Tran Ngoc Thanh, GR Liu, Nguyen-Xuan H, **Nguyen-Thoi T** (2009) An edge-based smoothed finite element method for primal-dual shakedown analysis of structures. *International Journal for Numerical Methods in Engineering*; 10.1002/nme.2804.

24. **Nguyen-Thoi T**, Liu GR, Nguyen-Xuan H (2009) An n -sided polygonal edge-based smoothed finite element method (nES-FEM) for solid mechanics. *Communications in Numerical Methods in Engineering*; accepted.
25. Liu GR, Chen L, **Nguyen-Thoi T**, Zeng K (2009) A novel singular node-based smoothed finite element method (NS-FEM) for upper bound solutions of cracks. *International Journal for Numerical Methods in Engineering*; (accepted)
26. Chen L, Zeng KY, **Nguyen-Thoi T**, Jiao PG (2009) An edge-based smoothed finite element method (ES-FEM) for adaptive analysis. *CMES-Computer Modeling in Engineering and Sciences*; (revised)
27. Liu GR, Nguyen-Xuan H, **Nguyen-Thoi T** (2009) A theoretical study on NS/ES-FEM: properties, accuracy and convergence rates. *International Journal for Numerical Methods in Engineering*; (revised)
28. Liu GR, Nguyen-Xuan H, **Nguyen-Thoi T** (2009) A variationally consistent α FEM (VC α FEM) for solid mechanics problems. *International Journal for Numerical Methods in Engineering*; (revised)
29. Nguyen-Xuan H, Liu GR, **Nguyen-Thoi T**, Vu-Do HC (2009) An edge-based smoothed finite element method with stabilized discrete shear gap technique for functionally graded Reissner-Mindlin plates. *Smart Materials and Structures*; (submitted)
30. Nguyen-Xuan H, Liu GR, **Nguyen-Thoi T**, Vu-Do HC (2009) An edge-based smoothed finite method with stabilized discrete shear gap technique for skew rhombic plate analysis. *International Journal of Solids and Structures*; (submitted)
31. Nguyen-Xuan H, Liu GR, **Nguyen-Thoi T** (2009) An alpha finite element method (α FEM) for analysis of 2-D piezoelectric structures. *Smart Materials and Structures*; (submitted)